JYU DISSERTATIONS 628

Zhuoran Geng

Piezoelectrically Mediated Acoustic Phonon Tunneling

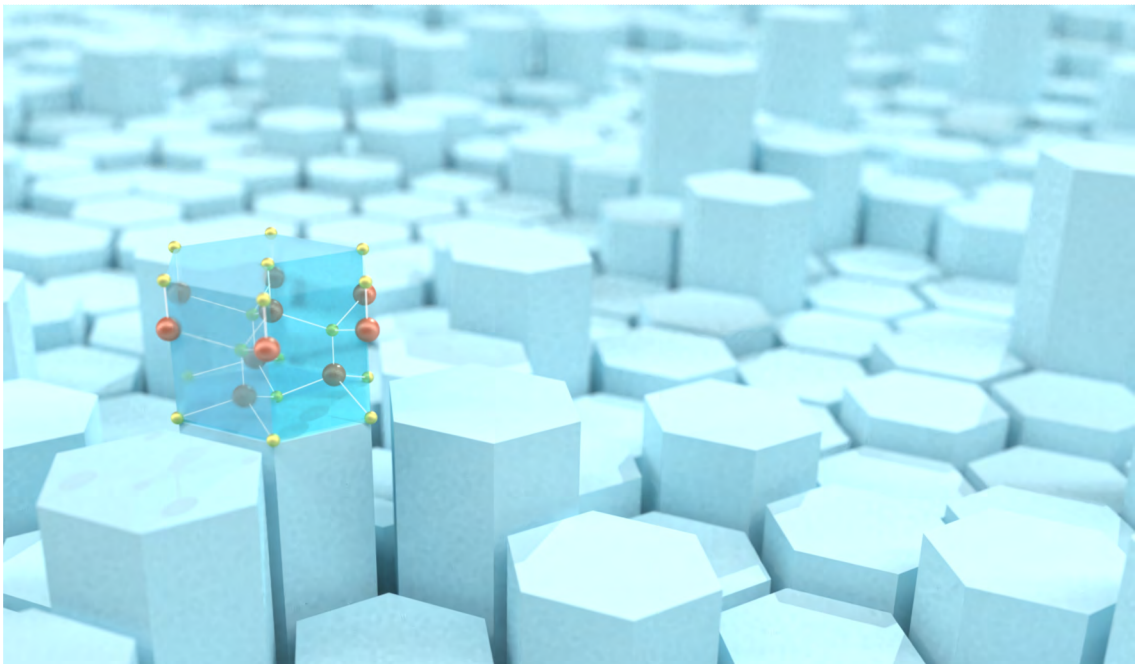

UNIVERSITY OF JYVÄSKYLÄ
FACULTY OF MATHEMATICS
AND SCIENCE

JYU DISSERTATIONS 628

Zhuoran Geng

Piezoelectrically Mediated Acoustic Phonon Tunneling

Esitetään Jyväskylän yliopiston matemaattis-luonnontieteellisen tiedekunnan suostumuksella
julkisesti tarkastettavaksi Ylistönrinteen auditoriossa FYS1
huhtikuun 21. päivänä 2023 kello 12.

Academic dissertation to be publicly discussed, by permission of
the Faculty of Mathematics and Science of the University of Jyväskylä,
in Ylistönrinne, auditorium FYS1, on April 21, 2023, at 12 o'clock.

JYVÄSKYLÄN YLIOPISTO
UNIVERSITY OF JYVÄSKYLÄ

JYVÄSKYLÄ 2023

Editors
Ilari Maasilta
Department of Physics, University of Jyväskylä
Päivi Vuorio
Open Science Centre, University of Jyväskylä

ISBN 978-951-39-9532-4 (PDF)
URN:ISBN:978-951-39-9532-4
ISSN 2489-9003

Permanent link to this publication: http://urn.fi/URN:ISBN:978-951-39-9532-4

ABSTRACT

Geng, Zhuoran
Piezoelectrically mediated acoustic phonon tunneling

Although purely acoustic waves cannot exist in vacuum by definition, an acoustic phonon can in fact "jump" or "tunnel" across a vacuum gap between two piezoelectric solids. The dissertation presents the author's work to provide a generally applicable theoretical formulation and an experimental demonstration of acoustic phonon tunneling between arbitrarily anisotropic and oriented piezoelectric crystals.

Within the continuum anisotropic linear elasticity theory and the quasistatic approximation, this work solves the acoustic wave tunneling problem with two different approaches for a plane-plane geometry, acquiring the solutions of reflection and transmission of all the partial waves for any incoming wave mode, taking fully into account mode conversions. Such formalism can be applied to a practical numerical or even an analytical implementation, as a few chosen analytical and numerical examples demonstrate.

A strikingly simple resonant tunneling condition was discovered in this work, which leads to the complete tunneling of an acoustic phonon, a unity transmission of the acoustic wave across vacuum without reflection. The detailed analytical proof and numerical demonstration of such complete phonon tunneling are presented.

Furthermore, this formalism was applied to investigate the heat flux associated with the phonon tunneling mediated by piezoelectricity. A few numerical results are demonstrated and compared with other near-field heat transfer mechanisms. In particular, this work shows that such heat transfer is significant when a vacuum gap size is smaller than the phonon characteristic wavelength, and even becomes the dominant mechanism at temperatures lower than 50 K.

Lastly, an experimental demonstration of the heat transfer mediated by acoustic phonon tunneling is presented, using two suspended piezoelectric microscopic beams at sub-kelvin temperatures. The results of the measurements provide qualitative evidence of the heat transfer, with comparisons between different vacuum gap widths and with non-piezoelectric devices. However, the quantitatively determined transferred power is not in good agreement with the theoretical estimations, and possible causes of the discrepancy are discussed.

Keywords: Phonon tunneling, near field heat transfer, Stroh formalism, arbitrary crystal orientation, piezoelectricity, low temperature heat transfer.

TIIVISTELMÄ (ABSTRACT IN FINNISH)

Geng, Zhuoran
Pietsosähköilmiön avustama akustisten fononien tunnelointi

Vaikka puhtaat akustiset aallot eivät voi esiintyä tyhjiössä määritelmänsä mukaan, akustinen fononi voi itse asiassa "hypätä" tai "tunneloitua" tyhjiöraon yli kahden pietsosähköisen materiaalin välillä. Tässä väitöskirjassa esitetään uusi yleisesti sovellettava teoria sekä kokeellinen demonstraatio akustisten fononien tunneloitumiselle kahden mielivaltaisesti anisotrooppisen ja suunnatun pietsosähköisen kiteen välillä.

Käyttäen anisotrooppista jatkuvan aineen lineaarista elastisuusteoriaa ja kvasistaattista approksimaatiota, tässä työssä ratkaistaan akustisten aaltojen tunnelointiongelma käyttäen kahta eri lähestymistapaa taso-taso geometriassa, saaden ratkaisut kaikkien osa-aaltojen heijastuksille ja läpäisyille, minkä tahansa sisääntulevan aaltomoodin tapauksessa, ottaen täysin huomioon moodikonversiot. Formalismia voidaan käyttää käytännön numeerisiin tai jopa analyyttisiin sovelluksiin, kuten muutamin esimerkein osoitetaan.

Työssä löydettiin silmiinpistävän yksinkertainen resonanssitunnelointi-ehto, joka johtaa akustisen fononin täydelliseen tunnelointiin, eli akustisen aallon transmissioon tyhjiön yli ilman heijastuksia. Myös yksityiskohtainen analyyttinen todistus tälle täydelliselle fononitunneloinnille esitetään, kuten myös numeerinen todistus.

Lisäksi formalismia käytettiin pietsosähköisen kytkennän mahdollistaman fononitunnelointi-lämpövuon tutkimiseen. Muutama numeerinen esimerkki esitetään, ja niitä verrataan muihin lähikentän lämmönsiirtomekanismeihin. Eiryisesti tämä työ osoitti, että tällainen lämmönsiirtomekanismi on merkittävä, kun tyhjiörako on pienempi kuin fononien karakteristinen aallonpituus, ja muodostuu dominoivaksi alle 50 K lämpötiloissa.

Lopuksi esitetään kokeellinen demonstraatio akustisten fononien tunneloinnin mahdollistamasta lämmönsiirrosta, käyttäen kahta itsekantavaa pietsosähköistä palkkia alle Kelvinin lämpötiloissa. Mittausten tulokset todistavat kvalitatiivisesti lämmönsiirron eri raon leveyksillä, seka verraten sitä ei-pietsosähköisiin näytteisiin. Mitattu lämpöteho ei kuitenkaan ole kvantitatiivisesti yhtenevä teoreettisten arvioiden kanssa. Tähän eroavuuteen johtavia mahdollisia syitä pohditaan lopuksi.

Author

Zhuoran Geng
Department of Physics
University of Jyväskylä
Finland

Supervisor

Professor Ilari Maasilta
Department of Physics
University of Jyväskylä
Finland

Reviewers

Research Director Philippe Ben-Abdallah
Institut d'Optique, CNRS
Université Paris-Saclay
France

Research Director Jean-François Robillard
Institut d'Electronique de Microélectronique et de Nanotechnologie (IEMN), CNRS
Université Lille
France

Opponent

Professor Achim Kittel
Department of Physics
Carl-von-Ossietzky Universität Oldenburg
Germany

PREFACE

The work presented in this thesis has been carried out at the Department of Physics in the Nanoscience Center in the University of Jyväskylä.

First and foremost, I'm deeply grateful to my supervisor Prof. Ilari Maasilta for giving me the opportunity and for guiding me to conduct my Ph.D. research. It is his willingness to share knowledge and wisdom, and our numerous discussions that made this thesis possible.

I wish to express my sincere gratitude to Dr. Saumyadip Chaudhuri, Dr. Kimmo Kinnunen, Mr. Tarmo Suppula, Dr. Minna Nevala, Dr. Juhani Julin, Dr. Tero Isotalo and Mr. Anderii Torgovkin. Their help, advice and support in the fabrication, cryogenics and measurements were vital to the success of this work. Special gratitude also belongs to Dr. Tuomas Puurtinen for the useful guidance and fruitful discussions on scientific computing, which was an uncharted water to me before this work.

I would like to thank all the former and present group members for the great experience to work together during all these years. Particularly, I wish to thank Dr. Panu Koppinen, Dr. Yaolan Tian, Mr. Ari Helenius, Mr. Aki Ruhtinas, Mr. Tatu Korkiamäki, Mr. Jaakko Mastomäki, Dr. Samuli Heiskanen, Mr. Teemu Loippo, Mr. Ilmo Räisänen, Dr. Mikko Palosaari and Mr. Toivo Hakanen for the nice working atmosphere they created and the always warm welcome they provided. It has been a pleasure to work with you.

Many thanks also go to Dr. Boxuan Shen, Dr. Chuan Wang and Dr. Xi Chen. They have been my dearest friends, walking alongside with me for this whole journey. My life becomes so lively with the fun hours we spent together, no matter how far away we were physical separated.

Lastly, I will be forever grateful to my parents and my family for their unconditional support and encouragement. And most importantly, I wish to thank the love of my life, my wife Tianbai Zhao, for her limitless patient understanding and love.

Jyväskylä, February 2023

Zhuoran Geng

LIST OF INCLUDED ARTICLES

PI Z. Geng & I. J. Maasilta. *Acoustic wave tunneling across a vacuum gap between two piezoelectric crystals with arbitrary symmetry and orientation*. Phys. Rev. Research **4** 033073 (2022).

PII Z. Geng & I. J. Maasilta. *Complete tunneling of acoustic waves between piezoelectric crystals*. arXiv:2209.08287 Submitted manuscript.

PIII Z. Geng & I. J. Maasilta. *Heat transfer across a vacuum gap induced by piezoelectrically mediated acoustic phonon tunneling*. arXiv:2303.05084 Manuscript.

PIV Z. Geng & I. J. Maasilta. *Experimental demonstration of heat transfer mediated by acoustic phonon tunneling between vacuum separated piezoelectric solids*. Manuscript.

Author's contribution

The main results of this thesis have been reported in articles P.I, P.II, P.III and P.IV. The author of this thesis has written the first drafts of articles P.I and the manuscripts P.II P.III and P.VI. The theory developments in P.I, P.II and P.III were performed by the author in collaboration with the supervisor, all numerical computations in P.I, P.II and P.III were fully done by the author. The sample fabrication, the measurements and the data analysis were fully done by the author in P.IV, with contributions to the experimental and sample designs.

OTHER PUBLICATIONS TO WHICH THE AUTHOR HAS CONTRIBUTED

API **Z. Geng** & K. M. Kinnunen & I. J. Maasilta, *Development of an Inductive NIS Thermometer*. J. Phys.: Conf. Ser. **400** 052005 (2012).

APII I. J. Maasilta & T. A. Puurtinen & Y. Tian & **Z. Geng**, *Phononic Thermal Conduction Engineering for Bolometers: From Phononic Crystals to Radial Casimir Limit*. J. Low Temp. Phys. **184** 211-216 (2016)

APIII Y. Tian & T. J. Isotalo & M. P. Konttinen & J. Li & S. Heiskanen & **Z. Geng** & I. J. Maasilta, *Intregrating metallic wiring with three-dimensional polystyrene colloidal crystals using electron-beam lithography and three-dimensional laser lithography*. J. Phys. D: Appl. Phys. **50** 055302 (2017)

APIV I. M. W. Räisänen & **Z. Geng** & K. M. Kinnunen & I. J. Maasilta, *Normal metal-insulator-superconductor thermometers and coolers with titanium-gold bilayer as the normal metal*. J. Phys.: Conf. Series **969** 012090 (2018)

APV Y. Tian & T. A. Puurtinen & **Z. Geng** & I. J. Maasilta, *Minimizing Coherent Thermal Conductance by Controlling the Periodicity of Two-Dimensional Phononic Crystals*. Phys. Rev. Appl. **12** 014008 (2019)

APVI **Z. Geng** & A. P. Helenius & I. J. Maasilta, *Superconductor Ferromagnet Tunnel Junction Thermoelectric Bolometer and Calorimeter with a SQUID Readout*. J. Low Temp. Phys. **199** 585-592 (2020).

APVII S. Heiskanen & **Z. Geng** & J. Mastomäki & I. J. Maasilta, *Nanofabrication on 2D and 3D Topography via PositiveTone Direct-Write Laser Lithography*. Adv. Eng. Mater. **22** 1901290 (2020)

APVIII **Z. Geng** & I. J. Maasilta, *Analytical Models for the Pulse Shape of a Superconductor-Ferromagnet Tunnel Junction Thermoelectric Microcalorimeter*. J. Low Temp. Phys. **209** 419-426 (2022)

APIX **Z. Geng** & A. Hijano & S. Ilić & M Ilyn & I. J. Maasilta & A. Monfardini & S. Khorshidian & M. Spies & E. Strambini & P. Virtanen & M. Calvo & A. P. Helenius & S. Khorshidian & C. I. Levartoski de Araujo & F. Levy-Bertrand & C. Rogero & F. Giazotto & F. S. Bergeret & T. T. Heikkilä, *Superconductor-ferromagnet hybrids for non-reciprocal electronics and detectors*. arXiv:2302.12732 (2023)

CONTENTS

1 GENERAL INTRODUCTION

There is a famous saying from an ancient influential Chinese philosopher *Zhuang Zhou* from around 4th century BC: One foot-long of a wood stick, cut off half each day, eternally inexhaustible. There is a little bit inaccuracy in his statement: after 30 days of wood-cutting, what left is only 0.5 nm-long[1], a length scale of an atom, and is hardly to be called as "wood stick" anymore. Of course, for people from ancient times without the knowledge of modern science, it is impossible to know the physical and chemical properties at a microscopic level.

There is another well-known statement from a modern influential American entrepreneur *Gordon Moore* in 1965: the number of components per integrated circuit will be doubling every two years[2]. Such prediction worked beautifully since then, and became known as *Moore's law*. However, approaching the 30th two-year-period, Moore's law is nearing to its end [Waldrop, 2016]. Just as that ancient wood stick, things got too small, and the changes of the properties and the rise of new phenomena demand more understanding on their underlying physics, becoming limitations for the growth of the transistor density.

One of such challenges is heat management, the ability to control heat transfer between bodies for suitable temperatures. For a macroscopic system, heat transfer mainly takes form as convection, conduction and radiation, among which only radiation[3], carried by propagating thermal photons, can transport heat between bodies that are separated by vacuum. However, when the separation becomes microscopic, radiation is not the only form anymore, and new heat transfer mechanisms emerge.

Near-field radiative heat transfer (NFRHT) is discovered to be capable of transporting orders of magnitude higher heat flux if the gap width is below the dominant photon thermal wavelength[4], compared to that of (far-field) radiation.

---

1 The length of the wood stick L is a function of the number of days n, reads as $L(n) = 0.3/2^{n-1}$ m. After 30 days, $L(30) = 0.56$ nm.

2 The *Moore's law* is originally posited to be a *doubling of every year* in 1965 [Moore, 1965], but later is revised to be a *doubling of every two year* in 1975 [Moore, 1975].

3 To be more precise, this is *far-field radiation* that is carried by propagating photons, in contrast to the near-field radiative heat transfer which is enabled by photon tunneling.

4 About 10 μm at room temperature.

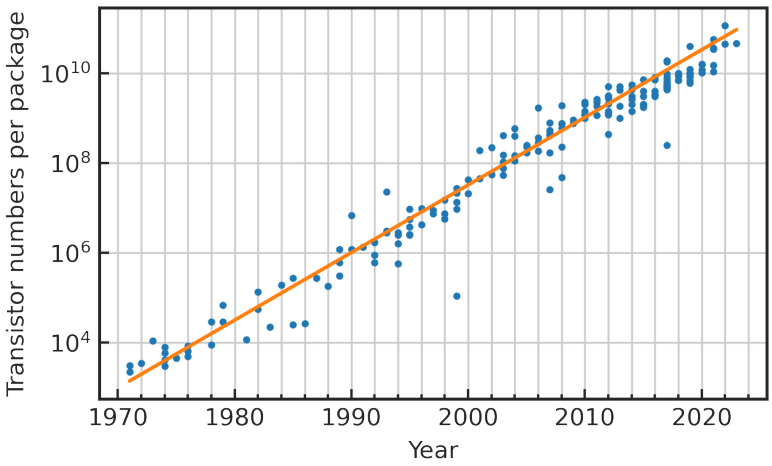

FIGURE 1 Transistor numbers per package as a function of time [Wikipedia, 2023].

From the decades-long collective efforts devoted by the scientists and engineers [5], NFRHT has opened promising applications in the fields of heat management [Guha et al., 2012; Ben-Abdallah and Biehs, 2014; Zhu et al., 2019], energy harvesting [Fiorino et al., 2018; Bhatt et al., 2020; Lucchesi et al., 2021a], and thermal spectroscopy [Kittel et al., 2008; Jones and Raschke, 2012; Ben-Abdallah, 2019], to name a few.

Yet there is another much less known heat transfer mechanism unveiling its appearance in the microscopic world, which is *acoustic phonon tunneling*. Acoustic phonon is a particle-like quantum mechanical description for the propagation of the vibrations in a solid, and is the major heat carrier for insulating, dielectric materials. From its definition, it may be hard to imagine that a phonon could travel across a vacuum gap transferring the heat it carries. However, theoretical and experimental work presented in this dissertation will show that, if using materials that can generate an electric field when deformed, called the piezoelectric effect, an acoustic phonon can in fact transfer heat across a vacuum gap via tunneling.

This work is not the first to suggest taking advantage of piezoelectricity in such a way. Several pioneering studies have been reported in the past [Kaliski, 1966; Balakirev and Gorchakov, 1977; Balakirev et al., 1978; Al'shits et al., 1993; Darinskii and Weihnacht, 2003; Prunnila and Meltaus, 2010]. However, this work is the first to provide a generally applicable theoretical formulation for the acoustic phonon tunneling[Geng and Maasilta, 2022a] and an experimental demonstration of the piezoelectrically mediated heat transfer (PEMHT) between vacuum separated piezoelectric crystals[Geng and Maasilta, 2023a]. The approach described in this dissertation can be applied for any anisotropic and arbitrarily oriented piezoelectric crystals, acquiring the solutions of reflection and transmission of all partial waves for any incoming mode, taking fully into account mode

[5] There are numerous theoretical and experimental studies that have been carried out regarding NFRHT, here we list some selected seminal works and reviews: Rytov [1953]; Polder and Van Hove [1971]; Pendry [1999]; Joulain et al. [2005]; Volokitin and Persson [2007]; Basu et al. [2009]; Song et al. [2015]; Kim et al. [2015]; Kloppstech et al. [2017]; Lucchesi et al. [2021b], and this list is not mean to be exhaustive.

conversions.

Moreover, this work presents a strikingly simple resonance tunneling condition that leads to a complete tunneling of the acoustic phonon[Geng and Maasilta, 2022b], an unity transmission of the acoustic wave across vacuum without reflection. In addition, the numerical calculation[Geng and Maasilta, 2023b] shows that the PEMHT between the solids will become the dominant heat carrying mechanism at cryogenic temperatures, compared to channels mediated by photon and other phonon tunneling mechanisms.

The main body of this dissertation is divided into three chapters. In Chapter 2, the elasticity theory of piezoelectricity will be briefly introduced, focusing on the the basic definitions, notations and the mathematical formalism that are involved in the dissertation. In particular, the main aspects of the *extended Stroh formalism*, a powerful mathematical tool for the anisotropic scattering problem in piezoelectric materials, will be derived here. Chapter 3 presents the overview of the theoretical work done by the author. The acoustic wave tunneling problem will be solved with two different approaches, and will be also be illustrated with both analytical and numerical examples. Complete tunneling of the phonon will be analytically proved and discussed in detail. Lastly, heat transfer associated with the tunneling will be investigated. Chapter 4 discusses the experimental part of the author's work. The experimental scheme, device fabrication and measurement procedures will be presented first, and the measurement results will be qualitatively and quantitatively discussed.

2 ELASTICITY THEORY OF PIEZOELECTRICITY

Although it is tempting to directly dive into the intriguing results of this work, the definitions, notations and mathematical formalism involved in this dissertation can be quite complicated for the readers that are not familiar with the field. In addition, the *Extended Stroh formalism*, which is a powerful mathematical tool used for dealing with the anisotropic scattering problem in piezoelectric materials, may also be unfamiliar to many physicists. For these reasons, the author dedicates this chapter to the foundations this study is built upon. In the first section, the basic framework of *continuum anisotropic linear elasticity theory* will be briefly introduced. *Piezoelectricity* will be added into this framework in the second section. In the last section, the main aspects of the extended Stroh formalism will be presented with derivations. While walking through these sections, the conventions of the definitions, notations and coordinate system of this dissertation will also be established and clarified.

2.1 Acoustic field in solids

Elasticity theory is a mathematical tool to describe the relation between force and deformation of a solid material. The main body of this work is built within the continuum anisotropic linear elasticity theory, which implies four underlying assumptions. Firstly, the material is modeled as a continuous medium rather than discrete atoms, so that properties such as density or elastic constants are regarded as continuous functions representing averages of microscopic quantities. Secondly, the material deforms elastically under the influence of the force, and thereby will return to its initial shape and size upon the removal of the external loads, perfectly reversible. Moreover, the deformations are considered to be small, thus the relationship between the *strain*, the measure of the deformation, and the *stress*, the traction force within the solid, is linearized and approximated by Hooke's law which was originally formulated by Robert Hooke in the 17th century. Finally, the solids that are studied in this work are not generally

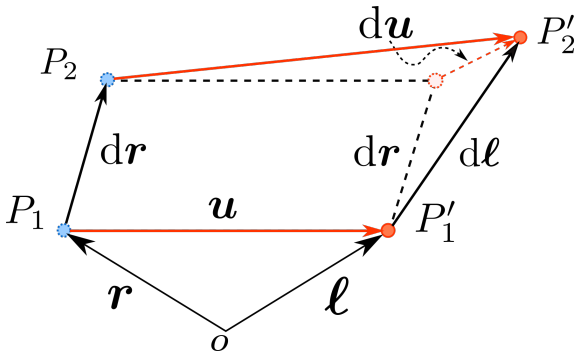

FIGURE 2 Deformation of a solid.

isotropic, and may only be symmetric with respect to particular transformations of the coordinates.

2.1.1 Deformation of a solid

Consider an infinitesimal volume element P_1 at its equilibrium position $\boldsymbol{r}$ with respect to some origin $\boldsymbol{o}$ in a continuum medium, as illustrated in Figure.2. If a deformation occurs at time t, this point displaces itself to P_1' which is at a new position $\boldsymbol{\ell}(\boldsymbol{r}, t)$. The difference between these two positions is the *displacement* vector:

$$\boldsymbol{u}(\boldsymbol{r}, t) = \boldsymbol{\ell}(\boldsymbol{r}, t) - \boldsymbol{r}, \tag{1}$$

which can be divided into three components along Cartesian xyz axes, and is conventionally denoted with a vertical vector form:

$$\boldsymbol{u} = \begin{bmatrix} u_x \\ u_y \\ u_z \end{bmatrix}. \tag{2}$$

In this dissertation a common and useful shorthand form of vectors will be frequently used for the sake of simplicity, *e.g.* u_i where the subscript i is an index that is assumed to run over x, y, z.

However, the displacement vector u_i, or a more restricting quantity *displacement gradient* $\nabla_j u_i \equiv \partial u_i / \partial r_j$ is not a good measure of the deformation, because they can be produced solely by a rigid translation or a rotation. A more appropriate metric is the differential displacement $\mathrm{d}u_i = \mathrm{d}\ell_i - \mathrm{d}r_i$ from the point P_1 to a neighboring point P_2, as illustrated in Figure 2. Consequently, the material deformation Δ_d is conventionally defined as:

$$\begin{aligned} \Delta_d &\equiv \mathrm{d}\ell_i^2 - \mathrm{d}r_i^2 \\ &= 2\mathrm{d}r_i S_{ij} \mathrm{d}r_j, \end{aligned} \tag{3}$$

where S_{ij} is an element of the second-order *strain tensor* $\boldsymbol{S}$. A summation convention for repeated indices is applied where subscript indices i, j needed to be summed over the ranges x, y, z.

Subscript L	Expression ij
1	xx
2	yy
3	zz
4	yz, zy
5	xz, zx
6	xy, yx

TABLE 1 The abbreviated Voigt notation.

The exact expression of the strain tensor reads as $S_{ij} = (\nabla_j u_i + \nabla_i u_j + \sum_k \nabla_i u_k \nabla_j u_k)/2$, but with the small deformation assumption the quadratic terms can be neglected, leading to a linearized *strain-displacement relation*:

$$S_{ij} \equiv \frac{1}{2}\left(\nabla_j u_i + \nabla_i u_j\right). \tag{4}$$

This strain tensor has an off-diagonal symmetry, thus it can be transformed into a more convenient, six-element column vector form:

$$S_L = \nabla_{Lj} u_j \tag{5}$$

following the *Voigt notation convention* with the translation rule presented in Table.1. With Voigt convention, the 3×6 differential operator matrix ∇_{Lj} reads as:

$$\nabla_{Lj} \rightarrow \begin{bmatrix} \partial/\partial r_x & 0 & 0 \\ 0 & \partial/\partial r_y & 0 \\ 0 & 0 & \partial/\partial r_z \\ 0 & \partial/\partial r_z & \partial/\partial r_y \\ \partial/\partial r_z & 0 & \partial/\partial r_x \\ \partial/\partial r_y & \partial/\partial r_x & 0 \end{bmatrix}. \tag{6}$$

2.1.2 Constitutive relations in solid

When a solid begins to vibrate acoustically, the displacement u_i and strain S_L capture the motion and deformation of the medium. At the same time, *stresses* develop between the neighboring volume elements acting as restoring forces with respect to the equilibrium state. Such vibration can be driven by external forces $\boldsymbol{F}$ either by the long-range *body force* or by the surface *traction force*.

The body force, *e.g.* given rise by gravity or electric field, acts directly upon the interior of the solid, and can be expressed for each volume element $\mathrm{d}V$ as:

$$\mathrm{d}\boldsymbol{F} = \boldsymbol{F}^V \mathrm{d}V, \tag{7}$$

where $\boldsymbol{F}^V$ is the body force with a unit of N/m^3. On the other hand, the surface force that is applied upon the boundary of a solid relies on the internal stresses to transmit the excitations throughout the body. These internal stresses act at the

interfaces between the neighboring volume elements, and can be expressed as internal tractions exerting the forces on the interfaces as:

$$\mathrm{d}\boldsymbol{F} = \boldsymbol{\sigma} \cdot \boldsymbol{n} \mathrm{d}A, \tag{8}$$

where $\boldsymbol{n}$ is the unit vector normal to surface element $\mathrm{d}A$, and $\boldsymbol{\sigma}$ is the second-order *stress tensor* with the unit of N/m^2. Additionally, within the scope of this work, the stress tensor has also off-diagonal symmetry[1], thus when the Voigt notation convention is applied, $\sigma_{ij} \rightarrow \sigma_L$, in a similar way as for the abbreviated strain tensor.

With given stimuli, the medium of a solid responses dynamically through its motion and deformation. Under the linear elasticity framework, the *stress-strain relation* can be described by *Hooke's Law*:

$$\sigma_K = c_{KL} S_L, \tag{9}$$

in which a proportionality factor c_{KL}, the *elastic stiffness tensor*, linearly maps two second-order tensors, and $K, L = 1, ..., 6$ are the Voigt indices.

The total forces that are exerted by the stimuli are the integrals of the body force over the volume δV and the surface force over the area δA. *Newton's law of motion* then states:

$$\int_{\delta A} \boldsymbol{\sigma} \cdot \boldsymbol{n} \mathrm{d}S + \int_{\delta V} \boldsymbol{F}^V \mathrm{d}V = \int_{\delta V} \rho \frac{\partial^2 \boldsymbol{u}}{\partial t^2} \mathrm{d}V, \tag{10}$$

where ρ is the mass density of the medium.

By assuming a sufficiently small volume $\delta V \rightarrow 0$, the differential form of the above equation can be obtained by taking divergences of both sides, and reads as:

$$\nabla_{iK} \sigma_K \equiv \rho \frac{\partial^2 u_i}{\partial t^2} - F_i^V. \tag{11}$$

Eqs.(9) and (11) are called the *constitutive equations* of elastic solids. Together with Eq.(5), the relations among the displacement u_i, strain S_L and stress σ_L are thus established.

2.1.3 Acoustic Poynting's theorem

As one of the main objectives of this work is to study the heat transfer carried by tunneling phonons, the knowledge of how the power flows inside the solid associated with the acoustic vibration is necessary. In this section, the energy conservation relation of the elastic medium will be formulated, analogous to the *Poynting's theorem* used in electromagnetism, and the power flow (flux), which has a unit of W/m^2, will be derived and presented as *acoustic Poynting vector* $\boldsymbol{P}$.

[1] Under the linearized vibration theory, the body torque is negligible and thus the stress matrix is always symmetric.

Since the Voigt notation convention is adopted in this dissertation, $\boldsymbol{\nu}$, a tensor representation of a velocity vector, is introduced customarily to match to the strain and stress tensor, and is defined as:

$$\nabla_j \nu_{jL} = \frac{\partial}{\partial t}(\nabla_{Lj} u_j) = \frac{\partial S_L}{\partial t}. \tag{12}$$

An equality [Auld, 1969]:

$$\nabla_j(\nu_{jL}\sigma_L) = \frac{\partial u_j}{\partial t}(\nabla_{jL}\sigma_L) + \sigma_L(\nabla_j \nu_{jL}), \tag{13}$$

which is an analog of the divergence identity, can be found to relate the velocity tensor to the stress tensor.

By inserting the Eqs.(11) and (12) into the right-hand side (RHS), integrating over a volume V, and applying the divergence theorem (Gauss's theorem), Eq.(13) becomes:

$$\oint_A (-\boldsymbol{\nu}\cdot\boldsymbol{\sigma})\cdot\boldsymbol{n}\,\mathrm{d}A = -\int_V \rho\frac{\partial \boldsymbol{u}}{\partial t}\cdot\frac{\partial^2 \boldsymbol{u}}{\partial t^2}\,\mathrm{d}V - \int_V \boldsymbol{\sigma}\cdot\frac{\partial \boldsymbol{S}}{\partial t}\,\mathrm{d}V + \int_V \frac{\partial \boldsymbol{u}}{\partial t}\cdot\boldsymbol{F}^V\,\mathrm{d}V\,, \tag{14}$$

where A is the surface enclosing the volume with $\boldsymbol{n}$ the unit vector normal to the surface directed outward.

The first term on the RHS of Eq.(14) can be identified as the rate of change of the total *stored kinetic energy* in the medium, and its integrand is thus the rate of change of the stored kinetic energy density[2] u_K:

$$\frac{\partial \mathrm{u}_K}{\partial t} = \rho\frac{\partial u_j}{\partial t}\frac{\partial}{\partial t}\frac{\partial u_j}{\partial t}. \tag{15}$$

Interchanging the subscript indices i, j leads to the same value of u_K, thereby one finds[3]:

$$\mathrm{u}_K = \frac{1}{2}\rho\left(\frac{\partial u_j}{\partial t}\right)^2. \tag{16}$$

Using the same approach, the second term is identified to be the rate of change of the total *stored elastic energy*, whose density u_S reads as:

$$\mathrm{u}_S = \frac{1}{2}S_K c_{KL} S_L. \tag{17}$$

The last term is the total power supplied to the medium by the body force.

Because there is no energy loss in the system, the left-hand side (LHS) of Eq.(14) is the sum of the supplied power and the reductions in the stored energy, and thereby can be interpreted as the total power flow outward through the surface A. Thus its integrand is recognized as the acoustic analog of the *Poynting's vector* in electromagnetism:

$$\boldsymbol{P} = -\boldsymbol{\nu}\cdot\boldsymbol{\sigma}. \tag{18}$$

---

2 To avoid confusion with the displacement vector u_i, the energy *density* will be designated with the Roman font u. The unit is J/m^3.

3 Here the product rule of the derivative is used: $\mathrm{d}u_j u_j = u_j \mathrm{d}u_j + u_j \mathrm{d}u_j$

2.1.4 Acoustic plane wave in a solid

For a plane wave, a general form of the wave solution to the equation of motion (11) reads as:

$$\boldsymbol{u} = \sum_{\alpha} \boldsymbol{A}_{\alpha} e^{-i\boldsymbol{k}\cdot\boldsymbol{r}+i\omega t}, \tag{19}$$

where $\boldsymbol{k}$ is the wave vector, ω is the angular frequency, i is the imaginary unit, and $\boldsymbol{A}_{\alpha}$ is the amplitude of an orthogonal α component, which is commonly referred as the *wave mode* α, where the full wave solution is a linear combination of all the modes. Such a solution, although simple, is commonly known as the complex *harmonic plane wave* solution, whose real part describes the physical observable, whereas the imaginary part signifies the phase. It is widely used as a good approximation in many studies, such as electromagnetic waves in a homogeneous medium and *bulk waves* in elasticity theory. In the scope of this work, the plane wave solution will be exclusively used for its simplicity, so that a deeper understanding or even analytical solutions can be achieved for the phonon tunneling phenomena. In addition, for the most part of this work, the medium is considered to be source-free, thereby the body force is zero, $\boldsymbol{F}^V = 0$, unless specifically noted.

With the general wave solution, Eq.(19), the results that were obtained in previous sections can be developed further for each mode (linear term). Firstly, the differential operators can be substituted by $\nabla_j \rightarrow -ik_j$ and $\nabla_{Lj} \rightarrow -ik_{Lj}$, in which k_{Lj} is explicit defined as:

$$k_{Lj} \rightarrow \begin{bmatrix} k_x & 0 & 0 \\ 0 & k_y & 0 \\ 0 & 0 & k_z \\ 0 & k_z & k_y \\ k_z & 0 & k_x \\ k_y & k_x & 0 \end{bmatrix}. \tag{20}$$

Other simplified equations for plane waves are also summarized below:

$$\text{Strain-displacement relation:} \quad S_L = -ik_{Lj}u_j, \tag{21}$$

$$\text{Stress-strain relation:} \quad \sigma_K = -ic_{KL}k_{Lj}u_j, \tag{22}$$

$$\text{Equation of motion:} \quad ik_{iK}\sigma_K = \rho\omega^2 u_i, \tag{23}$$

$$\text{Velocity tensor:} \quad k_j v_{jL} = i\omega k_{Lj} u_j, \tag{24}$$

$$\text{Peak stored kinetic energy density:} \quad (\mathrm{u}_K)_{peak} = \frac{1}{2}\rho\omega^2 u_i^* u_i, \tag{25}$$

$$\text{Peak stored elastic energy density:} \quad (\mathrm{u}_S)_{peak} = \frac{1}{2} u_i k_{iK} c_{KL} k_{Lj} u_j^*, \tag{26}$$

$$\text{Complex Poynting vector:} \quad P_i = \frac{i}{2} v_{iK}^* c_{KL} k_{Lj} u_j. \tag{27}$$

The equation of motion, Eq.(23), governs the dynamics of the wave solution, and, by substituting the stress-strain relation Eq. (22), it becomes the *Christoffel*

equation, which reads as:

$$(k^2\Gamma_{ij} - \rho\omega^2\delta_{ij})u_j = 0, \tag{28}$$

where $\delta_{ij} = [i = j]$ is the *Kronecker delta*[4], $k = |\boldsymbol{k}|$ is the norm of the wave vector, and $\Gamma_{ij} = k_{iK}c_{KL}k_{Lj}/k^2$ is the *Christoffel matrix*.

The *phase velocity* $v = \omega/k$ of the wave can be obtained by solving the secular equation:

$$\Omega(\omega, \boldsymbol{k}) \equiv ||k^2\Gamma_{ij} - \rho\omega^2\delta_{ij}|| = 0, \tag{29}$$

in which the operator $||...||$ denotes the determinant. For an infinite anisotropic medium, there are generally three solutions, each having a corresponding displacement vector u_i and a phase velocity. These solutions are commonly referred as the three uniform *bulk wave modes*, and their linear combination is the wave solution Eq.(19).

There are two different conventions that have been applied to categorize these bulk wave modes. One of the approaches is to examine the relation between the displacement vector $\boldsymbol{u}$ and the wave propagation direction $\boldsymbol{k}$: when the displacement of an elastic wave is (mostly) parallel to the propagation direction, it is identified as a *(quasi-) longitudinal* wave, or an L mode for short; if the displacement is (mostly) perpendicular to the propagation direction, it is a *(quasi-) shear* wave, or an S mode. For anisotropic medium, there are one (quasi-) longitudinal solution and two (quasi-) shear solutions, and they are most commonly the quasi modes.

The other convention is to sort the phase velocities $v = \omega/k$ of the wave modes from fastest to the slowest, and to assigns the modes, *(quasi-) longitudinal* wave (L), *fast (quasi-) transverse* wave (FT), and *slow (quasi-) transverse* wave (ST), in that order.

The *complex Poynting vector*, whose real part is the *time-averaged power flow* and the imaginary part is the *peak reactive power flow*, can be formulated starting from the equality:

$$\nabla_j(v_{jL}^*\sigma_L) = \frac{\partial u_j^*}{\partial t}(\nabla_{jL}\sigma_L) + \sigma_L(\nabla_j v_{jL}^*), \tag{30}$$

which is similar to Eq.(13).

The conservation of the complex power is then:

$$\oint_S \frac{-\boldsymbol{v}^* \cdot \boldsymbol{\sigma}}{2} \cdot \boldsymbol{n}\, \mathrm{d}S = i\omega \int_V \left[(\mathrm{u}_S)_{peak} - (\mathrm{u}_K)_{peak}\right] \mathrm{d}V + i\omega \int_V \frac{-\boldsymbol{u}^* \cdot \boldsymbol{F}^V}{2}\, \mathrm{d}V\,, \tag{31}$$

where:

$$\begin{aligned} (\mathrm{u}_K)_{peak} &= \frac{1}{2}\rho \left|\frac{\partial \boldsymbol{u}}{\partial t}\right|^2 \\ (\mathrm{u}_S)_{peak} &= \frac{1}{2}\,\boldsymbol{\sigma} \cdot \boldsymbol{S}^*, \end{aligned} \tag{32}$$

[4] It is the index form of the unit matrix $\boldsymbol{I}$, and the condition takes the values $[True] = 1$ and $[False] = 0$.

are the peak kinetic and elastic stored energy density, respectively. The *complex acoustic Poynting vector* is thus defined as:

$$\boldsymbol{P} = -\frac{1}{2}\,\boldsymbol{v}^* \cdot \boldsymbol{\sigma}. \tag{33}$$

Since the scope of this work is focused on the time-averaged power, from hereafter the vector $\boldsymbol{P}$ is exclusively used as the complex Poynting vector, and

$$\boldsymbol{P}_{\mathrm{AV}} = -\frac{1}{2}\mathrm{Re}(\boldsymbol{v}^* \cdot \boldsymbol{\sigma}) \tag{34}$$

is the time-averaged power flow.

The acoustic wave in a solid often travels also with a modulated envelope, whose velocity is generally different from the wave's phase velocity in anisotropic medium, and is referred to as *group velocity*. A good example is the concept of *acoustic phonon*, whose propagation speed and direction are represented by its group velocity $\boldsymbol{g}$, and can be found from the expression $\boldsymbol{g} = \partial\omega/\partial\boldsymbol{k}$.

A common practice for finding the group velocity is to use the implicit differentiations of the Christoffel determinant, Eq.(29), written in the form:

$$\left(\frac{\partial\Omega}{\partial\omega}\delta\omega + \frac{\partial\Omega}{\partial k_i}\delta k_i\right)_{k_j} = 0, \tag{35}$$

from which one finds that the group velocity can be evaluated as:

$$\boldsymbol{g} = -\frac{\nabla_k\Omega}{\partial\Omega/\partial\omega}. \tag{36}$$

Alternatively, a more intuitive expression[Auld, 1990] will be derived and presented next, under the framework of this dissertation and the assumptions of source-free and lossless medium.

With two slightly different plane wave solutions

$$\begin{aligned}
\boldsymbol{u}_1 &= \boldsymbol{u}e^{i\omega t - i\boldsymbol{k}\cdot\boldsymbol{r}} \\
\boldsymbol{u}_2 &= (\boldsymbol{u} + \delta\boldsymbol{u})e^{i(\omega+\delta\omega)t - i(\boldsymbol{k}+\delta\boldsymbol{k})\cdot\boldsymbol{r}} \\
\boldsymbol{\sigma}_1 &= \boldsymbol{\sigma}e^{i\omega t - i\boldsymbol{k}\cdot\boldsymbol{r}} \\
\boldsymbol{\sigma}_2 &= (\boldsymbol{\sigma} + \delta\boldsymbol{\sigma})e^{i(\omega+\delta\omega)t - i(\boldsymbol{k}+\delta\boldsymbol{k})\cdot\boldsymbol{r}},
\end{aligned} \tag{37}$$

the sum of the complex velocity tensor identity [Eq.(30)] of both waves can be rearranged using the product rule of derivative into:

$$\nabla\cdot(\boldsymbol{v}_2^*\cdot\boldsymbol{\sigma}_1 + \boldsymbol{v}_1\cdot\boldsymbol{\sigma}_2^*) = \frac{\partial}{\partial t}\left(\rho\frac{\partial\boldsymbol{u}_1}{\partial t}\cdot\frac{\partial\boldsymbol{u}_2^*}{\partial t} + \boldsymbol{\sigma}_1\cdot\boldsymbol{S}_2^*\right), \tag{38}$$

where $\boldsymbol{v}$ and $\boldsymbol{S}$ are functions of $\boldsymbol{u}$ using Eqs.(24) and (21). Inserting the wave solutions and evaluating only the first-order quantities of $\delta\omega, \delta\boldsymbol{k}, \delta\boldsymbol{u}, \delta\boldsymbol{\sigma}$, one obtains:

$$\delta\boldsymbol{k}\cdot\frac{1}{2}(-\boldsymbol{v}^*\cdot\boldsymbol{\sigma} - \boldsymbol{v}\cdot\boldsymbol{\sigma}^*) = \delta\omega\left(\frac{1}{2}\rho\left|\frac{\partial\boldsymbol{u}}{\partial t}\right|^2 + \frac{1}{2}\boldsymbol{\sigma}\cdot\boldsymbol{S}^*\right). \tag{39}$$

The RHS is the sum of the peak stored kinetic u_K and elastic u_S energy densities, whereas the LHS can be identified as the real part of the complex Poynting vector, which represents the time-averaged power flow. Therefore, Eq.(39) implies that the group velocity[5] is given by the ratio between the time-averaged power flow and the averaged stored energy, and reads as:

$$\boldsymbol{g} = \frac{2\boldsymbol{P}_{AV}}{(u_K)_{peak} + (u_S)_{peak}}. \tag{40}$$

2.1.5 Crystal rotation

To solve the wave problem in an anisotropic solid for an arbitrary crystal orientation, a method for transforming the material tensors from a standard crystallographic orientation to a specific arbitrary rotation needs to be provided.

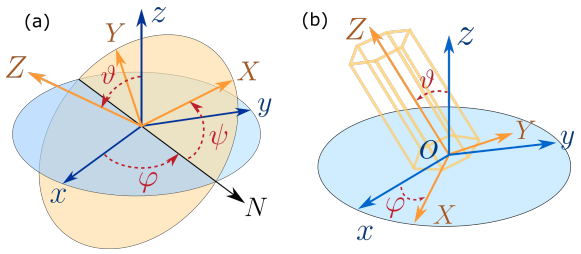

FIGURE 3 Demonstration of crystal rotation angles. (a) The general Euler angle system. (b) The cylindrical angle system for uniaxial crystals [Geng and Maasilta, 2022a], reproduced under the license CC BY 4.0.

The *Euler angle* system [Goldstein et al., 2011] has been commonly used to describe how a crystal is rotated with respect to a fixed laboratory coordinate system. In this system, two Cartesian frames, the XYZ which is the crystal intrinsic coordinates, and the xyz, the external fixed laboratory coordinates, are defined in this work. The relation between these two frames are fully described by three angles: ϑ, φ and ψ, as illustrated in Fig.3(a).

To achieve a specific crystal orientation $(\vartheta, \varphi, \psi)$, one needs to perform a sequence of rotations on the frames with respect to their axis. This dissertation adopts a widely used three-step extrinsic z-x-z rotation convention: Starting with the two frames overlapping with each other, coinciding with each of their axes, the crystal frame is firstly rotated about the laboratory z-axis by the angle ψ, following the right-hand rule (counterclockwise from top view); a second rotation is about the x-axis by the angle ϑ; and the third rotation is again about the z-axis by the angle φ.

After each crystal rotation step, material constant tensors, such as the elastic stiffness tensor c_{KL}, need to be transformed from the non-rotated ones. A tensor $\boldsymbol{T}_{mn}$, where $m, n = i, j, K, L$ are the abbreviated indices, can be transformed to $\boldsymbol{T}'_{mn}$ by the rotation matrix $\boldsymbol{R}$ using the relation:

$$\boldsymbol{T}'_{mn} = \boldsymbol{R}_m \boldsymbol{T}_{mn} \boldsymbol{R}_n^T, \tag{41}$$

[5] Strictly speaking it is the energy velocity. But with the lossless medium, the group velocity and the energy velocity are equal.

where $\boldsymbol{R}_m$ and $\boldsymbol{R}_n$ are two square rotation transformation matrices with dimensions $m \times m$ and $n \times n$, respectively, and the superscript T is the transpose operator. In this work, four rotation matrices are needed: $\boldsymbol{R}_{3,x}(\zeta_x)$ and $\boldsymbol{R}_{6,x}(\zeta_x)$ matrices for the x-axis rotation by the angle ζ_x, and $\boldsymbol{R}_{3,z}(\zeta_z)$ and $\boldsymbol{R}_{6,z}(\zeta_z)$ for the z-axis rotation by the angle ζ_z. The explicit expressions of these rotation transformation matrices are listed below:

$$\boldsymbol{R}_{3,x}(\xi_x) = \begin{bmatrix} 1 & 0 & 0 \\ 0 & \cos\xi_x & -\sin\xi_x \\ 0 & \sin\xi_x & \cos\xi_x \end{bmatrix}, \tag{42}$$

$$\boldsymbol{R}_{3,z}(\xi_z) = \begin{bmatrix} \cos\xi_z & -\sin\xi_z & 0 \\ \sin\xi_z & \cos\xi_z & 0 \\ 0 & 0 & 1 \end{bmatrix}, \tag{43}$$

$$\boldsymbol{R}_{6,x}(\xi_x) = \begin{bmatrix} 1 & 0 & 0 & 0 & 0 & 0 \\ 0 & \cos^2\xi_x & \sin^2\xi_x & -2\sin\xi_x\cos\xi_x & 0 & 0 \\ 0 & \sin^2\xi_x & \cos^2\xi_x & 2\sin\xi_x\cos\xi_x & 0 & 0 \\ 0 & \sin\xi_x\cos\xi_x & -\sin\xi_x\cos\xi_x & -\sin^2\xi_x+\cos^2\xi_x & 0 & 0 \\ 0 & 0 & 0 & 0 & \cos\xi_x & \sin\xi_x \\ 0 & 0 & 0 & 0 & -\sin\xi_x & \cos\xi_x \end{bmatrix}, \tag{44}$$

$$\boldsymbol{R}_{6,z}(\xi_z) = \begin{bmatrix} \cos^2\xi_z & \sin^2\xi_z & 0 & 0 & 0 & -2\sin\xi_z\cos\xi_z \\ \sin^2\xi_z & \cos^2\xi_z & 0 & 0 & 0 & 2\sin\xi_z\cos\xi_z \\ 0 & 0 & 1 & 0 & 0 & 0 \\ 0 & 0 & 0 & \cos\xi_z & \sin\xi_z & 0 \\ 0 & 0 & 0 & -\sin\xi_z & \cos\xi_z & 0 \\ \sin\xi_z\cos\xi_z & -\sin\xi_z\cos\xi_z & 0 & 0 & 0 & -\sin^2\xi_z+\cos^2\xi_z \end{bmatrix}, \tag{45}$$

where the higher rank matrices $\boldsymbol{R}_6$ are obtained from the Bond stress matrix [Auld, 1990].

In later chapters, wurtzite hexagonal crystals, *e.g.* AlN and ZnO, are used as analytical and numerical examples. This type of crystal has an uniaxial symmetry about its Z-axis, and thereby the material tensors are unchanged after the first z-axis rotation. As a result, the crystal orientation and the associated rotation procedure can be simplified. Instead of the Euler angle system, a cylindrical coordinate system is used, and the relation between the two frames can be described by two angles: a zenith angle ϑ and an azimuthal angle φ, as shown in Figure.3(b). A two-step rotation procedure is also adopted correspondingly: the crystal frame is firstly rotated about the x-axis by an angle ϑ, followed by a second rotation about the z-axis by an angle φ.

2.2 Piezoelectricity

The term "*piezoelectric*" is a combination of "electric" with the Greek word "piezo", which means "to press". This term describes well the effect itself, indicating the relation between the mechanical driving and the electrical response of this phenomenon.

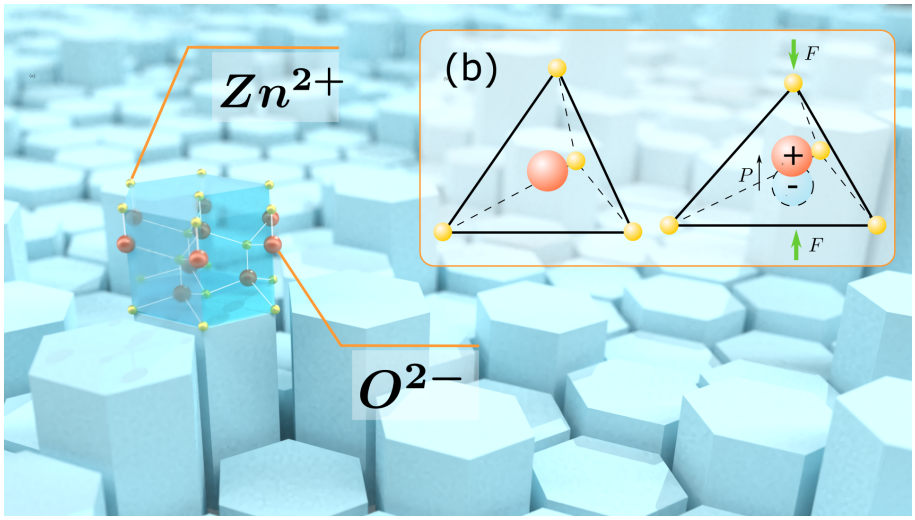

FIGURE 4 Illustration of piezoelectricity in a ZnO crystal.

First reported experimentally by Jacques and Pierre Curie in the 19th century, piezoelectricity became an interesting and credible topic in many scientific studies. However, the invention of the piezoelectric ultrasound resonator, which was used in SONAR to detect submarines during World War I, put piezoelectric materials under the spotlight, and soon more applications were developed and commercialized.

Nowadays, piezoelectric materials have already played a significant role in modern technologies and engineering practices, as it couples the acoustic deformations and electric fields, and has many applications such as acousto-optical modulators and actuators for optical signal processing, ultrasonic imaging, frequency control and processing devices, gas and fuel ignition generators, to name a few[Royer and Dieulesaint, 2000b].

There are a lot of piezoelectric materials that exist in nature as crystalline minerals, like quartz, topaz, Rochelle salt and tourmaline, and they all share a same feature in their crystal structure: *non-centrosymmetricity*.

Taking Zinc oxide (ZnO) as an example, it has a wurtzite hexagonal crystal structure, as shown in Fig.4. When in the equilibrium state, free of any stresses, the center of the positive and negative charge densities inside the crystal unit cell coincide, and thereby create zero net electric polarization. However, a deformation caused by stress may displace the centers of the charge densities, developing a finite electric dipole moment inside the cell, like the case shown in Fig.4(b). For a piezoelectric material, the collective effects of all the dipole moments throughout the crystal lead to a finite electric field, whereas for a centrosymmetric material, the net polarization stays zero.

In the following sections, the constitutive equations that couple the mechanical and electrical responses of a piezoelectric material will be derived, and an important approximation, the *quasistatic approximation*, will be discussed.

2.2.1 Piezoelectric constitutive equations

To form a piezoelectric (PE) system, both mechanical and electrical work must be done, and the *internal energy* $\mathrm{U}(S_L, D_i)$ of the system[6] is a function of two sets of state variables that represent the mechanical deformations and *electric displacements* in three-dimensional space, respectively. Consequently, a small change in the internal energy can be expressed as the sum of the increments of the mechanical and electrical work[Royer and Dieulesaint, 2000a]:

$$\mathrm{dU} = \sigma_L \mathrm{d}S_L + E_i \mathrm{d}D_i, \tag{46}$$

where E_i is the electric field, and D_i the electric displacement field.

Considering this PE system to be mechanically isolated but electrically coupled to the outside world, the electrical enthalpy (free energy) then reads as:

$$\mathrm{H} \equiv \mathrm{U} - E_i D_i. \tag{47}$$

The addition of the term $E_i D_i$ changes the state variables to $\mathrm{H}(S_L, E_i)$ via the *Legendre transformation* [Reichl, 2016], and thus leads to a differential form:

$$\mathrm{dH} = \sigma_L \mathrm{d}S_L - D_i \mathrm{d}E_i. \tag{48}$$

For small changes in the state variables, using the partial derivatives of the electric enthalpy give:

$$\mathrm{dH} = \left.\frac{\partial \mathrm{H}}{\partial S_L}\right|_E \mathrm{d}S_L + \left.\frac{\partial \mathrm{H}}{\partial E_i}\right|_S \mathrm{d}E_i, \tag{49}$$

where the first term of RHS is at constant electric field and the second term is at constant strain. Comparing Eqs.(49) with (48), one has:

$$\sigma_L = \left.\frac{\partial \mathrm{H}}{\partial S_L}\right|_E, \quad D_i = -\left.\frac{\partial \mathrm{H}}{\partial E_i}\right|_S. \tag{50}$$

The quantities σ_L and D_i are also the functions of the state variables and can be expressed with their partial derivatives:

$$\mathrm{d}\sigma_L = \left.\frac{\partial \sigma_L}{\partial S_K}\right|_E \mathrm{d}S_K + \left.\frac{\partial \sigma_L}{\partial E_i}\right|_S \mathrm{d}E_i, \tag{51}$$

$$\mathrm{d}D_i = \left.\frac{\partial D_i}{\partial S_L}\right|_E \mathrm{d}S_L + \left.\frac{\partial D_i}{\partial E_j}\right|_S \mathrm{d}E_j, \tag{52}$$

in which one can identify:

$$\left.\frac{\partial \sigma_K}{\partial S_L}\right|_E = c^E_{KL}, \quad \left.\frac{\partial D_i}{\partial E_j}\right|_S = \epsilon^S_{ij}, \tag{53}$$

[6] Thermal effects on the system are customarily neglected in the elasticity theory here.

as the elastic stiffness tensor at constant electric field and the *electric permittivity tensor* at constant strain, respectively. On the other hand, the remaining two factors can be expressed as[Royer and Dieulesaint, 2000a]:

$$e_{Li} \equiv -\left.\frac{\partial \sigma_L}{\partial E_i}\right|_S = -\left.\frac{\partial^2 \mathrm{H}}{\partial S_L \partial E_i}\right|_{E,S}, \tag{54}$$

$$e_{iL} \equiv \left.\frac{\partial D_i}{\partial S_L}\right|_E = -\left.\frac{\partial^2 \mathrm{H}}{\partial E_i \partial S_L}\right|_{E,S}, \tag{55}$$

where e_{iL} is defined as the *piezoelectric stress tensor*[7], which is symmetric $e_{iL} = e_{Li}$ according to the chain rule of partial differentiation.

In summary, the derivations in this section lead to the *piezoelectric constitutive equations*:

$$\sigma_K = c^E_{KL} S_L - e_{Kj} E_j \tag{56}$$

$$D_i = e_{iL} S_L + \epsilon^S_{ij} E_j. \tag{57}$$

2.2.2 The quasistatic approximation

Acoustic waves typically have velocities more than four orders of magnitude slower than that of light, and thereby have difficulties in exciting traveling electromagnetic waves via the rotational field. As a result, only the quasistatic part of the electric field $\boldsymbol{E} = -\nabla\Phi$, where Φ is the electric potential, is considered in this work, while the rotational part is set to zero and hence $\nabla \times \boldsymbol{E} = 0$. Such a method is commonly known as the *quasistatic approximation*, which is customarily used in piezoelectric problems.

What follows is that by applying the quasistatic approximation and the wave solution Eq.(19) to Eqs.(56) and (57), the following piezoelectric constitutive equations for the acoustic field are obtained:

$$\sigma_K = -ic^E_{KL} k_{Lj} u_j - ie_{Kj} k_j \Phi \tag{58}$$

$$D_i = -ie_{iL} k_{Lj} u_j + i\epsilon^S_{ij} k_j \Phi. \tag{59}$$

In addition, the electric displacement field without free charges follows the *Gauss's law* $\nabla \cdot \boldsymbol{D} = 0$, whose matrix notation reads as:

$$-ik_i D_i = 0. \tag{60}$$

The electric potential Φ can thus be expressed as a function of the displacement u_j as:

$$\Phi = \frac{k_i e_{iL} k_{Lj}}{k_i \epsilon^S_{ij} k_j} u_j \tag{61}$$

by inserting the constitutive Eq.(59) into the Gauss's law, Eq.(60). The piezoelectric version of the Christoffel equation can be obtained by substituting the

[7] The superscript E, S are removed as they are the only two state variables considered here, as well as to avoid crowded symbols.

constitutive Eq.(58) together with the expression of Φ into the equation of motion Eqs.(23). One finds the expression:

$$(k^2\Gamma_{ij}^{\mathrm{PE}} - \rho\omega^2\delta_{ij})u_j = 0, \tag{62}$$

which looks the same as Eq.(28), but with a different *piezoelectrically stiffened Christoffel matrix*[Auld, 1990]:

$$\Gamma_{ij}^{\mathrm{PE}} = \frac{1}{k^2}k_{iK}\left[c_{KL}^{E} + \frac{(e_{Kj}k_j)(k_i e_{iL})}{k_i\epsilon_{ij}^{S}k_j}\right]k_{Lj}. \tag{63}$$

It should be noted that, although the Eqs.(61) and (63) are correct in the case of bulk waves as discussed here, their denominators can be zero in some special wave modes in the scattering problems, *e.g.* for a reflected evanescent wave. Such cases may introduce ambiguities in the results of Φ, if orthogonality and completeness of the wave solutions are not carefully examined. This serves as one of the motivations to introduce the extended Stroh formalism in the next section.

With the addition of the coupling to the electrostatic field, the Poynting vector for the piezoelectric medium should also include the contribution stored in the electric field.

The complex Poynting vector of electromagnetism is well known:

$$\boldsymbol{P}_{EM} = \frac{1}{2}\boldsymbol{E}\times\boldsymbol{H}^*, \tag{64}$$

where $\boldsymbol{H}$ is the magnetic field strength. Taking the divergence of the Poynting vector leads to:

$$\nabla\cdot(\boldsymbol{E}\times\boldsymbol{H}^*) = (\nabla\times\boldsymbol{E})\cdot\boldsymbol{H}^* - \boldsymbol{E}\cdot(\nabla\times\boldsymbol{H}^*). \tag{65}$$

The first term on the RHS is zero under the quasistatic approximation, and the second term becomes:

$$-\boldsymbol{E}\cdot(\nabla\times\boldsymbol{H}^*) = \nabla\cdot\left(\Phi_V\frac{\partial\boldsymbol{D}^*}{\partial t}\right) - \Phi_V\nabla\cdot\frac{\partial\boldsymbol{D}^*}{\partial t}, \tag{66}$$

where Ampere's circuital law $\nabla\times\boldsymbol{H} = \partial\boldsymbol{D}/\partial t$ and the divergence product identity are applied. Without free charges inside the medium, so that $\nabla\cdot\boldsymbol{D} = 0$, the quasistatic complex Poynting vector becomes:

$$\boldsymbol{P}_{EM} = \frac{1}{2}\Phi\frac{\partial\boldsymbol{D}^*}{\partial t}. \tag{67}$$

Without any source currents or free charges, Gauss's law states that $\boldsymbol{k}\cdot\boldsymbol{D} = 0$, which has an interesting implication that the electric power flow is always *orthogonal* to the propagation direction of the wave. This property of the piezoelectrically stiffened acoustic wave will be exploited in the next chapter to enhance the power flow in the vacuum between two semi-infinite solids.

The total power flow of the piezoelectric medium is therefore the sum of the elastic and electrostatic contributions:

$$\boldsymbol{P} = -\frac{1}{2}\boldsymbol{v}^* \cdot \boldsymbol{\sigma} - \frac{1}{2} i\omega \Phi \boldsymbol{D}^*, \tag{68}$$

where the time derivative is replaced by $i\omega$ for a harmonic wave.

The peak stored kinetic and elastic energy densities $(\mathrm{u}_K)_{peak}$, $(\mathrm{u}_S)_{peak}$ have already been obtained in Eqs.(32) as:

$$(\mathrm{u}_K)_{peak} = \frac{1}{2}\rho\omega^2 |u_i|^2 \tag{69}$$

$$(\mathrm{u}_S)_{peak} = \frac{1}{2} i k_{iK}^* \sigma_K u_i^*. \tag{70}$$

The peak stored electrostatic energy is:

$$(\mathrm{u}_E)_{peak} = \frac{1}{2} E_i D_i^* = \frac{1}{2} i\Phi k_i D_i^*. \tag{71}$$

For a bulk wave whose k-vector is real, it is easy to show that the peak elastic and kinetic energy densities are equal, and the peak stored electrostatic energy is zero enforced by the Gauss's law [Eq.(60)]. Therefore, the group velocity of the bulk wave mode still has the same expression as in Eq.(40).

2.2.3 Piezoelectric crystal orientations

Piezoelectric AlN and ZnO will be used as analytical and numerical examples in this dissertation. These are uniaxial wurtzite crystals, whose orientations can be fully described by two angles (ϑ, φ) using a cylindrical angle system as discussed in section 2.1.5.

There are three material constant tensors that are used in the elasticity theory for the piezoelectric solid: the 6×6 tensor $\boldsymbol{c}_0^E$, the elastic stiffness tensor at constant electric field; the 3×6 tensor $\boldsymbol{e}_0$, the piezoelectric strain tensor; and the 3×3 tensor $\boldsymbol{\epsilon}_0^S$, the electric permittivity tensor at constant strain. The subscript 0 indicates they are the non-rotated tensors.

With the rotation and the corresponding transformation procedure that was described in the preceding section 2.1.5, the transformed tensors can then be obtained as:

$$\begin{aligned} \boldsymbol{c}^E &= \boldsymbol{R}_{6,z}(\varphi) \left[\boldsymbol{R}_{6,x}(\vartheta) \boldsymbol{c}_0^E \boldsymbol{R}_{6,x}(\vartheta)^T \right] \boldsymbol{R}_{6,z}(\varphi)^T \\ \boldsymbol{e} &= \boldsymbol{R}_{3,z}(\varphi) \left[\boldsymbol{R}_{3,x}(\vartheta) \boldsymbol{e}_0 \boldsymbol{R}_{6,x}(\vartheta)^T \right] \boldsymbol{R}_{6,z}(\varphi)^T \\ \boldsymbol{\epsilon}^S &= \boldsymbol{R}_{3,z}(\varphi) \left[\boldsymbol{R}_{3,x}(\vartheta) \boldsymbol{\epsilon}_0^S \boldsymbol{R}_{3,x}(\vartheta)^T \right] \boldsymbol{R}_{3,z}(\varphi)^T. \end{aligned} \tag{72}$$

In the scope of this work, the piezoelectric crystal is considered to be cut along a certain plane to form a semi-infinite solid. Therefore, it is also useful to introduce the four basis vector $\{hkil\}$ Miller-Bravais index system, which is commonly used to describe the crystallographic planes [Schwarzenbach, 2003]. For hexagonal crystals, the rotation angle $\vartheta = \angle_{\{hkil\}}$ describes the angle between

the crystal Z-axis and the normal of the plane $\{hkil\}$, and the relation between the angle and the indices is:

$$\begin{aligned}\angle_{\{hkil\}} &= \arccos\left(\frac{\overrightarrow{(hkl)}\cdot\overrightarrow{(001)}}{|\overrightarrow{(hkl)}||\overrightarrow{(001)}|}\right)\\ &= \arccos\left[al\left(\frac{4}{3}c^2(h^2+k^2+hk)+a^2l^2\right)^{-\frac{1}{2}}\right],\end{aligned}$$

where a and c are the in-plane (X,Y) and out-of-plane (Z) lattice constants of the crystal, respectively. In Table 2, the indices and the rotation angles of common crystallographic plane families of AlN and ZnO are given.

Plane name	Miller index	AlN $\angle_{\{hkil\}}$	ZnO $\angle_{\{hkil\}}$
a	$\{11\bar{2}0\}$	90°	90°
m	$\{10\bar{1}0\}$	90°	90°
c	$\{0001\}$	0°	0°
r	$\{1\bar{1}02\}$	42.73°	42.78°
n	$\{11\bar{2}3\}$	46.85°	46.89°
s	$\{10\bar{1}1\}$	61.58°	61.61°

TABLE 2 The common cut planes of hexagonal AlN and ZnO crystals.

2.3 Extended Stroh formalism

The elasticity theory that was introduced in previous sections is a very well developed formalism, and it can constitute a complete system to solve a scattering problem, the kind of problem this dissertation is focused on. However, for the problems involving an anisotropic medium and arbitrarily orientated crystals, it becomes complicated to apply the elasticity theory directly, because of the intricate material parameters and the coupled quasi-wave modes. In addition, it is also crucial to carefully examine the orthogonality and the completeness of the wave solutions, otherwise ambiguities can arise.

An example of the last point can be found in the textbook of elasticity theory written by Auld [1990]. In that example[8], the author gives an example of a case where the denominator of Eq.(61) is zero, and thus special procedure needs to be taken to find the correct wave solution.

In contrast, the *Extended Stroh formalism* reveals the underlying relations among the elasticity equations presented in the preceding sections, inherently ensures the orthogonality and the completeness of the wave solutions, and thus is a mathematically powerful and elegant tool to analyze the anisotropic piezoelectric elasticity.

[8] Example 5 in chapter 9 on page 52 in Volume II.

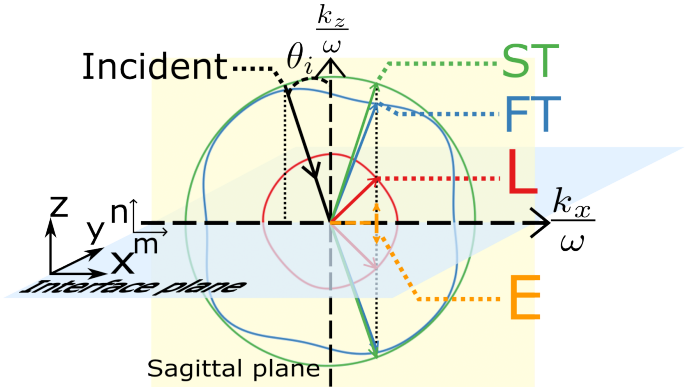

FIGURE 5 Schematic of the single surface scattering problem.

The original *sextic Stroh formalism* was proposed by Stroh [1962], and was developed into an eight-dimensional framework for arbitrary anisotropic piezoelectric crystal by Barnett and Lothe (1975; 1976). With further developments contributed by many authors [Al'shits et al., 1989, 1990, 1991; Chung and Ting, 1995; Akamatsu and Tanuma, 1997; Hwu, 2008], this formalism has been successfully applied to various studies, ranging from the analysis of the bulk [Al'shits et al., 1989, 1990, 1991], surface [Lothe and Barnett, 1976; Lyubimov et al., 1980; Darinskii and Weihnacht, 2003], and gap [Al'shits et al., 1993, 1994; Darinskii and Weihnacht, 2006] electroacoustic waves in anisotropic piezoelectric materials, to the material science applications such as piezoelectric ceramics and composites[Pak, 1992; Liang et al., 1995; Lu et al., 2006], and phononic crystals[Barnett and Lothe, 1975; Darinskii and Shuvalov, 2019].

In the following sections, the main aspects of the extend Stroh formalism will be introduced, and then the orthogonality and the completeness will be briefly discussed. Lastly, the Poynting vector, the group velocity and the energy density will be derived under the framework of this dissertation.

2.3.1 Stroh characteristic equation

Let's consider an incident plane wave impinging on an interface in a piezoelectric solid, and scattering into a linear combination of partial waves, either reflected or transmitted, as illustrated in Figure 5. Without losing generality, this incident wave is assumed to have a wave vector $\boldsymbol{k}$ such that $k_x > 0$, $k_y = 0$, and $k_z < 0$[9], and travels inside the xz-plane, the *saggital plane*, and is scattered at the interface $z = 0$. The unit vectors of the x-axis and z-axis are designated $\boldsymbol{m}$ and $\boldsymbol{n}$, respectively, and a factor $p \equiv k_z/k_x$ is defined as the ratio between the two non-zero wave vector components.

[9] $k_z < 0$ means traveling against the direction of $z - axis$, i.e. towards the interface

The general wave solutions can be expressed[Geng and Maasilta, 2022a] as:

$$\begin{aligned} \boldsymbol{u} &= \sum_{\alpha} b_\alpha \boldsymbol{A}_\alpha e^{-ik_x(x+p_\alpha z)+i\omega t} \\ \Phi &= \sum_{\alpha} b_\alpha \phi_\alpha e^{-ik_x(x+p_\alpha z)+i\omega t} \\ \boldsymbol{n}\cdot\boldsymbol{\sigma} &= ik_x \sum_{\alpha} b_\alpha \boldsymbol{L}_\alpha e^{-ik_x(x+p_\alpha z)+i\omega t} \\ \boldsymbol{n}\cdot\boldsymbol{D} &= ik_x \sum_{\alpha} b_\alpha D^n_\alpha e^{-ik_x(x+p_\alpha z)+i\omega t}\ , \end{aligned} \tag{73}$$

where b_α is the dimensionless amplitude of the partial wave mode α, $\boldsymbol{A}_\alpha, \phi_\alpha, \boldsymbol{L}_\alpha, D^n_\alpha$ are the constants describing the displacement, the electric potential, the traction force and the normal projection of the electric displacement of the α mode, respectively. It will be shown in the later part of this section that these constants form a normalized eigenvector $\boldsymbol{\xi}_\alpha = [\boldsymbol{A}_\alpha, \phi_\alpha, \boldsymbol{L}_\alpha, D^n_\alpha]^T$ to the Stroh characteristic equation with a corresponding eigenvalue p_α.

Under the quasistatic approximation, the normal projections of the piezoelectric constitutive equations (58) and (59) read as:

$$\begin{aligned} \boldsymbol{n}\cdot\boldsymbol{\sigma} &= -in_{iK}c^E_{KL}k_{Lj}u_j - in_{iK}e_{Kj}k_j\Phi \\ \boldsymbol{n}\cdot\boldsymbol{D} &= -in_i e_{iL}k_{Lj}u_j + in_i\epsilon^S_{ij}k_j\Phi, \end{aligned} \tag{74}$$

where n_i is the matrix notation of the normal vector $\boldsymbol{n}$ of the ith Cartesian component[10], and n_{iK} is a 3×6 matrix that has a form similar to the $k_{iK} = k^T_{Lj}$, explicitly defined as:

$$n_{iK} \rightarrow \begin{bmatrix} n_x & 0 & 0 & 0 & n_z & n_y \\ 0 & n_y & 0 & n_z & 0 & n_x \\ 0 & 0 & n_z & n_y & n_x & 0 \end{bmatrix}. \tag{75}$$

If we introduce a composite 4×4 matrix expression $(\boldsymbol{nk})$ that is defined as:

$$(\boldsymbol{nk}) \equiv \begin{bmatrix} n_{iK} & 0 \\ 0 & n_i \end{bmatrix} \begin{bmatrix} c^E_{KL} & e_{Kj} \\ e_{iL} & -\epsilon^S_{ij} \end{bmatrix} \begin{bmatrix} k_{Lj} & 0 \\ 0 & k_j \end{bmatrix}, \tag{76}$$

in which each element of the matrices represents sub-matrices, the constitutive equations (74) can be written into a more compact form as:

$$\begin{bmatrix} \boldsymbol{n}\cdot\boldsymbol{\sigma} \\ \boldsymbol{n}\cdot\boldsymbol{D} \end{bmatrix} = -i(\boldsymbol{nk}) \begin{bmatrix} \boldsymbol{u} \\ \phi \end{bmatrix}\ . \tag{77}$$

This matrix equation can be rearranged further by inserting the α partial mode solution from the solutions Eqs.(73), and by separating the unknown p_α, which is introduced by the decomposition of the k-vector $\boldsymbol{k}_\alpha = k_x(\boldsymbol{m} + p_\alpha \boldsymbol{n})$ into

[10] With the coordinates used in this dissertation, $n_z = 1$, and $n_x = n_y = 0$. In addition, $m_x = 1$, and $m_y = m_z = 0$.

the two orthogonal unit vectors $\boldsymbol{m}$ and $\boldsymbol{n}$, into the RHS of the equation. The resulting equation reads as:

$$-(\boldsymbol{nn})^{-1}(\boldsymbol{nm}) \begin{bmatrix} \boldsymbol{A}_\alpha \\ \Phi_\alpha \end{bmatrix} - (\boldsymbol{nn})^{-1} \begin{bmatrix} \boldsymbol{L}_\alpha \\ D^n_\alpha \end{bmatrix} = p_\alpha \begin{bmatrix} \boldsymbol{A}_\alpha \\ \Phi_\alpha \end{bmatrix} , \tag{78}$$

in which the expressions $(\boldsymbol{nn})$ and $(\boldsymbol{nm})$ are defined analogously to the Eq.(76) and depend only on the material parameters since $\boldsymbol{n}$ and $\boldsymbol{m}$ are unit vectors. It is worth mentioning that the inverse of the matrix $(\boldsymbol{nn})$ always exists for real materials.

In addition, starting from the equation of motion, Eq.(23), and the Gauss's law, Eq.(60), another similar matrix equation can be found as:

$$(\boldsymbol{kk}) \begin{bmatrix} \boldsymbol{u} \\ \Phi \end{bmatrix} = \rho\omega^2 \boldsymbol{I}' \begin{bmatrix} \boldsymbol{u} \\ \Phi \end{bmatrix} , \tag{79}$$

where $\boldsymbol{I}'$ reads as:

$$\boldsymbol{I}' = \begin{bmatrix} 1 & 0 & 0 & 0 \\ 0 & 1 & 0 & 0 \\ 0 & 0 & 1 & 0 \\ 0 & 0 & 0 & 0 \end{bmatrix} . \tag{80}$$

By introducing the unknown p_α from the decomposition of the k-vector as above and substituting the term $p_\alpha[\boldsymbol{A}_\alpha, \Phi_\alpha]^T$ from Eq.(78), one obtains:

$$\begin{aligned} -\left[(\boldsymbol{mn})(\boldsymbol{nn})^{-1}(\boldsymbol{nm}) - (\boldsymbol{mm}) + \rho v_x^2 \boldsymbol{I}'\right] \begin{bmatrix} \boldsymbol{A}_\alpha \\ \Phi_\alpha \end{bmatrix} \\ -(\boldsymbol{mn})(\boldsymbol{nn})^{-1} \begin{bmatrix} \boldsymbol{L}_\alpha \\ D^n_\alpha \end{bmatrix} = p_\alpha \begin{bmatrix} \boldsymbol{L}_\alpha \\ D^n_\alpha \end{bmatrix} , \end{aligned} \tag{81}$$

where $v_x \equiv \omega/k_x$.

Finally, Eqs.(78) and (81) can be combined linearly into an eight-dimensional characteristic equation

$$\boldsymbol{N}(v_x)\boldsymbol{\xi}_\alpha = p_\alpha \boldsymbol{\xi}_\alpha , \tag{82}$$

whose eigenvector is $\boldsymbol{\xi}_\alpha = [\boldsymbol{A}_\alpha, \phi_\alpha, \boldsymbol{L}_\alpha, D^n_\alpha]^T$, eigenvalue is p_α, and $\boldsymbol{N}$ is a 8×8 real matrix given by:

$$\boldsymbol{N}(v_x) = -\begin{bmatrix} (\boldsymbol{nn})^{-1}(\boldsymbol{nm}) & (\boldsymbol{nn})^{-1} \\ (\boldsymbol{mn})(\boldsymbol{nn})^{-1}(\boldsymbol{nm}) - (\boldsymbol{mm}) + \rho v_x^2 \boldsymbol{I}' & (\boldsymbol{mn})(\boldsymbol{nn})^{-1} \end{bmatrix} . \tag{83}$$

One of the key features of the extended Stroh formalism is that, besides the material parameters, the Stroh matrix $\boldsymbol{N}$ is only a function of v_x, which is a conserved quantity at the scattering interface due to the continuity conditions at the boundary, and is known if the incident wave is given. As a comparison, the stiffened Christoffel matrix $\boldsymbol{\Gamma}$ presented in Eq.(63) requires the knowledge of the k-vectors of the scattered wave modes (equivalent to the p_α), which are generally unknown for anisotropic scattering problems.

The characteristic equation (82) has eight distinct complex eigenvalues[11] $p_\alpha = p'_\alpha + ip''_\alpha$ with $\alpha = 1, ..., 8$ (p'_α and p''_α are the real and imaginary parts of the eigenvalue), as well as eight associated eigenvectors $\boldsymbol{\xi}_\alpha$ which are orthogonal and form a complete set [Lothe and Barnett, 1976]. These are the partial wave mode solutions, which can be either homogeneous plane waves with real eigenvalue ($p''_\alpha = 0$) or inhomogeneous waves ($p''_\alpha \neq 0$).

2.3.2 Orthonormalization

Customarily, a normalization method will be employed to ensure finding a unique and complete set of solutions to the characteristic equation. An intuitive and convenient choice is to normalize with the displacement vector $\boldsymbol{u}$ (or its time derivative $i\omega\boldsymbol{u}$) which is also the base vector of the elastic equations. However, it is not rare to see cases in piezoelectric materials, where a valid partial wave mode solution has no displacement such that $\boldsymbol{u} = 0$. Therefore, a four-dimensional eigenvector $[\boldsymbol{u}, \Phi]^T$ is quite often considered instead of $\boldsymbol{u}$ in the piezoelectric scattering problems [Yashiro and Goto, 1978; Every and Neiman, 1992].

Such normalization problem is addressed formally in the extended Stroh formalism. To ensure a distinct and complete set of solutions, an orthonormalization condition is applied [Chadwick and Smith, 1977; Darinskii and Weihnacht, 2003], which can be expressed as:

$$\boldsymbol{\xi}_\alpha \cdot \hat{\boldsymbol{T}}\boldsymbol{\xi}_\beta = \boldsymbol{\xi}_\alpha^T \hat{\boldsymbol{T}}\boldsymbol{\xi}_\beta = \delta_{\alpha\beta}, \quad \alpha, \beta = 1, ..., 8\,, \tag{84}$$

where $\delta_{\alpha\beta}$ is the Kronecker delta, and $\hat{\boldsymbol{T}}$ is a 8×8 matrix reading as:

$$\hat{\boldsymbol{T}} = \begin{bmatrix} \hat{\boldsymbol{O}}_{(4)} & \hat{\boldsymbol{I}}_{(4)} \\ \hat{\boldsymbol{I}}_{(4)} & \hat{\boldsymbol{O}}_{(4)} \end{bmatrix}, \tag{85}$$

where $\hat{\boldsymbol{O}}_{(4)}$ and $\hat{\boldsymbol{I}}_{(4)}$ are 4×4 zero and unit matrices.

In numerical practice, the normalization will be done as follows: the non-normalized eigenvector $\boldsymbol{\xi}'_\alpha$ is obtained first; this solution will then be normalized via equation $\boldsymbol{\xi}_\alpha = \boldsymbol{\xi}'_\alpha / \sqrt{(\boldsymbol{\xi}'_\alpha)^T \hat{\boldsymbol{T}} \boldsymbol{\xi}'_\alpha}$.

The orthogonality of Eq.(84) can be proved based on the symmetry relation of an auxiliary matrix $\hat{\boldsymbol{T}}\boldsymbol{N}$ [Chadwick and Smith, 1977; Ting, 1996]:

$$(\hat{\boldsymbol{T}}\boldsymbol{N})^T = \hat{\boldsymbol{T}}\boldsymbol{N}, \tag{86}$$

which can be verified using simple algebra as the Stroh matrix $\boldsymbol{N}$ depends only on v_x and the material parameters.

Left-multiplying the characteristic equation (82) by $\boldsymbol{\xi}_\beta \hat{\boldsymbol{T}}\cdot$ and writing it in matrix notation, it becomes:

$$(\xi_i)_\beta (\hat{T}N)_{ij} (\xi_j)_\alpha = p_\alpha (\xi_i)_\beta \hat{T}_{ij} (\xi_j)_\alpha. \tag{87}$$

[11] In only few isolated cases, nonsemisimple degeneracy can be found. Such cases can be solved by generalized eigenvectors[Chadwick and Smith, 1977; Darinskii and Weihnacht, 2003]. In this work, these cases are not considered because one can always solve the problem numerically in a limiting manner very close to such a special point.

The modes α and β can be interchanged:

$$(\xi_i)_\alpha(\hat{T}N)_{ij}(\xi_j)_\beta = p_\beta(\xi_i)_\alpha\hat{T}_{ij}(\xi_j)_\beta. \tag{88}$$

In the next step, one can transpose Eq.(87), followed by interchanging the indices i, j, and applying the symmetry relations $\hat{T}_{ij} = \hat{T}_{ji}$ and $(\hat{T}N)_{ij} = (\hat{T}N)_{ji}$ from Eq.(86). As a result, the new equation reads as:

$$(\xi_i)_\alpha(\hat{T}N)_{ij}(\xi_j)_\beta = p_\alpha(\xi_i)_\alpha\hat{T}_{ij}(\xi_j)_\beta. \tag{89}$$

Subtracting Eq.(89) from Eq.(88), one obtains:

$$(p_\alpha - p_\beta)(\xi_i)_\alpha\hat{T}_{ij}(\xi_j)_\beta = 0, \tag{90}$$

which states that $\boldsymbol{\xi}_\alpha^T\hat{\boldsymbol{T}}\boldsymbol{\xi}_\beta = 0$ when $p_\alpha \neq p_\beta$, and thereby the orthogonality is demonstrated.

The eigenvectors obtained from the Stroh characteristic equation form a complete set, satisfying the completeness condition:

$$\sum_\alpha \boldsymbol{\xi}_\alpha \otimes \hat{\boldsymbol{T}}\boldsymbol{\xi}_\alpha = \hat{\boldsymbol{I}}_{(8)}. \tag{91}$$

This condition can be demonstrated conveniently with the help of the *Dirac's bra-ket* notation [Sakurai and Napolitano, 2020][12]. Under such notation, the orthonormalization condition Eq.(84) reads as:

$$\langle\boldsymbol{\xi}_\alpha|\,\hat{T}\,|\boldsymbol{\xi}_\beta\rangle = \langle\hat{T}\boldsymbol{\xi}_\alpha|\boldsymbol{\xi}_\beta\rangle = \delta_{\alpha\beta}. \tag{92}$$

The second form in the above equation can be multiplied by an inner product of the γ and β modes $\langle\boldsymbol{\xi}_\gamma|\boldsymbol{\xi}_\beta\rangle$ with a summation over α. This leads to a relation:

$$\langle\boldsymbol{\xi}_\gamma|\boldsymbol{\xi}_\beta\rangle = \sum_\alpha \langle\boldsymbol{\xi}_\gamma|\boldsymbol{\xi}_\beta\rangle\,\langle\hat{T}\boldsymbol{\xi}_\alpha|\boldsymbol{\xi}_\beta\rangle = \sum_\alpha \langle\boldsymbol{\xi}_\gamma|\boldsymbol{\xi}_\alpha\rangle\,\langle\hat{T}\boldsymbol{\xi}_\alpha|\boldsymbol{\xi}_\beta\rangle\,, \tag{93}$$

from which the completeness of the eigenvector

$$\sum_\alpha |\xi_\alpha\rangle\,\langle\hat{T}\xi_\alpha| = \hat{\boldsymbol{I}} \tag{94}$$

is thereby proved.

It is important to point out here that $\boldsymbol{\xi}_\alpha^T\hat{\boldsymbol{T}}\boldsymbol{\xi}_\beta$ has a unit of force and does not keep the physical units of the eigenvectors. However, this is only a concern in computation, in which the eigenvectors are actually in reduced "Stroh units". From a theoretical point of view, the eigenvectors are always assumed to be a unique and complete set satisfying the orthonormalization condition, without the need of an additional normalization, and thus their units are correct in the derivation and development of the theory in this dissertation.

[12] Note that the complex conjugation is not taken here when using Dirac's bra.

2.3.3 Power flow, energy density and group velocity

The complex Poynting vector for the piezoelectric material is given in Eq.(68). By adopting the general solution of the Stroh formalism, Eqs.(73), the component of the complex Poynting vector of an α mode that is normal to the interface ($z = 0$) can thus be expressed as:

$$\boldsymbol{n} \cdot \boldsymbol{P}_\alpha = -\frac{\omega k_x}{2} |b_\alpha|^2 \left[\boldsymbol{A}_\alpha^* \cdot \boldsymbol{L}_\alpha + \Phi (D_\alpha^n)^* \right], \tag{95}$$

in which k_x is a conserved quantity because of the continuity conditions at the scattering interface, and is assumed to be real so that the incident wave is always a bulk plane wave.

The time-averaged power flow in the normal direction is the real part of the complex Poynting vector:

$$\begin{aligned} \boldsymbol{n} \cdot \boldsymbol{P}_{\mathrm{AV},\alpha} &= -\frac{\omega k_x}{4} |b_\alpha|^2 \left[\boldsymbol{A}_\alpha^* \cdot \boldsymbol{L}_\alpha + \boldsymbol{A}_\alpha \cdot \boldsymbol{L}_\alpha^* + \Phi (D_\alpha^n)^* + \Phi^* (D_\alpha^n) \right] \\ &= -\frac{\omega k_x}{4} |b_\alpha|^2 \boldsymbol{\xi}_\alpha^T \hat{\boldsymbol{T}} \boldsymbol{\xi}_\alpha^*. \end{aligned} \tag{96}$$

This result is interesting in several ways. Firstly, it can be simplified further for the bulk wave solutions. Bulk waves have real eigenvalues p_α, and because the Stroh matrix $\boldsymbol{N}$ is also real, the eigenvectors have to be either real, so that $\boldsymbol{\xi}_\alpha^* = \boldsymbol{\xi}_\alpha$, or pure imaginary, so that $\boldsymbol{\xi}_\alpha^* = -\boldsymbol{\xi}_\alpha$. This leads to:

$$\boldsymbol{\xi}_\alpha^T \hat{\boldsymbol{T}} \boldsymbol{\xi}_\alpha^* = \pm \boldsymbol{\xi}_\alpha^T \hat{\boldsymbol{T}} \boldsymbol{\xi}_\alpha = \pm 1, \tag{97}$$

in which the sign is determined by the orthonormalization procedure. As a result, the value of the power flow can be computed simply[13] from $\omega k_x |b_\alpha|^2 / 4$, and the direction of the power flow is determined by the sign of the factor $\boldsymbol{\xi}_\alpha^T \hat{\boldsymbol{T}} \boldsymbol{\xi}_\alpha^*$. Here it should be noted that the direction of the inhomogeneous wave is not determined by this factor, but rather simply by the imaginary part of p_α as it needs to ensure a decaying solution at infinity.

Moreover, Eq.(96) also reveals the physical interpretation of the amplitude b_α. Because the angular frequency ω and the component of k-vector k_x are unchanged for all the wave mode solutions, the power flow ratio between the bulk solutions α and β reduces to $|b_\alpha|^2 / |b_\beta|^2$, meaning b_α is the amplitude of power. Assuming an incident amplitude $b_{in} = 1$ in the scattering problem, b_α becomes the transmission or reflection amplitude coefficient, and $|b_\alpha|^2$ becomes the power transmittance and reflectance.

The peak stored energy densities $(\mathrm{u}_K)_{peak}, (\mathrm{u}_S)_{peak}, (\mathrm{u}_E)_{peak}$ can be obtained from Eqs.(69),(70) and (71). For the bulk wave modes, these expressions become:

$$\begin{aligned} (\mathrm{u}_K)_{peak} = (\mathrm{u}_S)_{peak} &= \frac{1}{2} \rho \omega^2 |b_\alpha|^2 |\boldsymbol{A}_\alpha|^2 \\ (\mathrm{u}_E)_{peak} &= 0. \end{aligned} \tag{98}$$

[13] With an extra force unit.

The group velocity of a bulk wave mode α is the ratio between the time-averaged power flow and the averaged peak stored energy density, as presented in Eq.(40) in the previous section. Its component normal to the interface, which is the power flow direction this work mainly concerns, reads as:

$$g_\alpha^n \equiv \boldsymbol{n} \cdot \boldsymbol{g} = -\frac{1}{2\rho v_x |\boldsymbol{A}_\alpha|^2} \boldsymbol{\xi}_\alpha^T \hat{\boldsymbol{T}} \boldsymbol{\xi}_\alpha^*. \tag{99}$$

where $v_x = \omega / k_x$.

2.3.4 Wave-mode assignment

As discussed already in section 2.1.4, there are two conventions to categorize the wave modes in the elasticity theory, which can also applied to a piezoelectric material. Besides a new evanescent *electrical potential* E mode, which is, as the name suggested, the energy is (mostly) contained in the electric field [Auld, 1990; Every and Neiman, 1992], there are three (mostly) elastic wave modes in a piezoelectric medium. With different displacement directions in relation to the propagation direction, also referred to as polarization in some literature, the wave can be identified as: a *(quasi-)longitudinal* wave, or an L mode, if the polarization is (mostly) parallel to the propagating direction; a *vertically polarized (quasi-)shear* wave, or an SV mode, if the polarization is (mostly) inside the sagittal plane and (not purely) perpendicular to the propagation direction; a *horizontally polarized (quasi-)shear* wave, or an SH mode, if the polarization is perpendicular to both the sagittal plane and the propagation direction.

The other alternative is to sort the phase velocity of the three elastic wave modes from the fastest to the slowest as *(quasi-)longitudinal* wave (L), *fast (quasi-)transverse* wave (FT) and *slow (quasi-)transverse* wave (ST).

The above two categorizations of the wave modes are only conceptual definitions originated from exactly the same set of solutions of the extended Stroh formalism. There are eight eigenvalues p_α and eight associated eigenvectors $\boldsymbol{\xi}_\alpha$, and they can be divided into reflected and transmitted waves, each direction containing four aforementioned wave modes. For the benefit of the topics in later discussions such as mode conversions, a programmable procedure will be described below, which can be used to identify the wave modes.

The eight solutions of the Stroh formalism will be examined with four different categorization methods:

1. Homogeneous or inhomogeneous wave

2. Transmitted or reflected wave

3. The mode categorized as longitudinal (L), fast transverse (FT), slow transverse (ST), or electric potential (E)

4. The mode categorized as longitudinal (L), vertically polarized shear (SV), horizontally polarized shear (SH), or electric potential (E)

Firstly, an eigenvalue of a wave solution is assumed to have a form of $p_\alpha = p'_\alpha + ip''_\alpha$. By examining the imaginary part: If $p''_\alpha = 0$ ($p''_\alpha \neq 0$), the wave will be identified as a homogeneous wave (an inhomogeneous wave).

Secondly, for an inhomogeneous wave, its eigenvalue has a non-zero imaginary part that if $p''_\alpha > 0$ ($p''_\alpha < 0$) the wave will be identified as a transmitted (reflected) wave. This reflects an underlying physics that the inhomogeneous wave can only decay (and not grow) from the surface. In contrast, the time-averaged power flow direction of a homogeneous wave, *i.e.* the normal component of the Poynting vector Eq.(96), should be examined such that the wave with $\hat{\boldsymbol{n}} \cdot \boldsymbol{P}_{\mathrm{AV},\alpha} < 0$ ($\hat{\boldsymbol{n}} \cdot \boldsymbol{P}_{\mathrm{AV},\alpha} > 0$) is identified as a transmitted (reflected) mode.

It should be stressed here that, the wave modes, *e.g.* FT, SV, *etc.*, are defined only from a partial set of aspects of the wave solutions, such as phase velocity or displacement. Consequently, it can be difficult and tricky in some special cases to fully map these modes to the solutions, creating ambiguities. One example that Every and Neiman [1992] showed, is a plane wave can be scattered into four bulk modes without the excitation of the inhomogeneous E mode in the case of strong electromechanical coupling. Hence, it is important to keep in mind that the mode categorization procedure presented here is not a fully robust algorithm, but for the benefit of the discussion and demonstration.

To assign the modes within the set L, FT, ST and E, the magnitudes of the imaginary parts $|p''_\alpha|$ of all the inhomogeneous evanescent waves ($p''_\alpha \neq 0$) will be compared first, and the modes are assigned based on the ordering $|p''_E| > |p''_L| > |p''_{FT}| \geq |p''_{ST}|$ until there is no inhomogeneous wave left. The modes of the remaining unassigned homogeneous waves will be assigned based on their phase velocities $v_\alpha^2 = v_x^2/(1 + p_\alpha^2)$ in the order $v_L^2 > v_{FT}^2 \geq v_{ST}^2$, starting from the first unassigned mode.

To assign the modes within the set (quasi-) L, SV, SH and E, the displacement constant $\boldsymbol{A}_\alpha$ from the eigenvector should be examined. However, this is not always possible since there are usually no clear general differences between the eigenvectors of the surface (inhomogeneous) modes. Hence, the inhomogeneous wave modes should be identified first using the method described above. After that, the homogeneous modes, for which the definitions based on the displacement vector exist, can be identified by comparing the direction of the displacement with the wave vector as well as the unit normal vector of the sagittal plane. A (quasi-)L mode can be identified from $|\boldsymbol{k} \cdot \boldsymbol{A}_L| > |\boldsymbol{k} \cdot \boldsymbol{A}_{SV,SH}|$, if it is still available for assignment, whereas the (quasi-)SV and (quasi-)SH modes follow the relation $|[0,1,0]^T \cdot \boldsymbol{A}_{SV}| < |[0,1,0]^T \cdot \boldsymbol{A}_{SH}|$, based on the coordinate system assumed in this dissertation.

3 PIEZOELECTRICALLY MEDIATED ACOUSTIC WAVE TUNNELING

In a solid, the propagation of the deformation or vibration is described by an acoustic wave or an *acoustic phonon* which is a particle-like quantum mechanical description of the acoustic wave, and its constitutive and dynamic equations were introduced in the preceding chapter. By definition, acoustic waves cannot exist in vacuum, thus a conclusion that the energy carried by acoustic waves cannot transport between two separated solids is seemingly correct. However, at the microscopic level, atoms are bonded by electric forces and are separated by vacuum, and their vibrations can propagate through vacuum and constitute the acoustic wave via interatomic interactions. An interesting question thus rises: are there interactions that can mediate the acoustic wave to travel across vacuum gap of larger than the atomic scale?

Several potential mechanisms have been suggested in the context of near-field heat transfer, such as the *van der Waals* force [Budaev and Bogy, 2011; Ezzahri and Joulain, 2014; Sasihithlu et al., 2017; Pendry et al., 2016] and electrostatic force[1] bias[Pendry et al., 2016; Volokitin, 2019, 2020]. In the most recent work, Viloria et al. [2023] have numerically demonstrated using molecular dynamic simulations that acoustic vibrational modes can transfer heat between polar crystals. Nevertheless, these mechanisms scale out rapidly with the separation distance of the solids, and are only non-trivial when the vacuum gap is less than $\sim$ 1 nm at room temperature. There is one recent experiment from Fong et al. [2019] claiming coupling between acoustic phonon modes across hundreds of nanometers wide vacuum gap with the help of Casimir force, but it has been pointed out by Biehs et al. [2020] that the transmitted heat flux in that experiment is 15 orders of magnitude smaller than that of the *near-field radiative heat transfer* (NFRHT) at the same conditions. Hence, such mechanism can be omitted in the scope of this work.

Another possible mechanism is piezoelectricity, which couples the defor-

[1] By applying electric potential difference across the vacuum gap, where both surfaces must be metallic.

mations of a solid with a macroscopic electric field and *vice versa*. As a result, an acoustic wave can extend into the vacuum as a decaying, evanescent electric field, when it impinges onto a free surface of a piezoelectric solid. It is interesting that such a field can have a macroscopic length scale, which is determined by the wavelength of that incoming acoustic wave, and can then be coupled back to the deformations of a second piezoelectric solid placed within that length scale. As such, the acoustic wave (acoustic phonon) is coherently transmitted between two solids across the vacuum.

This chapter is based on the author's original theoretical work on this topic. It will start with a review of previous relevant work on this topic, and then the tunneling problem, *i.e.* the coupling across vacuum, will be solved with two different approaches for a plane-plane geometry: one directly solves the extended Stroh formalism with the boundary conditions, and the other uses a multiple reflection factor[Geng and Maasilta, 2022a]. Then follow a few illustrative examples: analytical solutions will be derived with both approaches for a hexagonal wurtzite crystal with a high-symmetry orientation; and the tunneling transmission coefficients of two different crystallographic cuts of a hexagonal crystal will be calculated numerically with different orientations[Geng and Maasilta, 2022a]. Furthermore, there is even a possibility for a complete transmission of the acoustic wave across the vacuum gap, and a strikingly simple resonance condition for it will be presented with analytical proof and numerical demonstration[Geng and Maasilta, 2022b]. Finally, the formalism developed in this work will be applied to the investigation of the near field heat transfer of the acoustic phonons, and numerical results and comparison with other heat transfer mechanisms will be presented[Geng and Maasilta, 2023b].

3.1 A short review of the topic

To the best of the author's knowledge, the first discussion on the topic of the acoustic wave tunneling mediated by piezoelectricity was carried out by Kaliski [1966], who theoretically investigated the tunneling of the *horizontally polarized shear* (SH) waves between cubic piezoelectric crystals in the limit of zero vacuum width.

Later, Balakirev and Gorchakov [1977] presented an important seminal work, in which the transmission across a vacuum gap with a finite width is calculated for the SH wave modes. Two crystal symmetries with high-symmetry orientations were considered in that work: a cubic crystal with the surface aligned with YZ plane, and a hexagonal crystal with the surface parallel to the Z-axis, with numerical examples given for $Bi_{12}GeO_{20}$ and $LiIO_3$ crystals. One of the important findings is that the transmission coefficient can be large and even close to unity for angles close to glancing incidence. Following that study, an experimental demonstration of an observed transmission coefficient up to 0.5 using $LiIO_3$ crystals with an 15 MHz ultrasound was reported by the same authors [Balakirev

et al., 1978].

These early works were carried out using the standard elasticity theory of piezoelectricity that is presented in Section 2.2. The results and expressions provided from these works are only applicable to the highest symmetry crystal orientations and the simplest wave mode (SH), and thus have no generality.

More recently, Prunnila and Meltaus (2010) presented their study of acoustic phonon tunneling in the context of near-field heat transfer. In that work, the standard elasticity theory is used with a scattering matrix approach to numerically calculate the energy transmission coefficients as a function of the incident angle and wave vector. However, many simplifications and approximations have been applied in that study, including isotropic properties of the materials, single component piezoelectric stress tensor, and the omitted piezoelectric stiffening. In addition, there was only one crystal symmetry and orientation considered, where the crystal Z-axis was perpendicular to the surface, in which case only two wave modes contribute to the tunneling. Furthermore, their results are contradictory to those obtained in this work, which will also be discussed in a later section of this chapter.

On the other hand, there are a limited number of studies that have been performed under the framework of the extended Stroh formalism to investigate the tunneling of a bulk acoustic wave. To the author's knowledge, the first seminal work was done by Al'shits et al. [1993], in which a general solution of the transmission and reflection coefficients of an incident slow quasi-transverse (ST) bulk wave was formally introduced. In the later works presented by Darinskii, that framework had been developed further [Darinskii, 1997, 1998], and has later been applied to study the transmission and reflection mediated by the leaky gap wave [Darinskii and Weihnacht, 2006]. The results derived in those works were more general and can be applied to anisotropic piezoelectric solids. However, only one incident bulk wave mode, the ST mode, was considered, and these results have not been applied to the scope of heat transfer.

3.2 Theory

A system of two anisotropic, semi-infinite piezoelectric solids separated by a vacuum gap of width d is considered in this dissertation, as illustrated in Figure 6. Both solids can be oriented arbitrarily, and the relation between the crystal intrinsic coordinates XYZ and the external laboratory coordinates xyz is described by a set of Euler angles $(\vartheta, \varphi, \psi)$. The details of the coordinates and angle setups, as well as the rotation procedures have been presented in section 2.1.5, and the transformations of the piezoelectric tensors have been explained in section 2.2.3.

The solid-vacuum interfaces are set to be mechanically and electrically free, and are perpendicular to the xy-plane (the surface unit inward normal $\boldsymbol{n}$ is aligned with z-axis). The surfaces of the solid 1 and solid 2 are at $z = 0$ and $z = -d$, respectively. The incoming acoustic bulk wave is assumed to be a harmonic plane

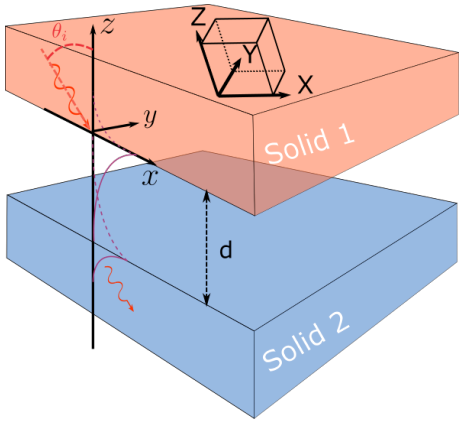

FIGURE 6 Schematic of two piezoelectric solids separated by a vacuum gap.

wave of the form $\sim \exp(i\omega t - i\boldsymbol{k}\cdot\boldsymbol{r})$, and, without losing generality, is always considered to propagate inside the xz-plane (sagittal plane) of the solid 1 from the positive z-axis and negative x-axis directions towards the surface ($z = 0$), hence $k_x > 0$ and $k_z < 0$. It should be stressed here that the sagittal plane has a rotational degree of freedom with respect to $\boldsymbol{n}$ measured by an azimuth angle. This angle is equivalent to the orientation angle φ from the crystal rotation, and, for the sake of simplicity and to avoid the duplication of the rotations on the same degree of freedom, only the azimuth angle φ of the crystal orientation will be unambiguously taken into account in this dissertation.

In addition, the quasistatic approximation, which is discussed in section 2.2.2, is applied in this work, and only low energy acoustic waves are considered so that a linear dispersion relation is assumed. Moreover, the modeling presented below is not applicable to solids that are not piezoelectric, or have one or more of the dimensions much smaller than the acoustic wavelength in question due to the breakdown of the bulk wave assumption, or are separated by an atomic length scale gap which would break down continuum elasticity.

3.2.1 Model solutions and Boundary conditions

An acoustic plane wave impinging onto the solid-vacuum interface will be scattered into a linear combination of partial waves, either transmitted or reflected. This scattering problem will be modeled using the extended Stroh formalism in this work. For the convenience of the reader, the general model solutions of the scattered wave solutions are listed again here, same as Eqs.(73):

$$\begin{aligned}
\boldsymbol{u} &= \sum_\alpha b_\alpha \boldsymbol{A}_\alpha e^{-ik_x(x+p_\alpha z)+i\omega t} \\
\Phi &= \sum_\alpha b_\alpha \phi_\alpha e^{-ik_x(x+p_\alpha z)+i\omega t} \\
\boldsymbol{n}\cdot\boldsymbol{\sigma} &= ik_x \sum_\alpha b_\alpha \boldsymbol{L}_\alpha e^{-ik_x(x+p_\alpha z)+i\omega t} \\
\boldsymbol{n}\cdot\boldsymbol{D} &= ik_x \sum_\alpha b_\alpha D^n_\alpha e^{-ik_x(x+p_\alpha z)+i\omega t},
\end{aligned} \tag{100}$$

where $p \equiv k_z/k_x$, b_α is the dimensionless amplitude of the partial wave mode α, and $\boldsymbol{A}_\alpha, \phi_\alpha, \boldsymbol{L}_\alpha, D^n_\alpha$ are the *Stroh normalized* (see section 2.3.2 for details) constants describing the displacement, the electric potential, the traction force and the normal projection of the electric displacement of the α mode, respectively. To avoid redundant writing in expressions, the common phase factor $\exp(i\omega t - ik_x x)$ will be omitted hereafter.

For a given incident wave, the angular frequency ω and the wave vector components along the surface k_x are known, and are conserved for all the wave solutions. Hence the unknown solutions are $\boldsymbol{\xi}_\alpha = [\boldsymbol{A}_\alpha, \phi_\alpha, \boldsymbol{L}^n_\alpha, D^n_\alpha]^T$, p_α and the amplitude b_α. $\boldsymbol{\xi}_\alpha$ and p_α are the eigenvector and eigenvalue of the eight-dimensional Stroh characteristic equation (82):

$$\boldsymbol{N}(v_x)\boldsymbol{\xi}_\alpha = p_\alpha \boldsymbol{\xi}_\alpha \,, \tag{101}$$

and can be readily solved with the knowledge of the material, the crystal orientation, and $v_x \equiv \omega/k_x$. Whereas b_α needs to be solved from the boundary conditions at the solid-vacuum interfaces.

The continuities of the electric potential and the normal component of the electric displacement, and the condition of mechanically free surface enforce the boundary conditions to be:

$$\begin{aligned} \Phi^{(i)} &= \Phi_V \\ \boldsymbol{n}\cdot\boldsymbol{D}^{(i)} &= \boldsymbol{n}\cdot\boldsymbol{D}_V \,, \\ \boldsymbol{n}\cdot\boldsymbol{\sigma}^{(i)} &= \boldsymbol{0} \end{aligned} \tag{102}$$

where the superscripts $(i) = 1, 2$ are used to indicate the solid 1 and 2, respectively, and the subscripts V indicate the corresponding fields are inside the vacuum.

The electric potential in vacuum needs to satisfy the *Laplace equation* $\nabla^2\Phi_V = 0$, which leads to $k_x^2 + k_z^2 = 0$ or $k_z = \pm ik_x$ for plane waves. The latter expression states that there are two partial waves in the vacuum: an exponentially decaying mode with $\sim \exp(k_x z)$ and an exponentially increasing mode with $\sim \exp(-k_x z)$, if looking from the surface of solid 1 ($z = 0$) towards to the vacuum ($z < 0$). Hence, the general model solutions of the waves in vacuum can be written in a form following Eqs.(100) as:

$$\Phi_V = b_{V_+}\phi_{V_+}e^{k_x z} + b_{V_-}\phi_{V_-}e^{-k_x z}, \tag{103}$$

in which the common phase factor $\exp(+i\omega t - ik_x x)$ is omitted. This solution strongly resembles the form of a wave function of a quantum-mechanical tunneling problem [Griffiths and Schroeter, 2018].

Using the relation $\boldsymbol{D}_V = -\epsilon_0 \nabla\cdot\Phi_V$, the normal component of the vacuum electric displacement can also be obtained:

$$\boldsymbol{n}\cdot\boldsymbol{D}_V = -\epsilon_0 k_x b_{V_+}\phi_{V_+}e^{k_x z} + \epsilon_0 k_x b_{V_-}\phi_{V_-}e^{-k_x z}. \tag{104}$$

Comparing this to the electric displacement solution in Eqs.(100), one finds that the Stroh normalized electric displacement constants $D^n_{V_\pm}$ can be expressed in

terms of the normalized potential $\phi_{V_\pm}$ as $D^n_{V_\pm} = \pm i\epsilon_0\phi_{V_\pm}$. The normalization condition Eq.(84), on the other hand, leads to $2\phi_{V_\pm}D_{V_\pm} = 1$ since the displacement and traction force are zero in vacuum. Thus, $\phi_{V_\pm} = 1/\sqrt{\pm 2i\epsilon_0}$ and $D^n_{V_\pm} = \sqrt{\pm 2i\epsilon_0}/2$ can be readily solved, independent to the parameters of the solids or the wave modes.

With all the relevant model solutions (100), (103) and (104) prepared, the next task is to insert them into the boundary conditions (102) to find the solutions for the amplitudes. Here, the explicit forms of the boundary conditions are expressed as:

$$\begin{aligned}
b^{(1)}_{in}\phi^{(1)}_{in} + \sum_{\alpha=1}^{4} b^{(1)}_{\alpha}\phi^{(1)}_{\alpha} &= b_{V+}\phi_{V+} + b_{V-}\phi_{V-} \\
b^{(1)}_{in}D^{n,(1)}_{in} + \sum_{\alpha=1}^{4} b^{(1)}_{\alpha}D^{n,(1)}_{\alpha} &= b_{V+}D^n_{V+} + b_{V-}D^n_{V-} \\
b^{(1)}_{in}\boldsymbol{L}^{(1)}_{in} + \sum_{\alpha=1}^{4} b^{(1)}_{\alpha}\boldsymbol{L}^{(1)}_{\alpha} &= \hat{\boldsymbol{O}}_{(3)} \\
\sum_{\alpha=1}^{4} \tilde{b}^{(2)}_{\alpha}\phi^{(2)}_{\alpha} &= b_{V+}\phi_{V+}e^{-k_x d} + b_{V-}\phi_{V-}e^{k_x d} \\
\sum_{\alpha=1}^{4} \tilde{b}^{(2)}_{\alpha}D^{n,(2)}_{\alpha} &= b_{V+}D^n_{V+}e^{-k_x d} + b_{V-}D^n_{V-}e^{k_x d} \\
\sum_{\alpha=1}^{4} \tilde{b}^{(2)}_{\alpha}\boldsymbol{L}^{(2)}_{\alpha} &= \hat{\boldsymbol{O}}_{(3)},
\end{aligned} \tag{105}$$

where the subscript in and $\alpha = 1, ..., 4$ designate the incident and the four scattered wave modes; the superscripts $(1), (2)$ indicate the wave modes in the corresponding solids 1 and 2; $z = 0$ and $z = -d$ are substituted for the surfaces of solid 1 and solid 2, respectively; and the shorthand amplitudes of solid 2 $\tilde{b}^{(2)}_{\alpha} \equiv b^{(2)}_{\alpha}\exp\left(ip^{(2)}_{\alpha}k_x d\right)$ are used.

The above explicit conditions can be written into two compact expressions:

$$\begin{aligned}
b^{(1)}_{in}\boldsymbol{U}^{(1)}_{in} + \sum_{\alpha=1}^{4} b^{(1)}_{\alpha}\boldsymbol{U}^{(1)}_{\alpha} &= b_{V_+}\boldsymbol{U}_{V_+} + b_{V_-}\boldsymbol{U}_{V_-}\,, \\
\sum_{\alpha=1}^{4} \tilde{b}^{(2)}_{\alpha}\boldsymbol{U}^{(2)}_{\alpha} &= b_{V_+}\boldsymbol{U}_{V_+}e^{-k_x d} + b_{V_-}\boldsymbol{U}_{V_-}e^{k_x d}\,,
\end{aligned} \tag{106}$$

by introducing a set of 5×1 column vectors $\boldsymbol{U}^{(i)}_{\gamma} = [\phi^{(i)}_{\gamma}, D^{n,(i)}_{\gamma}, \boldsymbol{L}^{(i)}_{\gamma}]^T$ for the wave modes $\gamma = in, \alpha$ inside the solid $i = 1, 2$.

As stated above, the solutions to these boundary conditions Eqs.(106) give the partial wave amplitudes $b^{(1)}_{\alpha}, \tilde{b}^{(2)}_{\alpha}, b_{V_\pm}$. With a given incident amplitude $b^{(1)}_{in}$, the transmission and reflection amplitude coefficients can then be acquired as:

$$t_\alpha \equiv \tilde{b}^{(2)}_{\alpha}/b^{(1)}_{in}, \quad r_\alpha \equiv b^{(1)}_{\alpha}/b^{(1)}_{in}. \tag{107}$$

It is also useful to note here that these coefficients represents the amplitude ratio of the power flow in the direction normal to the interface, as has been discussed in section 2.3.3. For a transmitted *bulk* partial wave mode α, its power flow in the normal direction can be written as:

$$\boldsymbol{n} \cdot \boldsymbol{P}^{(2)}_{\mathrm{AV},\alpha} = |t_\alpha|^2 \left[\boldsymbol{n} \cdot \boldsymbol{P}^{(1)}_{\mathrm{AV},in}\right]. \tag{108}$$

The above equation is obtained from Eq.(96) and using the facts that $\boldsymbol{\xi}^T_{in}\hat{\boldsymbol{T}}\boldsymbol{\xi}^*_{in} = \boldsymbol{\xi}^T_{\alpha}\hat{\boldsymbol{T}}\boldsymbol{\xi}^*_{\alpha} = -1$(see Eq.(97)), for a bulk incident wave and a bulk transmitted partial wave mode α.

In the next two sections, two approaches will be presented to solve the boundary conditions: the first one is to build and solve a matrix that combines the boundary conditions of both interfaces as a function of the incident wave using matrix algebra, and the second is to introduce a gap distance dependent multiple reflection factor, to connect the individual solutions of each interface together. Both approaches lead to identical results, the choice of the method should be based on the practicality and the computational efficiency, depending on which parameters, either the incident wave or the distance between the solids, is to be varied.

3.2.2 Combined boundary conditions approach

The goal of the first approach is to use simple matrix algebra to rearrange the boundary conditions into a simple linear matrix equation:

$$\hat{y} = \boldsymbol{M}\hat{x},$$

where $\hat{y}$ is a 8×1 column vector that contains the properties of the incident wave, $\boldsymbol{M}$ is a 8×8 matrix derived from the information of the system, *i.e.* the material properties and vacuum gap distance, and $\hat{x}$ is a 8×1 column vector which contains the wave amplitudes of all scattered waves, reading as:

$$\hat{x} = [b^{(1)}_1, ...b^{(1)}_4, \tilde{b}^{(2)}_1, ..., \tilde{b}^{(2)}_4]^T.$$

The derivations of this approach will be elaborated below.

Starting from the explicit boundary condition (105), the number of linear equations can be reduced from ten to eight by eliminating $b_{V_\pm}$:

$$\begin{aligned}
\boldsymbol{V}_1^{-1}\left(\begin{bmatrix}\phi^{(1)}_{in}\\ D^{n,(1)}_{in}\end{bmatrix} b^{(1)}_{in} + \sum_{\alpha=1}^{4}\begin{bmatrix}\phi^{(1)}_{\alpha}\\ D^{n,(1)}_{\alpha}\end{bmatrix} b^{(1)}_{\alpha}\right) &= \boldsymbol{V}_2^{-1}\left(\sum_{\alpha=1}^{4}\begin{bmatrix}\phi^{(2)}_{\alpha}\\ D^{n,(2)}_{\alpha}\end{bmatrix} \tilde{b}^{(2)}_{\alpha}\right)\\
b^{(1)}_{in}\boldsymbol{L}^{(1)}_{in} + \sum_{\alpha=1}^{4} b^{(1)}_{\alpha}\boldsymbol{L}^{(1)}_{\alpha} &= \hat{\boldsymbol{O}}_{(3)}\\
\sum_{\alpha=1}^{4} \tilde{b}^{(2)}_{\alpha}\boldsymbol{L}^{(2)}_{\alpha} &= \hat{\boldsymbol{O}}_{(3)}\,,
\end{aligned} \tag{109}$$

where

$$\boldsymbol{V}_1 = \begin{bmatrix}\phi_{V+} & \phi_{V-}\\ D^n_{V+} & D^n_{V-}\end{bmatrix}, \boldsymbol{V}_2 = \begin{bmatrix}\phi_{V+}e^{-k_x d} & \phi_{V-}e^{k_x d}\\ D^n_{V+}e^{-k_x d} & D^n_{V-}e^{k_x d}\end{bmatrix}.$$

Recalling that $\phi_{V_\pm} = 1/\sqrt{\pm 2i\epsilon_0}$ and $D^n_{V_\pm} = \sqrt{\pm 2i\epsilon_0}/2$, we point out that the matrices $\boldsymbol{V}_1$ and $\boldsymbol{V}_2$ only depend on the dimensionless factor $k_x d$.

In the next step, all the terms having $b^{(1)}_{in}$ will be moved to the LHS while other terms are moved to the RHS. In addition, the 5×1 column vector $\boldsymbol{U}^{(i)}_\gamma = [\phi^{(i)}_\gamma, D^{(i)}_\gamma, \boldsymbol{L}^{(i)}_\gamma]^T$, which was introduced in the previous section, is used to substitute the Stroh eigenvectors of the incident wave ($\boldsymbol{U}^{(1)}_{in}$), the reflected waves ($\boldsymbol{U}^{(1)}_\alpha$) and the transmitted waves ($\boldsymbol{U}^{(2)}_\alpha$). The new expressions read as:

$$
\begin{aligned}
-\left[\boldsymbol{V}_1^{-1} \;\; \hat{\boldsymbol{O}}_{(2\times 3)}\right] \boldsymbol{U}^{(1)}_{in} b^{(1)}_{in} &= \sum_{\alpha=1}^{4} \left(\left[\boldsymbol{V}_1^{-1} \;\; \hat{\boldsymbol{O}}_{(2\times 3)}\right] \boldsymbol{U}^{(1)}_{\alpha} b^{(1)}_{\alpha} - \left[\boldsymbol{V}_2^{-1} \;\; \hat{\boldsymbol{O}}_{(2\times 3)}\right] \boldsymbol{U}^{(1)}_{\alpha} \tilde{b}^{(2)}_{\alpha} \right) \\
-\left[\hat{\boldsymbol{O}}_{3\times 2} \;\; \hat{\boldsymbol{I}}_{(3)}\right] \boldsymbol{U}^{(1)}_{in} b^{(1)}_{in} &= \sum_{\alpha=1}^{4} \left(\left[\hat{\boldsymbol{O}}_{3\times 2} \;\; \hat{\boldsymbol{I}}_{(3)}\right] \boldsymbol{U}^{(1)}_{\alpha} b^{(1)}_{\alpha} - \left[\hat{\boldsymbol{O}}_{3\times 2} \;\; \hat{\boldsymbol{O}}_{(3\times 3)}\right] \boldsymbol{U}^{(2)}_{\alpha} \tilde{b}^{(2)}_{\alpha} \right) \\
-\left[\hat{\boldsymbol{O}}_{3\times 2} \;\; \hat{\boldsymbol{O}}_{(3\times 3)}\right] \boldsymbol{U}^{(1)}_{in} b^{(1)}_{in} &= \sum_{\alpha=1}^{4} \left(\left[\hat{\boldsymbol{O}}_{3\times 2} \;\; \hat{\boldsymbol{O}}_{(3\times 3)}\right] \boldsymbol{U}^{(1)}_{\alpha} b^{(1)}_{\alpha} - \left[\hat{\boldsymbol{O}}_{3\times 2} \;\; \hat{\boldsymbol{I}}_{(3)}\right] \boldsymbol{U}^{(2)}_{\alpha} \tilde{b}^{(2)}_{\alpha} \right),
\end{aligned}
\tag{110}
$$

where $\hat{\boldsymbol{O}}_{n\times m}$ is a zero matrix of dimensions $n \times m$, and $\hat{\boldsymbol{I}}_{(3)}$ is the 3×3 unit matrix.

The above equations can be written into a matrix equation form:

$$
-\boldsymbol{M}_1 \boldsymbol{U}^{(1)}_{in} b^{(1)}_{in} = \sum_{\alpha=1}^{4} \left(\boldsymbol{M}_1 \boldsymbol{U}^{(1)}_{\alpha} b^{(1)}_{\alpha} - \boldsymbol{M}_2 \boldsymbol{U}^{(2)}_{\alpha} \tilde{b}^{(2)}_{\alpha} \right), \tag{111}
$$

where $\boldsymbol{M}_1$ and $\boldsymbol{M}_2$ are 8×5 matrices defined as:

$$
\boldsymbol{M}_1 = \begin{bmatrix} \boldsymbol{V}_1^{-1} & \hat{\boldsymbol{O}}_{(2\times 3)} \\ \hat{\boldsymbol{O}}_{(3\times 2)} & \hat{\boldsymbol{I}}_{(3)} \\ \hat{\boldsymbol{O}}_{(3\times 2)} & \hat{\boldsymbol{O}}_{(3\times 3)} \end{bmatrix}, \boldsymbol{M}_2 = \begin{bmatrix} \boldsymbol{V}_2^{-1} & \hat{\boldsymbol{O}}_{(2\times 3)} \\ \hat{\boldsymbol{O}}_{(3\times 2)} & \hat{\boldsymbol{O}}_{(3\times 3)} \\ \hat{\boldsymbol{O}}_{(3\times 2)} & \hat{\boldsymbol{I}}_{(3)} \end{bmatrix}. \tag{112}
$$

Comparing the above expression with the targeted matrix equation $\hat{y} = \boldsymbol{M}\hat{x}$ and recalling that $\hat{x} = [b^{(1)}_1, ...b^{(1)}_4, \tilde{b}^{(2)}_1, ..., \tilde{b}^{(2)}_4]^T$, one finds that $\hat{y} = -\boldsymbol{M}_1 \boldsymbol{U}_{in} b_{in}$, and $\boldsymbol{M}$ is a 8×8 matrix constructed by joining eight 8×1 column matrices together as:

$$
\begin{aligned}
\boldsymbol{M} = \big[& \boldsymbol{M}_1 \boldsymbol{U}^{(1)}_1, \boldsymbol{M}_1 \boldsymbol{U}^{(1)}_2, \boldsymbol{M}_1 \boldsymbol{U}^{(1)}_3, \boldsymbol{M}_1 \boldsymbol{U}^{(1)}_4, \\
& -\boldsymbol{M}_2 \boldsymbol{U}^{(2)}_1, -\boldsymbol{M}_2 \boldsymbol{U}^{(2)}_2, -\boldsymbol{M}_2 \boldsymbol{U}^{(2)}_3, -\boldsymbol{M}_2 \boldsymbol{U}^{(2)}_4 \big],
\end{aligned}
$$

As a result of the above derivations, the scattering coefficients of the partial wave amplitudes $\hat{x}/b^{(1)}_{in}$, including all the reflection coefficients $r_\alpha \equiv b^{(1)}_\alpha / b^{(1)}_{in}$ in the solid 1 and all the transmission coefficients $t_\alpha \equiv \tilde{b}^{(2)}_\alpha / b^{(1)}_{in}$ in the solid 2, can therefore be solved simultaneously by the inversion of the matrix $\boldsymbol{M}$ as:

$$
\left[r_1, ...r_4, t_1, ..., t_4\right]^T = -\boldsymbol{M}^{-1} \boldsymbol{M}_1 \boldsymbol{U}^{(1)}_{in}. \tag{113}
$$

It is important to remark here that, for given materials, crystal orientations, vacuum gap size and the frequency, the matrices $\boldsymbol{M}$ and $\boldsymbol{M}_1$ in Eq.(113) depend only on k_x, which is a *conserved quantity* at the scattering interface for all partial wave modes due to the continuity conditions. On the other hand, the detailed

information of the incident wave, *i.e.* the normal component of the wave vector k_z and the displacement vector $\boldsymbol{A}_{in}$, are contained only in the column vector $\boldsymbol{U}_{in}^{(1)}$. Therefore, in the case of a varying incident wave with a given k_x, the matrices $\boldsymbol{M}$ and $\boldsymbol{M}_1$ can be computed only once, and the results of the reflection and transmission coefficients can be acquired simply by changing $\boldsymbol{U}_{in}^{(1)}$.

In contrast, the method suggested by Al'shits et al. [1993] uses Cramer's rule. This means that each time a new incident wave mode is given, the matrices in the formulations have to be re-constructed and re-calculated. As demonstrated in Eqs.(38) and (40) of Ref.[Al'shits et al., 1993], common columns of the matrices collect all the eigenvector solutions of the transmitted wave modes *except* the incident mode. This is to ensure the fully constructed matrices are linearly independent in their columns. In addition, the Cramer's rule requires computation of $n+1$ determinants to solve n linear equations, and is thus considered computationally inefficient compared to the single inversion operation of $\boldsymbol{M}$ in the approach presented above.

3.2.3 Multiple reflection approach

Alternatively, the reflections and transmissions from an incident acoustic wave can be considered as coupled results of a superposition of multiple reflected evanescent electric potential waves inside the vacuum gap between the two interfaces. Such *multiple reflection* picture has been adopted before to describe the "photon tunneling" of the frustrated total internal reflection of the electromagnetic waves in optics [Court and von Willisen, 1964; Born et al., 1999].

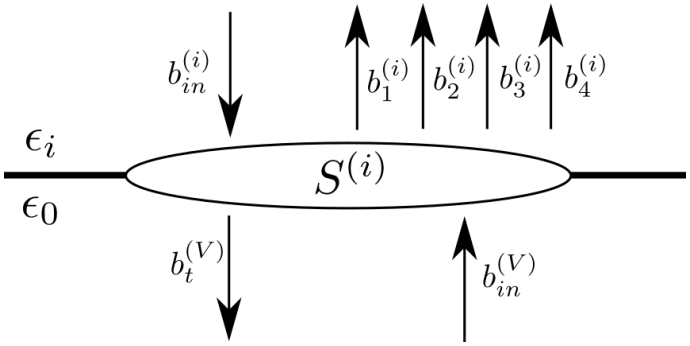

FIGURE 7 Illustration of the scattering matrix $\mathbb{S}^{(i)}$ and the single surface scattering coefficients $b_\alpha^{(i)}$ at a solid-vacuum interface.

To construct the coupled transmission and reflection coefficients using the multiple reflection picture, the definition of the *scattering matrix* should be explained and derived first. The scattering matrix contains a set of "uncoupled" reflection and transmission coefficients, which describe the scattering of the waves at the solid-vacuum interface as if there is no adjacent second solid. Consequently, these uncoupled coefficients will be referred to as *single surface coefficients* in this dissertation.

Consider an input wave scattering at an interface i between a piezoelectric

solid and the vacuum. All the output waves can be related to the input one using a scattering matrix $\mathbb{S}^{(i)}$, as illustrated in Figure 7. $\mathbb{S}^{(i)}$ is defined as:

$$\begin{bmatrix} b_1^{(i)} \\ b_2^{(i)} \\ b_3^{(i)} \\ b_4^{(i)} \\ b_t^{(V)} \end{bmatrix} = \mathbb{S}^{(i)} \begin{bmatrix} b_{in}^{(i)} \\ b_{in}^{(V)} \end{bmatrix} = \begin{bmatrix} \bar{\boldsymbol{r}}^{(i)} & \bar{\boldsymbol{t}}^{(i)} \\ \bar{t}_{in\to V}^{(i)} & \bar{r}_V^{(i)} \end{bmatrix} \begin{bmatrix} b_{in}^{(i)} \\ b_{in}^{(V)} \end{bmatrix}, \tag{114}$$

where the superscript $(i) = 1, 2$ signifies either the solid 1 or 2, the superscript (V) denotes the evanescent wave in the vacuum gap, $\bar{\boldsymbol{r}}^{(i)} = [\bar{r}_{in\to 1}^{(i)} ... \bar{r}_{in\to 4}^{(i)}]^T$ are the single surface coefficients of an incoming wave reflected into a partial wave mode $\alpha = 1, ..., 4$, $\bar{\boldsymbol{t}}^{(i)} = [\bar{t}_{V\to 1}^{(i)} ... \bar{t}_{V\to 4}^{(i)}]^T$ are the single surface coefficients of a vacuum wave transmitted into a partial wave mode $\alpha = 1, ..., 4$, $\bar{r}_V^{(i)}$ is the coefficient of a potential wave in vacuum reflected on the vacuum side of the interface $i = 1, 2$, and $\bar{t}_{in\to V}^{(i)}$ is the coefficient of an incoming wave transmitted as a potential wave into vacuum. To avoid confusion with those coefficients that denote the reflection and transmission *across* the vacuum gap, *i.e.* obtained in Eq.(113), overhead bars are used for the symbols here. It should stressed again that these "bare" coefficients are the *single surface coefficients*, describing the scattering of the waves as if there is no adjacent second solid.

The first boundary condition in Eqs.(106) can be rearranged by moving all the inputs to RHS and outputs to LHS, giving:

$$\begin{bmatrix} \boldsymbol{u}_1^{(1)}, \boldsymbol{u}_2^{(1)}, \boldsymbol{u}_3^{(1)}, \boldsymbol{u}_4^{(1)}, -\boldsymbol{u}_{V_+} \end{bmatrix} \begin{bmatrix} b_1^{(1)} \\ b_2^{(1)} \\ b_3^{(1)} \\ b_4^{(1)} \\ b_{V_+} \end{bmatrix} = \begin{bmatrix} -\boldsymbol{u}_{in}^{(1)}, \boldsymbol{u}_{V_-} \end{bmatrix} \begin{bmatrix} b_{in}^{(1)} \\ b_{V_-} \end{bmatrix}. \tag{115}$$

If we consider a similar scattering at the interface of the solid 2, the boundary condition follows the above equation, but the medium index is changed to (2), and the amplitudes of the incoming (b_{V_-}) and outgoing (b_{V_+}) vacuum waves are interchanged, giving:

$$\begin{bmatrix} \boldsymbol{u}_1^{(2)}, \boldsymbol{u}_2^{(2)}, \boldsymbol{u}_3^{(2)}, \boldsymbol{u}_4^{(2)}, -\boldsymbol{u}_{V_-} \end{bmatrix} \begin{bmatrix} b_1^{(2)} \\ b_2^{(2)} \\ b_3^{(2)} \\ b_4^{(2)} \\ b_{V_-} \end{bmatrix} = \begin{bmatrix} -\boldsymbol{u}_{in}^{(2)}, \boldsymbol{u}_{V_+} \end{bmatrix} \begin{bmatrix} b_{in}^{(2)} \\ b_{V_+} \end{bmatrix}. \tag{116}$$

By comparing the above two single surface boundary conditions with the scattering matrix definition in Eq.(114), one finds the expressions of the scattering

matrices $\mathbb{S}^{(1)}$ and $\mathbb{S}^{(2)}$:

$$\begin{aligned}\mathbb{S}^{(1)} &= \left[\boldsymbol{u}_1^{(1)},...,\boldsymbol{u}_4^{(1)},-\boldsymbol{u}_{V_+}\right]^{-1}\left[-\boldsymbol{u}_{in}^{(1)},\boldsymbol{u}_{V_-}\right],\\ \mathbb{S}^{(2)} &= \left[\boldsymbol{u}_1^{(2)},...,\boldsymbol{u}_4^{(2)},-\boldsymbol{u}_{V_-}\right]^{-1}\left[-\boldsymbol{u}_{in}^{(2)},\boldsymbol{u}_{V_+}\right].\end{aligned} \tag{117}$$

It is worth mentioning that $\boldsymbol{u}_{in}^{(2)}$ is formally written in the definition of $\mathbb{S}^{(2)}$ for completeness. However, it will not affect the transmission or reflection of an incident wave in solid 1 due to the linearity in the equations. In practice, *i.e.* computing $\mathbb{S}^{(2)}$ for the case of incoming wave from solid 1, $\boldsymbol{u}_{in}^{(2)}$ can be set arbitrarily, for example, to zero.

With the knowledge of the single surface coefficients, the transmission of an incident acoustic wave across the vacuum gap can be pictured in the following way: the incoming wave transmits first through the interface between solid 1 and vacuum ($\bar{t}_{in\to V}^{(1)}$) and becomes an evanescent wave; it traverses the gap once [$\exp(-k_x d)$], partly transmitted into a partial mode α in the solid 2 ($\bar{t}_{V\to\alpha}^{(2)}$), and partly reflected by the second interface ($\bar{r}_V^{(2)}$) and then the first one ($\bar{r}_V^{(1)}$); it traverses the third time across the vacuum [$\exp(-3k_x d)$] and arrives the second interface again; it will be reflected and so forth. As a result, a geometric series can be applied to the coupled transmission coefficient t_α for the partial mode α, giving:

$$\begin{aligned}t_\alpha =&\bar{t}_{in\to V}^{(1)}e^{-k_x d}\bar{t}_{V\to\alpha}^{(2)} + \bar{t}_{in\to V}^{(1)}\bar{r}_V^{(1)}\bar{r}_V^{(2)}e^{-3k_x d}\bar{t}_{V\to\alpha}^{(2)}\\ &+ \bar{t}_{in\to V}^{(1)}(\bar{r}_V^{(1)})^2(\bar{r}_V^{(2)})^2e^{-5k_x d}\bar{t}_{V\to\alpha}^{(2)} + \dots\\ =&\frac{\bar{t}_{in\to V}^{(1)}\bar{t}_{V\to\alpha}^{(2)}e^{-k_x d}}{1-\bar{r}_V^{(1)}\bar{r}_V^{(2)}e^{-2k_x d}},\end{aligned}$$

in which an attenuation factor $\exp(-k_x d)$ is applied each time the wave traverses the gap. The coupled reflection coefficient $r_\alpha^{(1)}$ can also be derived using the same approach, and the common *multiple reflection factor* of both coefficients reads as:

$$f_m(d) = \frac{e^{-k_x d}}{1-\bar{r}_V^{(1)}\bar{r}_V^{(2)}e^{-2k_x d}}. \tag{118}$$

Consequently, the expressions of the coupled transmission and reflection coefficients t_α and r_α from an incident wave into partial mode α across the vacuum can be written as:

$$t_\alpha = \bar{t}_{V\to\alpha}^{(2)}\bar{t}_{in\to V}^{(1)}f_m(d) \tag{119}$$

$$r_\alpha = \bar{r}_\alpha^{(1)} + \bar{r}_V^{(2)}\bar{t}_{V\to\alpha}^{(1)}\bar{t}_{in\to V}^{(1)}f_m(d)e^{-k_x d}. \tag{120}$$

These coupled coefficients are equivalent to those obtained from Eq.(113) of the combined boundary conditions approach. The results of both methods were numerically checked and found to be identical. The key difference of the multiple reflection approach is that only the multiple reflection factor $f_m(d)$ is a function of the gap width d. Therefore, the scattering matrices $\mathbb{S}^{(1)}$ and $\mathbb{S}^{(2)}$ can

be calculated for given materials, crystal orientations and the incident wave, and the variation of the vacuum gap width can be considered via the explicit factor $f_m(d)$ only. Such an approach benefits the case where a computation of a function of the gap width is of the interest, since the scattering matrices are computed only once. Furthermore, the multiple reflection picture provides an alternative physical interpretation of the phenomenon of the acoustic waves tunneling across the vacuum gap, analogous to the near-field electromagnetic wave "tunneling" [Court and von Willisen, 1964; Born et al., 1999]. Until now, such an interpretation has not been described in previous literature of bulk acoustic wave tunneling.

3.3 Illustrative examples

In this section, two example calculations will be presented to demonstrate how the framework developed in this dissertation can be used to solve the acoustic wave tunneling problem. In the first example, an analytical solution will be derived for a special crystal orientation using both presented approaches. In the second example, numerical results are presented for a hexagonal ZnO crystal with different orientations.

3.3.1 Analytical example

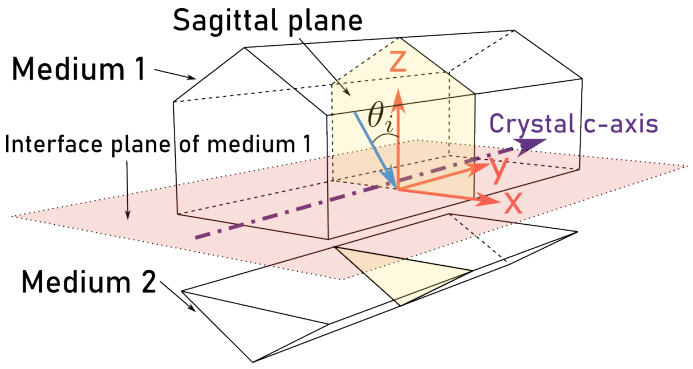

FIGURE 8 Schematic of the phonon tunneling in a wurtzite hexagonal crystal with a vacuum gap cut through a-plane $[11\bar{2}0]$ and with an azimuth angle $\varphi = 0$, [Geng and Maasilta, 2022a], reproduced under the license CC BY 4.0.

The tunneling problem involving piezoelectricity, an anisotropic medium, and an arbitrary crystal orientation can be extremely complicated, and is usually not possible to acquire an analytical solution to the transmission and reflection coefficients. However, there exists a special case in which a relatively simple analytical solution can be derived for a particular incident mode with a high-symmetry crystal configuration. Such a case is that of a fast transverse (FT) bulk wave tunneling across two identical $6mm$ symmetry crystals[2] oriented and cut [3]

[2] Taking ZnO, AlN as real world examples.

[3] Considering the vacuum gap is created in such a way that the solid is cut into two pieces

as illustrated in Figure 8. The crystallographic c-axes (Z-axes) of the solids are perpendicular to the sagittal plane, and thus parallel to the solid-vacuum interface.

Such a crystal orientation can be achieved by a single rotation, specifically, rotating the crystal about the x-axis by 90° following the right-hand rule (see section 2.1.5 for details about the crystal rotation). As a result, the material tensors are transformed to (see section 2.2.3 for details about the tensor transformation):

$$\boldsymbol{e} = \begin{bmatrix} 0 & 0 & 0 & 0 & 0 & -e_{15} \\ -e_{31} & -e_{33} & -e_{31} & 0 & 0 & 0 \\ 0 & 0 & 0 & -e_{15} & 0 & 0 \end{bmatrix} \tag{121}$$

$$\boldsymbol{\epsilon}^S = \begin{bmatrix} \epsilon_{11} & 0 & 0 \\ 0 & \epsilon_{33} & 0 \\ 0 & 0 & \epsilon_{11} \end{bmatrix} \tag{122}$$

$$\boldsymbol{c}^E = \begin{bmatrix} c_{11} & c_{13} & c_{12} & 0 & 0 & 0 \\ c_{13} & c_{33} & c_{13} & 0 & 0 & 0 \\ c_{12} & c_{13} & c_{11} & 0 & 0 & 0 \\ 0 & 0 & 0 & c_{44} & 0 & 0 \\ 0 & 0 & 0 & 0 & c_{66} & 0 \\ 0 & 0 & 0 & 0 & 0 & c_{44} \end{bmatrix}. \tag{123}$$

The incident FT bulk wave under the stated crystal configuration has its displacement only in the y-axis direction and is completely perpendicular to the sagittal (xz-) plane which contains the k-vector of the wave, and is thus referred to as a *horizontally polarized shear wave* (SH). Upon scattering at the surface, it can only excite waves with the same y-axis displacement in this case, and there is thus no mode conversion into other bulk modes, *i.e.* no plane waves are excited with a displacement in the xz-plane. Consequently, only the y-axis components, u_y, from the displacement and σ_{yz} from the stress enter the boundary conditions Eqs.(102), leading to a reduced dimensionality 4×4 Stroh matrix $\boldsymbol{N}$ reading as:

$$\boldsymbol{N}(v_x) = \begin{bmatrix} 0 & 0 & -\frac{\epsilon_{11}}{\epsilon_{11}c_{44}+e_{15}^2} & \frac{e_{15}}{\epsilon_{11}c_{44}+e_{15}^2} \\ 0 & 0 & \frac{e_{15}}{\epsilon_x c_{44}+e_{15}^2} & \frac{c_{44}}{\epsilon_{11}c_{44}+e_{15}^2} \\ c_{44}-\rho v_x^2 & -e_{15} & 0 & 0 \\ -e_{15} & -\epsilon_0 & 0 & 0 \end{bmatrix}. \tag{124}$$

For a given incident angle θ_i defined between the direction of the incident k-vector and the normal of the surface, the phase velocity component $v_x = v/\sin\theta_i$ can easily be derived from the dispersion relation $(c_{44} + e_{15}^2/\epsilon_{11})k^2 = \rho\omega^2$ as:

$$v_x^2 = \frac{\epsilon_{11}c_{44} + e_{15}^2}{\epsilon_{11}\rho \sin^2\theta_i}.$$

With the 4×4 Stroh matrix $\boldsymbol{N}$, the solutions to the characteristic equation (82) consequently reduce to four eigenvalues and the associated four sets of 4×1

and separated by some distance.

eigenvectors $\boldsymbol{\xi} = [u_y, \phi, L_{yz}, D^n]^T$. These solutions correspond to a reflected E mode, a transmitted E mode, a reflected SH mode, and a transmitted SH mode, and their explicit expressions are:

$$
\begin{aligned}
p_1 &= -i, & \boldsymbol{\xi}_1 &= \left[0, \sqrt{\frac{i}{2\epsilon_{11}}}, \frac{e_{15}\sqrt{-i}}{\sqrt{2\epsilon_{11}}}, \frac{\sqrt{-i\epsilon_{11}}}{\sqrt{2}}\right]^T \\
p_2 &= i, & \boldsymbol{\xi}_2 &= \left[0, \frac{\sqrt{-i}}{\sqrt{2\epsilon_{11}}}, \frac{e_{15}\sqrt{i}}{\sqrt{2\epsilon_{11}}}, \frac{\sqrt{i\epsilon_{11}}}{\sqrt{2}}\right]^T \\
p_3 &= \cot\theta_i, & \boldsymbol{\xi}_3 &= \left[\frac{\sqrt{2}}{2}\sqrt{\frac{-k^2\tan\theta_i}{\rho\omega^2}}, -\frac{\sqrt{2}e_{15}}{2\epsilon_{11}}\sqrt{\frac{-k^2\tan\theta_i}{\rho\omega^2}}, \frac{\sqrt{2}}{2}\sqrt{\frac{-\rho\omega^2}{k^2\tan\theta_i}}, 0\right]^T \\
p_4 &= -\cot\theta_i, & \boldsymbol{\xi}_4 &= \left[\frac{\sqrt{2}}{2}\sqrt{\frac{k^2\tan\theta_i}{\rho\omega^2}}, -\frac{\sqrt{2}e_{15}}{2\epsilon_{11}}\sqrt{\frac{k^2\tan\theta_i}{\rho\omega^2}}, \frac{\sqrt{2}}{2}\sqrt{\frac{\rho\omega^2}{k^2\tan\theta_i}}, 0\right]^T,
\end{aligned}
$$

which are normalized using $2(u_y L_{yz} + \phi D) = 1$ based on the orthonormalization condition Eq.(84).

Following the first approach described in section 3.2.2, the matrix $\boldsymbol{M}$ can be constructed from the above solutions straightforwardly as:

$$
\boldsymbol{M} = \frac{1}{2}\begin{bmatrix}
-U & i(\epsilon_0 - \epsilon_{11})V & -iUe^{k_x d} & -(\epsilon_0 + \epsilon_{11})Ve^{k_x d} \\
iU & (\epsilon_0 + \epsilon_{11})V & -Ue^{-k_x d} & i(\epsilon_0 - \epsilon_{11})Ve^{-k_x d} \\
-i\sqrt{2\epsilon_{11}}B & -i\sqrt{2i\epsilon_{11}}A & 0 & 0 \\
0 & 0 & -\sqrt{2\epsilon_{11}}B & -\sqrt{2i\epsilon_{11}}A
\end{bmatrix},
$$

where $A = e_{15}/\epsilon_{11}$, $B^2 = (A^2 + c_{44}/\epsilon_{11})\cot\theta_i$, $\{B \in \mathrm{Re}\,|B \geq 0\}$, $U = i\sqrt{i\epsilon_0}A/\sqrt{\epsilon_{11}}B$ and $V = 1/\sqrt{\epsilon_0\epsilon_{11}}$.

As a result, the reflection and transmission coefficients of the FT partial wave mode can thus be solved from Eq.(113), and the exact expressions are:

$$
r_{FT} = 2iA^2\epsilon_0\frac{Q_+e^{2k_x d} - Q_-}{Q_+^2 e^{2k_x d} - Q_-^2} - i \tag{125}
$$

$$
t_{FT} = -\frac{4iA^2B^2\epsilon_0\epsilon_{11}e^{k_x d}}{Q_+^2 e^{2k_x d} - Q_-^2}, \tag{126}
$$

where

$$
Q_\pm = A^2\epsilon_0 - iB^2(\epsilon_0 \pm \epsilon_{11}).
$$

Identical results can be obtained by using the multiple reflection method that was described in section 3.2.3. The single surface scattering coefficients that

are used to construct the results read as:

$$\bar{r}_{FT}^{(1)} = \frac{iA^2\epsilon_0 - B^2(\epsilon_0 + \epsilon_{11})}{Q_+},$$
$$\bar{r}_V^{(1)} = \frac{iQ_-}{Q_+}, \quad \bar{r}_V^{(2)} = \frac{-iQ_-}{Q_+},$$
$$\bar{t}_V^{(1)} = \bar{t}_{FT}^{(1)} = \bar{t}_{FT}^{(2)} = \frac{2iAB\sqrt{i\epsilon_0\epsilon_{11}}}{Q_+},$$

and the multiple reflection factor is

$$f_m(d) = \frac{Q_+^2 e^{k_x d}}{Q_+^2 e^{2k_x d} - Q_-^2}. \tag{127}$$

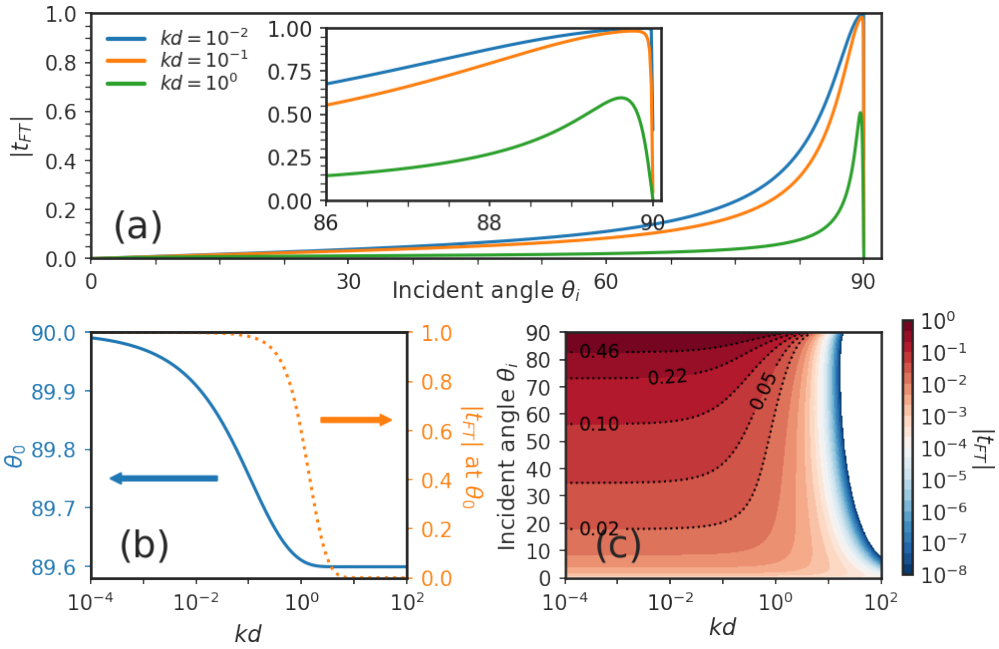

FIGURE 9 Tunneling of an incident FT wave between two ZnO solids. (a) Dependence of $|t_{FT}|$ as a function of the incident angle θ_i. (b) Dependence of the peak transmission angle θ_0 (left axis) on the scaled gap width kd, with the right axis showing the corresponding $|t_{FT}|$. (c) Colored contour plot of the $|t_{FT}|$ in a logarithmic scale versus incident angle θ_i and kd. From [Geng and Maasilta, 2022a], reproduced under the license CC BY 4.0.

With the above analytical expressions, it is easy to obtain the transmission coefficients t_{FT} with given material parameters. In Figure 9(a), $|t_{FT}|$ is calculated as a function of the incident angle θ_i for two closely spaced identical ZnO crystals, with three different scaled vacuum gap widths kd. The ZnO material constants are taken from Auld [1990], and are $\rho = 5680$ kgm^{-3}, $c_{44} = 4.247 \times 10^{10}$ Nm^{-2}, $e_{15} = -0.48$ Cm^{-2}, and $\epsilon_{11} = 8.55\epsilon_0$.

The plotted $|t_{FT}|$ shows a modest transmission until it reaches glancing angles near $\theta_i = 90^\circ$. For small enough gaps, *i.e.* $kd < 1$, the maximum transmission

is seen to be very close to unity. The peak can be found at θ_0, which is given by setting the real part of the denominator in Eq.(126) to zero, giving the condition:

$$B^4 \equiv \frac{(A^2 + c_{44}/\epsilon_{11})^2}{\tan^2\theta_0} = \frac{A^4\epsilon_0^2(e^{2k_x d} - 1)}{(\epsilon_0 + \epsilon_{11})^2 e^{2k_x d} - (\epsilon_0 - \epsilon_{11})^2}. \tag{128}$$

Furthermore, at the zero gap width limit, the expression of the transmission coefficient, Eq.(126), simplifies to $t_{FT} = A^2/(A^2 - iB^2)$, which approaches unity when $\theta \to 90°$. Conversely, this limiting case also shows that exact unity transmission can never be achieved for a finite gap size with the stated wave and crystal configuration.

In Figure.9(b), the angle θ_0 of the peak and its corresponding transmission is plotted as a function of the scaled gap width kd. The peak angle θ_0 can only be found in a narrow range of 0.4 degrees, and if the gap width increases over $kd \sim 1$, the transmission drops quickly to zero. The full dependency of the transmission coefficient on the gap width and incident angle is demonstrated in Figure 9(c). A switch-off of the acoustic wave tunneling can be found at about $kd \geq 1$, where the gap width is beyond the characteristic wave length of the incident wave. On the other hand, saturation of the transmission can be observed when the gap width is much smaller than the wave length, *i.e.* $kd \leq 10^{-2}$.

3.3.2 Numerical example

In the second example, the transmission coefficients will be computed numerically for arbitrarily oriented crystals. One of the goals of this example is to demonstrate the workflow how the theoretical framework developed in this work can be implemented numerically. Two identically oriented and closely separated hexagonal 6mm ZnO crystals are chosen in this example.

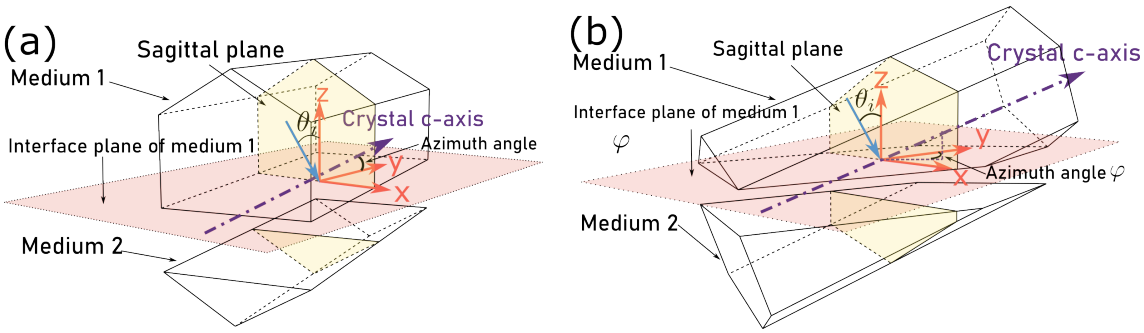

FIGURE 10 Schematics of the phonon tunneling in Wurtzite hexagonal crystals with a vacuum gap cut at (a) a-plane $[11\bar{2}0]$ or, (b) n-plane $[11\bar{2}3]$, and with the azimuthal angle rotated between 0° and 360°,[Geng and Maasilta, 2022a], reproduced under the license CC BY 4.0.

The orientations of the ZnO crystals can be described by two angles, a crystal zenith angle ϑ and a crystal azimuth angle φ, in a cylindrical coordinate system because of the uniaxial symmetry. The definitions of the orientation angles and the procedures of the rotation have been described in detail in section 2.1.5.

The configuration of the two ZnO crystals is considered having been created by a planar cut through a bulk solid with a width of d. Therefore, the orientation of both crystals are identical and the zenith angle ϑ, which is the angle between the crystal c-axis and the normal of the cut surface (z-axis), is fully determined as illustrated in Figure.10 for two different crystallographic cuts. The other degree of freedom of the orientation configuration is described by the rotation around the z-axis after the cut, from which the azimuth angle φ, the angle between the y-axis and the projection of the crystal c-axis on the xy-plane, is defined. Such a rotation can be achieved by two equivalent ways: one is to consider rotating both cut crystals around the z-axis, another is to consider rotating the sagittal plane, which contains the incident wave, around the same axis. To avoid duplication, φ is implemented in the computation only as a crystal rotation. Therefore, the sagittal plane is fixed and there is only one degree of freedom considered for the incident wave, the incident angle θ_i.

In summary, the orientation angle ϑ is determined by crystallographic cut (see section 2.2.3 for common cuts and corresponding ϑ angles for ZnO). The orientation angle φ describes the crystal rotation around z-axis, varying from 0° to 360°. The incident angle θ_i resides inside the sagittal plane, varying from 0° to 90°[4].

Anaconda Python distribution has been exclusively used in this work to implement the numerical algorithms. The workflow of the computation will be described in the following paragraphs, which implements the combined boundary condition approach (section 3.2.2) as an example.

The input parameters required for the computations are: the material constants including the non-rotated tensors $\boldsymbol{\epsilon}_0^S$, $\boldsymbol{e}_0$, $\boldsymbol{c}_0^E$, and the scalar ρ; the crystal rotation parameters including ϑ and φ; the gap distance d; the information of the incident bulk wave including the mode and the incident angle θ_i.

The material tensors are first transformed based on the given crystal orientation according to Eq.(72). The parallel component of the phase velocity v_x of the incident wave is then calculated based on the given incident angle and the solution of the secular equation of piezoelectrically stiffened Christoffel Eq.(62). The 8×8 Stroh matrix $\boldsymbol{N}(v_x)$ can now be constructed using the definition Eq.(83), and then its eigenvalues p_α and eigenvectors $\boldsymbol{\xi}_\alpha$ can be solved from Eq.(82). The obtained eigenvectors need to be normalized using the Stroh-normalization condition from Eq.(84).

At this stage, one of the two approaches developed in sections 3.2.2 and 3.2.3 can be chosen to solve the boundary conditions for the scattering amplitudes. In this example, the combined boundary condition approach will be used

[4] For this illustrative example, it is easier to present the k-vector of the incident wave residing inside the half-plane of the crystal ($k_z > 0$). However, strictly speaking, from the perspective of power flow, the direction of the incidence should be determined by the Poynting vector, as described in section 2.3.4. In some cases, the power flow direction along the z-axis is opposite to the direction of k_z, hence θ_i should be considered from -90° to 90°, and a step function is needed to "filter out" the directions where the power flows into the depth of the solid. This topic will be discussed in a later section regarding the heat transfer, and, for the sake of simplicity, will be dismissed in this example.

for a demonstration. Two 8×5 vacuum matrices $\boldsymbol{M}_1$ and $\boldsymbol{M}_2$ are first built from Eqs.(112). Then the 8×8 matrix $\boldsymbol{M}$ are constructed by combining the vacuum matrices and the 5×1 column vectors $\boldsymbol{U}_\alpha$ which are obtained from the eigenvector solutions $\boldsymbol{\xi}_\alpha$. The incident column vector $\boldsymbol{U}_{in}^{(1)}$ can also be built with the given incident wave mode. Lastly, the matrix product of $-\boldsymbol{M}^{-1}\boldsymbol{M}_1\boldsymbol{U}_{in}^{(1)}$ [Eq.(113)] leads to the transmission and reflection coefficients of the given incident bulk wave.

Each process stated above costs less than 1 ms of computational time, and the overall time is within 5 ms using a standard modern laptop. In Figure 11 and 12, two sets of calculated transmission coefficients with a varying incident angle θ_i and rotation angle φ are presented, where each plot cost 6 minutes of computational time.

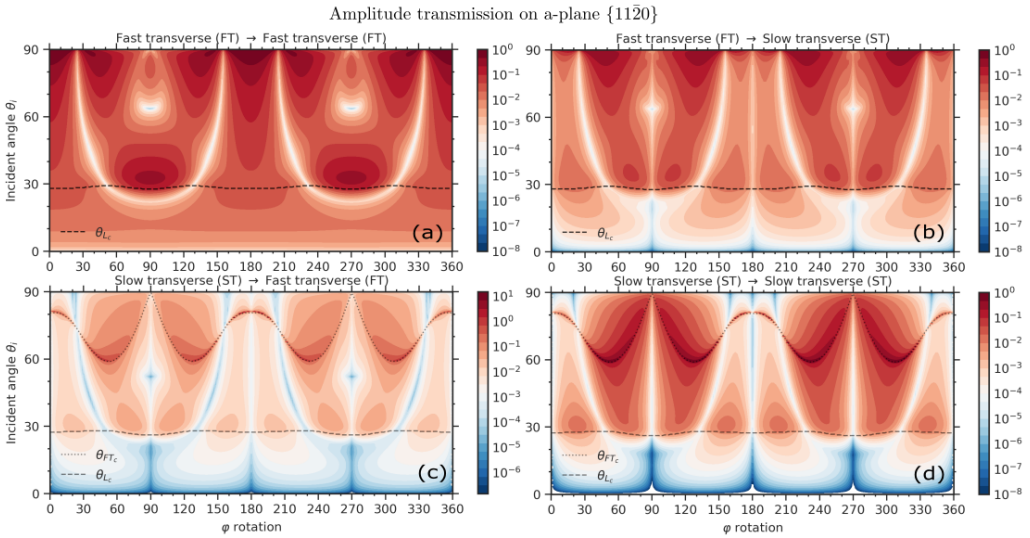

FIGURE 11 The transmission coefficients $|t_\alpha|$ (color scale) as function of the incident angle θ_i and the rotation angle φ for an a-plane cut ZnO crystal [11$\bar{2}$0]. From [Geng and Maasilta, 2022a], reproduced under the license CC BY 4.0.

These two sets of results are meant for demonstrating the capabilities of the formalism developed in this work, and thus only the most interesting cases have been chosen. An incident acoustic wave, either a fast transverse (FT) mode or slow transverse (ST) mode, impinges onto the surface of the a-plane cut (Figure 11) or n-plane cut (Figure 12) crystals, and then tunnels across a gap of width $kd = 10^{-2}$ into the adjacent identical crystal. The transmission coefficients of the FT and ST partial wave modes are plotted as functions of both incident angle θ_i and azimuth rotation angle φ. In these plots, mode conversions are also presented, *i.e.* FT→ FT, FT→ ST, ST→ ST, ST→ FT. In addition, critical incident angles, beyond which a faster partial wave mode will be reflected as an evanescent wave, are also plotted.

A mirrored twofold symmetry can be seen along the φ rotation in the plots with the a-plane cut, Figure 11. Such symmetry is expected, as the rotation axis of the φ angle is perpendicular to the uniaxial c-axis. Comparing the incident FT [panels (a) and (b)] and ST [panels (c) and (d)] modes, several interesting fea-

tures can be observed. The high transmission areas with incident FT modes are isolated, mainly populated at the extreme glancing angles. In particular, the line segment of $\varphi = 0^\circ$ with incident angles varying from 0° to 90° is the same result that was demonstrated using the analytical example in section 3.3.1. There is one exception: for the FT→FT case with orientations around $\varphi = 90^\circ$ and 270°, highest transmission is located at the incident angles just beyond the critical angle θ_{L_c} (dashed line).

In contrast, the high transmission areas with an incident ST mode are tightly located in a narrow band of incident angles that lies just beyond the critical angle θ_{FT_c} of the FT partial mode. In addition, the transmission is significantly enhanced when rotated to $\varphi = n\pi/3, n = 1, 2, ...$ This can be interpreted as a resonant transmission induced by the excitation of leaky surface wave modes coupling across the gap [Darinskii and Weihnacht, 2006].

Furthermore, significant enhancement of the transmission can be observed when the incident angle is beyond the critical angle θ_{L_c} of the L partial mode in all plots. This can be interpreted to happen because part of the incident energy is more concentrated near the surface due to the reflected L partial wave becoming evanescent, enhancing the coupling across the gap. It is good to stress here that the electric power flow is always orthogonal to the propagation direction of the wave, as has been shown in section 2.2.2, and, in this case, is perpendicular to the surface towards the adjacent solid as L mode become evanescent.

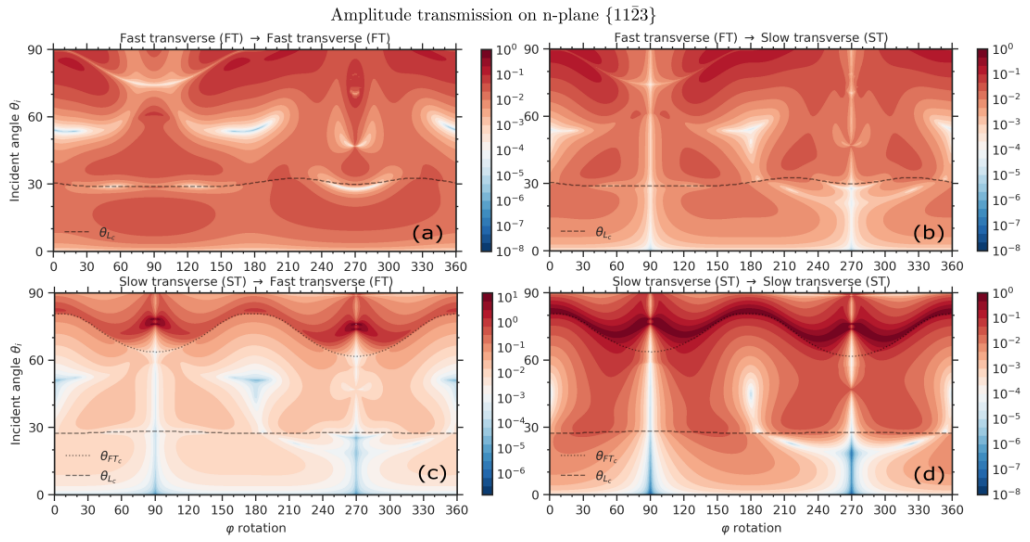

FIGURE 12 The transmission coefficients $|t_\alpha|$ (color scale) as function of the incident angle θ_i and the rotation angle φ for an n-plane cut ZnO crystal [11$\bar{2}$3]. From [Geng and Maasilta, 2022a], reproduced under the license CC BY 4.0.

Similar mirrored twofold symmetry is not observed with the crystallographic n-plane cut example, as shown in Figure 12. Significant differences in the transmission are seen by comparing the two cuts. The transmission is generally attenuated for the n-plane crystal cut with an incident FT mode. To understand this, let's look for example at the rotation $\varphi = 0$. With the n-plane crystal cut, the incident FT mode is a quasi-transverse mode which couples to all other acoustic

modes at the interface, whereas with the a-plane crystal cut, it is a pure horizontal shear wave (SH), as demonstrated in the analytical example. As a result, it is intuitive to expect a stronger FT→FT transmission with the a-plane cut case.

It is also very interesting to note here that significant transmission resonances can also be observed just beyond the critical angle θ_{FT_c} with the n-plane crystal cut. This is a robust feature in both cases, and, in particular, there exists exact unity transmission in the case of ST→ST transmission in Figure 12 (c). Such complete transmission will be analytically studied and discussed in the next section.

3.4 Complete tunneling of acoustic waves

One interesting observation in the previous numerical example is that there exists specific crystal orientations and incident angles where the peak transmission coefficient approaches unity, which means that the incident power flow is *completely tunneled* to the adjacent solid across the vacuum gap. Similar claims have been suggested by Prunnila and Meltaus [2010]; Balakirev and Gorchakov [1977]; Darinskii and Weihnacht [2006], however those results are limited either by the simplified models or concern only the highest symmetry crystal orientations. To the best of the author's knowledge, up until now, no generally valid condition has been given for complete acoustic wave tunneling.

In this section, the existence of the complete tunneling of an acoustic wave will be analytically proved using the formalism developed in this work. Furthermore, a strikingly simple resonance tunneling condition will be presented with a few numerical examples with ZnO crystals. This part of work has been described in Geng and Maasilta [2022b].

3.4.1 Resonant tunneling

As this section only focuses on the power flows in the direction perpendicular to the solid-vacuum interface, the *time-averaged normal component Poynting vector* in solid will be designated as:

$$P_\alpha^{(i)} \equiv \boldsymbol{n} \cdot \boldsymbol{P}_{\mathrm{AV},\alpha}^{(i)} \tag{129}$$

to avoid redundant notation. Thus, the normal Poynting vector of a transmitted bulk partial wave mode α in the second solid, following Eq.(108), reads as:

$$P_\alpha^{(2)} = |t_\alpha|^2 P_{in}^{(1)}, \tag{130}$$

in which t_α is given in Eq.(119) as the transmission coefficient of an tunneled partial wave mode α, and $P_{in}^{(1)}$ is the normal direction power flow of the incident wave with amplitude $b_{in}^{(1)}$ and reads as:

$$P_{in}^{(1)} = -\frac{1}{4}\omega k_x |b_{in}^{(1)}|^2. \tag{131}$$

It is worth mentioning that the reflected and transmitted evanescent partial waves have no power flow in the normal direction into the depth of the solid ($P_\alpha = 0$ if α is evanescent mode), since these waves are bound onto the surface of the solid.

The total power transmitted into solid 2 in the normal direction, denoted by $P_\Sigma^{(2)}$, is obviously the sum of $P_\alpha^{(2)}$ over all the *bulk* wave modes, and it can be expressed as:

$$P_\Sigma^{(2)} = \sum_\alpha |t_\alpha|^2 P_{in}^{(1)} = \sum_\alpha |\bar{t}_{in\to V}^{(1)} \bar{t}_{V\to\alpha}^{(2)} f_m(d)|^2 P_{in}^{(1)}, \tag{132}$$

where $\bar{t}_{in\to V}^{(1)}$ is the single surface coefficient of an incident mode transmitted into a vacuum from solid 1, $\bar{t}_{V\to\alpha}^{(2)}$ is the single surface coefficient of a vacuum wave transmitted into solid 2 as a partial wave mode α, and $f_m(d)$ is the multiple reflection factor defined in Eq.(118), and α runs only over all the possible transmitted bulk modes, the number of which can be from zero to up to four [Every and Neiman, 1992]. If there is no available bulk mode, then there is no power that flows into the depth of solid 2.

When there is power transmitted into the second solid, there must exist energy flow inside the vacuum. The normal direction time-averaged electrostatic power flow in vacuum, denoted by P_V, can be expressed using the complex Poynting vector derived in section 2.2.2 as:

$$P_V = -\frac{1}{2}\mathrm{Re}\left[i\omega\Phi_V(\boldsymbol{n}\cdot\boldsymbol{D}_V)^*\right], \tag{133}$$

in which the vacuum electric potential Φ_V and the normal direction of the electric displacement $\boldsymbol{n}\cdot\boldsymbol{D}_V$ are given in Eqs.(103) and (104).

Using the single surface scattering coefficients that were defined and discussed in section 3.2.3, the two dimensionless amplitudes $b_{V_\pm}$ in the expressions in Φ_V and $\boldsymbol{n}\cdot\boldsymbol{D}_V$, representing the decaying and increasing partial waves in vacuum, can be expressed as:

$$\begin{aligned} b_{V_+} &= \bar{t}_{in\to V}^{(1)} b_{in}^{(1)} + \bar{r}_V^{(1)} b_{V_-} \\ b_{V_-} &= \bar{r}_V^{(2)} b_{V_+} e^{-2k_x d}, \end{aligned} \tag{134}$$

in which $\bar{r}_V^{(1)}$ and $\bar{r}_V^{(2)}$ are the single surface reflection coefficients of the vacuum wave at the surface of the solid 1 and 2, respectively.

By inserting the expressions of Φ_V and $\boldsymbol{n}\cdot\boldsymbol{D}_V$ with Eqs.(134) into the vacuum power flow Equation (133), one obtains:

$$P_V = 2|\bar{t}_{in\to V}^{(1)} f_m(d)|^2 \mathrm{Re}\left[\bar{r}_V^{(2)}\right] P_{in}^{(1)}, \tag{135}$$

in which the expression of $f_m(d)$ from Eq.(118) and $P_{in}^{(1)}$ from Eq.(131) are applied.

The system studied in this work has no dissipation inside the vacuum gap, consequently, the normal direction power flow in the vacuum P_V is equal to the

total transmitted power $P_\Sigma^{(2)}$ in solid 2. Comparing their expressions in Eqs.(132) and (135), a simple yet important relation can be found:

$$2\mathrm{Re}\left[\bar{r}_V^{(2)}\right] = \sum_{\alpha=\mathrm{bulk}} |\bar{t}_{V\to\alpha}^{(2)}|^2 \,, \tag{136}$$

from which the total transmitted power can be calculated using a single surface reflection coefficient $\bar{r}_V^{(2)}$, without the need to sum over all the transmitted bulk modes.

For a system of two identical crystals with the same orientations, additional relations between the single surface coefficients of the two solids can be found by exploiting the completeness condition of the extended Stroh formalism [Eq.(91)]. However, the derivations of these relations are not straightforward, hence they will be presented with details in the following sub-section between the horizontal lines, which can then be skipped if those details are of no interest to the reader.

By explicitly writing down the completeness condition $\boldsymbol{\xi}_\alpha \otimes \hat{\boldsymbol{T}}\boldsymbol{\xi}_\alpha = \hat{\boldsymbol{I}}_{(8)}$, where $\alpha = 1, ..., 8$ corresponds to the eight wave mode solutions, one finds $\sum_\alpha \phi_\alpha D_\alpha^n = 1$ and that $\sum_\alpha \phi_\alpha\phi_\alpha$, $\sum_\alpha D_\alpha^n D_\alpha^n$, $\sum_\alpha \boldsymbol{L}_\alpha^T\boldsymbol{L}_\alpha$, $\sum_\alpha \phi_\alpha\boldsymbol{L}_\alpha$, $\sum_\alpha D_\alpha^n\boldsymbol{L}_\alpha$ are all zero or zero matrices. For two identical crystals, the eight solutions can be sorted into two groups such that: the first four solutions $\alpha = 1, ..., 4$ are the reflected wave modes in solid 1, and are denoted by mode indices $i = 1, ..., 4$; the last four solutions $\alpha = 5, ..., 8$ are the transmitted wave modes in solid 2, and are also denoted using mode indices $i = 1, ..., 4$ but with superscript (2) to avoid ambiguities.

Recalling the definition of the column vector $\boldsymbol{U}_i = [\phi_i, D_i^n, \boldsymbol{L}_i]$, one can construct the dyadic multiplication of $\boldsymbol{U}_i$ as:

$$\sum_i^4 \boldsymbol{U}_i^{(1)} \otimes \boldsymbol{U}_i^{(1)} + \sum_i^4 \boldsymbol{U}_i^{(2)} \otimes \boldsymbol{U}_i^{(2)} = \begin{bmatrix} 0 & 1 & 0 & 0 & 0 \\ 1 & 0 & 0 & 0 & 0 \\ 0 & 0 & 0 & 0 & 0 \\ 0 & 0 & 0 & 0 & 0 \\ 0 & 0 & 0 & 0 & 0 \end{bmatrix} . \tag{137}$$

Using the normalization conditions of the vacuum wave $\phi_{V_+} D_{V_+} + \phi_{V_-} D_{V_-} = 1$, and the relations $\phi_{V_+}\phi_{V_+} + \phi_{V_-}\phi_{V_-} = D_{V_+} D_{V_+} + D_{V_-} D_{V_-} = 0$ which are calculated from $\phi_{V_\pm} = 1/\sqrt{\pm 2i\epsilon_0}$ and $D_{V_\pm} = \pm i\epsilon_0\phi_{V_\pm}$, and the fact $\boldsymbol{L}_{V_\pm} = \boldsymbol{0}$, one finds:

$$\sum_i^4 \boldsymbol{U}_i^{(1)} \otimes \boldsymbol{U}_i^{(1)} + \sum_i^4 \boldsymbol{U}_i^{(2)} \otimes \boldsymbol{U}_i^{(2)} = \boldsymbol{U}_{V_+} \otimes \boldsymbol{U}_{V_+} + \boldsymbol{U}_{V_-} \otimes \boldsymbol{U}_{V_-} \,. \tag{138}$$

The outer products of the above equations can be transformed further into products of determinants of 5×5 matrices constructed from horizontally stacked column vectors of $\boldsymbol{U}$. The conversion is done by using the Laplace expansion of the determinant:

$$||\boldsymbol{A}|| = \sum_{i=1}^n (-1)^{i+j} a_{ij} M_{ij}, \tag{139}$$

where the operator $||...||$ signifies the determinant of matrix $\boldsymbol{A}$, a_{ij} is the element of a $n \times n$ matrix $\boldsymbol{A}$, and M_{ij} is defined to be the determinant of a $(n-1) \times (n-1)$ matrix that results from $\boldsymbol{A}$ by removing the i-th row and the j-th column. One sees that the determinant can be calculated from the product of one of the columns of the matrix $\boldsymbol{A}$ *e.g.* a_{i5} where $j = 5$, with a corresponding cofactor *e.g.* $C = (-1)^{i+5} M_{i5}$, which is independent of the column a_{i5}. As result, if introducing a 5×5 matrix $\boldsymbol{A}(\boldsymbol{U}_\alpha) = [\boldsymbol{U}_1^{(1)} \boldsymbol{U}_2^{(1)} \boldsymbol{U}_3^{(1)} \boldsymbol{U}_4^{(1)} \boldsymbol{U}_\alpha]$ as a function of $\boldsymbol{U}_\alpha$ which can be any possible wave solution, including $\boldsymbol{U}_i^{(1)}$, $\boldsymbol{U}_i^{(2)}$ or $\boldsymbol{U}_{V_\pm}$, one has:

$$||\boldsymbol{A}(\boldsymbol{U}_\alpha)|| = \sum_i (-1)^{i+5} a_{i5} M_{i5} = \boldsymbol{C} \boldsymbol{U}_\alpha, \tag{140}$$

where a_{i5} is the element of column vector $\boldsymbol{U}_\alpha$, and the cofactors can be combined into a row vector $\boldsymbol{C}$, which is independent of $\boldsymbol{U}_\alpha$ and can be calculated from the remaining columns of $\boldsymbol{A}$ excluding $\boldsymbol{U}_\alpha$.

Let's now construct two cofactors $\boldsymbol{C}^L$ and $\boldsymbol{C}^R$ from the matrices $\boldsymbol{A}^L(\boldsymbol{U}_\alpha) = [\boldsymbol{U}_1^{(1)} \boldsymbol{U}_2^{(1)} \boldsymbol{U}_3^{(1)} \boldsymbol{U}_4^{(1)} \boldsymbol{U}_\alpha]$ and $\boldsymbol{A}^R(\boldsymbol{U}_\alpha) = [\boldsymbol{U}_1^{(2)} \boldsymbol{U}_2^{(2)} \boldsymbol{U}_3^{(2)} \boldsymbol{U}_4^{(2)} \boldsymbol{U}_\alpha]$, respectively. By left multiplying $\boldsymbol{C}^L$ and right multiplying $\boldsymbol{C}^R$ to the dyadic multiplication Eq.(138), one obtains:

$$\begin{aligned} &\sum_i^4 ||\boldsymbol{A}^L(\boldsymbol{U}_i^{(1)})|| \cdot ||\boldsymbol{A}^R(\boldsymbol{U}_i^{(1)})|| + \sum_i^4 ||\boldsymbol{A}^L(\boldsymbol{U}_i^{(2)})|| \cdot ||\boldsymbol{A}^R(\boldsymbol{U}_i^{(2)})|| \\ &= ||\boldsymbol{A}^L(\boldsymbol{U}_{V_+})|| \cdot ||\boldsymbol{A}^R(\boldsymbol{U}_{V_+})|| + ||\boldsymbol{A}^L(\boldsymbol{U}_{V_-})|| \cdot ||\boldsymbol{A}^R(\boldsymbol{U}_{V_-})||. \end{aligned} \tag{141}$$

Since the determinant equals zero when it has linearly dependent columns, *e.g.* $||\boldsymbol{A}^L(\boldsymbol{U}_i^{(1)})|| = 0$ for $i = 1, ..., 4$, the above equation has zeros on the LHS and thus can be rearranged to:

$$\frac{||\boldsymbol{U}_1^{(1)} \boldsymbol{U}_2^{(1)} \boldsymbol{U}_3^{(1)} \boldsymbol{U}_4^{(1)} \boldsymbol{U}_{V_-}||}{||\boldsymbol{U}_1^{(1)} \boldsymbol{U}_2^{(1)} \boldsymbol{U}_3^{(1)} \boldsymbol{U}_4^{(1)} \boldsymbol{U}_{V_+}||} = -\frac{||\boldsymbol{U}_1^{(2)} \boldsymbol{U}_2^{(2)} \boldsymbol{U}_3^{(2)} \boldsymbol{U}_4^{(2)} \boldsymbol{U}_{V_+}||}{||\boldsymbol{U}_1^{(2)} \boldsymbol{U}_2^{(2)} \boldsymbol{U}_3^{(2)} \boldsymbol{U}_4^{(2)} \boldsymbol{U}_{V_-}||}. \tag{142}$$

Considering a boundary condition:

$$\sum_{i=1}^4 b_i^{(1)} \boldsymbol{U}_i^{(1)} = b_{V_+} \boldsymbol{U}_{V_+} + b_{V_-} \boldsymbol{U}_{V_-}, \tag{143}$$

where an incident wave is coming from vacuum with amplitude b_{V_-} and reflected back with amplitude b_{V_+}. It can be rearranged and expressed in a matrix form:

$$\begin{bmatrix} \boldsymbol{U}_1^{(1)} & \boldsymbol{U}_2^{(1)} & \boldsymbol{U}_3^{(1)} & \boldsymbol{U}_4^{(1)} & -\boldsymbol{U}_{V_+} \end{bmatrix} \begin{bmatrix} b_1^{(1)} \\ b_2^{(1)} \\ b_3^{(1)} \\ b_4^{(1)} \\ b_{V_+} \end{bmatrix} = b_{V_-} \boldsymbol{U}_{V_-}. \tag{144}$$

The *Cramer's rule* allows to solve for the amplitude b_{V_+} as:

$$\frac{b_{V_+}}{b_{V_-}} = -\frac{||\boldsymbol{u}_1^{(1)}\boldsymbol{u}_2^{(1)}\boldsymbol{u}_3^{(1)}\boldsymbol{u}_4^{(1)}\boldsymbol{u}_{V_-}||}{||\boldsymbol{u}_1^{(1)}\boldsymbol{u}_2^{(1)}\boldsymbol{u}_3^{(1)}\boldsymbol{u}_4^{(1)}\boldsymbol{u}_{V_+}||}, \tag{145}$$

in which $\bar{r}_V^{(1)} \equiv b_{V_+}/b_{V_-}$ is defined from the scattering matrix introduced in section 3.2.3, and it is the LHS of the Eq.(142) with an opposing sign.

Similarly, by considering the boundary condition on the surface of solid 2:

$$\sum_{i=1}^{4} b_i^{(2)}\boldsymbol{u}_i^{(2)} = b_{V_+}\boldsymbol{u}_{V_+} + b_{V_-}\boldsymbol{u}_{V_-}, \tag{146}$$

one finds that the RHS of Eq.(142) is $\bar{r}_V^{(2)}$. As a result, a relation

$$\bar{r}_V \equiv \bar{r}_V^{(2)} = -\bar{r}_V^{(1)} \tag{147}$$

is derived, which states that the single surface reflection coefficients of the vacuum wave of two identical solids have the same absolute value but opposing signs.

Taking the same above approach, but with differently constructed cofactors $\boldsymbol{C}^L$ from the matrix $\boldsymbol{A}^L(\boldsymbol{u}_\alpha) = [\boldsymbol{u}_1^{(1)}\boldsymbol{u}_2^{(1)}\boldsymbol{u}_3^{(1)}\boldsymbol{u}_4^{(1)}\boldsymbol{u}_\alpha]$ and $\boldsymbol{C}^R$ from matrix $\boldsymbol{A}^R(\boldsymbol{u}_\alpha) = [\boldsymbol{u}_2^{(2)}\boldsymbol{u}_3^{(2)}\boldsymbol{u}_4^{(2)}\boldsymbol{u}_{V_-}\boldsymbol{u}_\alpha]$, one obtains:

$$||\boldsymbol{A}^L(\boldsymbol{u}_1^{(2)})|| \cdot ||\boldsymbol{A}^R(\boldsymbol{u}_1^{(2)})|| = ||\boldsymbol{A}^L(\boldsymbol{u}_{V_+})|| \cdot ||\boldsymbol{A}^R(\boldsymbol{u}_{V_+})||, \tag{148}$$

where only the non-zero terms (non-linearly dependent terms) remain. Writing the above equation explicitly gives:

$$\frac{||\boldsymbol{u}_1^{(1)}\boldsymbol{u}_2^{(1)}\boldsymbol{u}_3^{(1)}\boldsymbol{u}_4^{(1)}\boldsymbol{u}_1^{(2)}||}{||\boldsymbol{u}_1^{(1)}\boldsymbol{u}_2^{(1)}\boldsymbol{u}_3^{(1)}\boldsymbol{u}_4^{(1)}\boldsymbol{u}_{V_+}||} = \frac{||\boldsymbol{u}_2^{(2)}\boldsymbol{u}_3^{(2)}\boldsymbol{u}_4^{(2)}\boldsymbol{u}_{V_-}\boldsymbol{u}_{V_+}||}{||\boldsymbol{u}_2^{(2)}\boldsymbol{u}_3^{(2)}\boldsymbol{u}_4^{(2)}\boldsymbol{u}_{V_-}\boldsymbol{u}_1^{(2)}||}. \tag{149}$$

The column vector $\boldsymbol{u}_1^{(2)}$ is clearly a solution of the transmitted wave in solid 2. Using Cramer's rule with the same boundary condition, Eq.(146), one finds that the RHS of Eq.(149) is the single surface transmitted coefficient $\bar{t}_{V\to 1}^{(2)} \equiv b_1^{(2)}/b_{V_+}$ of an incoming vacuum wave.

Assuming $\boldsymbol{u}_1^{(2)}$ is a bulk wave solution and is also the solution representing the incident bulk wave, which is true for two identical solids, the boundary condition of a single surface of solid 1 with an incident bulk wave can be written as:

$$b_{in}^{(1)}\boldsymbol{u}_1^{(2)} + \sum_{i=1}^{4} b_i^{(1)}\boldsymbol{u}_i^{(1)} = b_{V_+}\boldsymbol{u}_{V_+}, \tag{150}$$

from which one finds the LHS of Eq.(149) is $\bar{t}_{1\to V}^{(1)} \equiv b_{V_+}/b_{in}^{(1)}$.

As a result, another relation:

$$\bar{t}_{\gamma\to V}^{(1)} = \bar{t}_{V\to\gamma}^{(2)} \tag{151}$$

is derived, which states that if a transmitted bulk wave mode γ in the solid 2 is the same mode as the incident wave in solid 1, then the single surface coefficients $\bar{t}^{(1)}_{\gamma\to V}$ and $\bar{t}^{(2)}_{V\to\gamma}$ are equal.

To summarize the lengthy derivations in the above sub-section, three simple yet important relations that link the single surface scattering coefficients are discovered, given as:

$$\begin{aligned} 2\mathrm{Re}(\bar{r}_V) &= \sum_{\alpha=\text{bulk}} |\bar{t}^{(2)}_{V\to\alpha}|^2 \quad \text{in Eq.(136)}, \\ \bar{r}^{(2)}_V &= -\bar{r}^{(1)}_V = \bar{r}_V \qquad \text{in Eq.(147)}, \\ \bar{t}^{(1)}_{\gamma\to V} &= \bar{t}^{(2)}_{V\to\gamma} \qquad \text{in Eq.(151)}. \end{aligned}$$

In addition, an inequality can be found by comparing Eqs.(136) with (151), reading as:

$$2\mathrm{Re}(\bar{r}_V) \geq |\bar{t}^{(1)}_{in\to V}|^2 \,, \tag{152}$$

in which the equality is satisfied when there exists only one transmitted bulk wave mode in solid 2 and that mode is the same as the incident wave in solid 1.

The expression of the total tunneled power flow $P^{(2)}_\Sigma$ in Eq.(132) can thus be simplified with the help of the relations Eqs.(136) and (147), giving:

$$\begin{aligned} \frac{P^{(2)}_\Sigma}{P^{(1)}_{in}} &= \frac{2\mathrm{Re}(\bar{r}_V)|\bar{t}^{(1)}_{in\to V}|^2 e^{-2k_x d}}{\left|1+\bar{r}_V^2 e^{-2k_x d}\right|^2} \\ &= \frac{2\mathrm{Re}(\bar{r}_V)|\bar{t}^{(1)}_{in\to V}|^2}{4\mathrm{Re}(\bar{r}_V)^2 + \left(e^{2k_x d} - |\bar{r}_V|^2\right)^2 e^{-2k_x d}} \,, \end{aligned} \tag{153}$$

where $P^{(2)}_\Sigma / P^{(1)}_{in}$ defines the *total power transmittance* (will be designated as $\mathcal{T}$ in later section), and only explicitly depends on two single surface coefficients: $\bar{t}^{(1)}_{in\to V}$ and $\bar{r}_V$. By applying the inequality relation,Eq. (152), the above equation shows that $P^{(2)}_\Sigma / P^{(1)}_{in} \leq 1$. This result has important implications. Firstly, complete tunneling cannot be achieved if more than one transmitted bulk wave modes exist, as the inequality (152) takes the "greater-than" sign leading to $P^{(2)}_\Sigma < P^{(1)}_{in}$ from Eq.(153). This statement is in contradiction to the claims made by Prunnila and Meltaus [2010].

On the other hand, the "equal to" sign is valid if there is only one transmitted bulk mode which is the same mode as the incident wave, and the power transmittance [Eq.(153)] can be simplified further to

$$\begin{aligned} \frac{P_\Sigma}{P_{in}} &= \frac{4\mathrm{Re}(\bar{r}_V)^2 e^{-2k_x d}}{\left|1+\bar{r}_V^2 e^{-2k_x d}\right|^2} \\ &= \frac{4\mathrm{Re}(\bar{r}_V)^2}{4\mathrm{Re}(\bar{r}_V)^2 + \left(e^{2k_x d} - |\bar{r}_V|^2\right)^2 e^{-2k_x d}}. \end{aligned} \tag{154}$$

It is clear that the above equation has a maximum of unity ($P_\Sigma = P_{in}$), which means the transmitted power is *exactly* equal to the incident power, when the resonance condition

$$|\bar{r}_V| = e^{k_x d}\,, \tag{155}$$

is satisfied. This proves it is possible for an acoustic wave to have an unity transmission across a vacuum gap, and the condition of such complete tunneling only explicitly depends on a single surface reflection coefficient $\bar{r}_V$ and the a scaled gap width $k_x d$.

In the system defined in this dissertation, $k_x d > 0$, so that the resonance tunneling can only be excited if $|\bar{r}_V| > 1$. Furthermore, it is interesting to note that $k_x d$ doesn't contain any information about the materials or orientations, whereas $\bar{r}_V$, having been called the *single* surface coefficient, is independent of the existence of the second solid[5]. Hence, an intuitive guess is that $\bar{r}_V$ should be a material parameter, which should be possible to determine without the knowledge of the gap or, in a more general sense, about the acoustic wave tunneling.

3.4.2 Effective permittivity

There is a great interest to study the single surface reflection coefficient $\bar{r}_V$, since it plays a crucial role in calculating the transmitted power and determining the resonant tunneling.

In electromagnetism, a dependency between the electrical potential Φ_V and the normal component of the electric displacement D_V^n can be found at the surface using the Maxwell's equations. For a wave propagating inside the xz-plane, their relation reads as [Ingebrigtsen, 1969]:

$$\frac{\Phi_V}{D_V^n} = \frac{i v_x^2}{\omega} Z_p, \tag{156}$$

where Z_p is defined by $Z_p \equiv E_x / H_y$, the ratio of the transverse electric and magnetic fields, and is referred to as the *TM-wave surface impedance*.

The expressions of $\Phi_V(z)$ and $D_V^n(z)$ in the framework of this dissertation are given by Eqs.(103) and (104). Hence at the surface of the solid 2 ($z = -d$), one obtains:

$$Z(\omega, v_x) = \frac{i}{v_x \epsilon_0} \frac{b_{V_+} \phi_{V_+} e^{-k_x d} + b_{V_-} \phi_{V_-} e^{k_x d}}{b_{V_+} \phi_{V_+} e^{-k_x d} - b_{V_-} \phi_{V_-} e^{k_x d}}\,. \tag{157}$$

With the help of the equation $\phi_{V_-} = i\phi_{V_+}$ that can be derived from the definition of $\phi_{V_\pm}$ given in section 3.2.1, and with $b_{V_-} = \bar{r}_V b_{V_+} \exp(-2k_x d)$ from Eqs.(134), the reflection coefficient $\bar{r}_V$ can be expressed in terms of the surface impedance Z_p as:

$$\bar{r}_V = i \frac{1 + i v_x \epsilon_0 Z_p}{1 - i v_x \epsilon_0 Z_p}. \tag{158}$$

[5] Mathematically speaking, even without an incoming vacuum wave, *i.e.* when its amplitude is zero, there still exists the reflection coefficient $\bar{r}_V$.

It has been shown by Ingebrigtsen [1969]; Zhang et al. [1992] that the *effective surface permittivity* can be obtained from the surface impedance as $\epsilon_{eff} = i/[v_x Z_p(\omega, v_x)]$, hence it can also be related to $\bar{r}_V$ giving:

$$\bar{r}_V = i\frac{\epsilon_{eff} - \epsilon_0}{\epsilon_{eff} + \epsilon_0}\,. \tag{159}$$

The concept of effective surface permittivity has been used in many studies of piezoelectric materials, such as in the generation and detection of acoustic waves by transducers [Milsom et al., 1977] and in determining of gap wave modes between piezoelectric solids [Darinskii and Weihnacht, 2006]. The above derived relation (159) could allow $\bar{r}_V$ to be determined experimentally by measuring $\epsilon_{eff}(v_x)$.

In addition, it is interesting to show here the striking similarity between the acoustic wave tunneling and the near-field photon tunneling, using the effective surface permittivity.

With the same wave form and coordinate setup, *i.e.* when the wave vector is in the xz-plane and the z-axis is perpendicular to the surface, the *Fresnel reflection coefficient* of a TM electromagnetic wave reflected at solid-vacuum interface reads as [Born et al., 1999; Polder and Van Hove, 1971; Volokitin and Persson, 2004]:

$$r_{TM} = \frac{\epsilon_r k_z - k_z'}{\epsilon_r k_z - k_z'}, \tag{160}$$

where k_z and k_z' are the normal components of the k-vector in the solid and in vacuum, and ϵ_r is the relative permittivity in the solid. Under the quasistatic approximation, $k_z = k_z' \approx ik_x$, since the electrostatic potential needs to satisfy the Laplace equation $\nabla^2\Phi = 0$.

Assuming an effective surface permittivity such that $\epsilon_{eff} = \epsilon_r\epsilon_0$, one finds that the reflection coefficient becomes:

$$r_{TM} = \frac{\epsilon_{eff} - \epsilon_0}{\epsilon_{eff} + \epsilon_0}, \tag{161}$$

which leads to an equivalence $r_{TM} = -i\bar{r}_V$ by comparing with Eq.(159).

Furthermore, the power transmittance $\mathcal{T}_{ph}$ of the photon tunneling [Pendry, 1999; Volokitin and Persson, 2004; Joulain et al., 2005] is given as:

$$\begin{aligned}\mathcal{T}_{ph} &= \frac{4\mathrm{Im}(r_{TM})^2 e^{-2k_x d}}{\left|1 - r_{TM}^2 e^{-2k_x d}\right|^2} \\ &= \frac{4\mathrm{Re}(\bar{r}_V)^2 e^{-2k_x d}}{\left|1 + \bar{r}_V^2 e^{-2k_x d}\right|^2},\end{aligned} \tag{162}$$

which has exactly the same expression as Eq.(154), if the relation $r_{TM} = -i\bar{r}_V$ is applied.

Lastly, it is also interesting to mention that the symmetric and antisymmetric conditions of the subsonic gap waves [Darinskii and Weihnacht, 2006]:

$$\begin{aligned} \epsilon_0 \tanh\left(\frac{k_x d}{2}\right) + \epsilon_{eff} &= 0 \\ \epsilon_0 \coth\left(\frac{k_x d}{2}\right) + \epsilon_{eff} &= 0\,, \end{aligned} \tag{163}$$

can also be expressed using $\bar{r}_V$ by inserting Eq.(159). The above conditions are thereby simplified to:

$$\bar{r}_V = \pm i e^{k_x d}, \tag{164}$$

which implies that the gap waves must always satisfy the resonance condition Eq.(155), whereas resonant tunneling does not necessary excite pure gap waves, since $\bar{r}_V$ can have real (leaky) part.

3.4.3 Numerical examples

To demonstrate the effect of complete tunneling, in this subsection a few numerical examples will be presented for two identical ZnO crystals, using the formulation developed above.

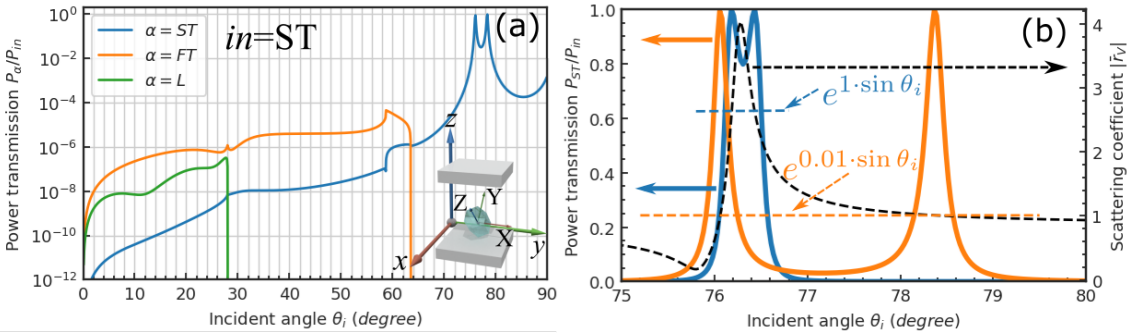

FIGURE 13 Power transmittance (a) P_α / P_{in} (b) P_{ST} / P_{in} as a function of incident angles.

In the first example (Figure.13), two ZnO crystals are separated with a scaled gap width of $kd = 0.01$, and are both rotated first with respect to the x-axis by $\vartheta = 46.89°$ and then to the z-axis by $\varphi = 88°$. A slow quasi-transversal wave (ST) is chosen to be the incident wave in this example, as it allows a critical incident angle beyond which only one transmitted bulk mode can be found, satisfying the general condition for complete tunneling.

The power transmittance $P_\alpha^{(2)} / P_{in}^{(1)}$ of each tunneled bulk mode is plotted in the left panel of Figure 13 as a function of the incident angle θ_i. Abrupt cut-offs can be seen for the transmitted quasi-longitudinal (L) and fast quasi-transversal (FT) modes, corresponding to the critical incident angles $\theta_{L_c} \approx 28°$ and $\theta_{FT_c} \approx 63.5°$. Beyond these critical angles, the respective wave becomes evanescent and bound onto the surface of the solid, hence no power flows into the bulk. In addition, the transmittance is generally low for most of the incident

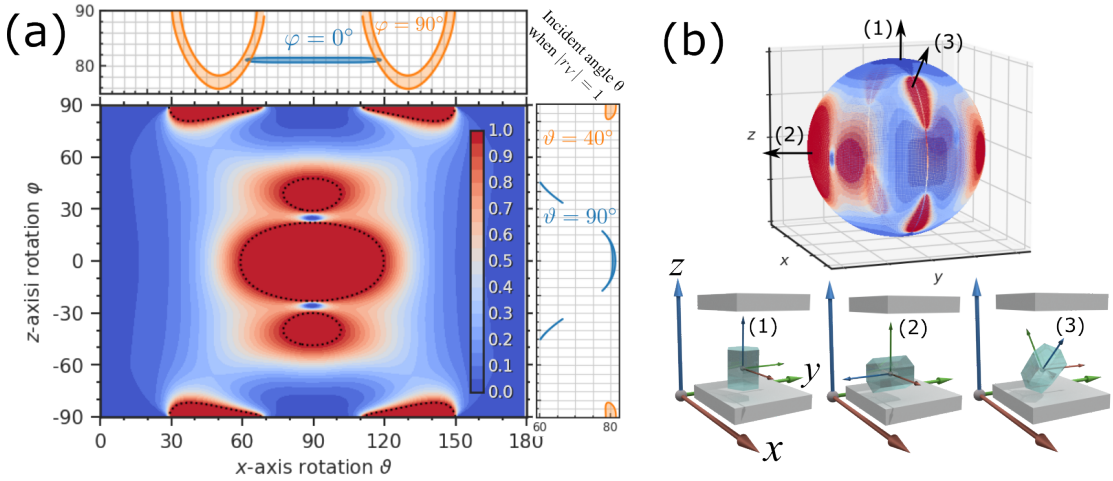

FIGURE 14 (a) Color scale of the ST→ST maximum power transmittance P_{ST}/P_{in} over all incident angles as function of crystal rotation angles ϑ and φ. (b) A spherical representation of the plot (a) where the surface normal signifies the orientation of c-axis of the crystal.

angles, except that there are two sharp transmission peaks,for the ST mode at angles between 75° and 80°, achieving exactly unity transmission.

A zoomed view on these resonant transmission peaks (orange solid line) are demonstrated in the right panel of the Figure.13. An additional transmittance curve with a scaled gap value $kd = 1$ (blue solid line,) and an overlay of the $|\bar{r}_V|$ curve (black dashed line) are also presented to help to understand the doublet structure. By plotting the values of $\exp(kd \sin\theta_i)$ where the blue dashed line represents $kd = 1$ and the orange dashed line $kd = 0.01$, one can clearly see that the unity transmission occurs at where the resonance condition $|\bar{r}_V| = \exp(kd \sin\theta_i)$ [Eq.(155)] is valid, proving the consistency between the analytical theory and the numerical approach.

In addition, with the increase of the scaled gap width from 0.01 to 1, the separation of the peaks is reduced. With the parameters and orientation of this example, the two solutions eventually merge together into one at a maximum of $|\bar{r}_V| \sim 4$, which corresponds to a maximum possible gap width of $kd \approx 1.4$ for complete tunneling. To be more specific, for the ZnO used in this case which has an ST wave velocity $v = 2780$ m/s, a wave with 2 GHz frequency can achieve complete tunneling across a gap corresponding to a distance of $d = 300$ nm.

Generally speaking, complete tunneling is not an extremely rare effect in crystals and can be found for a range of orientations. For an incident ST mode that tunnels across a vacuum gap of width $k_x d = 0.01$ into a transmitted ST mode, the numerically calculated maximal power transmittance P_{ST}/P_{in} over all incident angles θ_i is plotted in Figure.14, as a function of all possible crystal rotations (ϑ and φ). It is clear that a significant parameter space of orientations, with multiple separate regions, can be found to have complete tunneling.

In particular, a set of dotted contour lines are plotted in Figure 14(a) to encircle the orientations satisfying $|\bar{r}_V| > 1$. These regions are in excellent agreement

with the dark red areas where the the unity transmission is found numerically, providing a validation of the analytical condition developed in section 3.4.1.

It is also important to point out that the incident angle θ_i satisfying the complete tunneling condition varies with the crystal orientation, and the values can be as low as 60° in certain cases as shown in the right panel of Fig. 14(a).

To provide a better spatial understanding of the relation between the maximal power transmittance and the crystal orientation, the data presented in Figure 14(a) are plotted on the surface of a 3-D sphere, as shown in Figure 14(b), in which each surface normal of the sphere denotes a crystal c-axis direction under the laboratory xyz-coordinate frame.

To understand the physics, the three ellipsoidal unity transmission regions around $\vartheta = 90°$ in Figure.14(a) can be examined first. The incident ST waves are not pure shear waves inside these areas, and thus couple to the other partial waves (L, FT) at the surface. Consequently, when the incident angle is beyond the critical angle of the FT mode, the reflected FT wave is bound onto the surface, concentrating its energy on the surface. The displacement direction of these FT waves are predominately aligned with the crystal c-axis, the direction of the piezoelectric dipole, creating a strong piezoelectric response. Therefore, large electric potential differences will be excited on the solid surface, leading to strong electrostatic coupling across the gap and enabling the resonant tunneling.

Conversely, the incident ST mode becomes a pure shear mode and decouples from all other partial modes when the azimuth rotations approach $\varphi = \pm 90°$ with $\vartheta = 90°$. At these orientations, the c-axis aligns with the x-axis, whereas the polarization of the ST mode is perpendicular to the xz-plane. As a result, the incident ST wave becomes very weakly piezoelectric leading to minimal transmission.

It is also interesting to mention that there are nodes having low transmission at around $\varphi = \pm 25°$ and $\vartheta = 90°$, as shown in Figure 14. At these nodes, the electric potentials excited by the reflected FT mode waves change polarity, giving rise to minimized electric potential differences and weak coupling between the two interfaces. In addition, unity transmission is also observed in four small regions around $\varphi = \pm 90°$. In these areas, the single surface reflection coefficient $\bar{r}^{(1)}_{ST \to FT}$ increases significantly (not shown), indicating a strong mode conversion between the ST and FT partial waves. As the FT waves become evanescent beyond their critical angles, the enhanced mode conversion will give rise to a large electric coupling between the surfaces, leading to strong tunneling.

These numerical results emphasize the importance of the existence of the evanescent modes to the acoustic wave tunneling. In particular, complete tunneling requires the resonances of evanescent modes between two solids to excite large electric potentials and to concentrate the energy of the waves at the surface. In the next discussion, numerical results of the particle displacement $\boldsymbol{u}$, the electric potential Φ, and the time-averaged power flow P_x (parallel) and P_z (normal) at the surface will be presented, to provide a deeper understanding of the resonant tunneling effect.

Let us take one of the resonance peaks of Figure 13 ($\theta = 78.37°$) as an ex-

ample. As the incident wave completely tunnels across the vacuum gap, there is no reflected bulk partial mode which can propagate into the depth of the solid 1. Instead, the reflected (coupled) wave has its displacement vector decaying along the z-axis towards the bulk, as shown in Figure 15(a), and the only possible non-decaying (bulk) partial mode, the reflected ST mode, has an amplitude exactly zero. On the other hand, the coupled reflected wave propagates along the surface of the solid 1, having periodic displacement along x-axis as demonstrated in panel (c).

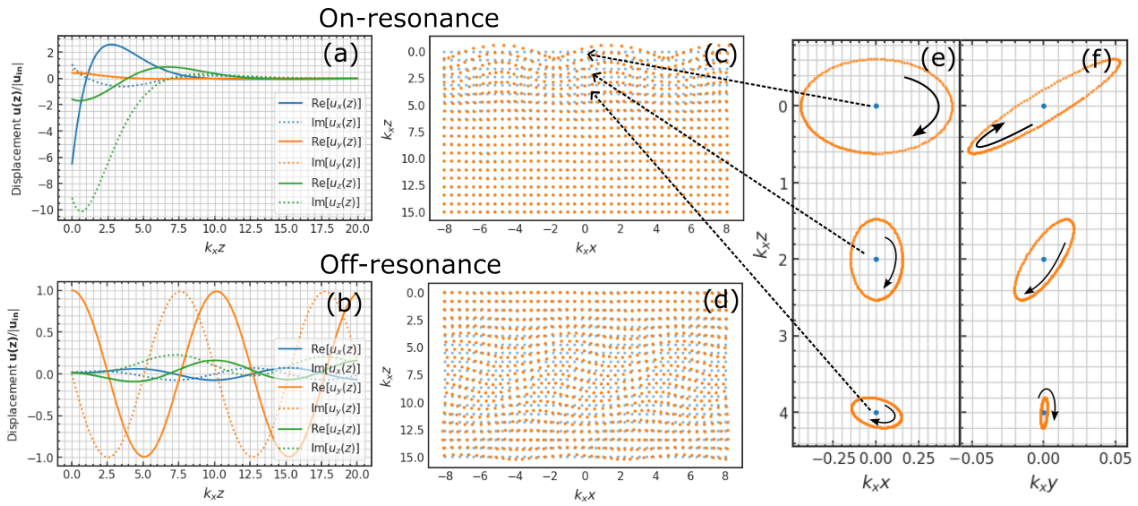

FIGURE 15 The reflected particle displacement $\boldsymbol{u}$ as function of spatial positions when the resonant tunneling condition is on (a,c), or off (b,d). Panels (e) and (f) show the time evolutions of the particle motion in $xz-$ and $yz-$ planes of three particles [(x,z)=(0,0), (0,2) and (0,4)] for the case (c).

It is interesting to visualize the displacements of this reflected (coupled) wave schematically with a point grid, to show how each mass element of the solid moves spatially when the resonant tunneling condition is "on" or "off". In Figure 15(c), the orange dots depict how the mass elements displace from their equilibrium positions, signified by the blue dots, at the resonant case. Strong wave motion can be observed at the surface of the solid ($k_x z = 0$), disappearing into the depth of the solid. In contrast, the wave motion is strong with no clear decay inside the solid in panel (d), where the incident angle is set to $\theta = 60°$. A more intriguing phenomenon is presented in panels (e) and (f), in which the mass elements that are close to the surface move in an elliptical motion (the orange dots) in the xz- and yz-planes around their equilibrium positions (blue dots), strongly resembling the Rayleigh-type surface waves.

However, it should be stressed that such "surface wave-like" solution is a result of the resonant tunneling, and thus can not exist on a single surface. Consequently, it is sensitive to the conditions, *i.e.* the incident angle, the gap distance, and the crystal orientation. A small change could instantaneously break the resonance leading to a finite reflection via the bulk ST wave.

In Figure 16, the normalized[6] electric potential Φ inside solid 1 for two dif-

6 Normalized to the incident amplitude.

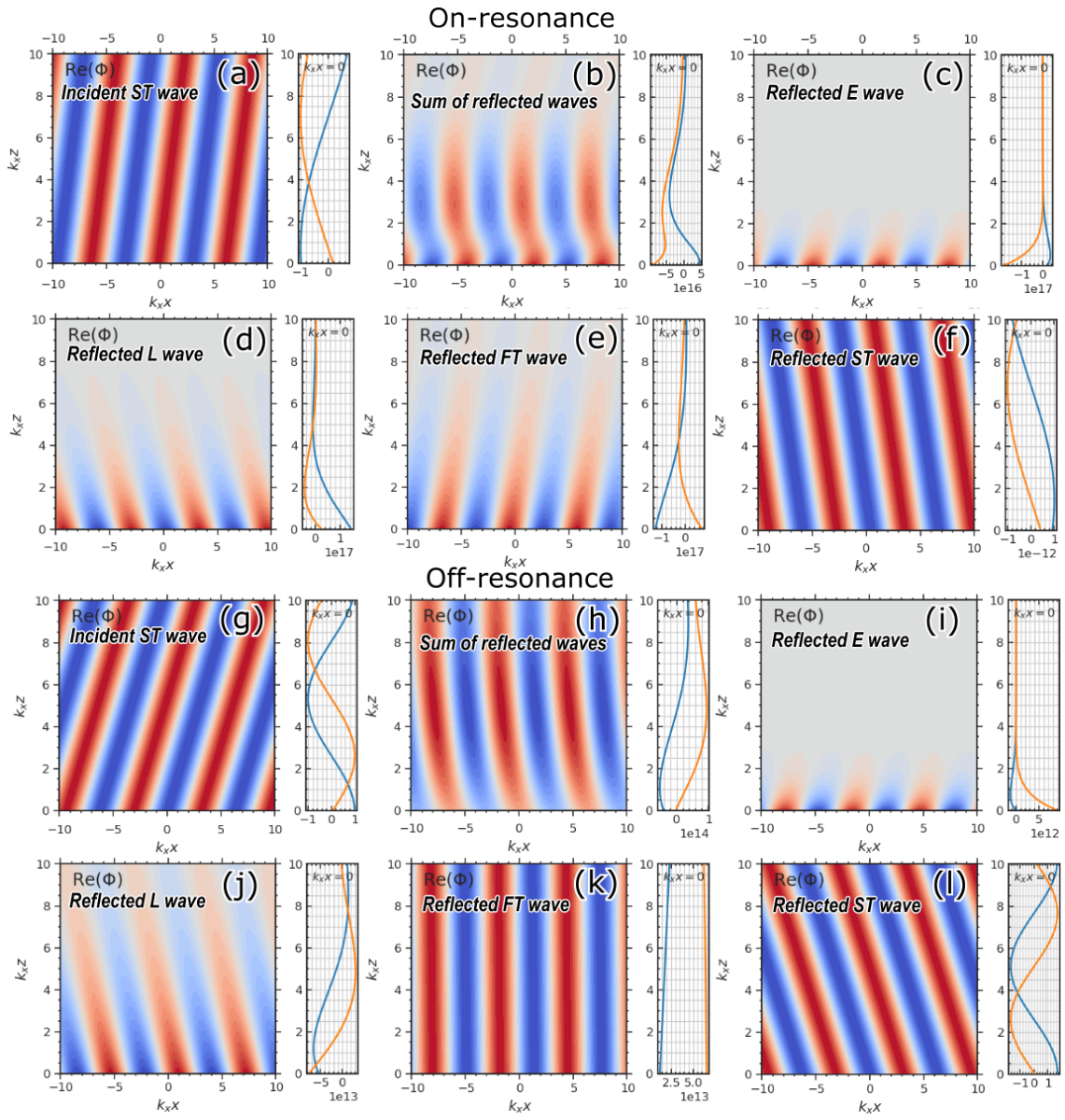

FIGURE 16 The normalized electric potential Φ of all partial waves in solid 1 are plotted as functions of the position in the xz-plane. (a-f) are at resonance, (g)-(l) off-resonance.

ferent incident angles, $\theta = 76.06°$ [on-resonance, in panels (a-f)] and $\theta = 60°$ [off-resonance, in panels (g-l)] are presented for each partial wave mode. In the resonant tunneling case, the total electric potential of all the reflected partial modes is bound at the surface ($k_x z = 0$), and decays to zero in the depth of the solid, as shown in Figure 16(b). The amplitude of the total reflected Φ is much higher than that of the incident ST wave [Figure 16(a)], there is more than 17 orders of magnitude difference between their peaks. This high amplitude is mostly contributed by the reflected E [panel (c)], L [panel (d)] and FT [panel (e)] waves, whereas the reflected bulk ST mode has practically zero amplitude ($\sim 10^{-12}$)[7].

In contrast, the total reflected wave in a non-resonant case [Figure 16(h)] can propagate into the bulk, and has a maximum potential at the surface ($\sim 10^{13}$) about 4 orders of magnitude smaller than that of the resonance case. In this case the potential is contributed dominantly by the reflected partial L [panel (j)] and FT [panel (k)] modes, whereas the FT wave remains a bulk mode (critical angle is about 64°), which gives rise to a significant bulk reflection. In addition, there is a reflected ST partial wave which has an amplitude comparable to the incident wave.

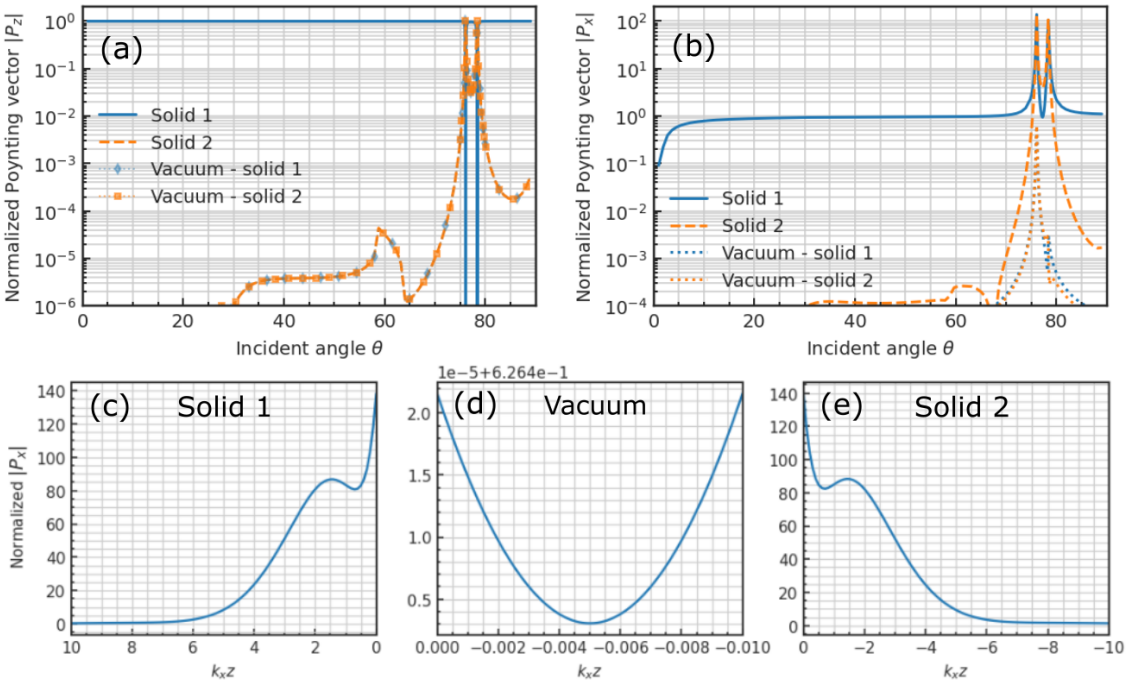

FIGURE 17 The normal (a) and parallel (b) component of the time-averaged Poynting vector at the surface, plotted as a function of the incident angle. In addition, the parallel components of the Poynting vectors are also plotted as a function of z-axis positions inside solid 1 (c), vacuum (d) and solid 2 (e).

The total power flow $\boldsymbol{P}_{\mathrm{AV}}$ on the surfaces of the solids is plotted as a function of the incident angle in Figure 17, both (a) the normal component ($|P_z|$) and (b) the parallel component ($|P_x|$). The blue solid line designates the reflected power flow

[7] The small but finite amplitude of the reflected ST mode is because of the numerical imprecision in the computation, and it is exactly zero theoretically.

at the solid 1 surface on the solid side, the orange dashed line is the transmitted power flow at the solid 2 surface on the solid side, and the blue and orange dotted lines are the transmitted power flow at the surface of solid 1 and 2 on the vacuum side. These power flows are normalized to their respective components of the incident Poynting vector by setting the incident components to 1.

The reflected power flow (ratio) in the normal direction $|P_z|$ at the surface of solid 1 is close to unity with a large range of incident angles. However, it quickly drops to zero and the transmitted power rises to unity when the resonant tunneling is excited. The normal direction power flow in vacuum is equal to the transmitted power in solid 2, as has been pointed out already in previous sections.

It is also interesting to look at the parallel component of the power flow, which is presented in Figure 17(b). There are two resonant peaks at the surfaces of both solids, both have the power flow (ratio) more than two orders of magnitude higher than the incident wave. Such high power flow is the result of the excitation of the quasi-surface wave, which concentrates the energy of the scattered wave on the surfaces and becomes the key to enabling the resonant tunneling. It should be noted here that the higher-than-unity power flow ratio is not breaking energy conservation, because the energy density increases only in the vicinity of the surface and decays exponentially into the bulk, as demonstrated in panels (c) and (e) in both solids for the resonance case ($\theta = 76.06^\circ$). In panel (d) the power flow $|P_x|$ inside the vacuum gap is presented as a function of the z-axis position, and we see that $|P_x|$ is distributed symmetrically inside the vacuum gap at the resonant tunneling conditions.

3.5 Heat transfer across vacuum

As the last part of the theoretical modeling in this dissertation, the topic of heat transfer across the vacuum gap carried by acoustic phonon tunneling[Geng and Maasilta, 2023b] will be presented in this section.

A general formula for such *piezoelectrically mediated heat transfer* (PEMHT) will be briefly derived first. A few numerical results will be investigated and compared to the heat transfer carried by other phonon and photon tunneling mechanisms. The piezoelectric material constants that are adopted in the calculation in the following sections are listed in Table 3

3.5.1 Heat flux of thermal phonons

There are many angles used in this work to describe the crystal orientation, *i.e.* ϑ, φ and ψ, and the direction of the incident wave, *i.e.* θ and φ, as illustrated in Figure 18. At the start of this section, it is particularly important to stress that the azimuth angle φ, which is used both for the crystal orientation angle and the incident wave angle for a semi-infinite half-space solid, signifies an equivalent rotational degree of freedom, as has been discussed in section 3.2. Therefore,

	ZnO	AlN	$LiNbO_3$
c^E $(10^{10} Nm^{-2})$			
c_{11}	20.97	34.5	20.3
c_{33}	21.09	39.5	24.5
c_{44}	4.247	11.8	6
c_{66}	4.43	11	7.5
c_{12}	12.11	12.5	5.3
c_{13}	10.51	12	7.5
c_{14}			0.9
e (Cm^{-2})			
e_{15}	-0.48	-0.48	3.7
e_{22}			2.5
e_{31}	-0.573	-0.58	0.2
e_{33}	1.32	1.55	1.3
ϵ^S (ϵ_0)			
ϵ_{xx}	8.55	9.04	44
ϵ_{zz}	10.2	10.7	29
Density ρ (kgm^{-3})	5680	3260	4700
Crystal class	$6mm$	$6mm$	$3m$

TABLE 3 Anisotropic piezoelectric material constants used in the calculations. These parameters are taken from Refs.Auld [1990]; Tsubouch and Mikoshiba [1985]

the rotation of φ should only be taken into account once in the mathematical formulation to avoid the duplication. Logically, the straightforward way is to consider that the direction of an incoming wave is a function of the angles θ and φ, spanning a full unit sphere, whereas the orientation of the crystal is completely fixed and should be described by the two given rotation angles ϑ and ψ[8]. Hence the derivations presented in this section will assume that the crystal orientation (ϑ, ψ) is given, and the formulations depend explicitly on the incident angles (θ, φ). However, in practice it is more convenient to directly use φ as part of the rotations of crystal to compute the material constants.

Consider an incident acoustic phonon of mode α impinging onto the surface of solid 1 and tunneling across the vacuum gap into the adjacent solid 2, as illustrated in Fig. 18. Up to four transmitted partial wave modes can be excited inside solid 2, but only the bulk phonon modes can carry the tunneled energy into the depth of solid 2. The total power transmittance of the incoming, tunneling α mode phonon (summed over all transmitted modes) denoted by $\mathcal{T}_\alpha$, can be expressed as [Eq.(132)]:

$$\mathcal{T}_\alpha(\theta, \varphi, k, d) = \frac{2\mathrm{Re}\left[\bar{r}_V^{(2)}\right] \left|\bar{t}_{\alpha\to V}^{(1)}\right|^2 e^{-2kd\sin\theta}}{\left|1 - \bar{r}_V^{(1)}\bar{r}_V^{(2)} e^{-2kd\sin\theta}\right|^2}, \tag{165}$$

[8] In such a case, the rotational degree of freedom from angle φ influences the results from the direction of the incident wave rather than the orientation of the crystal. Hence, one can choose any initial value of φ for the rotation the crystal, and the material constants become independent to the change of φ after the rotation.

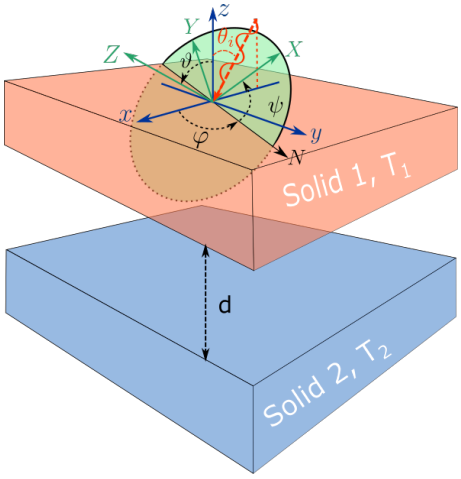

FIGURE 18 Schematic of two piezoelectric solids at temperatures T_1 and T_2, separated by a vacuum gap of width d.

in which $\mathcal{T}_\alpha$ is a function that explicitly depends on the incident angles θ and φ, the norm of the incident k-vector k, and the gap width d, whereas the single surface scattering coefficients $\bar{t}^{(1)}_{\alpha\to V}$, $\bar{r}^{(1)}_V$, and $\bar{r}^{(2)}_V$ defined in Eq.(117) are determined by the materials, crystal orientations, and the incident angles θ and φ.[9] In this work, the temperature range of interest is from room temperature ($\sim 300\,K$) down to the cryogenic ($\sim 10\,mK$) temperatures, hence the heat transfer of acoustic phonons is dominated by the phonons whose wave vector values (k) are far from the Brillouin zone boundaries. Therefore, the dispersion relation is considered to be linear (but not isotropic!), $v_\alpha = \omega_\alpha / k$, where v_α is the phase velocity of the wave mode α.

Starting from the above transmittance, the phonon heat flux can be considered as the tunneling of phonons with statistically averaged energy:

$$\Pi(\omega, T) = \frac{\hbar\omega}{\exp(\hbar\omega/k_B T) - 1}, \tag{166}$$

where ω and T are the angular frequency and the temperature of the incident phonon, and $\hbar$ and k_B are the Planck and Boltzmann constants, respectively. These phonons move with a group velocity in the normal direction of the surface

$$g^n_\alpha(\theta,\varphi) \equiv \boldsymbol{n}\cdot\frac{\partial\omega_\alpha}{\partial\boldsymbol{k}} = -\frac{\sin\theta}{2\rho v_\alpha(\theta,\varphi)|\boldsymbol{A}_\alpha(\theta,\varphi)|^2}\boldsymbol{\xi}^T_\alpha\hat{\boldsymbol{T}}\boldsymbol{\xi}^*_\alpha, \tag{167}$$

derived in Eq.(99)[10], and then tunnel across the vacuum gap with a power transmittance $\mathcal{T}_\alpha(\theta,\varphi,k,d)$ carried by the transmitted bulk phonon modes. It should

[9] We only need the eigenvector solutions $\boldsymbol{\xi}$ to solve for the single surface coefficients from Eq.(117). Although the Stroh characteristic function Eq.(82) is a function of $v_x = \omega/k_x$, which seemingly depends on both ω and k, v_x can be computed from $v_x = v/\sin\theta$ where v is the solution to the secular equation of piezoelectrically stiffened Christoffel equation Eq.(62). Hence, all the single surface coefficients can be obtained only with the knowledge of the material, orientation and the incident angle.

[10] Note that the group velocity depends explicitly neither on ω nor k using the extended Stroh formalism.

be noted here that in the coordinate system used in this dissertation, the incident phonon must have a negative-valued group velocity component, since $\boldsymbol{n}$ is the *inward* normal of the surface of solid 1, hence a net power flow from solid 1 to solid 2 should have a negative value.

As a result, the total heat flux of incoming phonons at temperature T tunneling to an adjacent solid at 0 K, summed over all of k-space and all incoming bulk modes α, can be expressed as:

$$J^{\mathrm{PE}}(T,d) = \sum_{\alpha} \int \frac{\mathrm{d}^3k}{(2\pi)^3} \Pi\big[\omega_\alpha(k), T\big] g_\alpha^n(\theta,\varphi) \Theta\big[-g_\alpha^n(\theta,\varphi)\big] \mathcal{T}_\alpha(\theta,\varphi,k,d), \quad (168)$$

where $\omega_\alpha(k)$ is the phonon frequency of mode α, and $\Theta\big[-g_\alpha^n(\theta,\varphi)\big]$ is the Heaviside step function that equals to unity (zero) when the group velocity $g_\alpha^n < 0$ ($g_\alpha^n > 0$).

It is important to point out that the group velocity, which signifies the speed and direction of the phonon propagation, generally has a different direction from the phase velocity, which describes the movement of the wave phase. There therefore exist cases where the normal components of these two velocities have opposing directions. In other words, a phonon that tunnels from solid 1 to 2 may have its wave vector (k-vector) pointing away from the surface. Consequently, in order to correctly account for all the possible incident acoustic phonons in solid 1 propagating towards the surface, the integration must cover the full k-space in Eq.(168), including the half-hemisphere on the vacuum side. By applying a Heaviside step function Θ, only the phonons propagating from solid 1 to 2 will then contribute to the integration.

With the expressions given in Eqs.(165), (166) and (167), the tunneled heat flux from solid 1 at a temperature T to a solid 2 at 0 K can be written into a more explicit form by introducing spherical coordinates in the integration over the full k-space as $\mathrm{d}^3k = k^2 \sin\theta \mathrm{d}\theta \mathrm{d}\varphi \mathrm{d}k$, giving:

$$\begin{aligned} J^{\mathrm{PE}}(T,d) =& \frac{1}{8\pi^3} \sum_{\alpha} \int_0^{2\pi} \mathrm{d}\varphi \int_0^{\pi} \mathrm{d}\theta g_\alpha^n \Theta\big[-g_\alpha^n\big] \int_0^{\infty} \mathrm{d}k \, \Pi\big[\omega_\alpha, T\big] \mathcal{T}_\alpha \\ =& -\frac{\hbar}{8\pi^3\rho} \sum_{\alpha} \int_0^{2\pi} \mathrm{d}\varphi \int_0^{\pi} \mathrm{d}\theta \frac{\sin^2\theta}{|\boldsymbol{A}_\alpha|^2} \mathrm{Re}\big[r_V^{(2)}\big] \big|t^{(1)}_{\alpha\to V}\big|^2 \boldsymbol{\xi}_\alpha^T \hat{\boldsymbol{T}} \boldsymbol{\xi}_\alpha^* \Theta\big[\boldsymbol{\xi}_\alpha^T \hat{\boldsymbol{T}} \boldsymbol{\xi}_\alpha^*\big] \\ & \times \int_0^{\infty} \mathrm{d}k \frac{k^3}{e^{v_\alpha \hbar k/k_B T} - 1} \frac{e^{-2kd\sin\theta}}{\big|1 - r_V^{(1)} r_V^{(2)} e^{-2kd\sin\theta}\big|^2}, \end{aligned} \quad (169)$$

in which $\boldsymbol{\xi}_\alpha^T \hat{\boldsymbol{T}} \boldsymbol{\xi}_\alpha^* = \pm 1$, if α is a bulk mode and zero for evanescent modes, and the sign signifies the direction of the phonon: it is positive for a transmitted phonon and negative for a reflected phonon (see section 2.3.3 for more details).

The net heat flux between solid 1 at temperature T_1 and solid 2 at temperature T_2 is the difference between their corresponding heat fluxes to 0 K, and reads as $\Delta J^{\mathrm{PE}}(T_1,T_2,d) = J^{\mathrm{PE}}(T_1,d) - J^{\mathrm{PE}}(T_2,d)$.

Furthermore, if we take the extreme limiting conditions of setting the power transmittance to unity, $\mathcal{T} = 1$, and assume that the group velocity is isotropic and equals the phase velocity, giving $g_\alpha^n = v_\alpha \cos\theta$, then the heat flux equation (169)

is simplified significantly to:

$$J(T) = \sum_{\alpha} \frac{\pi^2 k_B^4 T^4}{120 v_\alpha^2 \hbar^3}, \tag{170}$$

which has been referred to as the phonon blackbody radiation for isotropic matter [Swartz and Pohl, 1989].

3.5.2 Numerical examples

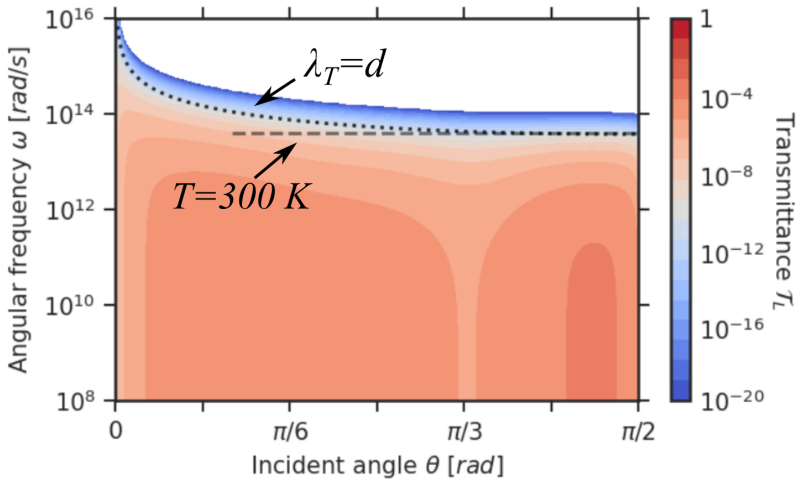

FIGURE 19 Contour plot of power transmittance $\mathcal{T}_L$ as function of incident angle θ and angular frequency ω. The vacuum gap is set to $d = 1$ nm.

The power transmittance $\mathcal{T}_\alpha$ is the key to the heat flux, bearing the underlying physics of the piezoelectrically mediated heat transfer (PEMHT). In the first numerical example, an incident longitudinal (L) phonon is considered to tunnel across a $d = 1$ nm vacuum gap between two ZnO crystals, which are identically rotated to an orientation $(\vartheta, \psi) = (\pi/2, 0)$, with an azimuth angle of $\varphi = \pi/3$. The power transmittance $\mathcal{T}_L$ is plotted as a function of the incident angle θ and the phonon frequency ω in Figure 19.

The most noticeable feature of the plot is that the transmittance decreases with the increasing of the phonon frequency, and has a sharp roll-off at about 10^{14} Hz. For a given incident angle and phase velocity, the rise of the phonon frequency leads to a proportionally increased $k = \omega/v_\alpha$, which, in turn, affects the transmittance via the exponential factors $\exp(-\omega d/v_\alpha)$ of the Eq.(165): at low frequency $\omega \ll v_\alpha/d$, it approaches 1 leading to a constant transmittance; at high frequency $\omega \gg v_\alpha/d$, it decays quickly to zero. By introducing a *characteristic wavelength* λ_T of temperature T defined as[11]:

$$\lambda_T = \frac{2\pi v_\alpha \hbar}{k_B T}, \tag{171}$$

[11] This definition has been consistently quoted in the studies of near-field phonon heat transfer[Prunnila and Meltaus, 2010; Pendry, 1999; Pendry et al., 2016; Volokitin and Persson, 2007; Volokitin, 2019, 2020], and also been used in literature regarding to the phonon heat transfers[Schwab et al., 2001; Sun and Murthy, 2006; Chen et al., 2008; Nomura et al., 2015].

the switching-off of the power transmittance can be described approximately by the frequency $\omega = 2\pi v_L/\lambda_T \sin\theta$, where $\lambda_T = d$, as plotted with the dotted line in Figure 19 for the case of $d = 1$ nm.

The temperature corresponding to $\lambda_T = 1$ nm is approximately 300 K (the relevant frequency $\omega = k_B T/\hbar \approx 4 \times 10^{13}$ rad s^{-1}), or in other words, the power transmittance from the PEMHT rapidly decays to zero if a vacuum width is larger than 1 nm at room temperature. On the other hand, as the gap width d increases, the relevant temperature T and frequency ω describing the roll-off of the transmittance decrease proportionally. For example, a 1 μm gap, a dimension easily accessible by current technology, corresponds to a temperature of 0.3 K and a frequency about 10^{10} rad s^{-1}.

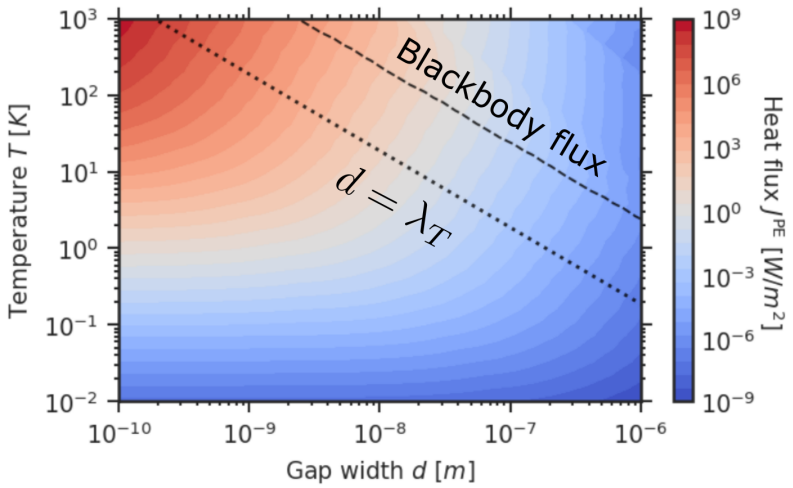

FIGURE 20 Contour plot of emitted heat flux J^{PE} from all phonon wave modes as a function of temperature T and gap width d. The adjacent solid is assumed to be at $T = 0$.

In Figure 20, the heat flux J^{PE} (assuming the adjacent solid is at $T = 0$) is plotted as a function of the phonon temperature T and the gap width d, for two identical ZnO solids with orientation $(\vartheta, \psi) = (\pi/2, 0)$, the same as in the previous example. This color-scaled contour plot can be roughly divided into two regions separated by the black dotted line $T = 2\pi\bar{v}\hbar/k_B d$, which represents the condition $d = \lambda_T$, and $\bar{v} = 3900$ m/s is chosen as an "averaged" phonon phase velocity for the illustration.

Towards the lower-left region, the heat flux decreases strongly with decreasing temperature, but saturates with the gap width. This comes about because, when the gap width d is much smaller than the characteristic wavelength λ_T, the power transmittance $\mathcal{T}$ [Eq.(165)] saturates and the phonon state energy Π [Eq.(166)], which is strongly modified by T but independent of d, determines the heat flux. In contrast, the exponential cutoff of the power transmittance dominates the heat flux towards the upper-right section. For example, at the large-gap

It is also worth noting that such definition is different by a factor of 1/2.82[Ziman, 1960] from the *dominant phonon wavelength*[Ramiere et al., 2017], which is the wavelength corresponding to the peak frequency of the phonon spectral energy distribution.

limit ($d \gg \lambda_T$), the heat flux is practically "switched-off" and becomes insensitive to the change of temperature. In addition, a black dashed line marks where the heat flux equals that of the photon blackbody radiation as a function of temperature [$J(T) = \pi^2 k_B^4 T^4 / 60 c^2 \hbar^3$ where c the speed of light]. The comparison between the dashed and dotted lines suggests that the PEMHT, if "switched-on" ($d \leq \lambda_T$), generally contributes at least 3 orders of magnitude more heat flux than that of blackbody radiation at a given temperature, making it an non-trivial source in the context of near-field heat transfer.

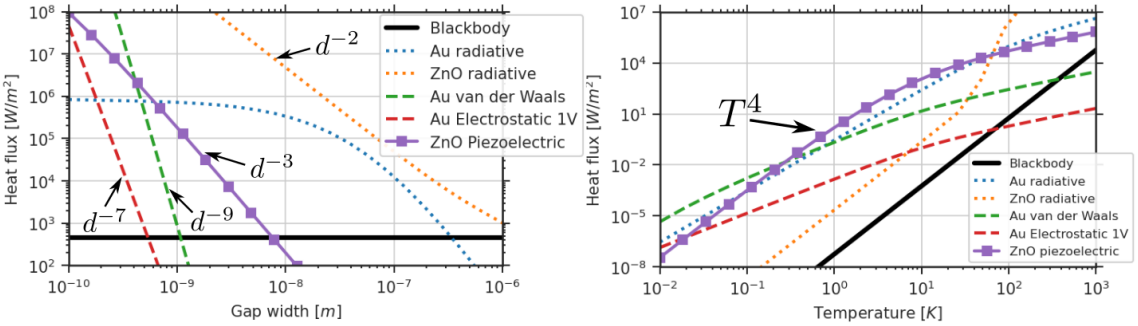

FIGURE 21 Comparison of the heat flux driven by different short range mechanisms. Left: Heat flux as a function of gap width at 300 K. Right: Heat flux as as a function of temperature with a fix gap width of 1 nm.

In addition, at room temperature, the PEMHT is stronger than the blackbody radiation even at a gap width close to 10 nm. This heat transfer, in fact, is very different to what has been suggested in previous studies of other acoustic phonon tunneling mechanisms [Ezzahri and Joulain, 2014; Pendry et al., 2016; Volokitin, 2019, 2020], in which the effective ranges at a room temperature are extremely limited, in sub-nanometer scales. In Figure 21, the heat flux carried by various relevant close-range mechanisms are compared, including the near-field radiative heat transfer (NFRHT, Pendry [1999]; Joulain et al. [2005]) of ZnO[12] and Au[13] , phonon tunneling in Au mediated by the van der Waals force [Pendry et al., 2016] ,and by the electrostatic force Volokitin [2019, 2020][14] , and the blackbody radiation (far-field radiative heat transfer).

On the left panel of Figure.21, the heat fluxes of all the mentioned mechanisms at 300 K are plotted as a function of the gap width d. It is clear that at room temperature, the near-field radiative heat transfer, also called "photon tunneling", for both Au and ZnO (blue and orange dotted lines) are significantly stronger than all the acoustic phonon tunneling mechanisms. In particular, heat fluxes driven by the van der Waals force and the electrostatic force scale as d^{-9} and d^{-7}, respectively [Volokitin, 2020]. Hence they only have non-trivial contributions at gap sizes $<$ 1 nm at room temperature, and will fall off rapidly with the increase of the gap. In contrast, the PEMHT, plotted as square symbols, scales as d^{-3}, which is similar to that for photon tunneling. Consequently, it quickly

12 Material constants are taken from Ashkenov et al. [2003]; Ooi et al. [2011].

13 Material constants are taken from Chapuis et al. [2008].

14 Assuming a 1 V potential difference is biased across the vacuum gap.

dominates the other phonon tunneling mechanisms at nanometer scales, being a relatively "long-range" effect.

One interesting observation in the left panel is that the NFRHT of ZnO is particularly large. The reason[Joulain et al., 2005] is because the surface-phonon polariton of ZnO can be excited at infrared frequencies [Ashkenov et al., 2003; Ooi et al., 2011], matching the spectrum of the room temperature thermal photons, and hence enhancing the heat flux. But this also infers that one should expect an attenuation of the NFRHT once the excitations are stopped, *i.e.* when the temperature is lowered. This is confirmed by the right panel of Figure 21, in which the heat fluxes are plotted as a function of the temperature for a fixed gap width of 1 nm. There is a clear cutoff of the NFRHT flux at about 100 K for ZnO.

More interestingly, the PEMHT becomes stronger than the fluxes from all other mechanisms, including NFRHTs, between $T = 0.1$ K to $T = 50$ K. At this temperature range, the power transmittance of the PEMHT increases exponentially as the characteristic wavelength of the acoustic phonon increases, and eventually saturates at the sub-Kelvin range (see Figure 20). With the temperature lowered even further, the PEMHT flux is determined by the phonon state energy term (phonon thermal spectrum), and therefore has a T^4 dependence on the temperature[15] , similar to the NFRHT of ZnO at the low temperature limit. Meanwhile, other acoustic phonon tunneling mechanisms, scaling more slowly than the PEMHT, begin to dominate the heat transfer at temperatures below 0.1 K.

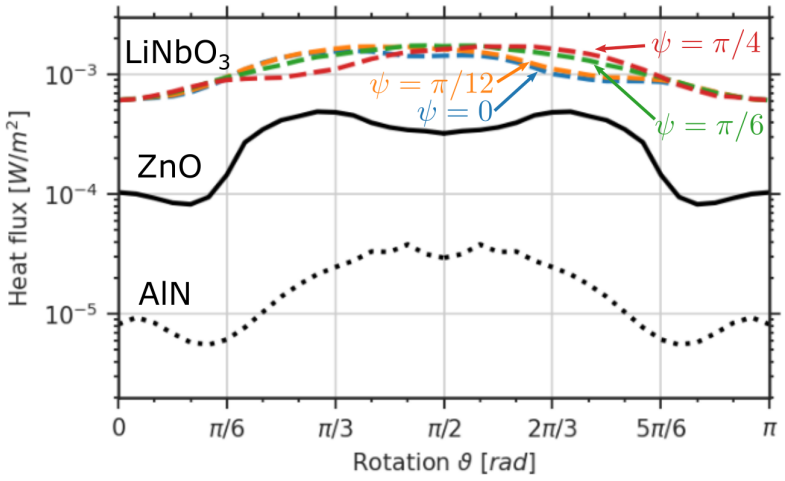

FIGURE 22 Comparison of emitted PEMHT as a function of the crystal rotation angle ϑ for ZnO (solid line), AlN (dotted line) and $LiNbO_3$ (dashed lines).

Lastly, the influences of the materials and orientations will be demonstrated in Figure 22. Three piezoelectric materials, ZnO, AlN and $LiNbO_3$ are considered, and their PEMHTs are presented as a function of an identically rotated ϑ

[15] This temperature dependence can be shown by analytically computing the integration $f = \int_0^\infty \mathrm{d}k\{v_\alpha \hbar k^3/[\exp(v_\alpha \hbar k/k_B T) - 1]\}$, using the *Riemann zeta function*, giving $f = \pi^4 (k_B T)^4/15(v_\alpha \hbar)^3$.

orientation[16] at a gap width of 1 nm and a temperature of 0.1 K.

There is a similarity shared by the heat fluxes of ZnO, plotted as a solid line, and AlN, plotted as a dotted line. For example, their fluxes are generally stronger around the orientations of $\vartheta = \pi/2$, contrasting to those around 0 and π; sharp slopes appear around 20° and 40°, leading to more than five-fold variation in the heat fluxes. This similarity comes about because they share the same crystal symmetry, namely they both are $6mm$ wurtzite crystals. The underlying physics of these features is that ϑ is the angle between the normal of the solid-vacuum interface and the piezoelectric axis of the crystal (the c-axis), and when ϑ is close to 90°, the c-axis is more aligned with the surface. As a result, the reflected evanescent modes, which propagate only on the surface, can excite stronger piezoelectric response, leading to an enhanced electrostatic coupling across the vacuum. As been shown in the previous section, *e.g.* in Figure.14, a high power transmittance can be found between $\vartheta \in (\pi/3, 2\pi/3)$ for certain partial wave modes, even achieving unity.

Meanwhile, PEMHT is stronger with ZnO about one order of magnitude over that of AlN. This is mostly due to the differences in their phase velocities. When the characteristic wavelength is much larger than the gap width, the heat flux scales roughly with v_α^{-3}. In the presented case, AlN has a transverse phase velocity about $v_T \approx 6000\,\mathrm{m/s}$, whereas ZnO has about $v_T \approx 2700\,\mathrm{m/s}$, and hence a ten-fold difference in heat flux is expected.

On the other hand, $LiNbO_3$ has a trigonal crystal system without uniaxial symmetry. Consequently, its PEMHT changes with the ψ rotations (see Fig.18), as demonstrated with the colored dash-lines in Figure 22. It is obvious that $LiNbO_3$ has even higher heat flux compared to ZnO, even if they share similar phase velocities. This can be explained simply by the fact that $LiNbO_3$ has much larger piezoelectric stress constants e, as listed in Table.3, which leads to an enhanced piezoelectric response on the solid-vacuum interface.

[16] Among the three angles ϑ, ψ and φ that are relevant to the orientation, ψ has no effect on the uniaxial crystals, *e.g.* ZnO and AlN, whereas φ is integrated in computing the heat flux [Eq.(169)] since it is equivalent to the incident azimuth angle.

4 EXPERIMENT ON ACOUSTIC PHONON HEAT TUNNELING

In the previous chapter, a theory on the piezoelectrically mediated phonon tunneling has been established step by step, starting from the basic continuum anisotropic linear elasticity theory, and ending with the discussion on the heat transfer of phonons between solids. An attractive yet crucial question arises: can this phenomenon be demonstrated in an experiment?

Heat, as one of the most studied phenomenon in nature, can be a great candidate to be measured in an experiment. Far-field radiation, which is well understood by Planck's law of blackbody radiation, is considered as the fundamental heat transfer channel between solids separated by vacuum. When the separation is small enough, super-Planckian heat transfer can be observed in experiments [Song et al., 2015; Lucchesi et al., 2021b], several orders of magnitude higher than that of the blackbody radiation. One of the most well-known mechanisms responsible for this is the near-field radiative heat transfer (NFRHT), mediated by photon tunneling [Polder and Van Hove, 1971; Pendry, 1999; Volokitin and Persson, 2001; Joulain et al., 2005], which becomes operable at the length scale of $\lambda_{ph} \sim 10\,\mu$m at room temperature[1].

With the advances in nanotechnology, heat transfer in the extreme near-field with gap width of nanometers becomes accessible to real devices and experiments [Kim et al., 2015; Kloppstech et al., 2017; Cui et al., 2017]. However, concrete experimental demonstrations of the heat transfer mediated by acoustic phonon tunneling is still lacking, and, to the best of the author's knowledge, there exist no report on piezoelectrically mediated heat transfer (PEMHT). It is perhaps not a surprise, because there are numerous difficulties to realize and verify the PEMHT in an experiment. For instance, the effect is weak at room temperature compared to photon tunneling. In particular, the surface phonon-polaritons in the piezoelectric material, such as ZnO, can be excited at room temperature, overwhelmingly dominating the heat transfer. In addition, the room temperature

[1] The Wien wavelength of a thermal photon is $\lambda_{ph} = c\hbar/k_B T$ where c the speed of light [Biehs and Greffet, 2010; Joulain et al., 2005]

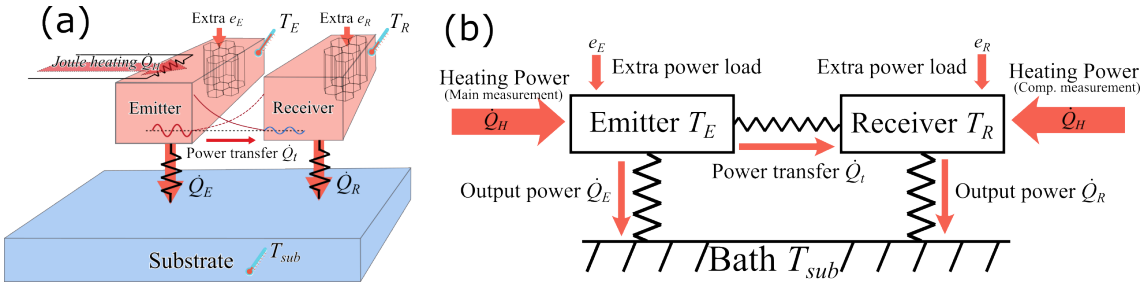

FIGURE 23 (a) Schematic of the measurement scheme. (b) The thermal model of the device used in the measurements.

characteristic wavelength of an acoustic phonon λ_T [Eq.(171)] is still too short, *e.g.* in gold it is $\sim$ 0.5 nm at 300 K, and it is therefore hard to achieve such gap widths even by the state-of-art lithography technologies. Although it has been shown in the previous chapter that PEMHT of ZnO can be higher than that of the blackbody radiation up to vacuum gap width of 10 nm, it still puts severe challenges on both the device fabrication and the heat flux measurement.

Measuring the heat transfer in a cryogenic environment can be an attractive solution to these difficulties. As has been discussed previously, at sufficiently low temperatures, there is no excitation of the surface phonon-polariton, and the PEMHT becomes the dominant heat transfer channel. Furthermore, with the increase of the characteristic wavelength of the acoustic phonons, it is possible to observe the enhanced heat transfer even at a sub-micrometer vacuum gap widths, making the device fabrication more feasible with standard nano-lithography.

In this work, an experimental demonstration on PEMHT is proposed and conducted using a microscopic device at sub-Kelvin temperatures. The strategy of the measurement, fabrication of the device and the discussion of the measurement results will be presented in the following sections.

4.1 Experimental scheme

Two sets of measurements will be carried out in the experiment using a microscopic on-chip device consisting two closely spaced piezoelectric AlN suspended beams: the enhanced heat transfer will be demonstrated *qualitatively* in the first set of measurements; then the transferred heat flux will be *quantitatively* determined via a set of followed complementary measurements.

4.1.1 Experimental design

The model for the first qualitative measurement is shown schematically in Figure 23(a). Two piezoelectric beams (AlN in this work) are separated by a few hundred nanometer-wide vacuum gap, and are suspended from the bulk of the device by weak thermal links. The measurement starts from a complete thermal equilib-

rium of the device at a sub-Kelvin temperature[2]. The temperature T_E of one of the beams, labeled as emitter, is increased by applying local Joule heating power $\dot{Q}_H$. Simultaneously, the temperature T_R of the unheated beam, labeled as receiver, is measured. Hence, the observation of the rise of T_R over the device substrate temperature T_{sub} indicates heat transfer across the vacuum gap. In addition, a second identically designed but non-piezoelectric (SiN in this work) device will be measured in the same manner. A much lower increase in T_R is expected for such a device, because the heat transfer from photon tunneling of the dielectric material is strongly suppressed at such low temperatures, and other acoustic phonon tunneling mechanisms are also considered to be weak due to their strong decay with gap width. As a result, the contrast between the measurement of the two devices signifies the presence of PEMHT, demonstrating tunneling of acoustic phonons.

It is also possible to quantitatively determine the tunneled power $\dot{Q}_t$[3] between the two beams by a second set of measurements that complements the first set in a reciprocal manner. Considering the system consisting of both beams in a steady-state, there is a balance between the input and output power of the system. In the first measurement, where the Joule heating is applied to the emitter beam (referred to as *main measurement* hereafter), this power balance can be expressed as [see Figure 23(b)]:

$$\dot{Q}_H + e_E + e_R = \dot{Q}_E(T_E, T_{sub}) + \dot{Q}_R(T_R, T_{sub}). \tag{172}$$

In this equation, in the LHS there are the three power input sources that are considered in this model: a Joule heating power $\dot{Q}_H$ that is steadily applied to the emitter beam, and two extra power loads e_E and e_R applied to each beam from the sources[4] that are independent to the application of $\dot{Q}_H$, *e.g.* the heating from the thermometer biases and noise, the Peltier cooling from the superconducting junction [Nahum et al., 1994; Leivo et al., 1996; Koppinen and Maasilta, 2009], *etc*.

The RHS of Eq.(172) represents the rate of heat that flows out of the system via thermal conduction between the beams and the bulk when a temperature difference is present: $\dot{Q}_E(T_E, T_{sub})$ is the power transported from the emitter beam at temperature T_E to the bulk at temperature T_{sub}, and $\dot{Q}_R(T_R, T_{sub})$ flows from the receiver beam at temperature T_R to the bulk. Such power transport is customarily modeled using a temperature dependent expression [Klitsner et al., 1988; Anghel et al., 1998]:

$$\dot{Q}_a(T_a, T_{sub}) = K_a(T_a^{n_a} - T_{sub}^{n_a}), \tag{173}$$

where K_a and n_a are the device specific parameters of the beam $a = E, R$ determined by the details of the materials and geometry. Meanwhile, the differential thermal conductance can also be defined from Eq.(173), giving:

$$G_a(T) \equiv \frac{\mathrm{d}\dot{Q}_a(T, T_{sub})}{\mathrm{d}T} = n_a K_a T^{n_a - 1}. \tag{174}$$

---

2 In the measurement, this means the readings of all thermometers do not change with time.

3 The heat transferred between the beams is estimated to be $Q_t = AJ^{\mathrm{PE}}$, where A is the surface area between the beams and J^{PE} is the heat flux.

4 The direction of the power is assigned such that heating is positive and cooling is negative.

It should be noted that the blackbody radiation between the system and the environment is omitted in the presented thermal model, because of its vanishingly small contribution ($< 10^{-20}$ W) at sub-Kelvin temperatures and the device dimensions concerning this work.

In the second set of measurements, the *complementary measurement*, the Joule heating is applied to the receiver beam instead of the emitter [see Figure 23(b)], and consequently the power balance is $\dot{Q}'_H + e'_E + e'_R = \dot{Q}'_E(T'_E, T'_{sub}) + \dot{Q}_R(T'_R, T'_{sub})$, in which the prime superscripts signify the quantities of the complementary set. If in this measurement the temperature of the emitter and the substrate are adjusted to be the same as their respective values in the main measurement, *i.e.* $T'_E = T_E$ and $T'_{sub} = T_{sub}$, the power balance can be stated as:

$$\dot{Q}'_H + e'_E + e'_R = \dot{Q}_E(T_E, T_{sub}) + \dot{Q}_R(T'_R, T_{sub}), \tag{175}$$

where the power flows from the emitter to the bulk $\dot{Q}_E(T_E, T_{sub})$ are the same in both measurements.

The difference of Eqs.(172) and (175) gives:

$$\Delta\dot{Q}_H + \Delta e = K_R\left[(T'_R)^{n_R} - (T_R)^{n_R}\right], \tag{176}$$

where $\Delta\dot{Q}_H = \dot{Q}'_H - \dot{Q}_H$ is the difference between the heating powers of the two measurements, $\Delta e = e_E + e_R - e'_E - e'_R$ is the difference of the extra heat loads, and K_R and n_R are the receiver parameters of Eq.(173). Taking the derivative of T'_R on Eq.(176), and noting that Δe is independent of T'_R from the model assumptions, an expression:

$$\frac{\mathrm{d}\Delta\dot{Q}_H}{\mathrm{d}T'_R} = G_R(T'_R) - G_R(T_R)\frac{\mathrm{d}T_R}{\mathrm{d}T'_R} \tag{177}$$

is obtained, in which $G_R(T) = n_R K_R T^{n_R - 1}$ is the thermal conductance of the receiver beam.

The receiver parameters K_R and n_R can be extracted from the measured quantities $\Delta\dot{Q}_H$, T_R and T'_R in the experiment[5] using either Eq.(176) or Eq.(177). As a result, the power transferred between the two beams in the main measurement $\dot{Q}_t$ can be determined from the power balance of the receiver beam, reading as:

$$\dot{Q}_t = K_R(T_R^{n_R} - T_{sub}^{n_R}) - e_R, \tag{178}$$

in which e_R, the extra power load on the receiver beam in the main measurement, can be inferred from the quiescent temperature of the receiver beam $T_{R,quiet}$ as $e_R = K_R(T_{R,quiet}^{n_R} - T_{sub}^{n_R})$. It is also worth mentioning here that the tunneled power can also be expressed as $\dot{Q}_t = \Delta J^{\mathrm{PE}} A$, where ΔJ^{PE} is the net power flux of PEMHT, and A is the surface area normal to the flux direction.

4.1.2 Heater and thermometer

The above experimental scheme depends highly on the accuracy of the measured Joule heating power and temperatures of the beams. This requires that the heaters

[5] Δe is a free parameter in fitting Eq.(176) from the measurement results.

and the thermometers are capable of functioning at sub-Kelvin temperatures, being integrated onto the suspended structures, and working only locally on the beams.

Based on these requirements, superconducting junction heaters and temperature sensors are selected for the experiment. Symmetric *normal metal-superconductor* (NS) junctions are used as the heater, which provide a nearly ideal local heating to the beam. The Joule heating can be generated uniformly across the normal metal wires on the beams, whereas the NS junctions act as perfect thermal insulators due to the *Andreev reflection* process [Karvonen et al., 2005]. Thus, by measuring the heating current I_H and the voltage drop between the NS junctions V_H, using a four-terminal sensing method, the Joule heating power $\dot{Q}_H = I_H V_H$ is determined, reflecting only the power inputs to the beam, as there is no leakage or resistive dissipation on the superconducting sides of the leads.

The temperatures of both beams and the substrate are measured using symmetric *normal metal-insulator-superconductor* (NIS) tunnel junctions [Rowell and Tsui, 1976], which are also known as SINIS thermometers [Giazotto et al., 2006]. This type of a sensor provides an extremely sensitive temperature measurement of its normal metal island, which can be confined in a targeted area, for example only at the top of the beam, and thus offers a sensing of only the local temperature. In addition, such sensors are perfectly compatible with the cryogenic environment and easily integrated onto micro-devices due to their nano-scale size, and therefore are ideal for the measurements in this work.

Thermometry is not the point of this dissertation, but for the sake of offering the readers with a more tangible understanding of the temperature measurement technique carried out in this work, a very brief introduction of the working principle of the SINIS thermometer is presented here.

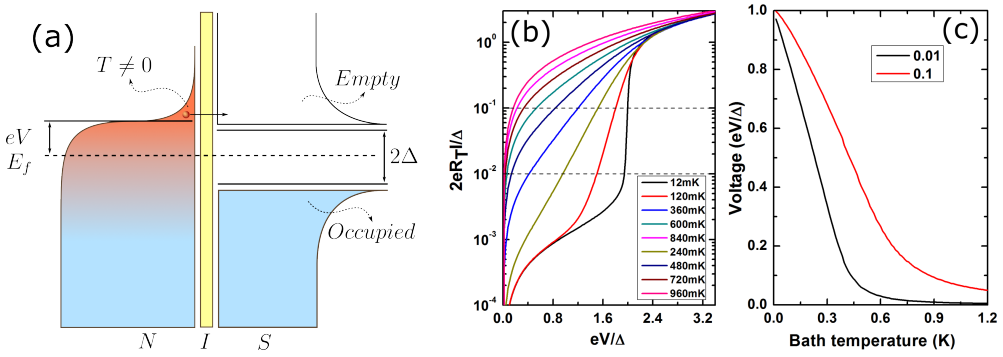

FIGURE 24 (a) The energy-band model of NIS junction. (b) Current-voltage (c) voltage-temperature characteristics of a typical SINIS thermometer.

In an energy-band model of an NIS junction, which is valid when excitations are thermally distributed and described by temperature T, as shown in Figure 24(a), the presence of the superconducting gap 2Δ forbids the tunneling of electrons from the normal metal to the superconductor across the thin insulator barrier, except for those that are highly thermally excited. The probability

of finding an electron of energy E at temperature T is described by the Fermi distribution:

$$f(E,T) = \frac{1}{\exp\left[(E-E_f)/k_BT\right]-1}, \tag{179}$$

where E_f is the Fermi-energy of the normal metal. By applying a voltage bias V over the junction, this probability is modified, and the tunneling current will change exponentially until the bias reaches $V = \Delta/e$.

Quantitatively, this tunneling current can be written as:

$$I_{NIS} = \frac{1}{eR_T}\int_{-\infty}^{\infty} \mathrm{d}E\, n_S(E,T_S)\left[f_S(E,T_S) - f_N(E+eV,T_N)\right], \tag{180}$$

where R_T is the resistance of the junction in the normal state, T_S and T_N are the temperatures of the superconductor and normal metal, n_s is the density of states of the superconductor in the weak-coupling limit and reads as:

$$n_S(E,T) = \left|\mathrm{Re}\left[\frac{E}{\sqrt{E^2-\Delta(T)^2}}\right]\right|. \tag{181}$$

The current of another symmetric NIS junction, assuming also biased by V, can be written similarly as:

$$I_{SIN} = \frac{1}{eR_T}\int_{-\infty}^{\infty} \mathrm{d}E\, n_S(E,T_S)\left[f_N(E-eV,T_N) - f_S(E,T_S)\right]. \tag{182}$$

Since the two junctions are connected in series via a shared common normal metal island, their currents are equal and thus can be expressed in a combined form as:

$$I_{SINIS} = \frac{1}{2eR_T}\int_{-\infty}^{\infty} \mathrm{d}E\, n_S(E,T_S)\left[f_N(E-eV,T_N) - f_N(E+eV,T_N)\right]. \tag{183}$$

It is clear that the distribution functions in the current expression, Eq.(183), depend only on the temperature of the normal metal[Giazotto et al., 2006]. Moreover, in practice, the SINIS thermometer almost always operates at a temperature far below the superconducting transition temperature T_c, *i.e.* $T_S < 0.4T_c$ where T_S is the temperature of the superconducting leads[6], thus the energy gap Δ of the superconductor is considered to be constant. The current of a SINIS sensor is thus only a function of the bias voltage and the temperature of the normal metal island, and thereby provides the capability of measuring the temperature locally.

The operational scheme of an SINIS thermometer is demonstrated in Figure 24(b) and (c), showing the computed I-V and V-T characteristics of the junction, respectively. Such a sensor is usually current biased, for example with a (reduced) current value $2eR_TI/\Delta = 0.1$ or 0.01, and the measurable quantity is the (reduced) voltage across the junction whose response to the temperature for different current biases are shown in panel (c). In addition, the SINIS junction could even be used as a primary thermometer, nevertheless, here it will be operated with a calibration to a commercially calibrated Ge thermistor (GR-200A-30, LakeShore) before each measurement, to ensure accuracy.

[6] The temperature of the superconducting leads in the experiment is expected to be close to that of the substrate in this work.

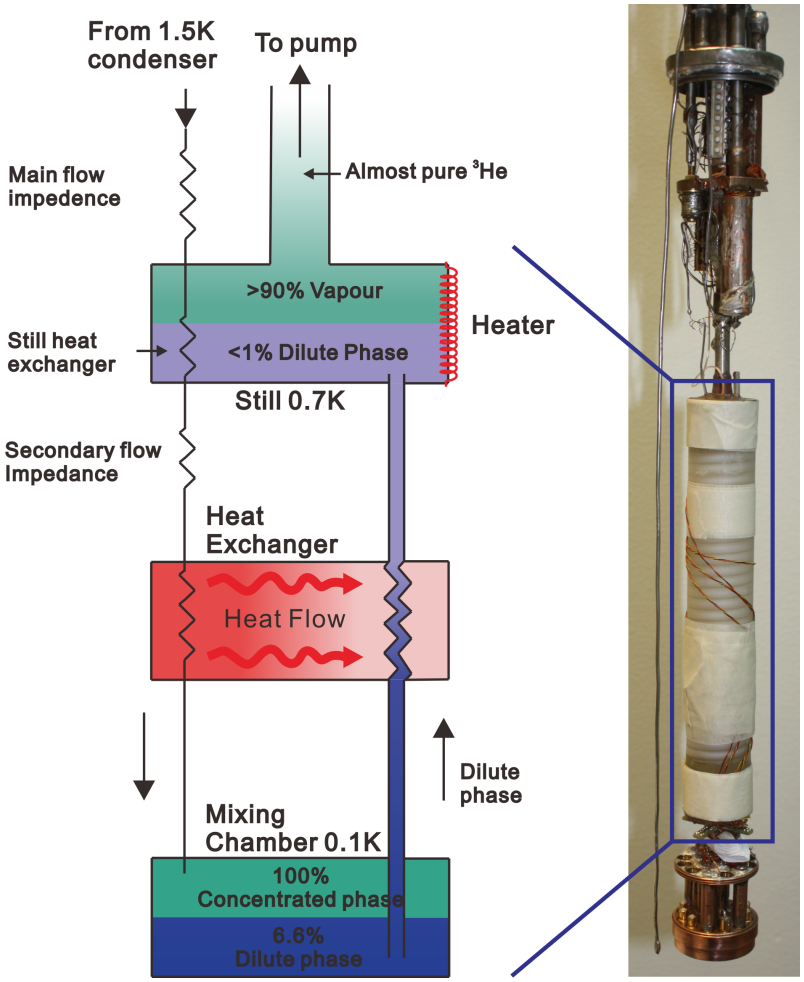

FIGURE 25 Schematic and the photo of the plastic dilution refrigerator used in this work.

4.1.3 Plastic dilution refrigerator

To achieve the sub-kelvin operational temperatures required in this work, an in-house built ^{3}He-^{4}He plastic dilution refrigerator (PDR) is used[Pekola and Kauppinen, 1994], which reaches a base temperature below 50 mK routinely, with a fast turn-around time and high cost-efficiency.

The basic principle of a dilution refrigerator is to utilize the heat absorption when the ^{3}He isotope is pumped and circulated across the phase boundary between the ^{3}He rich and diluted mixtures of ^{3}He/^{4}He liquid.

In practice, several pre-cooling stages are needed, as illustrated in Figure 25. The PDR has an ambient temperature of 4.2 K provided by a liquid Helium (LHe) bath, and the low temperature stages are located inside a pumped vacuum-jacket (not shown), to be thermally isolated from the environment. A small pot chamber, which contains ^{4}He replenished via a flow impedance connected to the LHe bath, is thermally anchored to a copper flange, and is continuously pumped to maintain a temperature of $\sim$ 1.5 K. In the next stage, a condensed mixture of ^{3}He/^{4}He liquid is pumped from another chamber located at the top of the plastic part, giving a temperature of $\sim$ 0.7 K, caused by the evaporation of mainly ^{3}He.

At the last stage, the dilution cooling happens at the bottom chamber of the plastic part, where the phase separated ^{3}He/^{4}He liquids are accommodated. A heat exchanger made from a sintered silver powder connects and thermalizes this chamber to the measurement stage at the bottom of the PDR.

The electrical wires inside the PDR system are thermalized to the sample stage and the stages above. In the refrigerator used in this work, cryogenic woven loom wire first connects the room temperature device-interface to a set of Pi filters (SBSMP5000223MX, Syfer) in direct contact with the LHe, and then to a circuit panel that is thermalized at the 1.5 K stage inside the vacuum jacket via a feed-through. Niobium superconducting wires are used to continue the connections from 1.5 K to a set of home-built low-pass filters at the measurement stage. This filter set is made from Eccosorb CR-124, providing a dissipative attenuation from 150 kHz and a strong cut-off at 1.4 MHz [Andrii, 2012].

The temperature of the measurement stage is monitored using a commercially calibrated germanium (Ge) thermistor (GR-200A-30, LakeShore) via a resistance bridge (Picowatt AVS-47), and is stabilized by applying heating through a resistor mounted on the stage via a PID controller (Picowatt TS-530).

4.2 Device fabrication

A total of four devices have been measured in the experiment of this work, including two piezoelectric aluminum nitride (AlN) devices with vacuum gap widths 400 nm and 500 nm, and two non-piezoelectric silicon nitride (SiN) devices with gap widths 500 nm and 600 nm [7]. The design and fabrication of these devices will be explained and discussed in this section.

4.2.1 Device design

All devices share the same design, varying only in dielectric materials and vacuum gap widths, hence Figure 26, a set of scanning electron microscope (SEM) images of one of the devices, can represent the design of the devices used in this work. The main structures of the device are two parallel suspended beams, each having a nominal length of 124 μm, fabricated either from a 500 nm thick stress-free SiN or from wurtzite [002] AlN[8]. These beams are suspended over a 10 μm deep cavity etched into silicon, and each beam is supported by four 44 μm $\times$4 μm bridges. The bridges are designed to anchor to the bulk substrate via two orthogonal directions, in order to reduce the degrees of freedom for the movement of the beams so that rolling, tilting or buckling of the beams are minimized, see Figure 27 for failed designs.

A pair of symmetric normal metal-superconductor (NS) junctions are used

[7] There were attempts to fabricate more devices with different gap widths, but those failed, for example due to the breaking of the suspended beams or tunnel junctions.

[8] In the [002] AlN, the crystallographic *c*-axis is perpendicular to the substrate surface.

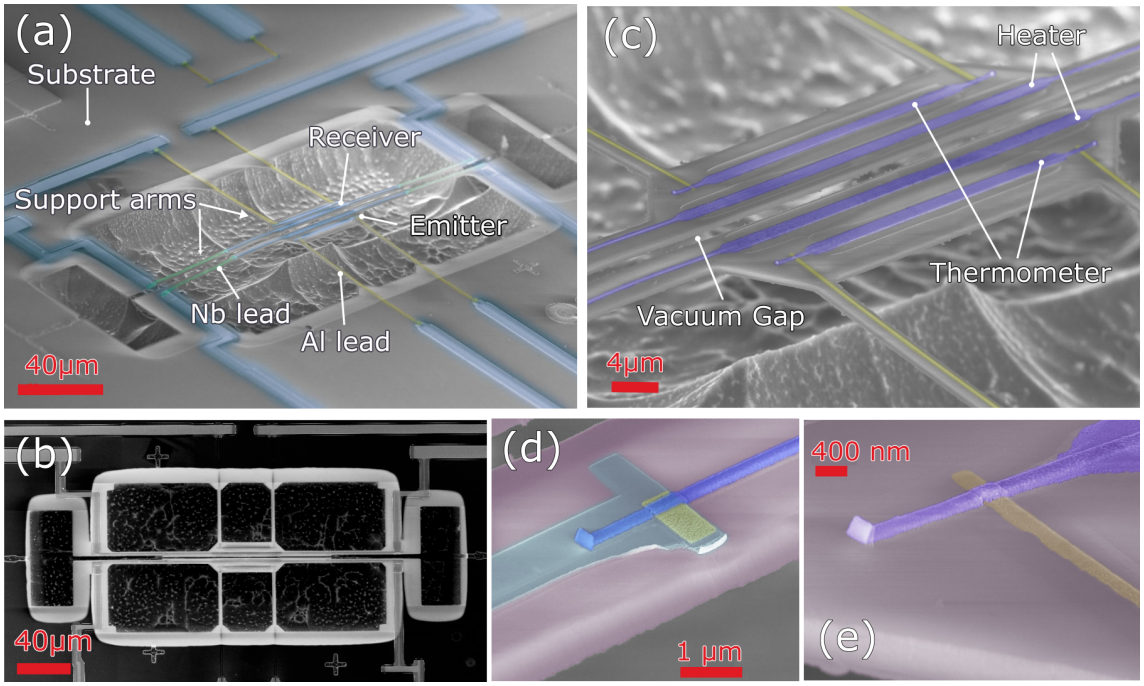

FIGURE 26 Scanning electron microscope images of a AlN device. (a) and (c) are fake-coloured bird-eye views of the device. (b) is the top view. (d) is the zoomed view of a NS junction. (e) is the zoomed view of a NIS junction.

as the local heater on each of the beam. The Joule heating is generated from a 120 μm$\times$300 nm$\times$70 nm (length$\times$width$\times$thickness) titanium-gold (Ti/Au) bi-layer wire. A NS junction is located at each end of the wire, consisting of a small area of Ti/Au bilayer over a 800 nm $\times$ 20 nm (width$\times$thickness) niobium (Nb) lead, as shown in Figure 26(d). It is worth mentioning that the bottom Nb lead [blue wire in panel (d)] and the top Ti/Au lead (purple wire) are fabricated separately with different pattern masks, and, to improve the quality of the metallic contact between the two leads, a 4 nm gold layer [yellow pad in panel (d)] is deposited on the top of the Nb lead covering the junction area, directly following the evaporation of Nb using an angular evaporation technique. The Nb leads run across those supporting bridges that align with the beam, and join with other electrical leads, which are also made mainly from Nb, on the substrate.

The temperatures of both beams and the substrate are monitored by symmetric normal metal-insulator-superconductor (SINIS) tunnel junctions. Each junction has an area of 300 nm $\times$ 300 nm [see Figure 26(e)], and, from the bottom up, consists of: a 300 nm $\times$ 40 nm (width$\times$thickness) superconducting aluminum (Al) lead running across the supporting bridge that is perpendicular to the beam; a native oxide layer (AlO_x), which grows with a controlled time and oxygen pressure; a 45 μm$\times$300 nm$\times$70 nm (length$\times$width$\times$thickness) Ti/Au bilayer wire, which connects to another identical junction and acts as the temperature sensing element of the structure it resides on.

It should be mentioned here that the minimum distance between the normal metal wires (Ti/Au) across the vacuum gap between different beams is designed to be 6 μm, much larger than the sub-micrometer gap width used in this work.

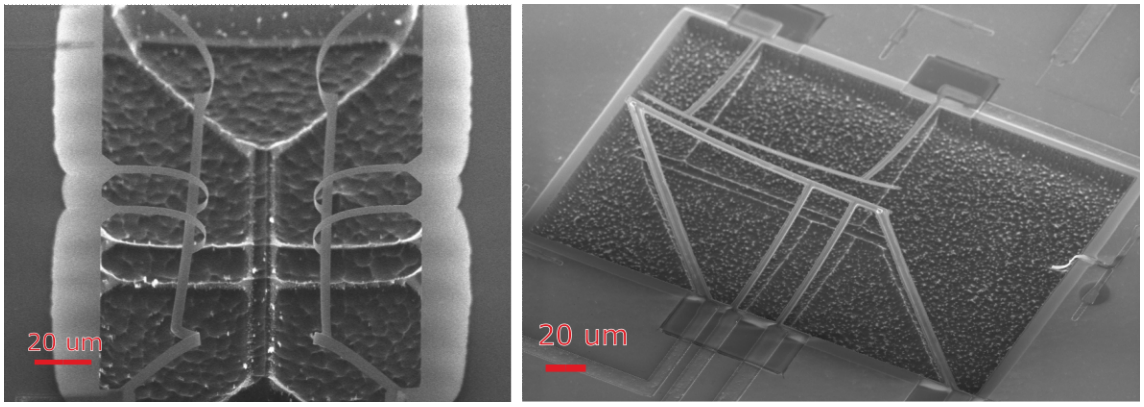

FIGURE 27 Failed designs due to deformations of the suspended structures.

As a result, the relevant gap width for near-field photon tunneling between the metal wires is thus much larger than that for the acoustic phonon tunneling.

4.2.2 Fabrication procedures

The work flow of the device fabrication is illustrated in Figure 28, which can be divided into four major steps: AlN etching, Nb deposition, junction deposition, and structure release.

In the first AlN etching procedure, the structures of the beam and the supporting bridges are defined by an etching process. For the AlN thin film chip, a 500 nm 4% 950 PMMA in anisole (A4) resist layer is patterned as an etching mask, using standard electron beam lithography (EBL) with a Raith eLiNE system. After the development, the AlN film is etched using a 25% wt. Tetramethylammonium Hydroxide (TMAH) solution for 15 seconds, followed with a deionized water rinse. During the etching process, the TMAH bath is agitated with a syringe to create turbulence around the patterned areas, in order to achieve better uniformity. With the SiN thin film chip, an 1 μm A4 resist mask is used instead, and after the development, a plasma reactive ion etching (RIE) process is carried out with a mixture of 50 sccm CHF_3 and 5 sccm O_2, at an RF power of 150 W for 10 min. Following either of the above etching processes, the etched gap between the beams will be thoroughly cleaned by using a focused neon ion beam from a Zeiss Orion helium ion microscope (HIM) system. This process is to ensure a controlled width and a clean cut of the vacuum gap without unwanted direct contacts, such as resist residues or the hillock-shaped structures surviving from the etching. The comparison of a vacuum gap in AlN before and after the HIM cleaning step is demonstrated in Figure 29.

Nb is used as the superconducting electrode material of the NS junctions, and as the common leads for all the electrical connection on the substrate. In the second, Nb deposition procedure, EBL is used to pattern a spin-coated bilayer resist mask consisting of a 300 nm 9% copolymer in ethyl lactate (EL9) at the bottom, and a 500 nm A4 on the top. After the development, the bottom EL9 layer creates a larger cavity in contrast to the top A4 layer, providing an undercut structure. In the next metal deposition process, a 5 nm titanium (Ti) is evaporated

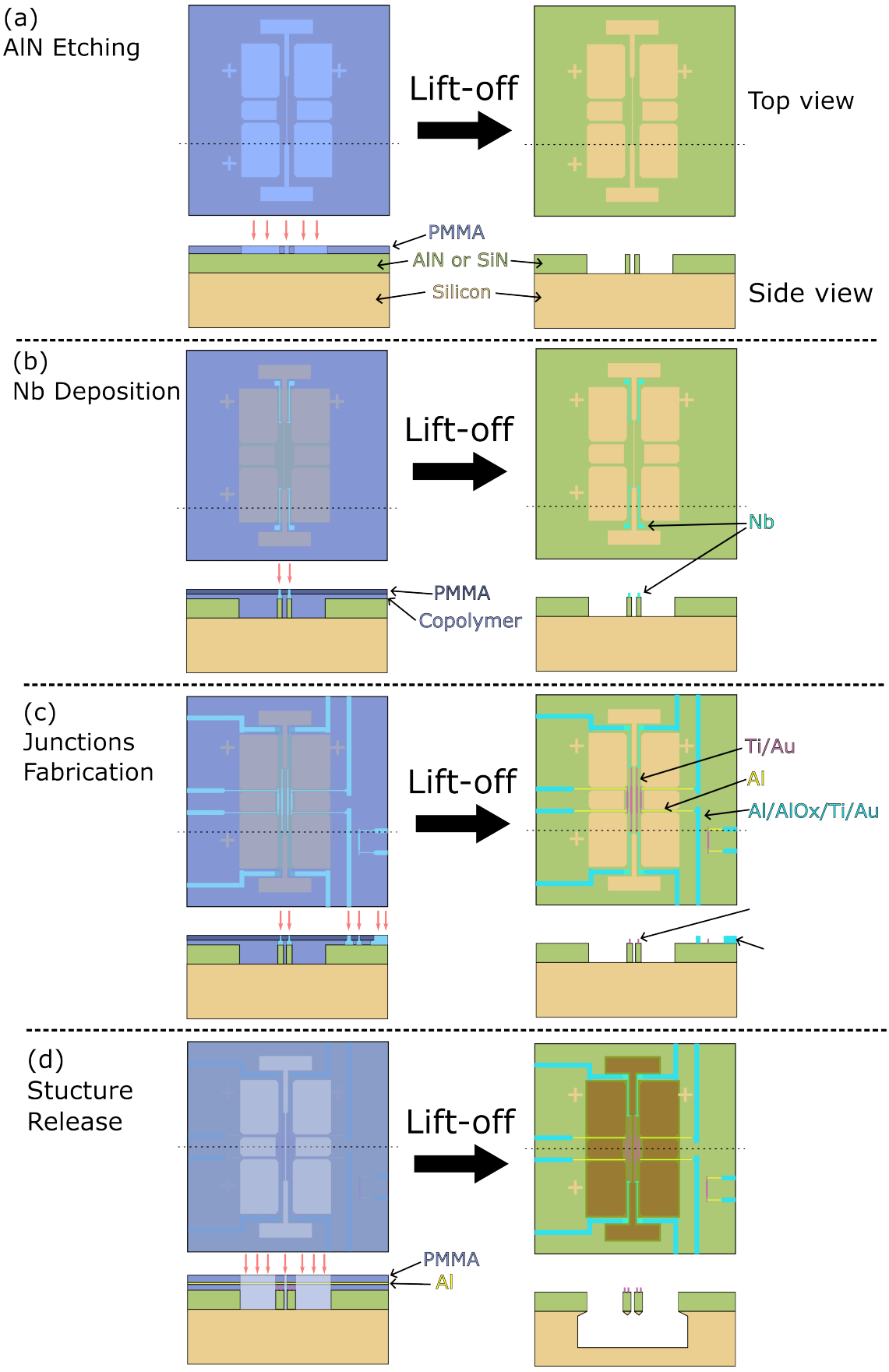

FIGURE 28 The general work flow for fabricating the devices used in this work. See main text for details.

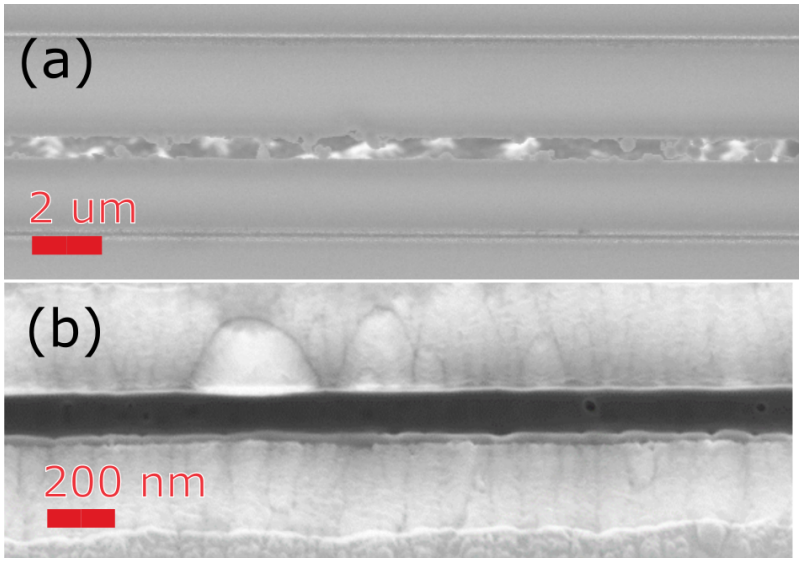

FIGURE 29 A comparison of a AlN vacuum gap before (a) and after (b) the HIM milling process.

first from the direction normal to the substrate, followed by a 20 nm Nb from the same direction. The thin bottom Ti layer is used to enhance the quality of the Nb leads[9]. Right after the Nb deposition, an 1 nm Ti/6 nm Au bilayer is evaporated to the device from an angle of 60° to the normal. Using such an *angular evaporation technique*, the deposited Ti/Au bilayer covers only two small areas of the Nb leads, where the NS junctions are designed to be formed, as shown in Figure 26. The purpose of these Ti/Au areas is to protect the Nb from directly contacting the atmosphere and other chemicals, to avoid oxidation, which would damage the junction.

In the third, junction fabrication procedure, a bottom 400 nm EL9 and a top 500 nm A4 bilayer resist mask is patterned with EBL. Since the insulator barriers of the NIS junctions require an accurately controlled oxidization process of the thin Al film, in the deposition process multiple metal layers are evaporated sequentially, including an oxidization process in between, without breaking the vacuum of the evaporation chamber. In addition, to avoid metals overlapping in unwanted areas, a two-axes rotation, multi-angular evaporation method is employed with the help of a specially designed deposition stage, as shown in Figure.30(a).

During the deposition, a nominal 35 nm Al layer[10] is first deposited from the direction that is perpendicular to the beams and with a set of evaporation angles, as illustrated in Figure.30(b). The evaporation angles begin from ±75° and reduce progressively to ±60°, with 5° decrement in each step, and, in each step, the angles are also switched back and forth once with respect to the normal of the substrate. Such multi-angular evaporation technique can reduce self-shadowing and enhance the coverage of the deposited metals. After the deposition, the thin Al film is immediately oxidized under 200 mbar of pure oxygen gas for 6 min, to

[9] The critical temperature of the Nb is increased on top of a Ti layer.

[10] This is the normal direction thickness, calculated from the actual evaporation angles.

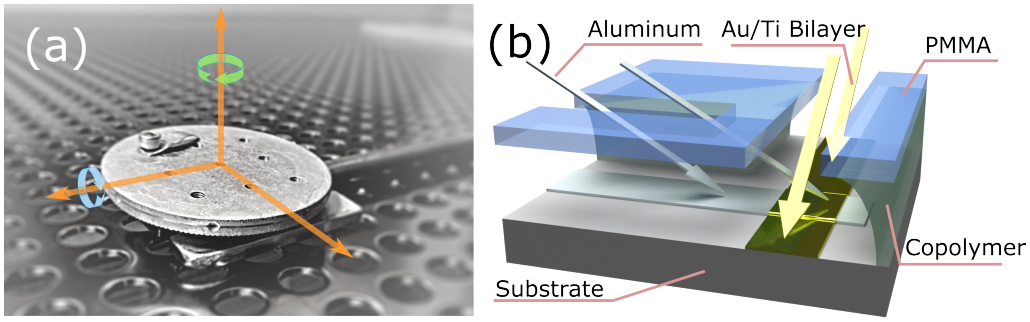

FIGURE 30 (a) Evaporation sample stage used in the deposition process. This stage can be rotated against two orthogonal axes inside the evaporator without breaking the vacuum. (b) Schematic of the two-axes angular evaporation method developed in this work.

form native AlO_x layers acting as the insulating barriers for the SINIS junctions.

Before depositing the next Ti/Au bilayer, the substrate is rotated 90° around its normal using the stage shown in the Figure 30(a), without breaking the vacuum. A 4 nm Ti/66 nm Au bilayer is then evaporated from the direction aligning with the beams [see Figure 30(b)], with the same set of evaporation angles that were used in the Al deposition. As a result, this bilayer covers only the pattern areas that overlap with the Al/AlO_x and Nb/Ti/Au at their respective SINIS and NS junction areas.

The last fabrication procedure is to release the beam structures from the substrate. This step is achieved by carrying out an RIE process of silicon etching using a mixture of 100 sccm SF_6 and 8 sccm O_2 at 50 W RF power for 100 min. A sandwiched resist mask, consisting of a total 1.5 μm A4 with a 8 nm Al layer inserted in between, is used to reduce the charging effect from both EBL and RIE processes, and to protect the tunnel junctions from being electrically shocked. At the end of this procedure, the device is thoroughly cleaned with heated acetone to lift-off the remaining resist masks.

4.3 Experimental results

The four devices that were fabricated following the procedures presented in Section 4.2 were measured with the scheme explained in Section 4.1. All the measurements were carried out inside an electromagnetically shielded room, and in this section the procedures and the results of the measurements will be described and discussed.

4.3.1 Measurement procedures

In the beginning of each measurement, all the SINIS thermometers on the device are characterized via a set of current-voltage (IV) measurements at different bath temperatures, to examine the quality of the junctions and to optimize the

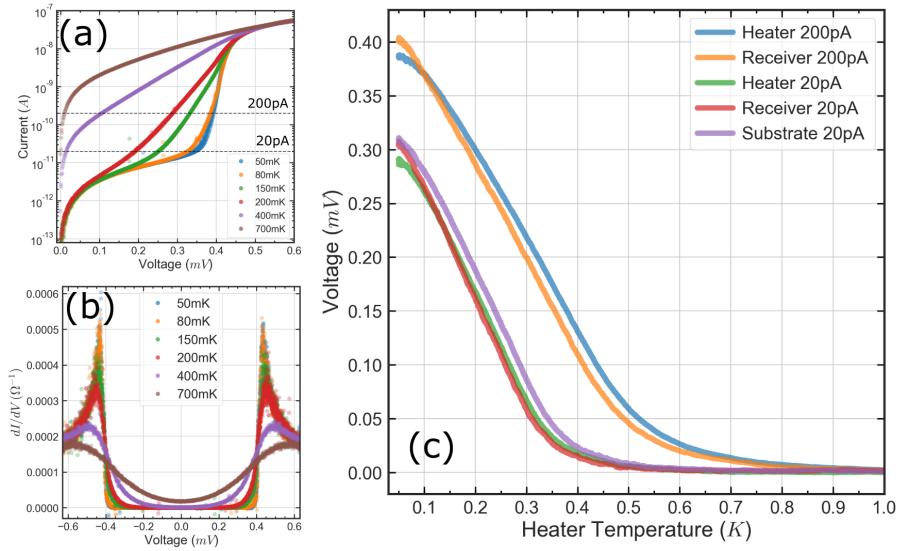

FIGURE 31 (a) IV characteristic and (b) dynamic conductance of a measured SINIS thermometer. (c) a calibrated VT characteristic of the thermometer.

current bias for the desired temperature range. Typical measured IV and tunneling spectroscopic (dI/dV) results are demonstrated in Figure 31(a) and (b), respectively. Usually, two bias values are chosen for their optimal sensitivities to different temperature ranges. A 20 $\sim$ 50 pA current bias has a higher sensitivity for a temperature range $<$ 0.4 K, whereas 100 $\sim$ 200 pA current bias performs better at 0.4 $\sim$ 1 K. A smaller current bias is, in general, preferred in this work, as the self-heating of the thermometer is undesired[11].

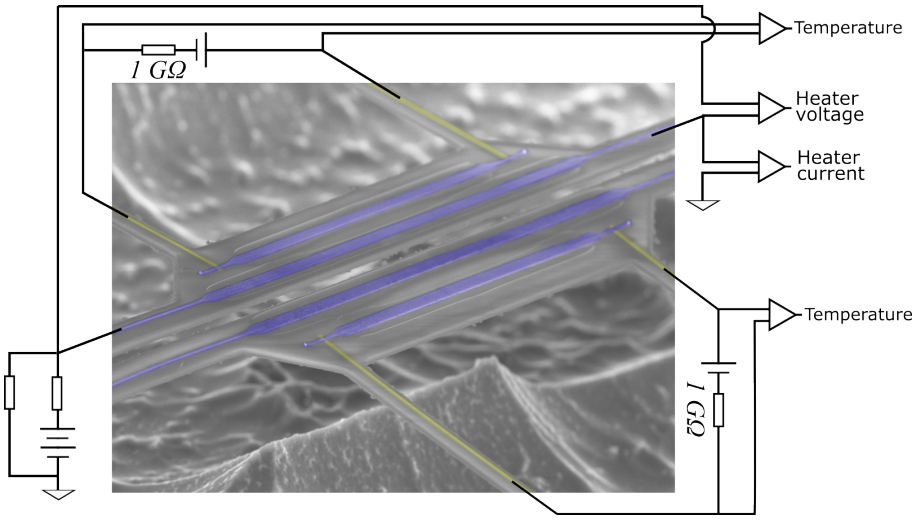

FIGURE 32 The schematic of measurement circuitry.

Next, the electrical instruments for the main measurements will be connected to the device-interface of the plastic dilution refrigerator (PDR), and the circuit configuration is schematically illustrated in Figure 32. All the SINIS thermometers are current-biased by a Zener-diode regulated nickel-metal hydride

11 Nevertheless, the self-heating is taken into account in the analysis.

(NiMH) battery via an 1 GΩ resistor in series, and the bias circuit has a floating configuration isolated from the common ground. The voltage signal of the junction is monitored by a Ithaco 1201 voltage pre-amplifier in a differential mode with a 3 Hz low pass filter. The voltage-to-temperature (VT) response of the thermometers are then calibrated against a commercially calibrated Ge thermistor (GR-200A-30, LakeShore) from 4 K to 50 mK, and the calibration is carried out during a slow cooling process over several hours to ensure a full thermalization between the on-chip thermometers and the Ge thermistor. A calibrated VT response of the example SINIS junction is presented in Figure 31(c).

In the following main and complementary measurements, the temperature of the device stage will be maintained at 60 mK, stablized by a PID controller (Picowatt TS-530). The Joule heating power is supplied to the beam (emitter or receiver, depending on the measurement) by a home-built analog voltage-sweep controller, powered by two 12 V lead-acid batteries. The voltage sweeps slowly between $\pm 1 \sim \pm 10$ V, with the voltage on the sample depending on the choice of the voltage division circuit, and the peak-to-peak time is usually about 30 minutes.

The current and the voltage across the heater junctions is measured using a four-terminal method by a current (Ithaco 1211) and a voltage (Ithaco 1201) pre-amplifiers. The output signals, along with the voltage readout of the thermometers, are collected by a data acquisition system (National Instrument DAQ) and recorded by lab-computer through an optical cable.

4.3.2 Results and discussion

The results of the main measurements are shown in Figure 33, in which the measured temperatures of the emitter T_E (red dots), receiver T_R (orange dots), and the bath T_b (blue dots) are plotted as functions of the Joule heating $\dot{Q}_H$ applied to the emitter beam. In panel (a), the AlN device with 400 nm gap width, and (b), AlN with 500 nm gap width, the rise of the receiver temperatures above the bath temperatures can be observed when their emitters are heated, and the temperature excursions of the receivers are particularly clear at emitter temperatures $T_E > 0.4$ K. Based on the thermal model described in Section 4.1.1, a net power transfer from the emitter to the receiver beam across the vacuum gap can be inferred.

In addition, to confirm that such power transfer is the result of the piezoelectrically mediated heat transfer (PEMHT), the results from the AlN devices are compared with that of the SiN device with 500 nm vacuum gap, as shown in Figure 33(c)[12]. The temperature of the SiN receiver beam exhibits only a small change when the emitter is heated up to close to $T_E = 1$ K, and its difference to the bath temperature is nearly zero. Contrasting with the results measured from the AlN devices, it is evident that piezoelectricity enables the power transfer between the vacuum separated beams, and a conclusion can be stated that the transferred power $\dot{Q}_t$ is significantly enhanced when the material changes from non-piezoelectric to piezoelectric.

[12] The 600 nm gap SiN device has a similar result.

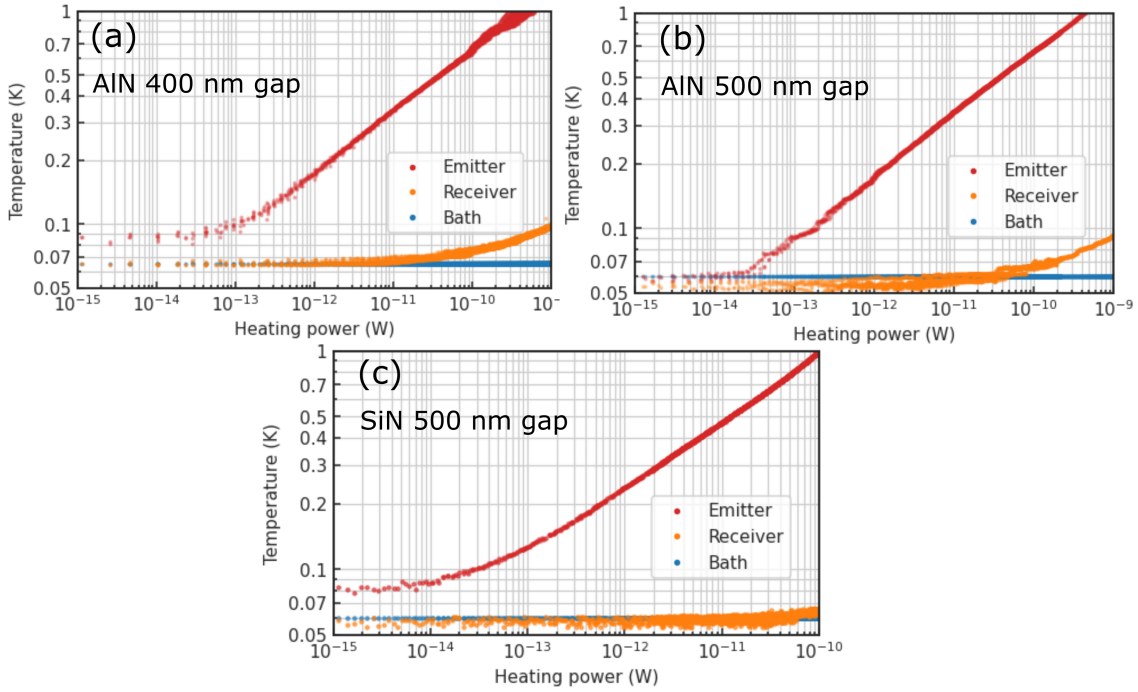

FIGURE 33 Measurement results from the main measurement. The temperature of the thermometers are plotted as function of the heating power.

As has been derived and described in Section 4.1.1, the transferred power $\dot{Q}_t$ can be quantitatively determined from Eq.(178) by using the receiver parameters K_R and n_R. Therefore, additional complementary measurements are performed for each device after the main measurements, to extract the two device parameters by fitting the results using either Eq.(177), or Eq.(176).

The results of both methods are presented in Figure 34, in which panel (a) shows the numerical differentiation $\mathrm{d}\Delta\dot{Q}_H/\mathrm{d}T'_R$ of the data, which is approximately equal to the differential thermal conductance of the beam $G_R(T'_R)$, as a function of the heater temperature T', whereas panel (b) demonstrates the $\Delta\dot{Q}_H$ as a function of T'. Since the devices used in this work have identically designed emitter and receiver beams, as well as their associated heaters and thermometers, the main and complementary measurements can be interchanged, as well as the roles of the emitter and receiver, and thereby the device parameters of both beams can be determined. The T' used here refers to the temperature of the beam that the Joule heating is applied to in the respective complementary measurement. It should also be noted that although the fitting of Eq.(177) requires one less parameter, the numerical differentiation introduces "noise-like" uncertainties into the data, as can be seen from the plot in panel (a), in contrast to the data representing Eq.(176) in panel (b). Nevertheless, the fitting results agree well with each other as demonstrated in the plots, and the following discussion will focus on panel (a).

The heat flow between the beam to the substrate via the respective supporting bridges is dominantly carried by phonons, and the corresponding thermal conductance obtained from the measurement is plotted in Figure 34(a). Based on

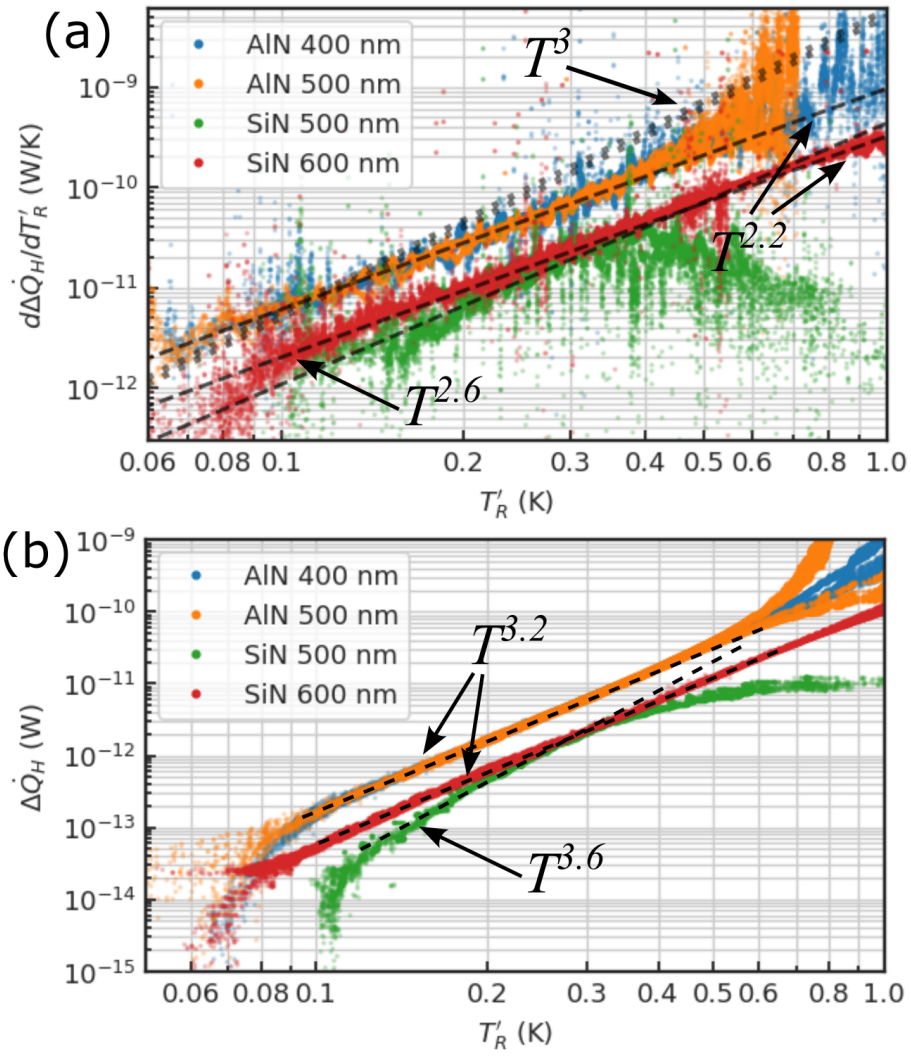

FIGURE 34 The results of the main and complementary heating measurements presented in the form of (a) Eq.(177) and (b) Eq.(176) for extracting the device parameters K_R and n_R. The dotted lines in panel (a) represent the maximum phononic heat conductivity in the ballistic limit.

Eq.(177), the presented thermal conductances are approximately equal to the differential thermal conductance $G(T')$, the first term of the RHS of Eq.(177), since the second term of the RHS is generally several orders of magnitude smaller. In the said plots, the blue and orange points are the measured data from the 400 nm and 500 nm gap width AlN devices including both their emitter and receiver beams, and the red and green points demonstrate both beams from the 500 nm and 600 nm gap SiN devices. One finds that the thermal conductances of the bridges at the temperature range between 0.1 K and 0.7 K are similar for both AlN devices, for example they are about 7×10^{-11} W/K at 0.3 K, and scale with a same power law $\sim T^{2.2}$ of the heater temperature. On the other hand, both SiN devices have a lower thermal conductance, *e.g.* 2×10^{-11} W/K at 0.3 K, but scale differently with temperature as $\sim T^{2.6}$ and $\sim T^{2.2}$ for 500 nm and 600 nm gap widths. All the extracted device parameters K_a and n_a are listed in Table 4, and the black dashed lines in both panels of Figure 34 are guides for the eye with the exponents that are given in the plots.

Device	Beam	Prefactor K (W/K^n)	exponent n
AlN 400nm	Emitter	3.0×10^{-10}	3.2
	Receiver	3.1×10^{-10}	3.2
AlN 500nm	Emitter	3.1×10^{-10}	3.2
	Receiver	2.7×10^{-10}	3.2
SiN 500nm	Emitter	1.2×10^{-10}	3.6
	Receiver	1.2×10^{-10}	3.6
SiN 600nm	Emitter	1.0×10^{-10}	3.2
	Receiver	1.0×10^{-10}	3.2

TABLE 4 Extracted device parameters.

The maximum phononic bulk heat conductivity in the ballistic limit can be expressed as $G_{\max} = 4\sigma A T^3$ [Klitsner et al., 1988; Holmes et al., 1998], where $A = 8\ \mu\text{m}^2$ is the total cross-sectional area of the supporting bridges in the devices presented here, and $\sigma = \sum_\alpha \pi^2 k_B^4 / 120 v_\alpha^2 \hbar^3$ [Swartz and Pohl, 1989] is the phonon blackbody radiation summed for all the bulk modes α. The comparison between the measured thermal conductance at 0.3 K of the devices and those computed in the ballistic limit are listed in Table 5.

	AlN at 0.3 K	SiN at 0.3 K
Computed $G_{\max}$	1.6×10^{-10} W/K	1.4×10^{-10} W/K
Computed $G_{\max}/A$	20 W/m^{2}K	18 W/m^{2}K
Measured G	7×10^{-11} W/K	2×10^{-11} W/K
Measured G/A	8.8 W/m^{2}K	2.5 W/m^{2}K

TABLE 5 Comparison of the computed thermal conductance $G_{\max}$ in the ballistic limit, the computed specific conductance $G_{\max}/A$ in the ballistic limit, the measured thermal conductance G and the measured specific conductance G/A. $A = 8\ \mu\text{m}^2$ is the total cross-sectional area of the supporting bridges in the devices.

With the AlN devices, an upper limit of $G_{\max} = 1.6 \times 10^{-10}$ W/K at 0.3 K can be estimated using the phase velocity values from Tsubouch and Mikoshiba [1985], in which two transversal modes have $v_t = 6016$ m/s and one longitudinal mode $v_l = 7891$ m/s. Similarly, the SiN devices are expected to have an upper limit of $G_{\max} = 1.4 \times 10^{-10}$ W/K at 0.3 K based on $v_t = 6200$ m/s and $v_l = 10300$ m/s from Holmes et al. [1998]. In addition, the heat conductance of ballistic phonons in bulk scales with the temperature as $\sim T^3$, and it is presented in Figure 34(a) as the dotted lines for AlN (top) and SiN (bottom) using the phase velocities given above. In contrast, the dashed lines, representing the measurement results from all the devices, have lower thermal conductances and smaller temperature exponents.

It has been shown by Kühn and Maasilta [2006] that the temperature exponent of the ballistic thermal conductance $(n - 1)$ is 1.5 for two-dimensional (2D) phonon gas in the low-temperature limit. When the temperature increases, the exponent recovers to 3, the three-dimensional (3D) result, in a continuous manner. Meanwhile, when the supporting bridge (2D like) joins the bulk substrate (3D), a strong scattering can occur as the dimension of the structure changes abruptly, and thereby both the conductance and the temperature exponent are modified further [Cross and Lifshitz, 2001; Zhou et al., 2009; Koppinen and Maasilta, 2009]. On the other hand, the extracted temperature exponents of the SiN devices agree well with those measured from SiN membranes [Hoevers et al., 2005; Zen et al., 2014], and the extracted specific heat conductance $G/A = 2.5$ W/m^{2}K at 0.3 K is in agreement with the reported $\sim 2 - 16$ W/m^{2}K for SiN membranes by Holmes et al. [1998] and ~ 2 W/m^{2}K by Zen et al. [2014]. For the AlN devices, to the best of author's knowledge, there are no similar experimental results regarding the heat conductance in the ballistic regime.

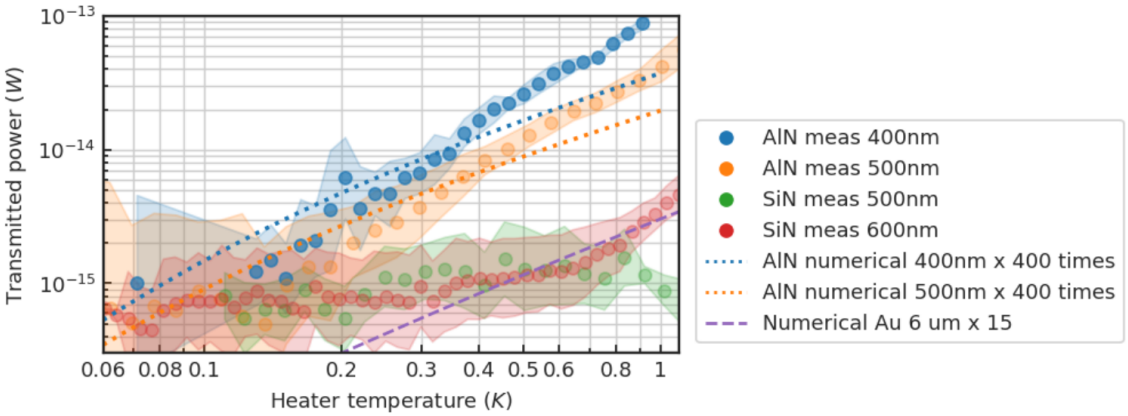

FIGURE 35 Measured transferred heat between two beams determined using Eq.(178). The standard deviation errors are presented as the colour-shadowed areas.

With the extracted device parameters listed in Table 4, the power transferred between the two vacuum separated beams $\dot{Q}_t$ can be determined using Eq.(178). The results are presented in Figure.35, in which the 400 nm and the 500 nm gap width AlN devices are plotted using blue and orange points, respectively, and the 500 nm and 600 nm gap SiN devices are plotted with green and red points,

respectively. There are clear differences in the transferred powers between the two AlN devices. For example at 0.3 K, the 400 nm gap AlN device has a transferred power of 7×10^{-15} W across the vacuum, whereas the 500 nm gap device has 4×10^{-15} W. Such differences can be observed over all the measured temperatures, and imply that the underlying heat transfer mechanism depends strongly on the vacuum width. These results qualitatively agree with the PEMHT discussed in Section 3.5, which states that strong phonon tunneling can be achieved when the separation of the piezoelectric solids is less than the length scale of the characteristic phonon wavelength, *i.e.* about $\lambda_T \approx 1$ μm for the transverse phonon in AlN ($v \approx 6000$ m/s) at 0.3 K, as computed from Eq.(171), and that the transferred heat depends exponentially on the vacuum gap width. Conversely, a direct phonon transport is mainly ballistic at low temperatures, and the associated power transfer is determined mostly by the interface scattering, rather than the distance in the heat flow direction.

In contrast, the two SiN devices appear to have a similar transferred power, roughly $\sim 1 \times 10^{-15}$ W, much smaller than the AlN devices, and it exhibits no clear dependency on the gap width. It is reasonable to attribute such results to the fact that SiN is non-piezoelectric, and thereby is incapable of enabling the PEMHT. Meanwhile, the near-field radiative heat transfer (NFRHT) of SiN is strongly suppressed at such low temperatures, since the surface phonon-polariton frequency is at $10 \sim 30$ THz[Cataldo et al., 2012], three orders of magnitude higher than the dominant phonon frequency ($\hbar\omega_{\text{dom}} \approx 2.8 k_B T$[Ziman, 1960]) at sub-Kelvin temperatures, *i.e.* 17 GHz at 0.3 K, leading to an estimated NFRHT of $< 10^{-18}$ W. As a result, the comparison between the SiN and AlN devices in Figure.35 strengthens the conclusion of the presence of piezoelectrically mediated acoustic phonon tunneling.

However, there is still a finite transferred power observed in the measurement results from the SiN devices, contradicting the expectation. Such power seems to saturate at about 8×10^{-16} W when the emitter temperature is below 0.3 K, and the data exhibits a large uncertainty (the shadow areas). This likely reflects that the precision of the measurements are limited at the femtowatt level, and the possible error sources can be the noise from the room temperature electronics and the tunnel junctions, as well as the fluctuations of the bath temperature from the PID controller. However, above 0.3 K, there is a clear increase in the transferred power, which could possibly be due to the NFRHT between the Au leads that reside on each of the beams. The closest pair of Au leads across the vacuum are separated by 6 μm and each has a nominal thickness of 70 nm. This gives rise to an estimated 4×10^{-17} W transferred power at 0.3 K, using a plane-plane NFRHT model [Joulain et al., 2005]. Such a value could be an underestimation, however, since the thickness of the Au lead is much smaller than the characteristic wavelength of the photon at the temperature in question, thereby breaking the plane-plane picture [Thompson et al., 2018]. Because the Au leads are identically designed for all devices, the same contributions from the Au NFRHT are applicable to all four devices, and seem to become the dominant power transfer mechanism for the SiN device at temperatures > 0.3 K. However, this Au NFRHT

mechanism is much weaker than that of PEMHT, judging from the measurement results, and these observations of the SiN devices will not undermine the conclusion of the presence of PEMHT in the AlN devices.

Quantitatively, the two AlN beams can be described as two identically rotated piezoelectric crystals with an orientation angle $\vartheta = 90^\circ$, following the crystal rotation method described in Section 2.1.5[13], and the PEMHT between them can thus be theoretically estimated using Eq.(169) with a plane-plane area of $A = 124 \times 0.5\,\mu\text{m}^2$ (length$\times$thickness), based on the device design. However, such calculated transferred power levels are two orders of magnitude smaller than the actual measured results demonstrated in Figure.35, where the theoretically estimated values are shown multiplied by a common factor of 400, plotted as blue and orange dotted lines corresponding to the 400 nm and 500 nm gap devices, respectively.

Such a big discrepancy between the experimental results and the theoretical estimations could be attributed to several possible reasons. The first obvious one is the breaking of the plane-plane geometry assumption, which has been taken in the theoretical work here. The thickness of the suspended AlN beam (500 nm) is significantly smaller than the other two dimensions (124 μm $\times$ 10 μm), making the beam a more 2D-like structure. Furthermore, at the lowest temperatures, the characteristic wavelength of thermal phonons can be even longer than the thickness, *e.g.* $\lambda_T > 500$ nm at temperature lower than 0.5 K. As a result, the power transmittance $\mathcal{T}$ from Eq.(165) could be strongly modified due to the breaking of the plane-plane geometry assumption. What is more intriguing is that it has been shown both theoretically [Fernández-Hurtado et al., 2018] and experimentally [Thompson et al., 2018] that far-field radiative heat transfer can in fact be enhanced by hundred-fold between two thin SiN plates with sub-wavelength thickness at room temperature. Similar effect has not yet been investigated for the acoustic phonon tunneling between the piezoelectric solids.

In addition, due to the thickness being in the sub-wavelength regime, the bulk wave assumption[14] also needs to be revised, since for thin plates the group velocities differ from the bulk modes. Different phonon modes, for example different *Lamb modes*[Auld, 1990; Graff, 1991], can be excited and contribute to heat transport.

Moreover, a possible presence of the acoustic gap waves can also contribute to the enhanced heat transfer. Darinskii and Weihnacht [2006] investigated the gap waves between two identical piezoelectric semi-infinite planes, and demonstrated the excitation conditions of the gap waves. On the other hand, Pendry et al. [2016] and Volokitin [2020] studied the contributions of the Rayleigh surface wave to the acoustic wave tunneling between two non-piezoelectric solids,

[13] In regard to the other two rotation angles, φ is equivalent to the incident phonon azimuth angle and thus will be taken into account in the heat flux calculation, whereas ψ is omitted due to the uniaxial symmetry of the AlN crystal.

[14] In a thick solid, higher order plate phonon modes converge to the bulk modes, and the *average group velocities* [Zen et al., 2014] of all the elastic modes resemble the velocities of the bulk wave.

and Volokitin [2020] suggested that the heat transfer due to the surface wave coupling can be of the same order than the bulk waves. Meanwhile, this work also concludes that the evanescent partial modes which propagate along the surfaces enhance the phonon tunneling (see Section.3.3.2), and a complete tunneling of the incident phonon can be achieved when the reflected bulk partial modes vanish (see Section.3.4.3). In particular, at such complete tunneling, the reflected coupled-wave strongly resembles the Rayleigh-type surface wave (see Figure 15), and the resonant tunneling condition Eq.(155) can also be related to the gap wave condition Eq.(164) as a *leaky* gap wave.

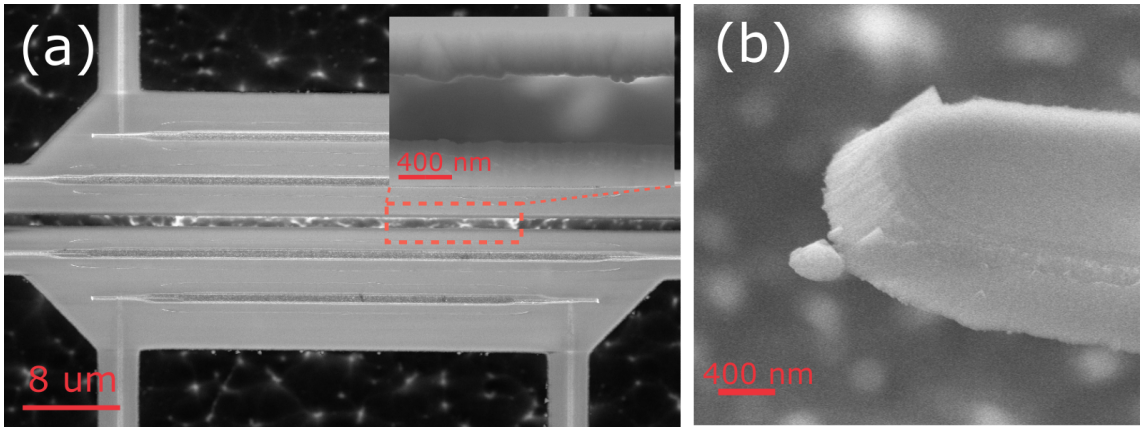

FIGURE 36 Rough edges of the chemically etched AlN.

It is then maybe possible to excite the real (non-leaky) gap waves in the AlN devices of this work, since the coupling between the thermal phonons and the gap modes can perhaps be enabled on the rough side-surfaces of the suspended beams. These rough surfaces were created via the chemical etching process of the AlN crystal, as shown in Figure 36. Indeed, a similar effect has been studied for NFRHT, in which the surfaces roughness allows the coupling between the propagating waves and the surface phonon polaritons, leading to enhanced heat transfer Biehs and Greffet [2010]; Xu et al. [2019].

In conclusion, the measurement results of the transferred heat between two vacuum separated piezoelectric beams are not quantitatively agreeing with the numerical estimations, which are computed from the PEMHT theory developed in this work. The discrepancy is most likely caused by the simplifications used in the model assumptions, namely the bulk wave assumption, the semi-infinite plane assumption, and the assumption of omitting of the coupling between the thermal phonons and the gap waves. Nevertheless, these results, in contrast with the results measured from non-piezoelectric beams, qualitatively demonstrated the presence of heat transfer associated with acoustic phonon tunneling between piezoelectric solids, which is one of the core arguments of this work.

5 SUMMARY

Acoustic phonon tunneling between vacuum-separated solids is an intriguing and not well-understood phenomenon. In this work, both theoretical and experimental studies were carried out to investigate piezoelectrically mediated acoustic phonon tunneling and the associated heat transfer for arbitrarily oriented and anisotropic crystals.

Chapter 2 set the foundations for the theory developed in this work, introduced the basic terminologies, definitions and formulations that were used in this dissertation. The most crucial part of that chapter was the introduction and discussions of the main aspects of the *extended Stroh formalism* (Section.2.3), which is an elegant and powerful mathematical tool to solve the scattering of an electroacoustic wave on the solid-vacuum interface. In particular, several important properties and propositions, which have been used for developing the theory of acoustic phonon tunneling, were derived and presented. In addition, the general crystal rotation method (Section.2.1.5), especially for the piezoelectric crystal (Section.2.2.3) was explained, since this work intends to provide a general formalism applicable to arbitrarily oriented and anisotropic crystals.

The theoretical part of the work was presented in Chapter 3. This chapter begun with a short review of the topic (Section.3.1), and then provided two approaches to solve the reflection and transmission coefficients for all partial wave modes for the acoustic wave tunneling: one was a direct solution of the boundary conditions (Section 3.2.2), the other was based on the physical picture of multiple reflections of the evanescent modes in the vacuum gap (Section 3.2.3). The usefulness and the workflow of these approaches were demonstrated with an explicit analytical solution, and a more general numerical example for two adjacent wurtzite ZnO crystals, in Section 3.3. An interesting observation in the latter example pointed out that there exist strongly enhanced, close to unity transmissions of the acoustic phonon tunneling with an incoming slow transverse wave. This part of the work has been published in Ref.[Geng and Maasilta, 2022a].

By advancing this formalism, three simple yet important relations [Eqs.(136), (147) and (151)] regarding the scattering coefficients were discovered in Section 3.4.1. With these relations, the observed enhancement was then shown to be an

exact *unity* transmission, and it was analytically proven. In particular, such *complete acoustic phonon tunneling* was found to be a resonant pehnomenon, with a simple resonance condition Eq.(155). In addition, the scattering coefficient $\bar{r}_V$ that dictates the resonance condition was discovered to be a material parameter in Section 3.4.2, and it relates to the *TM-wave surface impedance* [Eq.(158)] and the *effective surface permittivity* [Eq.(159)], and can also be used as a condition for finding gap waves [Eq.(164)]. This part of the theory development was then concluded with a set of demonstrations of numerical examples in Section 3.4.3. Not only the unity transmission and where to find them were presented, but the underlying physics of the resonant tunneling was discussed, with a close look on the partial modes and the associated power transfer. This part of the work appears in manuscript A.II [Geng and Maasilta, 2022b].

At the last part of the theoretical modeling, the formalism developed in this work was utilized to derive the heat flux of thermal phonon tunneling between adjacent piezoelectric solids (Section.3.5). It was found that such *piezoelectrically mediated heat transfer* (PEMHT) depends strongly on the length scale of the characteristic phonon wavelength λ_T and the gap width d, and only has a significant effect when $d < \lambda_T$. The numerical examples in Section 3.5.2 demonstrated the PEMHT as a function of gap width and temperature. In particular, the PEMHT was shown to decay with gap distance much more slowly than those of other acoustic phonon tunneling mechanisms, and can dominate the heat transfer at cryogenic temperature ranges over other near-field heat transfer mechanisms enabled by photon and phonon tunneling. This part of the work appears in manuscript A.III [Geng and Maasilta, 2023b].

The experimental part of the work was presented in Chapter 4 and in manuscript A.IV [Geng and Maasilta, 2023a]. The methodology of the experiment was explained first in Section 4.1.1. To be brief, a qualitative demonstration of the presence of PEMHT was carried out in the *main measurement*, which showed that heating of one suspended beam increases the temperature of another vacuum separated suspended beam. A following *complementary measurement*, in which reciprocal heating was applied, was performed to quantitatively extract the heat flux that was associated with phonon tunneling. The core devices and instruments of the experiment, the superconducting junction heaters and thermometers (Section 4.1.2) and the cryostat (Section 4.1.3), were also briefly introduced as part of the methods. After that, the design (Section 4.2.1) and fabrication (Section.4.2.2) of the devices that have been measured in the experiment were described.

Finally, the measurement procedures (Section 4.3.1) and results (Section 4.3.2) were presented and discussed. In the main measurements, upon heating one of the suspended beams, the temperature rise of the unheated beam was observed in the piezoelectric (AlN) device, but not in the non-piezoelectric device (SiN), which qualitatively demonstrated the presence of PEMHT. However, the quantitatively determined transferred powers did not agree with the estimations based on the theory developed in this work, which led to a number of discussions on the possible causes of the discrepancies at the end of the chapter.

The discrepancy discovered in the experiment calls on improvements of the

theoretical work, and the most straightforward objective is to relax some of the restrictive assumptions of the theory in the future. On the other hand, there are also many intriguing experimental opportunities that can be carried out based on the presented theoretical understanding, for example, quantitatively measuring the heat transfer between larger plane-plane structures, comparing the PEMHT between different piezoelectric materials, demonstrating the resonant tunneling of the acoustic waves, *etc*.

In conclusion, the theoretical and experimental work presented in this dissertation fills in many blanks in the understanding of acoustic phonon tunneling mediated by piezoelectricity. The formalism and the approaches derived in this work set the foundations for many future studies and applications of the electroacoustic wave tunneling, for example, in phononic crystals, thermal switches, phonon focusing, cryogenic near-field thermal imaging, optomechanics, quantum information science and *etc*. With the advances in nanotechnology, the vacuum gap in many state-of-art devices and experiments have already achieved the size where PEMHT is significant. It is the author's genuine hope that this dissertation can contribute to the physical understanding of the phenomena at such length scales, and can attract more attention to this topic.

REFERENCES

Akamatsu, M. and Tanuma, K. (1997). Green's function of anisotropic piezoelectricity. *Proc. R. Soc. Lond. Ser. A*, 453(1958):473–487.

Al'shits, V., Barnett, D., Darinskii, A., and Lothe, J. (1994). On the existence problem for localized acoustic waves on the interface between two piezocrystals. *Wave Motion*, 20(3):233–244.

Al'shits, V., Darinskii, A., and Shuvalov, A. (1989). Theory of reflection of acoustoelectric waves in a semiinfinite piezoelectric medium. I.Metallized surface. *Sov. Phys. Crystallogr.*, 6(34):808.

Al'shits, V., Darinskii, A., and Shuvalov, A. (1990). Theory of reflection of acoustoelectric waves in a semiinfinite piezoelectric medium. II.Nonmetallized surface. *Sov. Phys. Crystallogr.*, 1(35):1.

Al'shits, V., Darinskii, A., and Shuvalov, A. (1991). Theory of reflection of acoustoelectric waves in a semiinfinite piezoelectric medium. III. Resonance reflection in the neighborhood of a branch of outflowing waves. *Sov. Phys. Crystallogr.*, 2(36):145.

Al'shits, V., Darinskii, A., and Shuvalov, A. (1993). Acoustoelectric waves in bicrystal media in conditions of a rigid contact or a vacuum gap at an interface. *Crystallogr. Rep.*, 38(2):147–158.

Andrii, T. (2012). High-frequency filtering for low-temperature thermal transport studies in nanostructures. Master's thesis, University of Jyväskylä.

Anghel, D. V., Pekola, J. P., Leivo, M. M., Suoknuuti, J. K., and Manninen, M. (1998). Properties of the Phonon Gas in Ultrathin Membranes at Low Temperature. *Phys. Rev. Lett.*, 81(14):2958–2961.

Ashkenov, N., Mbenkum, B. N., Bundesmann, C., Riede, V., Lorenz, M., Spemann, D., Kaidashev, E. M., Kasic, A., Schubert, M., Grundmann, M., Wagner, G., Neumann, H., Darakchieva, V., Arwin, H., and Monemar, B. (2003). Infrared dielectric functions and phonon modes of high-quality ZnO films. *J. Appl. Phys.*, 93(1):126–133.

Auld, B. (1990). *Acoustic Fields and Waves in Solids*. Krieger, Malabar, second edition.

Auld, B. A. (1969). Application of Microwave Concepts to the Theory of Acoustic Fields and Waves in Solids. *IEEE Trans. Microw. Theory Techn.*, 17(11):800–811.

Balakirev, M., Bogdanov, S., and Gorchakov, A. (1978). Tunneling of an ultrasonic wave across a gap between lithium iodate crystals. *Sov. Phys. Solid state*, 20:338.

Balakirev, M. and Gorchakov, A. (1977). Leakage of an elastic wave across a gap between piezoelectrics. *Sov. Phys. Solid State*, 19(19):327.

Barnett, D. M. and Lothe, J. (1975). Dislocations and line charges in anisotropic piezoelectric insulators. *Phys. Status Solidi B*, 67(1):105–111.

Basu, S., Zhang, Z. M., and Fu, C. J. (2009). Review of near-field thermal radiation and its application to energy conversion. *Int. J. Energy Res.*, 33(13):1203–1232.

Ben-Abdallah, P. (2019). Multitip Near-Field Scanning Thermal Microscopy. *Phys. Rev. Lett.*, 123(26):264301.

Ben-Abdallah, P. and Biehs, S. A. (2014). Near-field thermal transistor. *Phys. Rev. Lett.*, 112(4):1–5.

Bhatt, G. R., Zhao, B., Roberts, S., Datta, I., Mohanty, A., Lin, T., Hartmann, J. M., St-Gelais, R., Fan, S., and Lipson, M. (2020). Integrated near-field thermophotovoltaics for heat recycling. *Nat. Comm.*, 11(1):1–7.

Biehs, S.-A. and Greffet, J.-J. (2010). Near-field heat transfer between a nanoparticle and a rough surface. *Phys. Rev. B*, 81(24):245414.

Biehs, S. A., Kittel, A., and Ben-Abdallah, P. (2020). Fundamental limitations of the mode temperature concept in strongly coupled systems. *Z. Naturforsch.*, 75(9):803–807.

Born, M., Wolf, E., and Bhatia, A. B. (1999). *Principles of Optics: Electromagnetic Theory of Propagation, Interference, and Diffraction of Light*. Cambridge University Press, seventh edition.

Budaev, B. V. and Bogy, D. B. (2011). On the role of acoustic waves (phonons) in equilibrium heat exchange across a vacuum gap. *Appl. Phys. Lett.*, 99:053109.

Cataldo, G., Beall, J. A., Cho, H.-M., McAndrew, B., Niemack, M. D., and Wollack, E. J. (2012). Infrared dielectric properties of low-stress silicon nitride. *Opt. Lett.*, 37(20):4200.

Chadwick, P. and Smith, G. D. (1977). Foundations of the Theory of Surface Waves in Anisotropic Elastic Materials. *Adv. Appl. Mech.*, 17(C):303–376.

Chapuis, P.-O., Volz, S., Henkel, C., Joulain, K., and Greffet, J.-J. (2008). Effects of spatial dispersion in near-field radiative heat transfer between two parallel metallic surfaces. *Phys. Rev. B*, 77(3):035431.

Chen, R., Hochbaum, A. I., Murphy, P., Moore, J., Yang, P., and Majumdar, A. (2008). Thermal Conductance of Thin Silicon Nanowires. *Phys. Rev. Lett.*, 101(10):105501.

Chung, M. Y. and Ting, T. C. T. (1995). Line Force, Charge, and Dislocation in Anisotropic Piezoelectric Composite Wedges and Spaces. *J. Appl. Mech.*, 62(2):423–428.

Court, I. N. and von Willisen, F. K. (1964). Frustrated Total Internal Reflection and Application of Its Principle to Laser Cavity Design. *Appl. Opt.*, 3(6):719.

Cross, M. C. and Lifshitz, R. (2001). Elastic wave transmission at an abrupt junction in a thin plate with application to heat transport and vibrations in mesoscopic systems. *Phys. Rev. B*, 64(8).

Cui, J., Zhang, J., Barayavuga, T., Wang, X., He, X., Yang, L., Xie, H., Mei, X., and Wang, W. (2017). Nanofabrication with the thermal AFM metallic tip irradiated by continuous laser. *Integr. Ferroelectr.*, 179(1):140–147.

Darinskii, A. N. (1997). On the theory of leaky waves in crystals. *Wave Motion*, 25(1):35–49.

Darinskii, A. N. (1998). Leaky waves and the elastic wave resonance reflection on a crystal-thin solid layer interface. II. Leaky waves given rise to by exceptional bulk waves. *J. Acoust. Soc. Am.*, 103(4):1845–1854.

Darinskii, A. N. and Shuvalov, A. L. (2019). Existence of surface acoustic waves in one-dimensional piezoelectric phononic crystals of general anisotropy. *Phys. Rev. B*, 99(17):174305.

Darinskii, A. N. and Weihnacht, M. (2003). Quasi-bulk surface and leaky waves in piezoelectrics of unrestricted symmetry. *Proc. R. Soc. Lond. Ser. A*, 459(2040):2977–2996.

Darinskii, A. N. and Weihnacht, M. (2006). Gap acousto-electric waves in structures of arbitrary anisotropy. *IEEE Trans. Ultrason. Ferroelectr. Freq. Control*, 53(2):412–419.

Every, A. G. and Neiman, V. I. (1992). Reflection of electroacoustic waves in piezoelectric solids: Mode conversion into four bulk waves. *J. Appl. Phys.*, 71(12):6018–6024.

Ezzahri, Y. and Joulain, K. (2014). Vacuum-induced phonon transfer between two solid dielectric materials: Illustrating the case of Casimir force coupling. *Phys. Rev. B*, 90(11):1–7.

Fernández-Hurtado, V., Fernández-Domínguez, A. I., Feist, J., García-Vidal, F. J., and Cuevas, J. C. (2018). Super-Planckian far-field radiative heat transfer. *Phys. Rev. B*, 97(4):1–11.

Fiorino, A., Zhu, L., Thompson, D., Mittapally, R., Reddy, P., and Meyhofer, E. (2018). Nanogap near-field thermophotovoltaics. *Nat. Nanotechnol.*, 13(9):806–811.

Fong, K. Y., Li, H. K., Zhao, R., Yang, S., Wang, Y., and Zhang, X. (2019). Phonon heat transfer across a vacuum through quantum fluctuations. *Nature*, 576(7786):243–247.

Geng, Z. and Maasilta, I. J. (2022a). Acoustic wave tunneling across a vacuum gap between two piezoelectric crystals with arbitrary symmetry and orientation. *Phys. Rev. Research*, 4(3):033073.

Geng, Z. and Maasilta, I. J. (2022b). Complete tunneling of acoustic waves between piezoelectric crystals. arXiv:2209.08287.

Geng, Z. and Maasilta, I. J. (2023a). Experimental demonstration of heat transfer mediated by acoustic phonon tunneling between vacuum separated piezoelectric solids.

Geng, Z. and Maasilta, I. J. (2023b). Heat transfer across vacuum gap induced by piezoelectricity mediated acoustic phonon tunneling. arXiv:2303.05084.

Giazotto, F., Heikkilä, T. T., Luukanen, A., Savin, A. M., and Pekola, J. P. (2006). Opportunities for mesoscopics in thermometry and refrigeration: Physics and applications. *Rev. Mod. Phys.*, 78(1):217–274.

Goldstein, H., Poole, C. P., and Safko, J. L. (2011). *Classical Mechanics*. Pearson, third edition.

Graff, K. F. (1991). *Wave Motion in Elastic Solids*. Dover Publications, revised edition.

Griffiths, D. J. and Schroeter, D. F. (2018). *Introduction to Quantum Mechanics*. Cambridge University Press, third edition.

Guha, B., Otey, C., Poitras, C. B., Fan, S., and Lipson, M. (2012). Near-Field Radiative Cooling of Nanostructures. *Nano Lett.*, 12(9):4546–4550.

Hoevers, H. F. C., Ridder, M. L., Germeau, A., Bruijn, M. P., De Korte, P. A. J., and Wiegerink, R. J. (2005). Radiative ballistic phonon transport in silicon-nitride membranes at low temperatures. *Appl. Phys. Lett.*, 86(25):1–3.

Holmes, W., Gildemeister, J. M., Richards, P. L., and Kotsubo, V. (1998). Measurements of thermal transport in low stress silicon nitride films. *Appl. Phys. Lett.*, 72(18):2250–2252.

Hwu, C. (2008). Some explicit expressions of extended Stroh formalism for two-dimensional piezoelectric anisotropic elasticity. *Int. J. Solids Struct.*, 45(16):4460–4473.

Ingebrigtsen, K. A. (1969). Surface waves in piezoelectrics. *J. Appl. Phys.*, 40(7):2681–2686.

Jones, A. C. and Raschke, M. B. (2012). Thermal infrared near-field spectroscopy. *Nano Lett.*, 12(3):1475–1481.

Joulain, K., Mulet, J.-P., Marquier, F., Carminati, R., and Greffet, J.-J. (2005). Surface electromagnetic waves thermally excited: Radiative heat transfer, coherence properties and Casimir forces revisited in the near field. *Surf. Sci. Rep.*, 57(3-4):59–112.

Kaliski, S. (1966). The passage of an ultrasonic wave across a contactless junction between two piezoelectric bodies. *Proc. Vibr. Probl. Warsaw*, 7:95.

Karvonen, J. T., Taskinen, L. J., and Maasilta, I. J. (2005). Observation of disorder-induced weakening of electron-phonon interaction in thin noble-metal films. *Phys. Rev. B*, 72(1):012302.

Kim, K., Song, B., Fernández-Hurtado, V., Lee, W., Jeong, W., Cui, L., Thompson, D., Feist, J., Reid, M. T., García-Vidal, F. J., Cuevas, J. C., Meyhofer, E., and Reddy, P. (2015). Radiative heat transfer in the extreme near field. *Nature*, 528(7582):387–391.

Kittel, A., Wischnath, U. F., Welker, J., Huth, O., Rüting, F., and Biehs, S.-A. (2008). Near-field thermal imaging of nanostructured surfaces. *Appl. Phys. Lett.*, 93(19):193109.

Klitsner, T., Vancleve, J. E., Fischer, H. E., and Pohl, R. O. (1988). Phonon radiative heat transfer and surface scattering. *Phys. Rev. B*, 38(11):7576–7594.

Kloppstech, K., Könne, N., Biehs, S. A., Rodriguez, A. W., Worbes, L., Hellmann, D., and Kittel, A. (2017). Giant heat transfer in the crossover regime between conduction and radiation. *Nat. Commun.*, 8:1–6.

Koppinen, P. J. and Maasilta, I. J. (2009). Phonon cooling of nanomechanical beams with tunnel junctions. *Phys. Rev. Lett.*, 102(16):012025.

Kühn, T. and Maasilta, I. (2006). Ballistic phonon transport in dielectric membranes. *Nucl. Instrum. Methods. Phys. Res. B NUCL INSTRUM METH A*, 559(2):724–726.

Leivo, M. M., Pekola, J. P., and Averin, D. V. (1996). Efficient Peltier refrigeration by a pair of normal metal/insulator/superconductor junctions. *Appl. Phys. Lett.*, 68(14):1996–1998.

Liang, J., Han, J., Wang, B., and Du, S. (1995). Electroelastic modelling of anisotropic piezoelectric materials with an elliptic inclusion. *Int. J. Solids and Struct.*, 32(20):2989–3000.

Lothe, J. and Barnett, D. M. (1976). Integral formalism for surface waves in piezoelectric crystals. Existence considerations. *J. Appl. Phys.*, 47(5):1799–1807.

Lu, P., Lee, H. P., and Lu, C. (2006). Exact solutions for simply supported functionally graded piezoelectric laminates by Stroh-like formalism. *Compos. Struct.*, 72(3):352–363.

Lucchesi, C., Cakiroglu, D., Perez, J.-P., Taliercio, T., Tournié, E., Chapuis, P.-O., and Vaillon, R. (2021a). Near-Field Thermophotovoltaic Conversion with High Electrical Power Density and Cell Efficiency above 14%. *Nano Lett.*, 21(11):4524–4529.

Lucchesi, C., Vaillon, R., and Chapuis, P. O. (2021b). Radiative heat transfer at the nanoscale: Experimental trends and challenges. *Nanoscale Horiz.*, 6(3):201–208.

Lyubimov, V. N., Al'shits, V., and Lothe, J. (1980). Body waves and quasi-body surface waves in a semi-infinite piezoelectric medium. *Sov. Phys. Crystallogr.*, 25:16.

Milsom, R. F., Reilly, N. H., and Redwood, M. (1977). Analysis of Generation and Detection of Surface and Bulk Acoustic Waves by Interdigital Transducers. *IEEE Trans. Sonics Ultrason.*, SU-24(3):147–166.

Moore, G. E. (1965). Cramming more components onto integrated circuits. *Electronics*, 38(8):4.

Moore, G. E. (1975). Progress in digital integrated electronics. *IEEE Tech. Digest (International Electron Devices Meeting)*.

Nahum, M., Eiles, T. M., and Martinis, J. M. (1994). Electronic microrefrigerator based on a normal-insulator-superconductor tunnel junction. *Appl. Phys. Lett.*, 65(24):3123–3125.

Nomura, M., Nakagawa, J., Kage, Y., Maire, J., Moser, D., and Paul, O. (2015). Thermal phonon transport in silicon nanowires and two-dimensional phononic crystal nanostructures. *Appl. Phys. Lett.*, 106(14):143102.

Ooi, P., Lee, S., Ng, S., Hassan, Z., and Hassan, H. A. (2011). Far Infrared Optical Properties of Bulk Wurtzite Zinc Oxide Semiconductor. *J. Mater. Sci. Technol.*, 27(5):465–470.

Pak, Y. E. (1992). Linear electro-elastic fracture mechanics of piezoelectric materials. *Int. J. Fract.*, 54(1):79–100.

Pekola, J. and Kauppinen, J. (1994). Insertable dilution refrigerator for characterization of mesoscopic samples. *Cryogenics*, 34(10):843–845.

Pendry, J. B. (1999). Radiative exchange of heat between nanostructures. *J. Phys.: Condens. Matter*, 11(35):6621–6633.

Pendry, J. B., Sasihithlu, K., and Craster, R. V. (2016). Phonon-assisted heat transfer between vacuum-separated surfaces. *Phys. Rev. B*, 94(7):1–10.

Polder, D. and Van Hove, M. (1971). Theory of Radiative Heat Transfer between Closely Spaced Bodies. *Phys. Rev. B*, 4(10):3303–3314.

Prunnila, M. and Meltaus, J. (2010). Acoustic phonon tunneling and heat transport due to evanescent electric fields. *Phys. Rev. Lett.*, 105(12):125501.

Ramiere, A., Volz, S., and Amrit, J. (2017). Heat flux induced blueshift of dominant phonon wavelength and its impact on thermal conductivity. *AIP Adv.*, 7(1):015017.

Reichl, L. E. (2016). *A Modern Course in Statistical Physics*. Wiley, fourth, revised edition.

Rowell, J. M. and Tsui, D. C. (1976). Hot electron temperature in InAs measured by tunneling. *Phys. Rev. B*, 14(6):2456–2463.

Royer, D. and Dieulesaint, E. (2000a). *Elastic Waves in Solids, Free and guided propagation*. Advanced Texts in Physics. Springer.

Royer, D. and Dieulesaint, E. (2000b). *Elastic Waves in Solids II, Generation, Acousto-Optic Interaction, Applications*. Advanced Texts in Physics. Springer.

Rytov, S. M. (1953). *Theory of Electric Fluctuations and Thermal Radiation*. Academy of Sciences Press.

Sakurai, J. J. and Napolitano, J. (2020). *Modern Quantum Mechanics*. Cambridge University Press, third edition.

Sasihithlu, K., Pendry, J. B., and Craster, R. V. (2017). Van der Waals Force Assisted Heat Transfer. *Z. Naturforsch.*, 72(2):181–188.

Schwab, K., Arlett, J., Worlock, J., and Roukes, M. (2001). Thermal conductance through discrete quantum channels. *Physica E*, 9(1):60–68.

Schwarzenbach, D. (2003). Note on bravais - miller indices. *J. of Appl. Crystallogr.*, 36(5):1270–1271.

Song, B., Fiorino, A., Meyhofer, E., and Reddy, P. (2015). Near-field radiative thermal transport: From theory to experiment. *AIP Adv.*, 5:053503.

Stroh, A. N. (1962). Steady State Problems in Anisotropic Elasticity. *J. Math. Phys.*, 41(1-4):77–103.

Sun, L. and Murthy, J. Y. (2006). Domain size effects in molecular dynamics simulation of phonon transport in silicon. *Appl. Phys. Lett.*, 89(17):171919.

Swartz, E. T. and Pohl, R. O. (1989). Thermal boundary resistance. *Rev. Mod. Phys.*, 61(3):605–668.

Thompson, D., Zhu, L., Mittapally, R., Sadat, S., Xing, Z., McArdle, P., Qazilbash, M. M., Reddy, P., and Meyhofer, E. (2018). Hundred-fold enhancement in far-field radiative heat transfer over the blackbody limit. *Nature*, 561(7722):216–221.

Ting, T. C. T. (1996). *Anisotropic Elasticity: Theory and Applications*. Oxford University Press.

Tsubouch, K. and Mikoshiba, N. (1985). Zero-Temperature-Coefficient SAW Devices on AlN Epitaxial Films. *IEEE Trans. Sonics Ultrason.*, 32(5):634–644.

Viloria, M. G., Guo, Y., Merabia, S., Messina, R., and Ben-Abdallah, P. (2023). Radiative heat exchange driven by the acoustic vibration modes between two solids at the atomic scale. arXiv:2302.00520.

Volokitin, A. I. (2019). Effect of an Electric Field in the Heat Transfer between Metals in the Extreme Near Field. *JETP Lett.*, 109(11):749–754.

Volokitin, A. I. (2020). Contribution of the acoustic waves to near-field heat transfer. *J. Phys.: Conden. Matter*, 32(21).

Volokitin, A. I. and Persson, B. N. (2001). Radiative heat transfer between nanostructures. *Phys. Rev. B*, 63(20):1–11.

Volokitin, A. I. and Persson, B. N. (2004). Resonant photon tunneling enhancement of the radiative heat transfer. *Phys. Rev. B*, 69(4):045417.

Volokitin, A. I. and Persson, B. N. (2007). Near-field radiative heat transfer and noncontact friction. *Rev. Mod. Phys.*, 79(4):1291–1329.

Waldrop, M. M. (2016). The chips are down for Moore's law. *Nature*, 530(7589):144–147.

Wikipedia (2023). Transistor count. [https://en.wikipedia.org/wiki/Transistor_count; accessed 20-Feb-2023].

Xu, D., Bilal, A., Zhao, J., Liu, L., and Zhang, Z. (2019). Near-field radiative heat transfer between rough surfaces modeled using effective media with gradient distribution of dielectric function. *Int. J. Heat Mass Transf.*, 142:118432.

Yashiro, K. and Goto, N. (1978). Analysis of Generation of Acoustic Waves on the Surface of a Semi-Infinite Piezoelectric Solid. *IEEE Trans. Sonics Ultrason.*, 25(3):146–153.

Zen, N., Puurtinen, T. A., Isotalo, T. J., Chaudhuri, S., and Maasilta, I. J. (2014). Engineering thermal conductance using a two-dimensional phononic crystal. *Nat. comm.*, 5:3435.

Zhang, Y., Desbois, J., and Boyer, L. (1992). New method to characterize the surface-generated bulk acoustic waves in piezoelectric substrates. *J. Acoust. Soc. Am.*, 92(5):2499–2508.

Zhou, L.-P., Wang, M.-P., Zhu, J.-J., Peng, X.-F., and Chen, K.-Q. (2009). Effects of dimensionality on the ballistic phonon transport and thermal conductance in nanoscale structures. *J. Appl. Phys.*, 105(11):114318.

Zhu, L., Fiorino, A., Thompson, D., Mittapally, R., Meyhofer, E., and Reddy, P. (2019). Near-field photonic cooling through control of the chemical potential of photons. *Nature*, 566(7743):239–244.

Ziman, J. M. (1960). *Electrons and Phonons: The Theory of Transport Phenomena in Solids*. Clarendon Press, first edition.

ORIGINAL PAPERS

PI

ACOUSTIC WAVE TUNNELING ACROSS A VACUUM GAP BETWEEN TWO PIEZOELECTRIC CRYSTALS WITH ARBITRARY SYMMETRY AND ORIENTATION

by

Z. Geng & I. J. Maasilta 2022

Phys. Rev. Research **4** , 033073

DOI: 10.1103/PhysRevResearch.4.033073

Acoustic wave tunneling across a vacuum gap between two piezoelectric crystals with arbitrary symmetry and orientation

Zhuoran Geng [*] and Ilari J. Maasilta [†]

Nanoscience Center, Department of Physics, University of Jyvaskyla, P. O. Box 35, FIN-40014 Jyväskylä, Finland

(Received 24 March 2022; accepted 27 June 2022; published 25 July 2022)

It is not widely appreciated that an acoustic wave can "jump" or "tunnel" across a vacuum gap between two piezoelectric solids, nor has the general case been formulated or studied in detail. Here, we remedy that situation, by presenting a general formalism and approach to study such an acoustic tunneling effect between two arbitrarily oriented anisotropic piezoelectric semi-infinite crystals. The approach allows one to solve for the reflection and transmission coefficients of all the partial-wave modes, and is amenable to practical numerical or even analytical implementation, as we demonstrate by a few chosen examples. The formalism can be used in the future for quantitative studies of the tunneling effect in connection not only with the manipulation of acoustic waves, but with many other areas of physics of vibrations such as heat transport, for example.

DOI: 10.1103/PhysRevResearch.4.033073

I. INTRODUCTION

Acoustic waves in solids (also known as elastic waves) have many applications ranging from acoustic wave filters for mobile phones, mechanical resonators for sensors, acousto-optical modulators for optical signal processing, to ultrasonic imaging devices, to name a few [1]. They are often generated with the help of piezoelectric (PE) transducers, converting an electrical signal to an acoustic wave, as piezoelectricity couples acoustic deformations and electric fields [2,3]. This also means that the elastic waves in piezoelectric materials are not purely elastic but contain electric waves as a by-product. To be more descriptive, such waves are sometimes also called acoustoelectric or electroacoustic waves. The main very well understood effect of piezoelectricity on the propagation of acoustic waves is that the acoustic velocities are slightly modified, due to the piezoelectric "stiffening" of the effective elastic constants for wave propagation [2,3].

However, when considering wave transmission and reflection problems, another intriguing and much less widely known effect due to piezoelectricity can happen: a bulk elastic wave can be transmitted across a vacuum gap between two piezoelectric solids. This transmission is not possible for purely elastic waves, which by definition cannot exist in vacuum, but is made possible by the evanescent electric-field components of the electroacoustic waves extending into the vacuum gap. The effect works for gap sizes of the order of the acoustic wavelength, which is much longer than the length scale of other possible mechanisms that can couple bulk acoustic wave energy across vacuum gaps in the nanometer to subnanometer scale (such as van der Waals, Casimir, and electrostatic interactions discussed in the context of heat transfer, see Refs. [4–9]). As such, the phenomenon is highly analogous to quantum-mechanical tunneling of a particle through a classically forbidden region, and for this reason, we also call this effect "acoustic wave tunneling" or "phonon tunneling," terminology that was already introduced by others [7–11].

To our knowledge, acoustic wave tunneling mediated by piezoelectricity was first discussed theoretically by Kaliski [12] for the case of horizontally polarized shear (SH) waves in a cubic piezoelectric crystal in the limit of zero gap width. Later, in an important seminal work, Balakirev and Gorchakov [13] extended the calculations for the same SH wave mode for finite gap widths (with the cubic axes aligned with the surfaces). They also provided results for hexagonal crystals with the c_6-symmetry axis oriented parallel to the surfaces, still considering only the SH wave mode, and plotted examples for the transmission coefficient vs incident angle for $Bi_{12}GeO_{20}$ (cubic) and $LiIO_3$ (hexagonal). An important result of that study was that the transmission coefficient was shown to be large and even approaching unity for angles close to glancing incidence. An experimental study by the same authors [10] with ultrasound ($f = 15$ MHz) using $LiIO_3$ crystals confirmed the phenomenon with observed transmission coefficients up to $\approx$0.5.

These early studies used the standard piezoelectrically stiffened elasticity theory [3,14] and were focused on finding explicit solutions, available only for the highest symmetry crystal orientations and for the simplest wave modes, therefore providing only expressions with no generality.

Much more recently, Prunnila and Meltaus revisited the topic in the context of thermal transport using a scattering matrix approach [11] and provided results for energy transmission coefficients as a function of the angle of incidence and wave vector. However, their approach assumed isotropic

[*] zhgeng@jyu.fi
[†] maasilta@jyu.fi

properties of the materials, a simplified single component piezoelectric tensor, no PE stiffening, and the results were limited to a single symmetry direction of the "crystal." Within these approximations only two modes contribute.

On the other hand, to study anisotropic piezoelectric insulators more generally, Barnett and Lothe [15,16] extended the so-called sextic Stroh formalism, an elegant and mathematically powerful tool to analyze anisotropic elasticity [17–20], to an eight-dimensional framework for *arbitrary* anisotropic piezoelectric crystals. This extended Stroh formalism was further developed by several authors [21–26] and has been successfully applied from the analysis of reflection of bulk electroacoustic waves [21–23] and anisotropic piezoelectric surface acoustic waves (SAW) [16,27,28] to the gap waves (GW) [29–31], which are surface waves guided and coupled by a gap between two piezoelectric surfaces [32,33]. It has also been used in material science applications for piezoelectric ceramics and composites [34–36] and recently [37] also to study the control SAW propagation using piezoelectric phononic crystals [38].

Even though the framework of extended piezoelectric Stroh formalism was developed some time ago, only a limited number of investigations have been carried out to study the phenomenon of bulk acoustic wave tunneling. Al'shits *et al.* [29] introduced formally a general solution of reflection and transmission coefficient for an incident slow quasitransverse bulk wave. Later, Darinskii developed this framework further [39,40] and investigated the reflection and transmission mediated by the leaky gap wave [31]. In these studies, only single transmitted bulk wave mode was considered, and the resonance conditions of the leaky gap waves were usually applied.

The purpose of this work is to demonstrate a general formalism and solution for transmission of elastic waves across a vacuum gap that is applicable to any incident bulk wave mode in any anisotropic crystallographic orientation. Furthermore, an alternative approach to the direct solution will be presented. In this method, the scattering problems of semi-infinite piezoelectric half-spaces are solved independently for both crystals using the extended Stroh formalism, and the reflection and transmission coefficients of the tunneling are acquired with a simple factor, which is determined from multiple reflections of evanescent electric waves inside the vacuum gap. To our knowledge, such an interpretation of acoustic wave tunneling has not been discussed in literature, although the multiple reflection picture has been widely adopted in the field of near-field electromagnetic wave tunneling [41–43].

This work is organized as follows: We first briefly introduce the main aspects of the extended Stroh formalism for plane interface scattering problems using generally applicable coordinate setup and plane-wave functions in Sec. II. The tunneling problem for the plane-plane geometry is then solved in Sec. III, first by directly applying the boundary conditions to the Stroh eigenfunctions, then followed by the alternative approach of using multiple reflection factor. In Sec. IV, we then present a few illustrative examples: first an analytical solution for a hexagonal crystal with a high-symmetry orientation derived using both methods, and finally numerical calculations of tunneling transmission coefficients for a couple of different crystallographic cuts of a hexagonal crystal in different orientations. At the end in Sec. V, we present conclusions and outlook on the applications of this study.

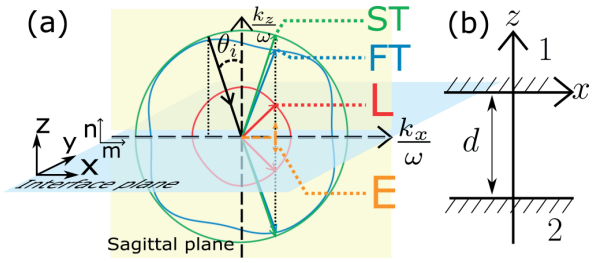

FIG. 1. (a) Schematic of the single interface scattering problem with the coordinate system used, with the interface plane at $z = 0$ and the sagittal plane at $y = 0$. The scattering and mode conversions of an incident bulk slow transverse (ST) wave from the angle θ_i are shown, with a hypothetical set of slowness surfaces. $\boldsymbol{m}$ and $\boldsymbol{n}$ are the unit vectors of the x axis and z axis. Under the quasistatic approximation, four wave modes are shown: longitudinal (L), fast transverse (FT), slow transverse (ST), and quasistatic electric potential (E). (b) Two piezoelectric media 1, 2 are separated by a vacuum gap of width d.

II. EXTENDED STROH FORMALISM FOR SCATTERING PROBLEMS

We consider acoustic waves within the continuum anisotropic linear elasticity theory. A bulk acoustic plane wave with a wave vector $\boldsymbol{k}$ in an anisotropic piezoelectric medium using Cartesian coordinates $\boldsymbol{r} = [x, y, z]^T$ ($[\ldots]^T$ stands for transposition) is incident on an interface plane $\boldsymbol{n} \cdot \boldsymbol{r} = z = 0$ between two media, with a plane of incidence (sagittal plane) $(\boldsymbol{n} \times \boldsymbol{m}) \cdot \boldsymbol{r} = y = 0$, where $\boldsymbol{n}$ is the unit normal vector of the interface plane and $\boldsymbol{m}$ the unit vector parallel to the interface and sagittal planes. With our coordinate system, they are the unit vectors of the z axis and x axis, respectively [see Fig. 1(a)]. Without losing generality, we always consider that the incident bulk wave has a positive x component of the wave vector $k_x > 0$ and propagates in the sagittal plane (the wave vector is contained in the plane), but the sagittal plane has a rotational degree of freedom with respect to the normal of interface plane (z axis).[1] The piezoelectric medium is characterized by its density ρ, piezoelectric stress tensor e_{iL}, elastic stiffness tensor at constant electric field c^E_{KL}, and electric permittivity tensor at constant strain ϵ^S_{ij}, where $i, j = x, y, z$ are the Cartesian coordinate indices and $K, L = 1, \ldots, 6$ are the abbreviated Voigt indices.

The sound velocities $v = \omega/k$ are typically more than four orders of magnitude slower than the speed of light, therefore it is possible and customary to apply the quasistatic approximation [3] to the piezoelectric scattering problems, ignoring the magnetic field. Under such conditions, the propagation of

[1]The sagittal plane has a rotational degree of freedom with respect to the normal of the interface plane (azimuth angle), which is equivalent to the rotation of the crystal azimuth angle φ. For the sake of simplicity and to avoid the duplication of the effect of this degree of freedom, we unambiguously take into account the azimuth angle by the rotation of the crystal (see Appendix F).

a time-harmonic plane wave $\propto \exp(-i\boldsymbol{k}\cdot\boldsymbol{r}+i\omega t)$ with wave vector $\boldsymbol{k}$ and angular frequency ω is governed by the elastic equation of motion $\nabla\cdot\boldsymbol{\sigma}=\rho\partial^2\boldsymbol{u}/\partial t^2$ and just one of the Maxwell's equations (Gauss's law) $\nabla\cdot\boldsymbol{D}=0$, which together with the piezoelectric constitutive relations read in the matrix notation [3]:

$$\begin{aligned} ik_{iK}\sigma_K &= \rho\omega^2 u_i,\\ -ik_iD_i &= 0,\\ \sigma_K &= -ic^E_{KL}k_{Lj}u_j - ie_{Kj}k_j\Phi,\\ D_i &= -ie_{iL}k_{Lj}u_j + i\epsilon^S_{ij}k_j\Phi, \end{aligned} \tag{1}$$

where $\boldsymbol{\sigma}$, $\boldsymbol{u}$, $\boldsymbol{D}$ are the elastic stress, mechanical displacement, and electric displacement fields, respectively, Φ is the electric potential, and k_{iK} is a 3×6 matrix defined by the wave-vector components [3] (see Appendix A for more details). As usual, repeated indices are summed.

An incident plane wave is scattered into a linear combination of partial waves at the interface, which are either reflected or transmitted, and can also be inhomogeneous modes. [An example where three reflected and transmitted homogeneous bulk acoustic waves and an inhomogeneous electric potential wave are generated is depicted in Fig. 1(a).] The general solutions of such partial waves that satisfy the governing equations can be written [21–23] as

$$\begin{aligned} \boldsymbol{u} &= \sum_\alpha b_\alpha \boldsymbol{A}_\alpha e^{-ik_x(x+p_\alpha z)+i\omega t},\\ \Phi &= \sum_\alpha b_\alpha \phi_\alpha e^{-ik_x(x+p_\alpha z)+i\omega t},\\ \boldsymbol{n}\cdot\boldsymbol{\sigma} &= ik_x\sum_\alpha b_\alpha \boldsymbol{L}_\alpha e^{-ik_x(x+p_\alpha z)+i\omega t},\\ \boldsymbol{n}\cdot\boldsymbol{D} &= ik_x\sum_\alpha b_\alpha D^n_\alpha e^{-ik_x(x+p_\alpha z)+i\omega t}, \end{aligned} \tag{2}$$

in which $\boldsymbol{A}_\alpha$, ϕ_α, $\boldsymbol{L}_\alpha$, D^n_α are normalized constants describing the displacement (polarization vector), the electric potential, the traction force and the normal projection of the electric displacement of a partial wave mode α, respectively. b_α is the dimensionless amplitude of the partial wave, and $p\equiv k_z/k_x$ where k_z and k_x are the normal and parallel components of the $\boldsymbol{k}$ vector. To avoid redundant writing in expressions, we omit from now on the common phase factor $\exp(-ik_xx+i\omega t)$ shared by all solutions.

With the above partial-wave formulation, the solution of the governing equations (1) reduces to determining the eigenvalues p_α and eigenvectors $\boldsymbol{\xi}_\alpha$ of an eight-dimensional eigenvalue problem [15,16] with a 8×8 real matrix $\boldsymbol{N}$:

$$\boldsymbol{N}(v_x)\boldsymbol{\xi}_\alpha = p_\alpha\boldsymbol{\xi}_\alpha, \tag{3}$$

where the matrix $\boldsymbol{N}(v_x)$ depends on the phase velocity along the interface $v_x\equiv\omega/k_x$, a conserved quantity due to continuity conditions on the boundary, and the orientation and material of the crystal. The eight-component eigenvector for mode α is defined as $\boldsymbol{\xi}_\alpha=[\boldsymbol{A}_\alpha,\phi_\alpha,\boldsymbol{L}_\alpha,D^n_\alpha]^T$. The derivation of Eq. (3) with the detailed definition of $\boldsymbol{N}(v_x)$ is presented in Appendix B.

The matrix $\boldsymbol{N}$ also satisfies the symmetry relation $(\hat{\boldsymbol{T}}\boldsymbol{N})^T=\hat{\boldsymbol{T}}\boldsymbol{N}$, where the 8×8 matrix $\hat{\boldsymbol{T}}$ is given by

$$\hat{\boldsymbol{T}} = \begin{bmatrix}\hat{\boldsymbol{0}} & \hat{\boldsymbol{I}}\\ \hat{\boldsymbol{I}} & \hat{\boldsymbol{0}}\end{bmatrix},$$

with $\hat{\boldsymbol{I}}$ and $\hat{\boldsymbol{0}}$ the 4×4 unit and zero matrices, respectively [17,18,44]. This relation provides an orthonormalization condition:

$$\boldsymbol{\xi}^T_\alpha\hat{\boldsymbol{T}}\boldsymbol{\xi}_\beta=\delta_{\alpha\beta},\quad \alpha,\beta=1,\ldots,8, \tag{4}$$

where $\delta_{\alpha\beta}$ is the Kronecker delta and ensures a unique and complete set of solutions for the extended Stroh eigenfunction.[2]

At this point it is good to point out that the above "Stroh-normalization", widely used in literature as it is, does not keep the physical units (as $\boldsymbol{\xi}^T_\alpha\hat{\boldsymbol{T}}\boldsymbol{\xi}_\alpha$ has units of force), but introduces computationally useful "Stroh units." This is not a problem, as the units cancel out in the end if transmission and reflection amplitudes are the observables to be calculated.

Totally eight partial-wave mode solutions can be obtained from Eq. (3), containing complex eigenvalues $p_\alpha=p'_\alpha+ip''_\alpha$ and the associated eigenvectors $\boldsymbol{\xi}_\alpha$ with $\alpha=1,\ldots,8$ (with p'_α denoting the real part and p''_α the imaginary part). These partial waves can be either homogeneous plane waves ($p''_\alpha=0$) or inhomogeneous waves ($p''_\alpha\neq 0$). For an inhomogeneous wave mode, the scattering direction of the wave is determined by the imaginary part of the eigenvalue such that if $p''_\alpha>0$ ($p''_\alpha<0$) the wave is transmitted (reflected), to ensure decaying solutions at infinity. For a plane-wave mode, the direction of the power flow normal to the interface is examined. By investigating the time-averaged acoustic Poynting vector component normal to the interface [21]

$$P_{n\alpha}\equiv\boldsymbol{n}\cdot\boldsymbol{P}_{AV,\alpha}=-\frac{\omega k_x}{4}|b_\alpha|^2\boldsymbol{\xi}^T_\alpha\hat{\boldsymbol{T}}\boldsymbol{\xi}^*_\alpha, \tag{5}$$

one can determine which wave mode is transmitted ($P_{n\alpha}<0$) or reflected ($P_{n\alpha}>0$).

If Stroh-normalization is used, Eq. (5) simplifies even further for the bulk modes. For them, the eigenvalues p_α are real, which means that the eigenvectors are real as well, $\boldsymbol{\xi}^*_\alpha=\boldsymbol{\xi}_\alpha$, as $\boldsymbol{N}$ is real. We then have $\boldsymbol{\xi}^T_\alpha\hat{\boldsymbol{T}}\boldsymbol{\xi}^*_\alpha=\boldsymbol{\xi}^T_\alpha\hat{\boldsymbol{T}}\boldsymbol{\xi}_\alpha=1$, and see from Eq. (5) that the power transmission and reflection coefficients (ratios of Poynting vector normal components) are simply given by the ratio $|b_\alpha/b_{in}|^2$. This is one justification for the usefulness of the used Stroh normalization.

[2]The above results are strictly true only if $\boldsymbol{N}$ is nondegenerate (has a nonzero determinant). Slightly modified eigenvectors and normalization conditions have been determined in the opposite case [28] taking place at the exact conditions for a critical angle (transonic state), where the reflected bulk wave carries energy only along the interface. Our discussion is meant for the general case to facilitate numerical computation, thus these conditions are special cases that do not have to be considered here, as numerical computation can be done very close to the exact conditions.

III. BULK ACOUSTIC WAVE TUNNELING ACROSS A VACUUM GAP

To formulate a generalized expression for bulk acoustic wave tunneling across a vacuum gap between two adjacent piezoelectric solids, we consider a geometry which consists of two parallel semi-infinite piezoelectric half spaces (medium 1 and medium 2) separated by a vacuum gap of distance d, as shown in Fig. 1(b). Our modeling is not applicable for nonpiezoelectric solids, or in situations where one or more of the dimensions of the solids are smaller than the acoustic wavelength in question (breakdown of the bulk wave assumption), or when the gap size or solid dimensions are in the atomic length scale (breakdown of continuum elasticity). The incident wave is propagating towards the gap from the positive z-coordinate direction in the sagittal plane, and the two solid-vacuum interfaces are located at $\boldsymbol{n}\cdot\boldsymbol{r}=0$ and $\boldsymbol{n}\cdot\boldsymbol{r}=-d$.

For a given incident wave propagating in a given crystal orientation, the wave vector and phase velocity components along the interface (k_x and v_x) are known. Therefore, the unknowns left in the partial-wave solutions in Eqs. (2) are the eigenvectors $\boldsymbol{\xi}_\alpha$ and eigenvalues p_α of the Stroh eigenequation (3), as well as the amplitude factors b_α. The eigenvectors and eigenvalues can readily be solved with the knowledge of the material, the crystallographic orientation and v_x, whereas the determination of b_α requires solving the boundary conditions of the solid-vacuum interfaces.

We assume for this study that both interfaces are mechanically free and without electrodes or net charge density on the surface, i.e., electrically free. For such a case, there are conditions for the continuity of the electric potential and the normal component of the electric displacement, giving for the boundary conditions

$$\begin{aligned}\Phi^{(i)}&=\Phi_V,\\ \boldsymbol{n}\cdot\boldsymbol{D}^{(i)}&=\boldsymbol{n}\cdot\boldsymbol{D}_V,\\ \boldsymbol{n}\cdot\boldsymbol{\sigma}^{(i)}&=\boldsymbol{0},\end{aligned}\tag{6}$$

in which the superscript $i=1,2$ indicates the medium index and the subscript V represents the fields in the vacuum gap.

In the vacuum region, the electric potential wave must satisfy the Laplace equation $\nabla^2\Phi_V=0$, which for the plane waves leads to the condition $k_x^2+k_z^2=0$. Thus, it can be expressed in terms of two partial wave modes with $k_z=\pm ik_x$. Following the form of the general solutions for the electric potential in Eq. (2) leads to a solution with decaying and increasing exponentials [omitting the common phase factor $\exp(-ik_x x+i\omega t)$]

$$\Phi_V=b_{V_+}\phi_{V_+}e^{k_x z}+b_{V_-}\phi_{V_-}e^{-k_x z},\tag{7}$$

and the normal component of the vacuum electric displacement can then be calculated directly from $\boldsymbol{D}_V=-\epsilon_0\nabla\cdot\Phi_V$, giving

$$\boldsymbol{n}\cdot\boldsymbol{D}_V=-\epsilon_0 k_x b_{V_+}\phi_{V_+}e^{k_x z}+\epsilon_0 k_x b_{V_-}\phi_{V_-}e^{-k_x z}.\tag{8}$$

From the form of solutions above, the analogy with quantum-mechanical tunneling is apparent.

Comparing the result for the electric displacement in Eq. (8) with the definitions of the Stroh formalism, Eqs. (2), we see that the components for the electric displacement $D_{V_\pm}$ and for the potential $\phi_{V_\pm}$ satisfy a simple relation $D_{V_\pm}=\pm i\epsilon_0\phi_{V_\pm}$. In addition, we have $\phi_{V_\pm}=1/\sqrt{\pm 2i\epsilon_0}$, as can be readily calculated from the Stroh-normalization condition $2\phi_{V_\pm}D_{V_\pm}=1$ obtained from Eq. (4) by setting the vacuum eigenvector components associated with the displacement and traction force to zero: $\boldsymbol{A}_{V_\pm}=\boldsymbol{0}, \boldsymbol{L}_{V_\pm}=\boldsymbol{0}$.

By inserting the general solutions of Eqs. (2), (7), and (8) into the boundary conditions in Eqs. (6), we obtain two sets of linear equations to express the boundary conditions at both interfaces as

$$\begin{aligned}b_{in}^{(1)}\boldsymbol{U}_{in}^{(1)}+\sum_{\alpha=1}^{4}b_\alpha^{(1)}\boldsymbol{U}_\alpha^{(1)}&=b_{V_+}\boldsymbol{U}_{V_+}+b_{V_-}\boldsymbol{U}_{V_-},\\ \sum_{\alpha=1}^{4}\tilde{b}_\alpha^{(2)}\boldsymbol{U}_\alpha^{(2)}&=b_{V_+}\boldsymbol{U}_{V_+}e^{-k_x d}+b_{V_-}\boldsymbol{U}_{V_-}e^{k_x d},\end{aligned}\tag{9}$$

in which we introduce a 5×1 column vector $\boldsymbol{U}_\gamma^{(i)}=[\phi_\gamma^{(i)},D_\gamma^{n,(i)},\boldsymbol{L}_\gamma^{(i)}]^T$ for the wave mode $\gamma=in,\alpha$, where the subscript in indicates the incident wave mode, $\alpha=1,\ldots,4$ corresponds to the four physically allowed wave modes in the corresponding media $i=1,2$ (the reflected and transmitted modes, respectively), and $\tilde{b}_\alpha^{(2)}\equiv b_\alpha^{(2)}\exp(ip_\alpha^{(2)}k_x d)$. As $\boldsymbol{U}_\gamma^{(i)}$ are known and defined by the Stroh eigenvectors (more explicit expressions can be found in Appendix C), Eqs. (9) can be used to solve for the partial-wave amplitudes $b_\alpha^{(i)}$, $b_{V_\pm}$, giving us finally the transmission and reflection amplitude coefficients $t_\alpha^{(2)}\equiv\tilde{b}_\alpha^{(2)}/b_{in}^{(1)}$ and $r_\alpha^{(1)}\equiv b_\alpha^{(1)}/b_{in}^{(1)}$.

We have considered two approaches to solve Eqs. (9): First, by directly solving the combined boundary conditions of both interfaces with matrix algebra, and second, by using a multiple reflection factor to connect the separate solutions on each interface. Both approaches are discussed in the following and give identical results. The choice of the method should be based on which parameters are to be varied: In the case where the incident wave is a variable, the first combined boundary-condition method is more efficient, whereas if the gap size is a variable, the second multiple reflection amplitude method is more practical, as will become clearer below.

A. Combined boundary conditions approach

In the first approach, where the boundary conditions are solved directly, we introduce two 8×5 matrices $\boldsymbol{M}_1$ and $\boldsymbol{M}_2$:

$$\boldsymbol{M}_1=\begin{bmatrix}\boldsymbol{V}_1^{-1}&\hat{\boldsymbol{O}}_{(2\times 3)}\\ \hat{\boldsymbol{O}}_{(3\times 2)}&\hat{\boldsymbol{I}}_{(3)}\\ \hat{\boldsymbol{O}}_{(3\times 2)}&\hat{\boldsymbol{O}}_{(3\times 3)}\end{bmatrix},\quad \boldsymbol{M}_2=\begin{bmatrix}\boldsymbol{V}_2^{-1}&\hat{\boldsymbol{O}}_{(2\times 3)}\\ \hat{\boldsymbol{O}}_{(3\times 2)}&\hat{\boldsymbol{O}}_{(3\times 3)}\\ \hat{\boldsymbol{O}}_{(3\times 2)}&\hat{\boldsymbol{I}}_{(3)}\end{bmatrix},\tag{10}$$

in which $\hat{\boldsymbol{O}}_{(m\times n)}$ and $\hat{\boldsymbol{I}}_{(m)}$ are the $m\times n$ zero matrix and the $m\times m$ identity (unit) matrix. $\boldsymbol{V}_1$, $\boldsymbol{V}_2$ are 2×2 matrices depending only on the wave-vector component k_x along the interface and the size of vacuum gap d:

$$\boldsymbol{V}_1=\begin{bmatrix}\phi_{V+}&\phi_{V-}\\ D_{V+}&D_{V-}\end{bmatrix},\quad \boldsymbol{V}_2=\begin{bmatrix}\phi_{V+}e^{-k_x d}&\phi_{V-}e^{k_x d}\\ D_{V+}e^{-k_x d}&D_{V-}e^{k_x d}\end{bmatrix},$$

as we recall that both $D_{V_\pm}$ and $\phi_{V_\pm}$ are simply set by the vacuum permittivity ϵ_0: $D_{V_\pm}=\pm i\epsilon_0\phi_{V_\pm}$, $\phi_{V_\pm}=1/\sqrt{\pm 2i\epsilon_0}$.

With the above definitions, the boundary conditions in Eqs. (9) can then be written in the following compact form (the detailed derivation can be found in Appendix C):

$$\boldsymbol{M}\big[b_1^{(1)},\ldots,b_4^{(1)},\tilde{b}_1^{(2)},\ldots,\tilde{b}_4^{(2)}\big]^T=-\boldsymbol{M}_1\boldsymbol{U}_{in}^{(1)}b_{in}^{(1)},$$

where $\boldsymbol{M}$ is a 8×8 matrix constructed by joining four ($\alpha=1\ldots4$) $\boldsymbol{M}_1\boldsymbol{U}_\alpha^{(1)}$ and four $-\boldsymbol{M}_2\boldsymbol{U}_\alpha^{(2)}$ 8×1 column vectors together as

$$\begin{aligned}\boldsymbol{M}=\big[&\boldsymbol{M}_1\boldsymbol{U}_1^{(1)},\boldsymbol{M}_1\boldsymbol{U}_2^{(1)},\boldsymbol{M}_1\boldsymbol{U}_3^{(1)},\boldsymbol{M}_1\boldsymbol{U}_4^{(1)},\\&-\boldsymbol{M}_2\boldsymbol{U}_1^{(2)},-\boldsymbol{M}_2\boldsymbol{U}_2^{(2)},-\boldsymbol{M}_2\boldsymbol{U}_3^{(2)},-\boldsymbol{M}_2\boldsymbol{U}_4^{(2)}\big].\end{aligned}\tag{11}$$

All the reflection coefficients $r_\alpha^{(1)}\equiv b_\alpha^{(1)}/b_{in}^{(1)}$ in medium 1 and all the transmission coefficients $t_\alpha^{(2)}\equiv\tilde{b}_\alpha^{(2)}/b_{in}^{(1)}$ in medium 2 of the partial-wave amplitudes can therefore be solved simultaneously as

$$\big[r_1^{(1)},\ldots,r_4^{(1)},t_1^{(2)},\ldots,t_4^{(2)}\big]^T=-\boldsymbol{M}^{-1}\boldsymbol{M}_1\boldsymbol{U}_{in}^{(1)}.\tag{12}$$

We remark that, with the given materials, crystallographic orientations, the size of the vacuum gap and the frequency, the matrices $\boldsymbol{M}$ and $\boldsymbol{M}_1$ depend only on the wave-vector component k_x along the interface, which is a *conserved quantity* for all partial-wave modes in a scattering problem. The detailed information about the incident wave, such as the normal component of the wave vector k_z and the polarization $\boldsymbol{A}_{in}$, are defined separately in the column vector $\boldsymbol{U}_{in}^{(1)}$. This means that the choice of the incident wave mode does not influence the calculation $\boldsymbol{M}$ and $\boldsymbol{M}_1$, therefore those matrices are only computed once for a given k_x, and the reflection and transmission coefficients for all the incident modes can readily be obtained simply by changing $\boldsymbol{U}_{in}^{(1)}$.

In contrast, in the approach described by Ref. [29] in which Cramer's rule is used, the matrices used in equations (38) and (39) of Ref. [29] have to be reconstructed and calculated each time a new incident wave mode is given. This is because the common columns of these matrices should be the eigenvector solutions of all the transmitted wave modes except the incident mode, to ensure the columns of the fully constructed matrices are linearly independent. Furthermore, Cramer's rule used in Ref. [29] requires computation of $n+1$ determinants to solve n linear equations, which is considered computationally inefficient compared with the single matrix inversion used in Eq. (12) in our approach.

B. Multiple reflection approach

In the second, alternative approach, the reflected and transmitted waves in both media can be considered to be coupled by a superposition of multiply reflected evanescent electric potential waves in the vacuum gap. A similar picture has been adopted before in the description of the analogous "photon tunneling", in other words the frustrated total internal reflection phenomenon for electromagnetic waves in optics [45,46].

In this approach, we define two 5×2 scattering matrices $\boldsymbol{S}^{(1)}$ and $\boldsymbol{S}^{(2)}$ for the two vacuum-solid interfaces (connecting the incoming and outgoing partial wave amplitudes for all modes), calculated separately for each interface [for the definitions, see Appendix D, Fig. 6 and Eq. (D1)]. These scattering matrices are generalized in the sense that they include evanescent modes, in particular the two evanescent vacuum gap modes. As shown in Appendix D, the resulting scattering matrices are

$$\begin{aligned}\boldsymbol{S}^{(1)}&=\begin{bmatrix}\bar{\boldsymbol{r}}^{(1)}&\bar{\boldsymbol{t}}^{(1)}\\\bar{t}_V^{(1)}&\bar{r}_V^{(1)}\end{bmatrix}\\&=\big[\boldsymbol{U}_1^{(1)},\ldots,\boldsymbol{U}_4^{(1)},-\boldsymbol{U}_{V_+}\big]^{-1}\big[-\boldsymbol{U}_{in}^{(1)},\boldsymbol{U}_{V_-}\big],\\\boldsymbol{S}^{(2)}&=\begin{bmatrix}\bar{\boldsymbol{r}}^{(2)}&\bar{\boldsymbol{t}}^{(2)}\\\bar{t}_V^{(2)}&\bar{r}_V^{(2)}\end{bmatrix}\\&=\big[\boldsymbol{U}_1^{(2)},\ldots,\boldsymbol{U}_4^{(2)},-\boldsymbol{U}_{V_-}\big]^{-1}\big[-\boldsymbol{U}_{in}^{(2)},\boldsymbol{U}_{V_+}\big],\end{aligned}\tag{13}$$

where $\bar{\boldsymbol{r}}^{(i)}=[\bar{r}_1^{(i)},\ldots,\bar{r}_4^{(i)}]^T$ are the reflection amplitude coefficients into modes $\alpha=1,\ldots,4$ of the incoming wave mode from medium $i=1,2$, $\bar{r}_V^{(i)}$ the reflection amplitude coefficient from medium i of an incoming vacuum mode, $\bar{\boldsymbol{t}}^{(i)}=[\bar{t}_1^{(i)},\ldots,\bar{t}_4^{(i)}]^T$ the transmission amplitude coefficients of an incoming vacuum mode into wave modes $\alpha=1,\ldots,4$ of medium i, and finally, $\bar{t}_V^{(i)}$ the transmission amplitude coefficient of the incoming wave mode from medium i into a vacuum mode. To avoid confusion with the coupled scattering coefficients calculated with the direct approach in Sec. III A [Eq. (12)], we have used bars on the top of the symbols here. These "bare" coefficients describe the scattering of the electroacoustic wave as if there is no second bulk medium and will be used below to construct the total tunneling transmission and reflection coefficients with the help of a multiple reflection factor generated by the vacuum gap.

The total transmission factor consists of sum of partial evanescent waves in the gap that have traversed the gap once, reflected at both interfaces and traversed the gap three times, and so on. We therefore get a geometric series for the total transmission coefficient into mode α, $t_\alpha^{(2)}$ as

$$\begin{aligned}t_\alpha^{(2)}&=\bar{t}_V^{(1)}e^{-k_xd}\bar{t}_\alpha^{(2)}+\bar{t}_V^{(1)}\bar{r}_V^{(1)}\bar{r}_V^{(2)}e^{-3k_xd}\bar{t}_\alpha^{(2)}\\&\quad+\bar{t}_V^{(1)}\big(\bar{r}_V^{(1)}\big)^2\big(\bar{r}_V^{(2)}\big)^2e^{-5k_xd}\bar{t}_\alpha^{(2)}+\cdots\\&=\frac{\bar{t}_V^{(1)}\bar{t}_\alpha^{(2)}e^{-k_xd}}{1-\bar{r}_V^{(1)}\bar{r}_V^{(2)}e^{-2k_xd}},\end{aligned}$$

where an attenuation factor e^{-k_xd} due to the wave path has been included each time wave passes through the gap. We can also calculate the total reflection coefficient the same way. Collecting in both cases the common multiple reflection factor

$$f_m(d)=\frac{e^{-k_xd}}{1-\bar{r}_V^{(1)}\bar{r}_V^{(2)}e^{-2k_xd}},\tag{14}$$

we arrive at the expressions for the total transmission and reflection coefficients $t_\alpha^{(2)}$ and $r_\alpha^{(1)}$ from the input mode into the mode $\alpha=1,\ldots,4$ in medium (2) (transmission) or in (1) (reflection):

$$t_\alpha^{(2)}=\bar{t}_\alpha^{(2)}\bar{t}_V^{(1)}f_m(d),\tag{15}$$

$$r_\alpha^{(1)}=\bar{r}_\alpha^{(1)}+\bar{r}_V^{(2)}\bar{t}_\alpha^{(1)}\bar{t}_V^{(1)}f_m(d)e^{-k_xd}.\tag{16}$$

We have checked that the results of the multiple reflection approach are identical to our previously derived scattering coefficients determined using the first, combined boundary conditions approach. The main difference is that in this second

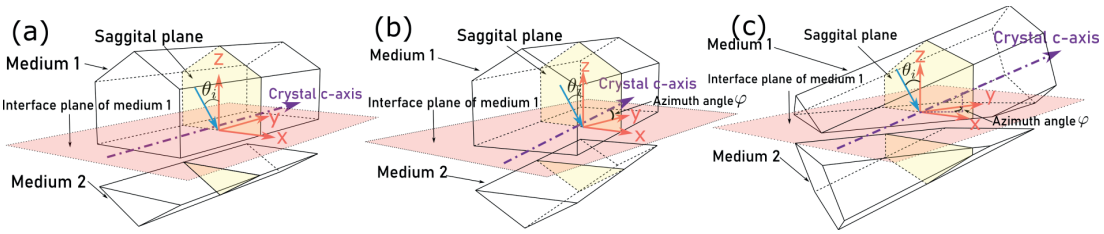

FIG. 2. Wurtzite hexagonal crystal orientations used in the illustrative examples. (a) In the analytical example (Sec. IV A), the vacuum gap is cut through the a plane $[11\bar{2}0]$ of the crystal. The azimuthal angle $\varphi = 0$ and the polarization of the wave is aligned with the crystallographic c axis. (b) In the first numerical example, vacuum gap is also cut through the a plane $[11\bar{2}0]$ of the crystal, while the azimuthal angle is rotated from 0° to 360° with respect to the z axis. (c) In the second numerical example, the vacuum gap is cut through the n plane $[11\bar{2}3]$ of the crystal. The crystallographic c axis is no longer parallel to the interface plane, while the azimuthal angle is rotated from 0° to 360° with respect to the z axis.

approach, the gap distance d is completely separated from the calculation of the matrices. For given materials, crystal orientations and the incident wave, the scattering matrices $\boldsymbol{S}^{(1)}$ and $\boldsymbol{S}^{(2)}$ are independent of the gap distance, and the effects of the gap to the scattering coefficients can easily be obtained through the explicit factor $f_m(d)$. This makes the computation as a function of the gap distance easier, as the scattering matrices are computed only once. In addition, the multiple reflection approach provides an alternative physical picture of the phenomenon of tunneling of acoustic waves through a vacuum gap, analogous to the near-field electromagnetic wave "tunneling" (frustrated total internal reflection) [45,46]. To the authors' knowledge, this multiple reflection picture has not been described in the literature before for the problem of bulk electroacoustic wave tunneling.

IV. ILLUSTRATIVE EXAMPLES

In this section, we provide some example calculations, first for a rare case that is analytically soluble. After that, we provide a limited set of examples of numerical results for a hexagonal ZnO crystal with varying crystal orientation. The results are not meant to be exhaustive, as the main focus of this work is the introduction of the formalism and the workflow how solutions can be obtained.

A. Analytical example for an incident fast transverse bulk wave

Generally speaking, for crystals with arbitrary anisotropy and orientation, it is not possible to obtain simple analytical expressions for the reflection and transmission coefficients for bulk acoustic wave tunneling. However, for some particular incident modes and high-symmetry crystal configurations, analytical solutions can be acquired. In this section, we demonstrate results for such an example: a fast transverse (FT) incident bulk wave scattering from a gap structure between two identical wurtzite hexagonal crystals ($6mm$ symmetry) with the same crystal orientation. The acoustic polarization direction of the incident wave is aligned with the crystallographic c axis, which is perpendicular to the sagittal plane [see Fig. 2(a)], in other words the c axis is aligned with the solid-vacuum interface planes. With such a high-symmetry configuration, one could also call the incident wave mode a horizontally polarized share wave (SH).

With the above configuration, there is no mode conversion and only acoustic waves with the same polarization can be excited and scattered [3], therefore the matrix $\boldsymbol{N}$ in the eigenequation (3) simplifies to a 4×4 matrix and the eigenvectors are four-vectors $[u_y, \phi, L_{yz}, D^n]^T$ (for details, see Appendix E):

$$\boldsymbol{N}(v_x) = \begin{bmatrix} 0 & 0 & -\frac{\epsilon_{11}}{\epsilon_{11}c_{44}+e_{15}^2} & \frac{e_{15}}{\epsilon_{11}c_{44}+e_{15}^2} \\ 0 & 0 & \frac{e_{15}}{\epsilon_{11}c_{44}+e_{15}^2} & \frac{c_{44}}{\epsilon_{11}c_{44}+e_{15}^2} \\ c_{44}-\rho v_x^2 & -e_{15} & 0 & 0 \\ -e_{15} & -\epsilon_0 & 0 & 0 \end{bmatrix}. \quad (17)$$

The phase velocity along the interface v_x contained in $\boldsymbol{N}$ can easily be found using the dispersion relation $(c_{44} + e_{15}^2/\epsilon_{11})k^2 = \rho\omega^2$ [3] and the definition of the incident angle θ_i in $v_x = v \sin\theta_i$:

$$v_x^2 = \frac{\epsilon_{11}c_{44} + e_{15}^2}{\epsilon_{11}\rho \sin^2\theta_i}.$$

A set of four eigenvalues ($p_\alpha = \pm\cot\theta_i$ and $\pm i$) and eigenvectors can be obtained, corresponding to two homogeneous (transverse modes) and two inhomogeneous (evanescent modes) partial waves. In particular, the particle displacement fields vanish in the solutions of inhomogeneous waves, but their stress fields exist. In contrast, for the bulk modes, the electrical displacement fields vanish, but not the electrical potential (Appendix E).

Matrix $\boldsymbol{M}$ can be constructed following our first approach and obtained using straightforward algebra as

$$\boldsymbol{M} = \frac{1}{2}\begin{bmatrix} -U & i(\epsilon_0-\epsilon_{11})V & -iUe^{k_x d} & -(\epsilon_0+\epsilon_{11})Ve^{k_x d} \\ iU & (\epsilon_0+\epsilon_{11})V & -Ue^{-k_x d} & i(\epsilon_0-\epsilon_{11})Ve^{-k_x d} \\ -i\sqrt{2\epsilon_{11}}B & -i\sqrt{2i\epsilon_{11}}A & 0 & 0 \\ 0 & 0 & -\sqrt{2\epsilon_{11}}B & -\sqrt{2i\epsilon_{11}}A \end{bmatrix},$$

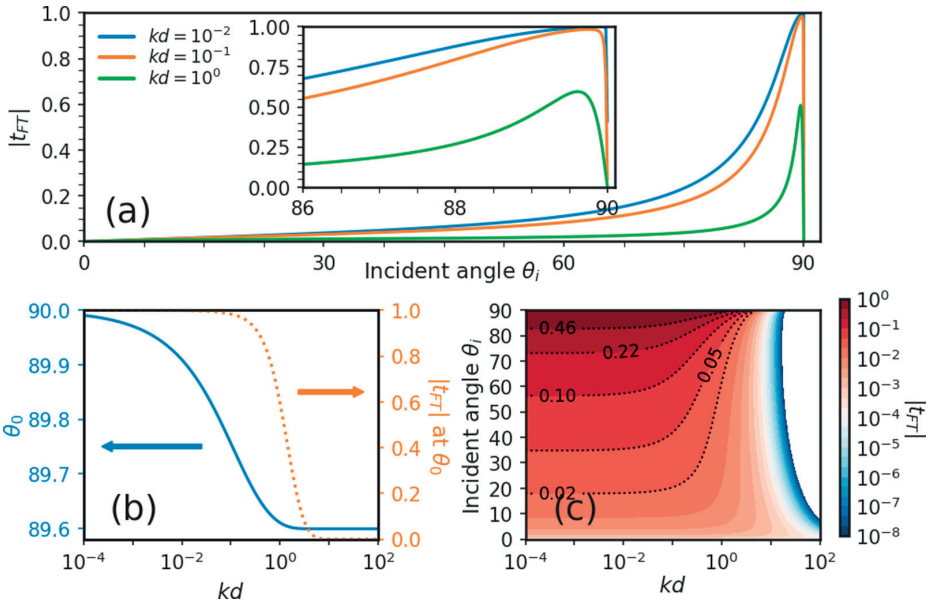

FIG. 3. (a) Dependence of the magnitude of the amplitude transmission coefficients $|t_{\rm FT}|$, from Eq. (19), of a fast transverse wave tunneling between two ZnO crystals aligned as in Fig. 2(a), as a function of the incident angle θ_i, with three different values of $kd = 0.01$, 0.1, 1, where d is the gap width and k the incident wave-vector magnitude. The inset zooms into the glancing angles. (b) Dependence of the peak transmission angle θ_0 (left axis) on kd, with the right axis showing the corresponding $|t_{\rm FT}|$ at θ_0. (c) Colored contour plot of the magnitude of the transmission coefficient $|t_{\rm FT}|$ in a logarithmic scale versus incident angle θ_i and kd.

where $A = e_{15}/\epsilon_{11}$, $B^2 = (A^2 + c_{44}/\epsilon_{11})\cot\theta_i$, $\{B \in \Re | B \geqslant 0\}$, $U = i\sqrt{i\epsilon_0}A/\sqrt{\epsilon_{11}}B$, and $V = 1/\sqrt{\epsilon_0\epsilon_{11}}$.

The exact solutions of the reflection and transmission coefficients of the fast transverse partial wave mode can be obtained from Eq. (12):

$$r_{\rm FT} = 2iA^2\epsilon_0\frac{Q_+e^{2k_xd} - Q_-}{Q_+^2e^{2k_xd} - Q_-^2} - i, \tag{18}$$

$$t_{\rm FT} = -\frac{4iA^2B^2\epsilon_0\epsilon_{11}e^{k_xd}}{Q_+^2e^{2k_xd} - Q_-^2}, \tag{19}$$

where

$$Q_\pm = A^2\epsilon_0 - iB^2(\epsilon_0 \pm \epsilon_{11}).$$

The alternative approach we presented in Eqs. (13)–(16) provides identical solutions, where the half-space scattering coefficients read

$$\bar{r}_{\rm FT}^{(1)} = \frac{iA^2\epsilon_0 - B^2(\epsilon_0 + \epsilon_{11})}{Q_+},$$

$$\bar{r}_V^{(1)} = \frac{iQ_-}{Q_+}, \quad \bar{r}_V^{(2)} = \frac{-iQ_-}{Q_+},$$

$$\bar{t}_V^{(1)} = \bar{t}_{\rm FT}^{(1)} = \bar{t}_{\rm FT}^{(2)} = \frac{2iAB\sqrt{i\epsilon_0\epsilon_{11}}}{Q_+},$$

and the multiple reflection factor is

$$f_m(d) = \frac{Q_+^2e^{k_xd}}{Q_+^2e^{2k_xd} - Q_-^2}. \tag{20}$$

Figure 3(a) shows plots of the magnitudes of the tunneling transmission coefficients $|t_{\rm FT}|$ of the fast transverse SH wave [calculated from Eq. (19)] across a vacuum gap structure separating ZnO crystals with 6*mm* hexagonal symmetry oriented as in Fig. 2(a), as a function of the incident angle θ_i, with three different scaled vacuum gap values kd, where k is the magnitude of the incident wave vector. The ZnO material constants adopted in the calculation are $\rho = 5680$ kg m^{-3}, $c_{44} = 4.247 \times 10^{10}$ N m^{-2}, $e_{15} = -0.48$ C m^{-2}, and $\epsilon_{11} = 8.55\epsilon_0$ [3]. The main observation is that transmission remains modest, except at small glancing angles (near 90° incidence), where a maximum can be found at θ_0. For small enough gaps with $kd < 1$, this transmission peak approaches unity. The peak transmission condition can be found by setting the real part of the denominator in Eq. (19) to zero, giving an equation for θ_0:

$$B^4 \equiv \frac{\left(A^2 + c_{44}/\epsilon_{11}\right)^2}{\tan^2\theta_0} = \frac{A^4\epsilon_0^2(e^{2k_xd} - 1)}{(\epsilon_0 + \epsilon_{11})^2e^{2k_xd} - (\epsilon_0 - \epsilon_{11})^2}. \tag{21}$$

Furthermore, when the gap size approaches zero, the transmission coefficient, Eq. (19), is simplified to the expression $t_{\rm FT} = A^2/(A^2 - iB^2)$, which approaches unity when $\theta \to 90°$. Conversely, our expressions demonstrate that the transmission is never mathematically exactly one for a finite gap size.

Similar analytical results for an incoming SH mode for the same crystal orientations have also been demonstrated for $LiIO_3$ (hexagonal class 6 symmetry) and $Bi_{12}GeO_{20}$ (cubic class 23 symmetry) by Balakirev and Gorchakov [13], who attributed the peak transmission to phase matching of the incident and transmitted waves. They did not, however, give

explicit formulas for 6*mm* symmetry. For the lower class 6 symmetry of their study, they showed that a range of angles can be found for complete transmission with a finite small gap size, in contrast with our findings for the 6*mm*-symmetry case.

Figure 3(b) gives a closer look of the angle of maximum transmission θ_0 and its corresponding peak transmission value. The range of angles that can satisfy the condition is tightly limited to lie within a range of 0.4 degrees, and with an increasing gap size beyond the characteristic length $kd \approx 1$, the peak transmission quickly drops to zero. The dependence of the transmission coefficient on the gap size is more clearly presented in Fig. 3(c). The bulk acoustic wave tunneling is switched off at about $kd \geqslant 1$, whereas the transmission is saturated for gap sizes smaller than about $kd \leqslant 10^{-2}$. The smallest incident angles providing a transmission factor larger than 10% are around $\approx 60^\circ$ for small gaps.

B. Numerical results for arbitrarily oriented hexagonal ZnO crystals

The reflection and transmission coefficients of arbitrarily oriented crystals can also be obtained numerically by following our theoretical approach. Here, we demonstrate two sets of results (two cuts) for hexagonal 6*mm* ZnO crystals that been cut into two pieces and separated by a vacuum gap of distance d. In other words, we only consider here that the two crystals have the same orientation.

Due to the uniaxial symmetry, the orientation of the crystals can be fixed by just two angles: the crystal zenith angle ϑ and the crystal azimuth angle φ [see Fig. 7(b)]. The details of the definition of the crystal orientation, the rotation procedure and the transformations of the material tensors are described in Appendix F. Both semi-infinite bulk crystals share this identical crystal orientation in which the zenith angle ϑ is fully determined by the plane of the cut (see Appendix H for the common cut planes for a hexagonal crystal), whereas the rotation of the crystal azimuth angle φ is equivalent to the rotational degree of freedom of the incident wave (the orientation of the sagittal plane) around the normal of the interface plane. The incident wave has two degrees of freedom: One is the incident angle θ_i that resides inside the sagittal plane and varies from 0° to 90°. The other is the incident azimuth angle that varies from 0° to 360°. For the cases demonstrated in this section, the rotation of the crystal azimuth angle φ can be considered either as a change of the incident wave azimuth angle, or a change of the crystal orientation. In the computations here, we implemented it as a rotation of the crystal, to avoid duplication.

The numerical algorithms were implemented by using the Anaconda Python distribution. Here, we briefly explain the workflow of the implementation of the combined boundary condition approach presented in Sec. III A. A set of input parameters specifying the material constants (tensors $\boldsymbol{\epsilon}_0^S$, $\boldsymbol{e}_0$, $\boldsymbol{c}_0^E$, and scalar ρ, values from Ref. [3]), the crystal orientation (ϑ, φ), the gap distance d, and the incident angle θ_i and the mode of the incident bulk wave are first given. With the material constants and crystal orientation, the rotated material parameters $(\boldsymbol{\epsilon}^S, \boldsymbol{e}, \boldsymbol{c}^E)$ can be obtained by using the formulation described in Appendix F.

Knowing the rotated material parameters and the incident angle and mode, the parallel component of the incident wave phase velocity v_x is solved from the piezoelectrically stiffened Christoffel equations (for details, see standard textbooks, e.g., Refs. [2,3]). By combining the rotated material constants and the phase velocity v_x, the 8×8 Stroh matrix $\boldsymbol{N}(v_x)$ given by Eq. (B9) can be constructed, whose eigenvalues p_α and eigenvectors $\boldsymbol{\xi}_\alpha$ are then solved from Eq. (3). The orthogonality of the eigenvectors are then checked and they are normalized using the Stroh-normalization condition, Eq. (4).

At this point, we can begin to solve the boundary-condition problem of Eq. (9). By following our first approach, two 8×5 vacuum matrices $\boldsymbol{M}_1$ and $\boldsymbol{M}_2$ can be constructed from Eq. (10) based on d and v_x; the 8×8 matrix $\boldsymbol{M}$ can be formed by combining the vacuum matrices and the eigenvector solutions of the Stroh matrix; and the column vector $\boldsymbol{U}_{in}^{(1)}$ can be constructed from the incident mode eigenvector $\boldsymbol{\xi}_{in}$. Finally, with these computed matrices, the transmission and reflection coefficients of the incident bulk electroacoustic wave can be acquired from Eq. (12). The computational time of each of the above processes took less than 1 ms, with an overall time less than 5 ms using a standard modern laptop. A set of results with a two varying incident angles, as shown in Figs. 4 and 5 then took 6 minutes each.

In the first set of results, shown in Fig. 4, we start from an a-plane-cut crystal with $\varphi = 0^\circ$, which describes an orientation that is identical to the analytical example in Sec. IV A. Then, we gradually rotate the crystal orientation around the z axis, the normal of the interfaces, from $\varphi = 0^\circ \rightarrow 360^\circ$ [see Fig. 2(b)].

We have chosen to plot just the most interesting example cases in Fig. 4, as our goal here is to demonstrate the capabilities of the formalism. We plot the magnitudes of tunneling amplitude transmission coefficients $|t_\alpha|$ of incident fast transverse (FT) and slow transverse (ST) wave modes, and their mode converted transmission amplitudes (i.e., FT $\rightarrow$ FT, FT $\rightarrow$ ST, ST $\rightarrow$ ST, ST $\rightarrow$ FT), as a function of the incident angle θ_i and the rotation angle φ, keeping the scaled gap $kd = 10^{-2}$ constant. (The mode assignment process is discussed in Appendix G). In comparison with the FT and ST modes, the transmission of the L mode is much weaker, does not show as many interesting features, and we choose not to use it as an example here. In addition, we plot the critical incident angles, beyond which a faster reflected partial-wave mode becomes evanescent. Thus, for the incident FT mode, only one critical angle exists, where the L mode becomes evanescent (θ_{L_c}), whereas for the incident ST mode, there are two critical angles: for the L mode θ_{L_c} and for the FT mode θ_{FT_c}.

Since for this first crystal orientation example the azimuthal rotation axis φ is perpendicular to the crystal uniaxial c axis, we expect and observe a mirrored twofold symmetry in the plots. With an incident FT mode, several isolated high transmission areas are observed, and they are primarily located at small glancing angles (large θ_i) around high-symmetry orientations. In particular, the line segment of $\varphi = 0^\circ$ and $\theta_i \in [0^\circ, 90^\circ]$ for FT $\rightarrow$ FT represents the same results as already discussed in the analytical calculation in Sec. IV A. However, with crystal orientations around $\varphi = 90^\circ$ and 270°, the high transmission region lies just after the critical angle θ_{L_c}. Another general observation is that for both modes, the

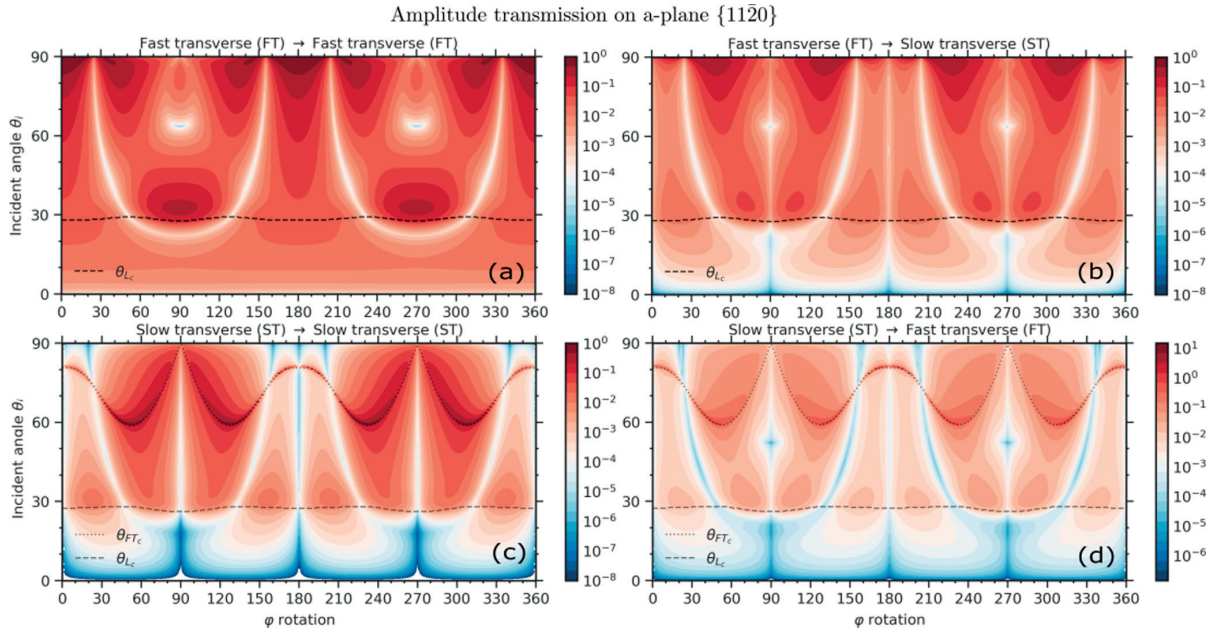

FIG. 4. The magnitudes of amplitude transmission coefficients $|t_\alpha|$ across a vacuum gap (color scale) of an a-plane-cut ZnO crystal (11$\bar{2}$0) versus incident angle θ_i and z axis rotation angle φ for a scaled gap $kd = 10^{-2}$. Two different incident wave modes (FT, ST) and two transmitted wave modes (FT, ST) are demonstrated: (a) FT-to-FT, (b) FT-to-ST, (c) ST-to-ST, and (d) ST-to-FT transmission. θ_{L_c} (dashed) and θ_{FT_c} (dotted) are the critical angles for scattered L and FT wave modes. Note that panel (d) has a different logarithmic scale, as in the mode conversion $|t_\alpha| > 1$ is possible.

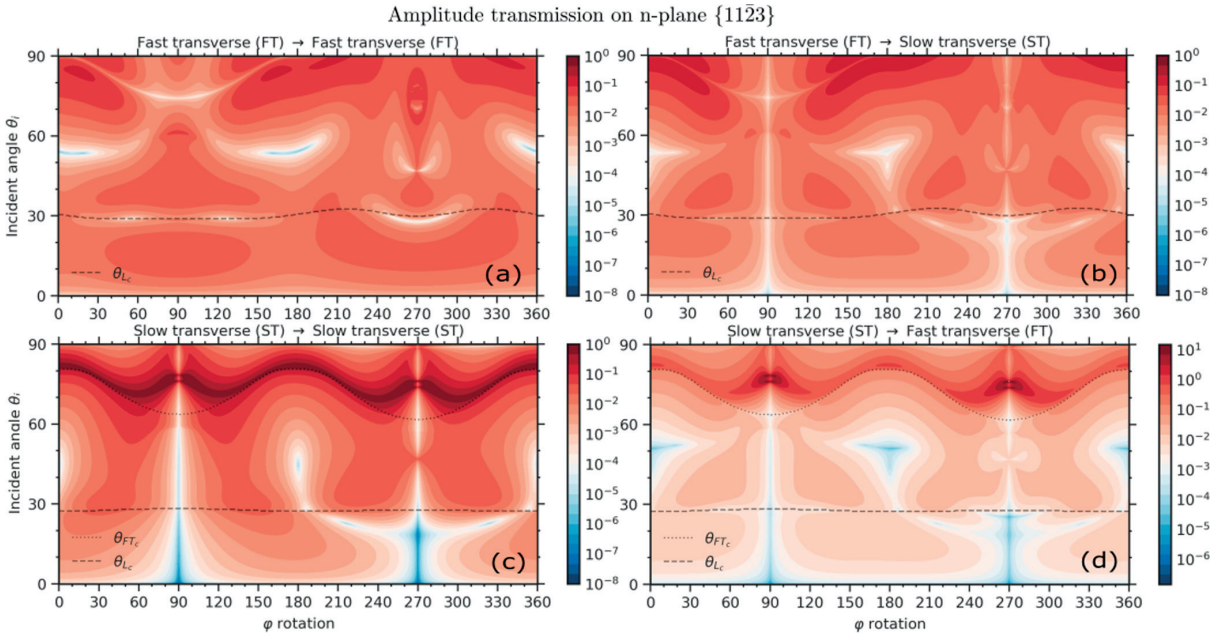

FIG. 5. The magnitudes of amplitude transmission coefficients $|t_\alpha|$ across a vacuum gap (color scale) of an n-plane-cut ZnO crystal (11$\bar{2}$3) versus incident angle θ_i and z-axis rotation angle φ, for a scaled gap $kd = 10^{-2}$. Two different incident wave modes (FT, ST) and two transmitted wave modes (FT, ST) are demonstrated: (a) FT-to-FT, (b) FT-to-ST, (c) ST-to-ST, and (d) ST-to-FT transmission. θ_{L_c} (dashed) and θ_{FT_c} (dotted) are the critical angles for scattered L and FT wave modes. Note that panel (d) has a different logarithmic scale, as in the mode conversion $|t_\alpha| > 1$ is possible.

transmission is significantly enhanced when θ_i is beyond θ_{L_c}, as more energy is then concentrated near the interfaces.

With an incident ST mode, in contrast, a narrow high transmission "resonance" exists close to the critical angle of the FT partial waves (θ_{FT_c}) in the first intersonic interval, and is significantly enhanced around $\varphi = n\pi/3, n = 1, 2, \ldots$. Such a resonant transmission could be interpreted as arising from the excitation of leaky surface wave modes coupling across the gap [31]. In addition to resonant features, "antiresonances," or sharp dips, can also be observed in the transmission. In particular the u-shaped feature between $\varphi \approx 20^\circ \ldots 160^\circ$ and $\varphi \approx 200^\circ \ldots 340^\circ$ is prominent in all plots.

In the second crystal cut example of Fig. 5, we demonstrate the same FT and ST mode results for ZnO, but which is now initially cut from a crystallographic plane of $\{11\bar{2}3\}$ [n plane, see Fig. 2(c) and Appendix H for common cut planes for a hexagonal crystal]. The change in the crystal orientation dramatically distorts the amplitude transmission as a function of both θ_i and φ. The twofold symmetry with respect to φ rotations is lost, and with an incident FT mode, the transmission is generally attenuated compared with the a-plane results. To understand this, we consider for example the case $\varphi = 0$ in the n-plane crystal cut, for which the incident FT mode is a quasitransverse mode which now couples to all other acoustic modes at the interface. As a result, the FT $\rightarrow$ FT transmission is attenuated, while the mode converted FT $\rightarrow$ ST transmission increases. In contrast, with the a-plane cut the incident FT mode wave is a pure horizontal shear wave (SH), as described in the analytical example, leading intuitively to a stronger FT $\rightarrow$ FT transmission and vanishing FT $\rightarrow$ ST transmission. Furthermore, it is interesting to see that, with an incident ST mode, significant transmission resonance just beyond the FT wave critical angle θ_{FT_c} still survives as a robust feature also for the n cut. As mentioned above, this can be interpreted as excitation of coupled leaky surface waves between the vacuum interfaces [31].

V. CONCLUSIONS AND OUTLOOK

We have shown that in general, bulk acoustic waves can be transmitted ("tunnel") across a finite vacuum gap between two piezoelectric crystals. This mechanism works not only in the nanoscale, but also for large gap widths of the order of the wavelength. Here, we presented a rigorous general approach and formalism that can be applied to study this effect for any anisotropic piezoelectric crystals with arbitrary crystallographic orientation, acquiring the solutions of reflection and transmission coefficients of all the partial waves. The extended Stroh formalism, briefly reviewed for the benefit of the reader, was used as a powerful tool to solve in general the scattering of an electroacoustic wave on the solid-vacuum interface. Two new approaches to solve the reflection and transmission coefficients of the coupled tunneling problem (two interfaces separated by a gap) were then derived: one based on the direct solution of the boundary conditions, the other on the physical picture of multiple reflections of evanescent waves in the vacuum gap. In particular, the multiple reflection method provides a physical insight of the acoustic tunneling that is analogous to near-field tunneling of evanescent electromagnetic waves. In this picture, the effect of the vacuum gap size on the reflection and transmission coefficients is conveniently separated and described by a single multiple reflection factor, offering a potential computational advantage.

To verify the usefulness and validity of the methodology, explicit example solutions for the case of two adjacent ZnO wurtzite hexagonal crystals were demonstrated. First, we presented analytical results for a fast transverse incident mode and high-symmetry crystal orientation. Simple expressions for the transmission and reflection coefficients and the multiple reflection factor were derived, and an explicit mathematical condition for the peak transmission was also presented. We made the observation that tunneling transmission is not necessarily small: For small glancing angle incidence, transmission was approaching one for gap sizes smaller than the wavelength.

Second, we described the workflow for numerical implementation for an arbitrary orientation and presented some numerical results for two cases of anisotropic ZnO crystals (two different crystal cut surfaces). We plotted the transmission coefficients of the fast and slow transverse partial modes, as well as the conversion between them, against the incident angle and the crystal azimuth rotation angle. In the numerical examples, we also find close to unity transmissions, and not only for small glancing angles. Such cases were mostly observed in the vicinity of the critical angles of the scattered partial-wave modes, where they become inhomogeneous surface modes. The enhancement of tunneling transmission was a particularly sharp and strong feature (resonance) for an incoming slow transverse wave with an incident angle just beyond the critical angle for the fast transverse wave, where coupled leaky surface waves can be excited.

With the formalism and the approaches derived in this work, we have set the foundation for many further studies of electroacoustic wave tunneling. The first straightforward objective is to map and understand the conditions for exceptionally high transmission, as there are indications of the possibility of complete acoustic wave tunneling. In addition to direct applications in the manipulation of acoustic waves, our formalism can be applied in the future in other areas of physics related to vibrations, such as heat transport, optomechanics, and quantum information science.

ACKNOWLEDGMENTS

This study was supported by the Academy of Finland Project No. 341823. We wish to acknowledge discussions with Dr. Tuomas Puurtinen.

APPENDIX A: PLANE-WAVE EQUATIONS OF MOTION AND CONSTITUTIVE EQUATIONS IN QUASISTATIC APPROXIMATION

Here we clarify the definitions of the variables in Eqs. (1), presented in the abbreviated (Voigt) matrix notation. The first equation in the set, the acoustic field equation, reads in general (if no external body forces are present)

$$\nabla \cdot \boldsymbol{\sigma} = \rho \frac{\partial^2 \boldsymbol{u}}{\partial t^2},$$

where $\boldsymbol{\sigma}$ is the stress tensor and $\boldsymbol{u}$ is the displacement vector. Transforming it into the abbreviated Voigt notation, where the capital Voigt index K runs over six coordinate pairs $K = xx$, yy, zz, yz, xz, xy, will result in a matrix equation $\nabla_{iK}\sigma_K = \rho\frac{\partial^2 u_i}{\partial t^2}$ where the index i denotes the usual Cartesian component and repeated indices are summed. Thus, ∇_{iK} defines a 3×6 differential operator matrix [see, for example, Ref. [3] Eq. (2.36) for an explicit expression]. For harmonic plane waves, such an operator is replaced by a 3×6 matrix formed by the wave-vector components $-ik_{iK}$, explicitly defined as [3]

$$\hat{\boldsymbol{k}} = \begin{bmatrix} k_x & 0 & 0 & 0 & k_z & k_y \\ 0 & k_y & 0 & k_z & 0 & k_x \\ 0 & 0 & k_z & k_y & k_x & 0 \end{bmatrix}, \tag{A1}$$

and the second derivative w.r.t time is replaced by $-\omega^2$, yielding the first equation in Eq. (1) in the main text,

$$ik_{iK}\sigma_K = \rho\omega^2 u_i. \tag{A2}$$

The second equation, Gauss's law $\boldsymbol{\nabla}\cdot\boldsymbol{D} = 0$, is the only Maxwell's equation that needs to be satisfied within the quasistatic approximation. It contains the usual vector divergence operator, and it can directly be written in the component form as $\nabla_i D_i = 0$, which gives for the plane waves the equation in the main text,

$$-ik_i D_i = 0, \tag{A3}$$

where k_i are now simply the Cartesian components of the wave vector.

The third and the fourth equations in Eqs. (1) are the constitutive relations for piezoelectrics, coupling the elastic and electric variables. They are given in abbreviated notation for the stress as $\sigma_K = c^E_{KL}s_L - e_{Kj}E_j$ and for the electric displacement $D_i = \epsilon^S_{ij}E_j + e_{iL}s_L$, where s_L is the strain tensor, E_i is the electric field, and c^E_{KL}, e_{Kj}, and ϵ^S_{ij} are the material parameters: the elastic stiffness tensor at constant electric field, the piezoelectric strain tensor, and the electric permittivity tensor at constant strain, respectively. The constitutive relations simplify in the quasistatic case by writing them in terms of the displacement u_i and the electric potential Φ, $s_L = \nabla_{Lj}u_j$, $E_i = -\nabla_i\Phi$, and as before for the plane waves the differential operators can be substituted by $\nabla_{Lj} \to -ik_{Lj}$, $\nabla_i \to -ik_i$, which lead to the forms presented in Eqs. (1):

$$\begin{aligned} \sigma_K &= -ic^E_{KL}k_{Lj}u_j - ie_{Kj}k_j\Phi, \\ D_i &= -ie_{iL}k_{Lj}u_j + i\epsilon^S_{ij}k_j\Phi. \end{aligned} \tag{A4}$$

APPENDIX B: EXTENDED STROH FORMALISM

In this Appendix, we provide the derivation for the piezoelectric Stroh eigenequation, Eq. (3), in the quasistatic approximation, including all necessary definitions, and provide a few remarks about the normalization. Under the framework of the quasistatic approximation, one can derive the normal projections of the stress and electric displacement fields using the piezoelectric constitutive equations in Eq. (1) as

$$\begin{aligned} \boldsymbol{n}\cdot\boldsymbol{\sigma} &= -in_{iK}c^E_{KL}k_{Lj}u_j - in_{iK}e_{Kj}k_j\Phi, \\ \boldsymbol{n}\cdot\boldsymbol{D} &= -in_i e_{iL}k_{Lj}u_j + in_i\epsilon^S_{ij}k_j\Phi, \end{aligned} \tag{B1}$$

where n_i is the ith Cartesian component of the inward unit normal vector $\boldsymbol{n}$ of the piezo-vacuum surface, and the 3×6 matrix n_{iK} has the same structure as k_{iK}, but is now formed by the unit normal components n_i, explicitly written as

$$\hat{\boldsymbol{n}} = \begin{bmatrix} n_x & 0 & 0 & 0 & n_z & n_y \\ 0 & n_y & 0 & n_z & 0 & n_x \\ 0 & 0 & n_z & n_y & n_x & 0 \end{bmatrix}. \tag{B2}$$

If we introduce a matrix expression $(\boldsymbol{nk})$ for a 4×4 matrix that is defined as

$$(\boldsymbol{nk}) \equiv \begin{bmatrix} n_{iK} & 0 \\ 0 & n_i \end{bmatrix}\begin{bmatrix} c^E_{KL} & e_{Kj} \\ e_{iL} & -\epsilon^S_{ij} \end{bmatrix}\begin{bmatrix} k_{Lj} & 0 \\ 0 & k_j \end{bmatrix}, \tag{B3}$$

where the elements of the matrices represent submatrices instead of scalars (n_{iK} represents the matrix $\hat{\boldsymbol{n}}$, etc.), it is straightforward to show that Eqs. (B1) can be written in the following more compact notation:

$$\begin{bmatrix} \boldsymbol{n}\cdot\boldsymbol{\sigma} \\ \boldsymbol{n}\cdot\boldsymbol{D} \end{bmatrix} = -i(\boldsymbol{nk})\begin{bmatrix} \boldsymbol{u} \\ \Phi \end{bmatrix}. \tag{B4}$$

By adopting the general field solutions for a mode α in Eqs. (2) and decomposing the k vector $\boldsymbol{k} = k_x(\boldsymbol{m} + p_\alpha\boldsymbol{n})$ using the two orthogonal unit vectors $\boldsymbol{m}$ and $\boldsymbol{n}$, where $\boldsymbol{m}$ is parallel to the piezo-vacuum interfaces, we can further arrange Eq. (B4) into a form where the unknown p_α is separated into the right-hand side of the equation:

$$-(\boldsymbol{nn})^{-1}(\boldsymbol{nm})\begin{bmatrix} \boldsymbol{A}_\alpha \\ \phi_\alpha \end{bmatrix} - (\boldsymbol{nn})^{-1}\begin{bmatrix} \boldsymbol{L}_\alpha \\ D^n_\alpha \end{bmatrix} = p_\alpha\begin{bmatrix} \boldsymbol{A}_\alpha \\ \phi_\alpha \end{bmatrix}. \tag{B5}$$

The matrices $(\boldsymbol{nn})$ and $(\boldsymbol{nm})$ are defined analogously to Eq. (B3) and thus depend only on the material parameters and the orientation of the crystal. We note that real materials do not present any pathological cases where the matrix inverse $(\boldsymbol{nn})^{-1}$ would not exist.

Furthermore, the equation of motion and Gauss's law can also be organized into a similar linear equations set:

$$(\boldsymbol{kk})\begin{bmatrix} \boldsymbol{u} \\ \Phi \end{bmatrix} = \rho\omega^2\boldsymbol{I}'\begin{bmatrix} \boldsymbol{u} \\ \Phi \end{bmatrix}, \tag{B6}$$

in which $\boldsymbol{I}'$ is a 4×4 matrix with elements $I'_{ii} = 1$, $i = 1, 2, 3$ and others zero.

By decomposing the k vector as above and substituting the expression for $p_\alpha[\boldsymbol{A}_\alpha, \Phi_\alpha]^T$ from Eq. (B5), we obtain

$$\begin{aligned} &-\left[(\boldsymbol{mn})(\boldsymbol{nn})^{-1}(\boldsymbol{nm}) - (\boldsymbol{mm}) + \rho v_x^2\hat{\boldsymbol{I}}'\right]\begin{bmatrix} \boldsymbol{A}_\alpha \\ \phi_\alpha \end{bmatrix} \\ &\quad - (\boldsymbol{mn})(\boldsymbol{nn})^{-1}\begin{bmatrix} \boldsymbol{L}_\alpha \\ D^n_\alpha \end{bmatrix} = p_\alpha\begin{bmatrix} \boldsymbol{L}_\alpha \\ D^n_\alpha \end{bmatrix}, \end{aligned} \tag{B7}$$

where $v_x = \omega/k_x$. Finally, combining Eqs. (B5) and (B7) by defining an eight-dimensional eigenvector $\boldsymbol{\xi}_\alpha = [\boldsymbol{A}_\alpha, \phi_\alpha, \boldsymbol{L}_\alpha, D^n_\alpha]^T$, we have derived the eigenequation for the piezoelectric scattering problem, Eq. (3):

$$\boldsymbol{N}(v_x)\boldsymbol{\xi}_\alpha = p_\alpha\boldsymbol{\xi}_\alpha, \tag{B8}$$

where the 8×8 real matrix $\boldsymbol{N}$ reads

$$\boldsymbol{N}(v_x) = -\begin{bmatrix} (\boldsymbol{nn})^{-1}(\boldsymbol{nm}) & (\boldsymbol{nn})^{-1} \\ (\boldsymbol{mn})(\boldsymbol{nn})^{-1}(\boldsymbol{nm}) - (\boldsymbol{mm}) + \rho v_x^2 \boldsymbol{I}' & (\boldsymbol{mn})(\boldsymbol{nn})^{-1} \end{bmatrix}. \tag{B9}$$

The set of eigenvectors ξ_α are orthogonal and form a complete set in the usual case, where the eigenvalues p_α are distinct [16]. In a few isolated situations, nonsemisimple degeneracy can occur, in which case generalized eigenvectors can be introduced [18,28]. We do not consider those special cases (transonic states) in this study because numerically one can always solve the problem in a limiting manner very close to such a special point.

In the main text, we quoted the orthonormalization condition in Eq. (4). It follows [18,19] from the symmetry condition for the auxiliary matrix $\hat{\boldsymbol{T}}\boldsymbol{N}$

$$\left(\hat{\boldsymbol{T}}\boldsymbol{N}\right)^T = \hat{\boldsymbol{T}}\boldsymbol{N},$$

where

$$\hat{\boldsymbol{T}} = \begin{bmatrix} \hat{\boldsymbol{O}}_{(4)} & \hat{\boldsymbol{I}}_{(4)} \\ \hat{\boldsymbol{I}}_{(4)} & \hat{\boldsymbol{O}}_{(4)} \end{bmatrix}, \tag{B10}$$

with which a reciprocal eigenvector set $\boldsymbol{T}\xi_\alpha$ orthogonal to $\boldsymbol{\xi}_\alpha$ can be defined. It follows that the eigenvectors satisfy the relation

$$\boldsymbol{\xi}_\alpha \cdot \hat{\boldsymbol{T}}\boldsymbol{\xi}_\beta = \boldsymbol{\xi}_\alpha^T \hat{\boldsymbol{T}}\boldsymbol{\xi}_\beta = \delta_{\alpha\beta}, \quad \alpha, \beta = 1, \ldots, 8, \tag{B11}$$

where $\delta_{\alpha\beta}$ is the Kronecker delta. We stress here that the dot symbol has the meaning of a matrix product in this context, as exemplified by the second form. In particular, it does not denote a complex inner product, in which case complex conjugation would be included for one of the vectors.

Equation (B11) [identical to Eq. (4) in the main text] is thus readily available as the orthonormalization condition to secure a unique normalized eigenvector solution for the $\boldsymbol{N}$ matrix. In addition, the orthonormalization condition Eq. (B11) leads to a completeness condition

$$\sum_\alpha \boldsymbol{\xi}_\alpha \otimes \hat{\boldsymbol{T}}\boldsymbol{\xi}_\alpha = \hat{\boldsymbol{I}}_{(8)}, \tag{B12}$$

providing us a powerful tool to ensure the accuracy of the solutions.

APPENDIX C: MATRIX SOLUTION OF THE BOUNDARY CONDITIONS

In this Appendix, to avoid cumbersome expressions $D_\alpha^{n,(i)}$ and $D_{V_\pm}^n$ with the explicit superscript n, we will use the shorthand notation $D_\alpha^{(i)}$ and $D_{V_\pm}$ in their place to represent the Stroh eigenvector components for the normal projection of the electric displacement in Eq. (2) in the solid $i = 1, 2$ and in vacuum (V), respectively.

The boundary conditions of the tunneling problem, Eqs. (9), provide a total of ten linear equations corresponding to ten partial-wave amplitude solutions $(b_1^{(1)}, \ldots, b_4^{(1)}, \tilde{b}_1^{(2)}, \ldots, \tilde{b}_4^{(2)}, b_{V\pm})$. Here, we list explicitly all the boundary conditions included in Eqs. (9):

$$\begin{aligned}
&b_{in}^{(1)}\phi_{in}^{(1)} + \sum_{\alpha=1}^{4} b_\alpha^{(1)}\phi_\alpha^{(1)} = b_{V+}\phi_{V+} + b_{V-}\phi_{V-}, \\
&b_{in}^{(1)}D_{in}^{(1)} + \sum_{\alpha=1}^{4} b_\alpha^{(1)}D_\alpha^{(1)} = b_{V+}D_{V+} + b_{V-}D_{V-}, \\
&b_{in}^{(1)}\boldsymbol{L}_{in}^{(1)} + \sum_{\alpha=1}^{4} b_\alpha^{(1)}\boldsymbol{L}_\alpha^{(1)} = \hat{\boldsymbol{O}}_{(3)}, \\
&\sum_{\alpha=1}^{4} \tilde{b}_\alpha^{(2)}\phi_\alpha^{(2)} = b_{V+}\phi_{V+}e^{-k_x d} + b_{V-}\phi_{V-}e^{k_x d}, \\
&\sum_{\alpha=1}^{4} \tilde{b}_\alpha^{(2)}D_\alpha^{(2)} = b_{V+}D_{V+}e^{-k_x d} + b_{V-}D_{V-}e^{k_x d}, \\
&\sum_{\alpha=1}^{4} \tilde{b}_\alpha^{(2)}\boldsymbol{L}_\alpha^{(2)} = \hat{\boldsymbol{O}}_{(3)}.
\end{aligned} \tag{C1}$$

The goal of this Appendix is to rearrange the above boundary conditions into a simple matrix equation that separates the incident wave properties, the information about the materials properties and the vacuum gap, and the scattered amplitudes, i.e., by writing

$$\hat{y} = \boldsymbol{M}\hat{x}, \tag{C2}$$

where $\hat{y}$ is a 8×1 column vector that contains the information about the incident wave and $\boldsymbol{M}$ is a 8×8 matrix, both to be derived below, and $\hat{x}$ and is a 8×1 column vector containing the wave amplitudes of all scattered waves (and therefore the information on the transmission and reflection coefficients):

$$\hat{x} = \left[b_1^{(1)}, \ldots b_4^{(1)}, \tilde{b}_1^{(2)}, \ldots, \tilde{b}_4^{(2)}\right]^T.$$

By eliminating $b_{V\pm}$ from Eq. (C1), the number of linear equations provided by the boundary conditions in Eq. (C1) can be reduced from ten to eight:

$$\begin{aligned}
&\boldsymbol{V}_1^{-1}\left(\begin{bmatrix}\phi_{in}^{(1)} \\ D_{in}^{(1)}\end{bmatrix} b_{in}^{(1)} + \sum_{\alpha=1}^{4}\begin{bmatrix}\phi_\alpha^{(1)} \\ D_\alpha^{(1)}\end{bmatrix} b_\alpha^{(1)}\right) = \boldsymbol{V}_2^{-1}\left(\sum_{\alpha=1}^{4}\begin{bmatrix}\phi_\alpha^{(2)} \\ D_\alpha^{(2)}\end{bmatrix}\tilde{b}_\alpha^{(2)}\right), \\
&b_{in}^{(1)}\boldsymbol{L}_{in}^{(1)} + \sum_{\alpha=1}^{4} b_\alpha^{(1)}\boldsymbol{L}_\alpha^{(1)} = \hat{\boldsymbol{O}}_{(3)}, \\
&\sum_{\alpha=1}^{4} \tilde{b}_\alpha^{(2)}\boldsymbol{L}_\alpha^{(2)} = \hat{\boldsymbol{O}}_{(3)},
\end{aligned} \tag{C3}$$

where

$$\boldsymbol{V}_1 = \begin{bmatrix}\phi_{V+} & \phi_{V-} \\ D_{V+} & D_{V-}\end{bmatrix}, \quad \boldsymbol{V}_2 = \begin{bmatrix}\phi_{V+}e^{-k_x d} & \phi_{V-}e^{k_x d} \\ D_{V+}e^{-k_x d} & D_{V-}e^{k_x d}\end{bmatrix}.$$

The 2×2 matrices $\boldsymbol{V}_1$ and $\boldsymbol{V}_2$ are not dependent on the incoming or scattered wave properties except for the conserved wave-vector component k_x.

To combine all equations in Eqs. (C3) into one matrix equation, we can move all the terms depending on $b_{in}^{(1)}$ to the right and all the others to the left and write all equations in terms of 5×1 column vectors $\boldsymbol{U}_\gamma^{(i)} = [\phi_\gamma^{(i)}, D_\gamma^{(i)}, \boldsymbol{L}_\gamma^{(i)}]^T$ containing the reflected ($\boldsymbol{U}_\alpha^{(1)}$), transmitted ($\boldsymbol{U}_\alpha^{(2)}$) and input wave ($\boldsymbol{U}_{in}^{(1)}$) Stroh eigenvector components for the electric potential, electric displacement and traction force. This way we obtain

$$\begin{aligned}
&\sum_{\alpha=1}^{4}\left([\boldsymbol{V}_1^{-1} \quad \hat{\boldsymbol{O}}_{(2\times3)}]\boldsymbol{U}_\alpha^{(1)} b_\alpha^{(1)} - [\boldsymbol{V}_2^{-1} \quad \hat{\boldsymbol{O}}_{(2\times3)}]\boldsymbol{U}_\alpha^{(1)} \tilde{b}_\alpha^{(2)}\right) = -[\boldsymbol{V}_1^{-1} \quad \hat{\boldsymbol{O}}_{(2\times3)}]\boldsymbol{U}_{in}^{(1)} b_{in}^{(1)},\\
&\sum_{\alpha=1}^{4}\left([\hat{\boldsymbol{O}}_{3\times2} \quad \hat{\boldsymbol{I}}_{(3)}]\boldsymbol{U}_\alpha^{(1)} b_\alpha^{(1)} - [\hat{\boldsymbol{O}}_{3\times2} \quad \hat{\boldsymbol{O}}_{(3\times3)}]\boldsymbol{U}_\alpha^{(2)} \tilde{b}_\alpha^{(2)}\right) = -[\hat{\boldsymbol{O}}_{3\times2} \quad \hat{\boldsymbol{I}}_{(3)}]\boldsymbol{U}_{in}^{(1)} b_{in}^{(1)},\\
&\sum_{\alpha=1}^{4}\left([\hat{\boldsymbol{O}}_{3\times2} \quad \hat{\boldsymbol{O}}_{(3\times3)}]\boldsymbol{U}_\alpha^{(1)} b_\alpha^{(1)} - [\hat{\boldsymbol{O}}_{3\times2} \quad \hat{\boldsymbol{I}}_{(3)}]\boldsymbol{U}_\alpha^{(2)} \tilde{b}_\alpha^{(2)}\right) = -[\hat{\boldsymbol{O}}_{3\times2} \quad \hat{\boldsymbol{O}}_{(3\times3)}]\boldsymbol{U}_{in}^{(1)} b_{in}^{(1)},
\end{aligned} \tag{C4}$$

where $\hat{\boldsymbol{O}}_{n\times m}$ denotes a zero matrix of dimensions $n \times m$, and $\hat{\boldsymbol{I}}_{(3)}$ is the 3×3 identity matrix.

From the above form, Eqs. (C4), we see that a single matrix equation

$$\sum_{\alpha=1}^{4}\left(\boldsymbol{M}_1 \boldsymbol{U}_\alpha^{(1)} b_\alpha^{(1)} - \boldsymbol{M}_2 \boldsymbol{U}_\alpha^{(2)} \tilde{b}_\alpha^{(2)}\right) = -\boldsymbol{M}_1 \boldsymbol{U}_{in}^{(1)} b_{in}^{(1)} \tag{C5}$$

can be written if we define the 8×5 matrices $\boldsymbol{M}_1$ and $\boldsymbol{M}_2$ as

$$\boldsymbol{M}_1 = \begin{bmatrix} \boldsymbol{V}_1^{-1} & \hat{\boldsymbol{O}}_{(2\times3)} \\ \hat{\boldsymbol{O}}_{(3\times2)} & \hat{\boldsymbol{I}}_{(3)} \\ \hat{\boldsymbol{O}}_{(3\times2)} & \hat{\boldsymbol{O}}_{(3\times3)} \end{bmatrix}, \quad \boldsymbol{M}_2 = \begin{bmatrix} \boldsymbol{V}_2^{-1} & \hat{\boldsymbol{O}}_{(2\times3)} \\ \hat{\boldsymbol{O}}_{(3\times2)} & \hat{\boldsymbol{O}}_{(3\times3)} \\ \hat{\boldsymbol{O}}_{(3\times2)} & \hat{\boldsymbol{I}}_{(3)} \end{bmatrix}. \tag{C6}$$

Finally, by comparing Eq. (C5) with the targeted expression $\hat{y} = \boldsymbol{M}\hat{x}$ [Eq. (C2), remembering that $\hat{x} = [b_1^{(1)}, \ldots b_4^{(1)}, \tilde{b}_1^{(2)}, \ldots, \tilde{b}_4^{(2)}]^T$], we obtain $\hat{y} = -\boldsymbol{M}_1 \boldsymbol{U}_{in} b_{in}$, with the 8×8 matrix $\boldsymbol{M}$ formed by combining eight 8×1 column matrix blocks as

$$\begin{aligned}
\boldsymbol{M} = \big[&\boldsymbol{M}_1 \boldsymbol{U}_1^{(1)}, \boldsymbol{M}_1 \boldsymbol{U}_2^{(1)}, \boldsymbol{M}_1 \boldsymbol{U}_3^{(1)}, \boldsymbol{M}_1 \boldsymbol{U}_4^{(1)},\\
&-\boldsymbol{M}_2 \boldsymbol{U}_1^{(2)}, -\boldsymbol{M}_2 \boldsymbol{U}_2^{(2)}, -\boldsymbol{M}_2 \boldsymbol{U}_3^{(2)}, -\boldsymbol{M}_2 \boldsymbol{U}_4^{(2)}\big],
\end{aligned}$$

which is the definition given in the main text in Eq. (11). From the above, we see that, in the matrix $\boldsymbol{M}$, the submatrices $\boldsymbol{M}_1$ and $\boldsymbol{M}_2$ depend only on the vacuum permittivity ϵ_0 ($D_{V_\pm} = \pm i\epsilon_0 \phi_{V_\pm}$ and $\phi_{V_\pm} = 1/\sqrt{\pm 2i\epsilon_0}$, Sec. III in the main text), the gap distance d and the conserved incident wave k-vector component k_x; vectors $\boldsymbol{U}_\gamma$ are the physical solutions obtained from the eigenvectors $\boldsymbol{\xi}_\gamma$ in the extended Stroh formalism.

Finally, the four reflection and four transmission coefficients of the wave amplitudes can readily be obtained as

$$\begin{bmatrix} \boldsymbol{r}_{(4\times1)} \\ \boldsymbol{t}_{(4\times1)} \end{bmatrix} = \frac{\hat{x}}{b_{in}} = -\boldsymbol{M}^{-1} \boldsymbol{M}_1 \boldsymbol{U}_{in}. \tag{C7}$$

APPENDIX D: SCATTERING MATRIX

If we consider a scattering problem for an interface i between a piezoelectric crystal and vacuum, as illustrated in Fig. 6, the scattering matrix $S^{(i)}$ determining how input waves scatter into output waves can be defined as

$$\begin{bmatrix} b_1^{(i)} \\ b_2^{(i)} \\ b_3^{(i)} \\ b_4^{(i)} \\ b_t^{(V)} \end{bmatrix} = S^{(i)} \begin{bmatrix} b_{in}^{(i)} \\ b_{in}^{(V)} \end{bmatrix} = \begin{bmatrix} \bar{r}_1^{(i)} & \bar{t}_1^{(i)} \\ \bar{r}_2^{(i)} & \bar{t}_2^{(i)} \\ \bar{r}_3^{(i)} & \bar{t}_3^{(i)} \\ \bar{r}_4^{(i)} & \bar{t}_4^{(i)} \\ \bar{t}_{in}^{(i)} & \bar{r}_{in}^{(i)} \end{bmatrix} \begin{bmatrix} b_{in}^{(i)} \\ b_{in}^{(V)} \end{bmatrix}, \tag{D1}$$

where the superscript (V) denotes the evanescent electric potential wave in the vacuum gap.

The first boundary condition in Eq. (9) can then be rearranged by moving all the outgoing (incoming) waves to the left (right) side, giving

$$\left[\boldsymbol{U}_1^{(1)}, \boldsymbol{U}_2^{(1)}, \boldsymbol{U}_3^{(1)}, \boldsymbol{U}_4^{(1)}, -\boldsymbol{U}_{V_+}\right] \begin{bmatrix} b_1^{(1)} \\ b_2^{(1)} \\ b_3^{(1)} \\ b_4^{(1)} \\ b_{V_+} \end{bmatrix} = \left[-\boldsymbol{U}_{in}^{(1)}, \boldsymbol{U}_{V_-}\right] \begin{bmatrix} b_{in}^{(1)} \\ b_{V_-} \end{bmatrix}. \tag{D2}$$

The second boundary condition follows from Eq. (D2) by changing the medium index, and exchanging the incoming

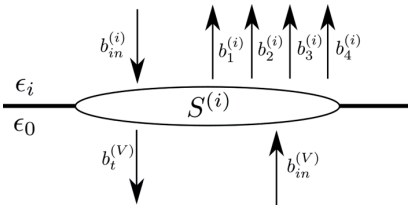

FIG. 6. Illustration of the scattering matrix $\boldsymbol{S}^{(i)}$ for an interface between medium i and vacuum. For the second medium on the receiving side, the incoming amplitude $b_{in}^{(i)}$ is zero.

and outgoing vacuum waves

$$\left[\boldsymbol{U}_1^{(2)}, \boldsymbol{U}_2^{(2)}, \boldsymbol{U}_3^{(2)}, \boldsymbol{U}_4^{(2)}, -\boldsymbol{U}_{V_-}\right]\begin{bmatrix} b_1^{(2)} \\ b_2^{(2)} \\ b_3^{(2)} \\ b_4^{(2)} \\ b_{V_-} \end{bmatrix} = \left[-\boldsymbol{U}_{in}^{(2)}, \boldsymbol{U}_{V_+}\right]\begin{bmatrix} b_{in}^{(2)} \\ b_{V_+} \end{bmatrix}. \tag{D3}$$

By comparing Eqs. (D2) and (D3) with Eq. (D1), we obtain the expressions for the scattering matrices $\boldsymbol{S}^{(1)}$ and $\boldsymbol{S}^{(2)}$ as given in Eq. (13). Note that, even if we have formally used an input wave from medium (2) in the definition of $\boldsymbol{S}^{(2)}$, due to the linearity of the problem it will not affect how an input wave from medium (1) is transmitted or reflected. In the actual computation of $\boldsymbol{S}^{(2)}$ for the case of input wave from medium (1), $-\boldsymbol{U}_{in}^{(2)}$ can be set arbitrarily, for example to zero.

APPENDIX E: DETAILS OF THE ANALYTICAL SOLUTION EXAMPLE

In the analytical example we presented in Sec. IV A, a hexagonal 6*mm* symmetry crystal was rotated in such way that its crystallographic c axis is aligned with the solid-vacuum interface and is perpendicular to the sagittal (incident) plane. The material parameters of the rotated crystal, $\boldsymbol{\epsilon}^S$ the electric permittivity at constant strain, $\boldsymbol{e}$ the piezoelectric stress, and $\boldsymbol{c}^E$ the elastic stiffness at constant electric field, can be obtained using the method provided in Appendix F. To be specific, the crystal is rotated about the x axis by 90° following the right-hand rule, after which the rotated material tensors read as

$$\boldsymbol{e} = \begin{bmatrix} 0 & 0 & 0 & 0 & 0 & -e_{15} \\ -e_{31} & -e_{33} & -e_{31} & 0 & 0 & 0 \\ 0 & 0 & 0 & -e_{15} & 0 & 0 \end{bmatrix}, \tag{E1}$$

$$\boldsymbol{\epsilon}^S = \begin{bmatrix} \epsilon_{11} & 0 & 0 \\ 0 & \epsilon_{33} & 0 \\ 0 & 0 & \epsilon_{11} \end{bmatrix}, \tag{E2}$$

$$\boldsymbol{c}^E = \begin{bmatrix} c_{11} & c_{13} & c_{12} & 0 & 0 & 0 \\ c_{13} & c_{33} & c_{13} & 0 & 0 & 0 \\ c_{12} & c_{13} & c_{11} & 0 & 0 & 0 \\ 0 & 0 & 0 & c_{44} & 0 & 0 \\ 0 & 0 & 0 & 0 & c_{66} & 0 \\ 0 & 0 & 0 & 0 & 0 & c_{44} \end{bmatrix}. \tag{E3}$$

In Appendix B, the general approach for computing the extended Stroh 8 × 8 matrix $\boldsymbol{N}$ was described. However, this matrix can be significantly simplified in the analytical example in Sec. IV A. This is because, for this high-symmetry case, the piezoelectric response appears only along the crystal c axis, which is aligned with the y axis of the laboratory coordinates after the rotation [as shown in Fig. 2(a)], and there is no mode conversion as stated in the main text. Therefore, only the y-axis components, u_y in displacement and σ_{yz} in stress, enter the boundary conditions, Eqs. (6), and thus a reduced 4 × 4 Stroh matrix $\boldsymbol{N}$ and four-dimensional eigenvectors $\boldsymbol{\xi} = [u_y, \phi, L_{yz}, D]^T$ are sufficient to solve the scattering problem at hand, involving only SH and E wave modes.

The explicit expression of the reduced Stroh matrix $\boldsymbol{N}$ is given in the main text in Eq. (17), and its eigenvalues and Stroh-normalized eigenvectors are

$$p_1 = -i, \quad \boldsymbol{\xi}_1 = \left[0, \sqrt{\frac{i}{2\epsilon_{11}}}, \frac{e_{15}\sqrt{-i}}{\sqrt{2\epsilon_{11}}}, \frac{\sqrt{-i\epsilon_{11}}}{\sqrt{2}}\right]^T,$$

$$p_2 = i, \quad \boldsymbol{\xi}_2 = \left[0, \frac{\sqrt{-i}}{\sqrt{2\epsilon_{11}}}, \frac{e_{15}\sqrt{i}}{\sqrt{2\epsilon_{11}}}, \frac{\sqrt{i\epsilon_{11}}}{\sqrt{2}}\right]^T,$$

$$p_3 = -\cot\theta_i, \quad \boldsymbol{\xi}_3 = \left[\frac{\sqrt{2}}{2}\sqrt{\frac{k^2\tan\theta_i}{\rho\omega^2}}, -\frac{\sqrt{2}e_{15}}{2\epsilon_{11}}\sqrt{\frac{k^2\tan\theta_i}{\rho\omega^2}}, \frac{\sqrt{2}}{2}\sqrt{\frac{\rho\omega^2}{k^2\tan\theta_i}}, 0\right]^T,$$

$$p_4 = \cot\theta_i, \quad \boldsymbol{\xi}_4 = \left[\frac{\sqrt{2}}{2}\sqrt{\frac{-k^2\tan\theta_i}{\rho\omega^2}}, -\frac{\sqrt{2}e_{15}}{2\epsilon_{11}}\sqrt{\frac{-k^2\tan\theta_i}{\rho\omega^2}}, \frac{\sqrt{2}}{2}\sqrt{\frac{-\rho\omega^2}{k^2\tan\theta_i}}, 0\right]^T.$$

The normalization conditions for the above solutions are $2(u_y L_{yz} + \phi D) = 1$, and the dispersion relation is $\rho\omega^2 = (c_{44} + e_{15}^2/\epsilon_{11})k^2$. The first two solutions (p_1, p_2) correspond to the two inhomogeneous E waves, and the last two (p_3, p_4) to the propagating SH waves.

APPENDIX F: CRYSTALLOGRAPHIC ORIENTATION

To solve the tunneling problem for an arbitrary crystal orientation, a method for transforming the material tensors from a standard crystallographic orientation to a specific arbitrary rotation needs to be provided. The tensors in question are the electric permittivity at constant strain, $\boldsymbol{\epsilon}_0^S$, the piezoelectric stress, $\boldsymbol{e}_0$, and elastic stiffness at constant electric field, $\boldsymbol{c}_0^E$, where the subscript 0 refers to the standard crystallographic orientation.

To describe the orientation of a crystal with respect to a fixed laboratory coordinate system, we adopt the Euler angle system [47]. In this system, we define two Cartesian frames XYZ and xyz, the crystal intrinsic coordinates and the external fixed laboratory coordinates, respectively. The relation between these two frames can be fully expressed by three angles: ϑ, φ, and ψ, as illustrated in Fig. 7(a).

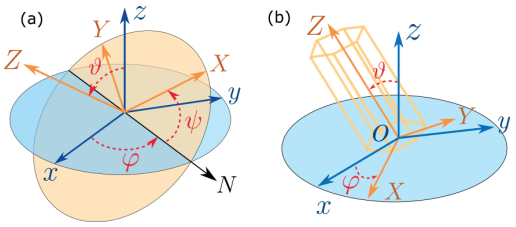

FIG. 7. Demonstration of crystal rotation angles. (a) The general Euler angle system. (b) The cylindrical angle system for uniaxial crystals

Several different conventions of the sequence of elemental rotations can be used to acquire the material constants for a specific crystal orientation $(\vartheta, \varphi, \psi)$. In this work, we adopted the widely used extrinsic z-x-z rotation sequence, which rotates the crystal frame from initial overlap with the laboratory coordinates to the desired orientation. In this procedure, the crystal frame will first be rotated about the z axis by an angle ψ defined by the right-hand rule (counterclockwise if viewed from top), followed by a second right-hand rotation of angle ϑ about the x axis, and finally a third right-hand rotation of angle φ about the z axis.

The material constant tensors (represented by $\boldsymbol{T}_{m\times n}$ matrices in the abbreviated index notation) can then be transformed to the rotated ones $\boldsymbol{T}'_{m\times n}$ by using rotation transformation matrices $\boldsymbol{R}$ [3],

$$\boldsymbol{T}'_{m\times n} = \boldsymbol{R}_m \boldsymbol{T}_{m\times n} \boldsymbol{R}_n^T, \tag{F1}$$

where $\boldsymbol{R}_m$ or $\boldsymbol{R}_n$ are the two rotation transformation matrices required for a general $m \times n$ matrix. In our case, $\boldsymbol{\epsilon}_0^S$ has $m, n = 3$, $\boldsymbol{e}_0$ has $m = 3$ and $n = 6$, and $\boldsymbol{c}_0^E$ $m, n = 6$, so we need only two different dimensionalities of rotation matrices $\boldsymbol{R}_3$ and $\boldsymbol{R}_6$ for both the z and x axes, for a total of four rotation matrices.

For the crystal rotations about the x and z axes by the right-hand rule angles ξ_x and ξ_z, respectively, $\boldsymbol{R}_3$ can be expressed [3] as

$$\boldsymbol{R}_{3,x}(\xi_x) = \begin{bmatrix} 1 & 0 & 0 \\ 0 & \cos\xi_x & -\sin\xi_x \\ 0 & \sin\xi_x & \cos\xi_x \end{bmatrix}, \tag{F2}$$

$$\boldsymbol{R}_{3,z}(\xi_z) = \begin{bmatrix} \cos\xi_z & -\sin\xi_z & 0 \\ \sin\xi_z & \cos\xi_z & 0 \\ 0 & 0 & 1 \end{bmatrix}. \tag{F3}$$

$\boldsymbol{R}_6$, required for the higher rank $\boldsymbol{e}$ and $\boldsymbol{c}$ tensors, can be obtained from the Bond stress matrix [3] as

$$\boldsymbol{R}_{6,x}(\xi_x) = \begin{bmatrix} 1 & 0 & 0 & 0 & 0 & 0 \\ 0 & \cos^2(\xi_x) & \sin^2(\xi_x) & -2\sin(\xi_x)\cos(\xi_x) & 0 & 0 \\ 0 & \sin^2(\xi_x) & \cos^2(\xi_x) & 2\sin(\xi_x)\cos(\xi_x) & 0 & 0 \\ 0 & \sin(\xi_x)\cos(\xi_x) & -\sin(\xi_x)\cos(\xi_x) & -\sin^2(\xi_x)+\cos^2(\xi_x) & 0 & 0 \\ 0 & 0 & 0 & 0 & \cos(\xi_x) & \sin(\xi_x) \\ 0 & 0 & 0 & 0 & -\sin(\xi_x) & \cos(\xi_x) \end{bmatrix}, \tag{F4}$$

$$\boldsymbol{R}_{6,z}(\xi_z) = \begin{bmatrix} \cos^2(\xi_z) & \sin^2(\xi_z) & 0 & 0 & 0 & -2\sin(\xi_z)\cos(\xi_z) \\ \sin^2(\xi_z) & \cos^2(\xi_z) & 0 & 0 & 0 & 2\sin(\xi_z)\cos(\xi_z) \\ 0 & 0 & 1 & 0 & 0 & 0 \\ 0 & 0 & 0 & \cos(\xi_z) & \sin(\xi_z) & 0 \\ 0 & 0 & 0 & -\sin(\xi_z) & \cos(\xi_z) & 0 \\ \sin(\xi_z)\cos(\xi_z) & -\sin(\xi_z)\cos(\xi_z) & 0 & 0 & 0 & -\sin^2(\xi_z)+\cos^2(\xi_z) \end{bmatrix}. \tag{F5}$$

As a result, the material tensors are then obtained with the composite z-x-z rotation as

$$\begin{aligned} \boldsymbol{\epsilon}^S &= \boldsymbol{R}_{3,z}(\varphi)\{\boldsymbol{R}_{3,x}(\vartheta)[\boldsymbol{R}_{3,z}(\psi)\boldsymbol{\epsilon}_0^S\boldsymbol{R}_{3,z}(\psi)^T]\boldsymbol{R}_{3,x}(\vartheta)^T\}\boldsymbol{R}_{3,z}(\varphi)^T, \\ \boldsymbol{e} &= \boldsymbol{R}_{3,z}(\varphi)\{\boldsymbol{R}_{3,x}(\vartheta)[\boldsymbol{R}_{3,z}(\psi)\boldsymbol{e}_0\boldsymbol{R}_{6,z}(\psi)^T]\boldsymbol{R}_{6,x}(\vartheta)^T\}\boldsymbol{R}_{6,z}(\varphi)^T, \\ \boldsymbol{c}^E &= \boldsymbol{R}_{6,z}(\varphi)\{\boldsymbol{R}_{6,x}(\vartheta)[\boldsymbol{R}_{6,z}(\psi)\boldsymbol{c}_0^E\boldsymbol{R}_{6,z}(\psi)^T]\boldsymbol{R}_{6,x}(\vartheta)^T\}\boldsymbol{R}_{6,z}(\varphi)^T. \end{aligned} \tag{F6}$$

For a solid with uniaxial symmetry about the crystal Z axis, such as in our example (the wurtzite hexagonal crystal ZnO), the first z-axis rotation will not change the material tensors. Thus for such a symmetry, the description of the orientation can be simplified from the Euler angle system to the cylindrical angle system, which uses only a zenith angle ϑ and an azimuthal angle φ, as shown in Fig. 7(b). The corresponding rotation transformations will also be reduced to a two-step procedure: first a right-hand rotation of ϑ about the x axis, followed by a second rotation of φ about the z axis. The material tensors will then be obtained as

$$\begin{aligned} \boldsymbol{\epsilon}^S &= \boldsymbol{R}_{3,z}(\varphi)[\boldsymbol{R}_{3,x}(\vartheta)\boldsymbol{\epsilon}_0^S\boldsymbol{R}_{3,x}(\vartheta)^T]\boldsymbol{R}_{3,z}(\varphi)^T, \\ \boldsymbol{e} &= \boldsymbol{R}_{3,z}(\varphi)[\boldsymbol{R}_{3,x}(\vartheta)\boldsymbol{e}_0\boldsymbol{R}_{6,x}(\vartheta)^T]\boldsymbol{R}_{6,z}(\varphi)^T, \\ \boldsymbol{c}^E &= \boldsymbol{R}_{6,z}(\varphi)[\boldsymbol{R}_{6,x}(\vartheta)\boldsymbol{c}_0^E\boldsymbol{R}_{6,x}(\vartheta)^T]\boldsymbol{R}_{6,z}(\varphi)^T. \end{aligned} \tag{F7}$$

APPENDIX G: WAVE-MODE ASSIGNMENT

Conventionally, there are two different approaches that have been widely used to categorize the three bulk elastic wave mode solutions. The first approach considers the relation between the particle displacement vector (also commonly known as the polarization vector) and the propagation direction of the wave (wave vector): when an elastic wave has a polarization that is (mostly) parallel to the propagating direction, it is identified as a *(quasi-)longitudinal* wave, or an L mode; if a transverse wave is polarized (mostly) inside the plane of incidence and (not purely) perpendicular to the propagation direction, it is a *vertically polarized (quasi-)shear* wave or an SV mode; and if a transverse wave is (mostly) perpendicular to both the plane of incidence and the propagation direction, it is a *horizontally polarized (quasi-)shear* or an SH mode. For anisotropic crystals, the quasiprefixes mostly apply, as pure L, SV, and SH polarizations appear only in certain high-symmetry propagation directions [3].

The second approach is to compare the phase velocities $v = \omega/k$ of the wave modes, and to designate the mode from the fastest to the slowest as *(quasi-)longitudinal* wave (L), *fast (quasi-)transverse* wave (FT), and *slow (quasi-)transverse* wave (ST).

It should be noted here that the choice for the categorization of the wave modes is a conceptual definition based on exactly the same set of solutions of the constitutive equations, and, therefore the choice of the categorization will not affect the results of the formalism discussed in this article. However, for completeness and for the benefit of the discussion of topics such as mode conversions, we provide here a procedure that can be programed to consistently identify the wave modes based on both categorization approaches in this work.

A total of eight eigenvalues p_α and their associated eigenvectors $\boldsymbol{\xi}_\alpha$ can be obtained by solving the eigenfunction (3). In this section, we will examine these solutions with four different categorization methods:

(1) homogeneous or inhomogeneous wave;

(2) transmitted or reflected wave;

(3) the mode categorized as longitudinal (L), fast transverse (FT), slow transverse (ST), or electric potential (E);

(4) the mode categorized as longitudinal (L), vertically polarized shear (SV), horizontally polarized shear (SH), or electric potential (E).

The electric potential mode E is an inhomogeneous wave mode solution that appears in piezoelectric scattering problems (within the quasistatic approximation), describing a solution where the energy is mostly contained in the electric fields [3,48].

First, for a wave solution that has an eigenvalue $p_\alpha = p'_\alpha + ip''_\alpha$, we examine the imaginary part: If $p''_\alpha = 0$ ($p''_\alpha \neq 0$), the wave will be categorized as a homogeneous wave (an inhomogeneous wave).

Second, for an inhomogeneous wave, the scattering direction of the wave can be determined by the imaginary part of the eigenvalue: If $p''_\alpha > 0$ ($p''_\alpha < 0$) the wave will be categorized as a transmitted (reflected) wave. This follows from the principle that the physically allowed inhomogeneous wave solution can only decay (and not grow) from the interface. In contrast, for a homogeneous plane wave, the direction of the power flow should be examined, as the normal components of the wave vector and the power flow can have different directions in general. By acknowledging the time-averaged Poynting vector in Eq. (5), a wave with $P_{n\alpha} < 0$ ($P_{n\alpha} > 0$) is categorized as a transmitted (reflected) wave.

The aforementioned wave modes (e.g., FT, SV, etc.) are defined from a partial set of characteristics of the wave solutions, such as phase velocity, polarization vector, etc. Therefore, it can in some cases be tricky to fully map such simplified mode definitions to the corresponding full solutions, and ambiguity can arise. For example, in some cases four scattered bulk modes can be excited simultaneously (without the excitation of the inhomogeneous E mode) due to a strong electromechanical coupling [48]. Therefore, it should be kept in mind that the mode categorization method presented here is not a fully robust and generally applicable algorithm.

To assign the modes within the set L, FT, ST, and E, we first compare the magnitudes of the imaginary parts $|p''_\alpha|$ of all the inhomogeneous evanescent waves ($p''_\alpha \neq 0$), and identify them based on the ordering $|p''_E| > |p''_L| > |p''_{\mathrm{FT}}| \geqslant |p''_{ST}|$ (always starting from the E-mode, if fewer than four inhomogeneous modes exist). For the remaining unassigned homogeneous modes, the phase velocities $v_\alpha^2 = v_x^2/(1 + p_\alpha^2)$ will be examined, and the wave modes are assigned in the order $v_L^2 > v_{\mathrm{FT}}^2 \geqslant v_{ST}^2$, starting from the first unassigned mode. This means that if, for example, the L mode was identified already as inhomogeneous, the fastest homogeneous mode would then be FT.

Finally, if one wishes to assign the modes within the set quasi-L, -SV, -SH, and -E, the polarization vectors $\boldsymbol{A}_\alpha$ of the eigenvector solutions should be examined. However, we still first identify the inhomogeneous wave modes with the method described above, based on the magnitudes of the imaginary parts of the eigenvalues because there are often no clear general differences between the eigenvectors of the surface (inhomogeneous) modes.

In contrast, for the homogeneous modes, definitions based on the polarization vector exist. We identify them by comparing the polarization vector with the wave vector and the unit normal vector of the sagittal plane. If the quasi-L mode is still available for assignment, it can be identified from $|\boldsymbol{k} \cdot \boldsymbol{A}_L| > |\boldsymbol{k} \cdot \boldsymbol{A}_{SV,SH}|$. Within the coordinate system of this article, quasi-SV and quasi-SH modes can be identified from the relation $|[0, 1, 0]^T \cdot \boldsymbol{A}_{SV}| < |[0, 1, 0]^T \cdot \boldsymbol{A}_{SH}|$.

TABLE I. The common cut planes of hexagonal crystals: plane names, Miller indices, and rotation angles (ZnO).

Plane name	Miller index	$\angle_{\{hkil\}}$
a	$\{11\bar{2}0\}$	90°
m	$\{10\bar{1}0\}$	90°
c	{0001}	0°
r	$\{1\bar{1}02\}$	42.78°
n	$\{11\bar{2}3\}$	46.89°
s	$\{10\bar{1}1\}$	61.61°

APPENDIX H: COMMON CUT PLANES FOR A HEXAGONAL CRYSTAL

For hexagonal crystals, the four basis vector Miller-Bravais index system $\{hkil\}$ is commonly used to designate a crystallographic plane family [49]. These indices can be related to the crystal rotations, described in Sec. F, by $\vartheta = \angle_{\{hkil\}}$, in which $\angle_{\{hkil\}}$ is the angle between the plane normal and the crystal Z axis, and can be calculated from

$$\angle_{\{hkil\}} = \arccos\left(\frac{\overrightarrow{(hkl)}\cdot\overrightarrow{(001)}}{|\overrightarrow{(hkl)}||\overrightarrow{(001)}|}\right) = \arccos\left[al\left(\frac{4}{3}c^2\left(h^2+k^2+hk\right)+a^2l^2\right)^{-\frac{1}{2}}\right],$$

where a and c are the in-plane (X, Y) and out-of-plane (Z) lattice constants of the crystal, respectively. The common crystallographic plane families for ZnO are given in Table I with their corresponding $\angle_{\{hkil\}}$.

[1] D. Royer and E. Dieulesant, *Elastic Waves in Solids II, Generation, Acousto-Optic Interaction, Applications* (Springer-Verlag, Berlin, Heidelberg, 2000).

[2] D. Royer and E. Dieulesant, *Elastic Waves in Solids I, Free and Guided Propagation* (Springer-Verlag, Berlin, Heidelberg, 2000).

[3] B. A. Auld, *Acoustic Fields and Waves in Solids*, 2nd ed. (Krieger, Malabar, 1990).

[4] B. V. Budaev and D. B. Bogy, On the role of acoustic waves (phonons) in equilibrium heat exchange across a vacuum gap, Appl. Phys. Lett. **99**, 053109 (2011).

[5] Y. Ezzahri and K. Joulain, Vacuum-induced phonon transfer between two solid dielectric materials: Illustrating the case of Casimir force coupling, Phys. Rev. B **90**, 115433 (2014).

[6] S. Xiong, K. Yang, Y. A. Kosevich, Y. Chalopin, R. D'Agosta, P. Cortona, and S. Volz, Classical to Quantum Transition of Heat Transfer between Two Silica Clusters, Phys. Rev. Lett. **112**, 114301 (2014).

[7] V. Chiloyan, J. Garg, K. Esfarjani, and G. Chen, Transition from near-field thermal radiation to phonon heat conduction at sub-nanometre gaps, Nat. Commun. **6**, 6755 (2015).

[8] J. B. Pendry, K. Sasihithlu, and R. V. Craster, Phonon-assisted heat transfer between vacuum-separated surfaces, Phys. Rev. B **94**, 075414 (2016).

[9] A. I. Volokitin, Contribution of the acoustic waves to near-field heat transfer, J. Phys.: Condens. Matter **32**, 215001 (2020).

[10] M. Balakirev, S. Bogdanov, and A. Gorchakov, Tunneling of an ultrasonic wave across a gap between lithium iodate crystals, Fiz. Tverd. Tela (Leningrad) **20**, 587 (1978) [Sov. Phys. Solid State, **20**, 338 (1978)].

[11] M. Prunnila and J. Meltaus, Acoustic Phonon Tunneling and Heat Transport due to Evanescent Electric Fields, Phys. Rev. Lett. **105**, 125501 (2010).

[12] S. Kaliski, The passage of an ultrasonic wave across a contactless junction between two piezoelectric bodies, Proc. Vibr. Probl. Warsaw **7**, 95 (1966).

[13] M. Balakirev and A. Gorchakov, Leakage of an elastic wave across a gap between piezoelectrics, Fiz. Tverd. Tela (Leningrad) **19**, 571 (1977) [Sov. Phys. Solid State **19**, 327 (1977)].

[14] B. A. Auld, Wave propagation and resonance in piezoelectric materials, J. Acoust. Soc. Am. **70**, 1577 (1981).

[15] D. M. Barnett and J. Lothe, Dislocations and line charges in anisotropic piezoelectric insulators, Phys. Status Solidi B **67**, 105 (1975).

[16] J. Lothe and D. M. Barnett, Integral formalism for surface waves in piezoelectric crystals. existence considerations, J. Appl. Phys. **47**, 1799 (1976).

[17] A. N. Stroh, Steady state problems in anisotropic elasticity, J. Math. Phys. (Cambridge, Mass.) **41**, 77 (1962).

[18] P. Chadwick and G. D. Smith, Foundations of the theory of surface waves in anisotropic elastic materials, Adv. Appl. Mech. **17**, 303 (1977).

[19] T. C. T. Ting, *Anisotropic Elasticity: Theory and Applications* (Oxford University Press, New York, 1996).

[20] T. C. T. Ting, Recent developments in anisotropic elasticity, Int. J. Solids Struct. **37**, 401 (2000).

[21] V. Al'shits, A. Darinskii, and A. Shuvalov, Theory of reflection of acoustoelectric waves in a semiinfinite piezoelectric medium. I. Metallized surface, Kristallografiya **34**, 1340 (1989) [Sov. Phys. Crystallogr. **34**, 808 (1989)].

[22] V. Al'shits, A. Darinskii, and A. Shuvalov, Theory of reflection of acoustoelectric waves in a semiinfinite piezoelectric medium. II. Nonmetallized surface, Kristallografiya **35**, 7 (1990) [Sov. Phys. Crystallogr. **35**, 1 (1990)].

[23] V. Al'shits, A. Darinskii, and A. Shuvalov, Theory of reflection of acoustoelectric waves in a semiinfinite piezoelectric medium. III. Resonance reflection in the neighborhood of a branch of outflowing waves, Kristallografiya **36**, 284 (1991) [Sov. Phys. Crystallogr. **36**, 145 (1991)].

[24] M. Y. Chung and T. C. T. Ting, Line force, charge, and dislocation in anisotropic piezoelectric composite wedges and spaces, J. Appl. Mech. **62**, 423 (1995).

[25] M. Akamatsu and K. Tanuma, Green's function of anisotropic piezoelectricity, Proc. R. Soc. London, Ser. A **453**, 473 (1997).

[26] C. Hwu, Some explicit expressions of extended Stroh formalism for two-dimensional piezoelectric anisotropic elasticity, Int. J. Solids Struct. **45**, 4460 (2008).

[27] V. N. Lyubimov, V. I. Al'shits, and J. Lothe, Body waves and quasi-body surface waves in a semi-infinite piezoelectric medium, Kristallografiya **25**, 33 (1980) [Sov. Phys. Crystallogr. **25**, 16 (1980)].

[28] A. N. Darinskii and M. Weihnacht, Quasi-bulk surface and leaky waves in piezoelectrics of unrestricted symmetry, Proc. R. Soc. London, Ser. A **459**, 2977 (2003).

[29] V. I. Al'shits, A. N. Darinskii, and A. L. Shuvalov, Acoustoelectric waves in bicrystal media in conditions of a rigid contact or a vacuum gap at an interface, Kristallografiya **38**, 22 (1993) [Crystallogr. Rep. **38**, 147 (1993)].

[30] V. I. Al'shits, D. M. Barnett, A. N. Darinskii, and J. Lothe, On the existence problem for localized acoustic waves on the interface between two piezocrystals, Wave Motion **20**, 233 (1994).

[31] A. N. Darinskii and M. Weihnacht, Gap acousto-electric waves in structures of arbitrary anisotropy, IEEE Trans. Ultrson. Ferroelectr. Freq. Control **53**, 412 (2006).

[32] Y. V. Gulyaev and V. P. Plessky, Shear surface acoustic waves in dielectrics in the presence of an electric field, Phys. Lett. A **56**, 491 (1976).

[33] Y. V. Gulyaev and V. P. Plesskii, Acoustic gap waves in piezoelectric materials, Akust. Zh. **23**, 716 (1977) [Sov. Phys. Acoustics **23**, 410 (1977)].

[34] Y. E. Pak, Linear electro-elastic fracture mechanics of piezoelectric materials, Int. J. Fract. **54**, 79 (1992).

[35] J. Liang, J. Han, B. Wang, and S. Du, Electroelastic modelling of anisotropic piezoelectric materials with an elliptic inclusion, Int. J. Solids Struct. **32**, 2989 (1995).

[36] P. Lu, H. P. Lee, and C. Lu, Exact solutions for simply supported functionally graded piezoelectric laminates by stroh-like formalism, Compos. Struct. **72**, 352 (2006).

[37] A. N. Darinskii and A. L. Shuvalov, Existence of surface acoustic waves in one-dimensional piezoelectric phononic crystals of general anisotropy, Phys. Rev. B **99**, 174305 (2019).

[38] S. Benchabane, A. Khelif, J. Y. Rauch, L. Robert, and V. Laude, Evidence for complete surface wave band gap in a piezoelectric phononic crystal, Phys. Rev. E **73**, 065601(R) (2006).

[39] A. N. Darinskii, On the theory of leaky waves in crystals, Wave Motion **25**, 35 (1997).

[40] A. N. Darinskii, Leaky waves and the elastic wave resonance reflection on a crystal-thin solid layer interface. ii. leaky waves given rise to by exceptional bulk waves, J. Acoust. Soc. Am. **103**, 1845 (1998).

[41] D. Polder and M. Van Hove, Theory of radiative heat transfer between closely spaced bodies, Phys. Rev. B **4**, 3303 (1971).

[42] J. B. Pendry, Radiative exchange of heat between nanostructures, J. Phys.: Condens. Matter **11**, 6621 (1999).

[43] K. Joulain, J.-P. Mulet, F. Marquier, R. Carminati, and J.-J. Greffet, Surface electromagnetic waves thermally excited: Radiative heat transfer, coherence properties and Casimir forces revisited in the near field, Surf. Sci. Rep. **57**, 59 (2005).

[44] K. Malén and J. Lothe, Explicit expressions for dislocation derivatives, Phys. Status Solidi B **39**, 287 (1970).

[45] I. N. Court and F. K. von Willisen, Frustrated total internal reflection and application of its principle to laser cavity design, Appl. Opt. **3**, 719 (1964).

[46] M. Born and E. Wolf, *Principles of Optics*, 7th ed. (Cambridge University Press, Cambridge, 1999).

[47] H. Goldstein, *Classical Mechanics*, 2nd ed. (Addison-Wesley Publishing, Reading, 1980).

[48] A. G. Every and V. I. Neiman, Reflection of electroacoustic waves in piezoelectric solids: Mode conversion into four bulk waves, J. Appl. Phys. **71**, 6018 (1992).

[49] D. Schwarzenbach, Note on Bravais-Miller indices, J. Appl. Crystallogr. **36**, 1270 (2003).

PII

COMPLETE TUNNELING OF ACOUSTIC WAVES BETWEEN PIEZOELECTRIC CRYSTALS

by

Z. Geng & I. J. Maasilta

arXiv:2209.08287

Submitted manuscript.

Complete tunneling of acoustic waves between piezoelectric crystals

Zhuoran Geng* and Ilari J. Maasilta†
Nanoscience Center, Department of Physics, University of Jyväskylä, P. O. Box 35, FIN-40014 Jyväskylä, Finland
(Dated: February 22, 2023)

Abstract
When two piezoelectric solids are placed in close proximity, acoustic waves (phonons) can "tunnel" across a vacuum gap transmitting energy between the two solids. Here, we demonstrate analytically that not only is such a phenomenon possible, but that a simple resonance condition exists for which complete transmission of the incoming wave is possible. This result is derived for an arbitrary anisotropic crystal symmetry and orientation. We also show that the complete transmission condition can be related to the surface electric impedance and the effective surface permittivity of the piezoelectric material, making it possible to be determined experimentally. In addition, we present numerical results for the maximum power transmittance of a slow transverse wave, tunneling between identical ZnO crystals, as function of all possible crystal orientations. The results show a large range of orientations for which complete tunneling can be achieved.

INTRODUCTION

Acoustic waves (acoustic phonons) are deformations or vibrations propagating through a material medium. As such, they do not exist in vacuum, leading to the initial conclusion that it is impossible for the vacuum to transmit the energy of an acoustic wave between two separated media. However, at the atomic scale the vibrations of the nuclei can propagate via their electrical interactions through vacuum. Thus, a question can be raised, whether acoustic phonons can also be transmitted across larger than atomic scale vacuum gaps through some electromagnetic mechanism. This is a relevant question, as with the advances in experimental techniques, nanometer to subnanometer scale vacuum gaps can be achieved[1–4]. The possibility of such acoustic phonon "tunneling", as it is often called in the literature, has attracted a considerable amount of theoretical work in recent years to investigate possible mechanisms of the effect such as Casimir and van der Waals forces, particularly in the context of near-field heat transfer[5–17].

One possible mechanism for acoustic wave tunneling is piezoelectricity, as in piezoelectric materials mechanical displacements carry along macroscopic electric fields. When an acoustic wave in a piezoelectric solid impinges on a free surface, it extends a decaying, evanescent electric field into the vacuum [18]. The length scale of this decay is determined by the wavelength of the acoustic wave, so by bringing another piezoelectric solid within a wavelength, acoustic power can be transmitted into the second piezoelectric solid across the vacuum gap. What makes this piezoelectrically mediated acoustic wave tunneling particularly attractive is its length scale: it is not fixed to be in the nanoscale, but operates on the typically much larger wavelength scale defined by the frequency (1 GHz would correspond to ~ 5 μm). The effect was introduced [19, 20] and observed [21] long ago (for more detailed background, see [22]), but developed further more recently[5, 22, 23]. In particular in Ref.[22], a general formalism was introduced that is applicable to any incident bulk wave mode for any anisotropic crystallographic orientation. One of the most interesting suggestions in Refs.[5, 20, 23] is the possibility of unity transmission for some particular conditions, meaning that the incident wave could perhaps be completely transmitted into the adjacent solid. However, the discussions in Refs.[5, 20, 23] are limited either by the simplified models used, or only show numerical results for the highest symmetry crystal orientations. Until now, no rigorous proof of complete acoustic wave tunneling has been presented, nor have generally valid complete tunneling conditions been put forward.

In this work, we use the general formalism developed for piezoelectric acoustic wave tunneling in Ref.[22] to analytically prove the existence of the complete tunneling phenomenon, in general. In addition, a strikingly simple resonant tunneling condition is also derived for identical crystals, and we propose that this condition could be checked experimentally. Further discussion of the results are presented with a few numerical examples for ZnO crystals. In particular, we find our results differ from those obtained in Ref.[5].

RESULTS AND DISCUSSION

Tunneling of acoustic waves. We study a system of two anisotropic, semi-infinite piezoelectric solids separated by a vacuum gap of width d, as shown in Figure 1. Two coordinate systems describe the relation between the crystal intrinsic orientation, denoted by XYZ, and the external laboratory space, denoted by xyz. The surfaces of the solids are assumed to be mechanically and electrically free [22], with surface normals aligned with the z-axis. We consider an incoming homogeneous acoustic plane (bulk) wave $\sim \exp(-i\boldsymbol{k}\cdot\boldsymbol{r}+i\omega t)$, where $\boldsymbol{k}$ and ω are the wave vector and angular frequency, propagat-

* zhgeng@jyu.fi
† maasilta@jyu.fi

ing inside the xz-plane (sagittal plane) from the positive z-axis direction towards the surface at $z = 0$, with a positive x-component of wave vector ($k_x > 0$). In addition, we only consider low frequency acoustic waves with linear dispersion and assume the usual quasistatic approximation for piezoelectric acoustic waves [18] satisfying $\boldsymbol{E} = -\nabla\Phi$, where $\boldsymbol{E}$ and Φ are the electric field and the electric potential, respectively.

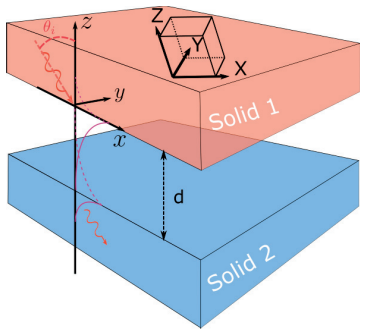

FIG. 1. **System under study.** Two piezoelectric solids 1, 2 are separated by a vacuum gap of width d. An incoming acoustic wave from solid 1 (positive z-axis of a laboratory coordinates xyz) with an incident angle θ_i tunnels across the vacuum gap into solid 2 inside the xz-plane. XYZ describe the intrinsic crystal coordinates, which can be rotated w.r.t. the xyz coordinates.

An incident bulk wave scatters into a linear combination of partial waves at an interface. These partial waves are either reflected or transmitted, and can either be homogeneous (bulk) waves or inhomogeneous (evanescent) waves bound on the surface of the solid [22]. The single surface reflection and transmission coefficients, which describe the amplitudes of these scattered waves, can be calculated following the multiple reflection method presented in Section III.B in Ref.[22]. We denote these coefficients with an overhead bar, as follows: $\bar{t}^{(1)}_{in\to V}$ is the coefficient of an incoming wave from solid 1 transmitted into a vacuum electric wave, $\bar{t}^{(2)}_{V\to\alpha}$ is the coefficient of an vacuum wave transmitted into mode α in solid 2, and $\bar{r}^{(i)}_V$ is the coefficient of an vacuum wave reflected on the vacuum side of the interface of solid $i = 1, 2$. In these coefficients, $\alpha = 1, ..., 4$ correspond to the four physically allowed partial wave modes in the corresponding solids 1 or 2.

A total transmission coefficient t_α, which describes the amplitude ratio of a transmitted partial wave α in solid 2 to an incoming bulk wave from solid 1, takes a form (for derivation, see Section I of the Supplementary Material)

$$t_\alpha = \frac{\bar{t}^{(1)}_{in\to V}\bar{t}^{(2)}_{V\to\alpha}}{e^{k_x d} - \bar{r}^{(1)}_V \bar{r}^{(2)}_V e^{-k_x d}} = \bar{t}^{(1)}_{in\to V}\bar{t}^{(2)}_{V\to\alpha} f_m(d) \ , \quad (1)$$

with k_x the wave vector component along the surfaces, which is conserved in the tunneling process. This expression can be interpreted as two single surface transmission coefficients $\bar{t}^{(1)}_{in\to V}$ and $\bar{t}^{(2)}_{V\to\alpha}$ coupled by a geometrical multiple reflection factor $f_m(d) = [\exp(k_x d) - \bar{r}^{(1)}_V \bar{r}^{(2)}_V \exp(-k_x d)]^{-1}$ [22]. It implicitly depends on the incident angle θ_i not only via $k_x = k \sin\theta_i$, but also via the coefficients $\bar{t}$ and $\bar{r}$, which are functions of $v_x = \omega/(k \sin\theta_i)$ (Section I in the Supplementary Material).

Derivation of the condition for complete tunneling. To fully describe the tunneling of the acoustic wave, we also look at the energy transfer between the solids. The time-averaged power flow density (energy flux, units [W/m^2]) of a transmitted partial wave in the direction normal to the surfaces (denoted as P_α) can be obtained from the real part of the normal component of piezoelectric Poynting vector (Section I in the Supplementary Material). For the tunneled bulk partial waves, the transmitted power relates to the normal component of the incident power by $P_\alpha = |t_\alpha|^2 P_{in}$, whereas the reflected or transmitted evanescent partial waves in solids 1,2 are bound onto the surface and carry no power in the normal direction ($P_\alpha = 0$ if α is an evanescent mode).

As there is no dissipation inside the vacuum gap, the normal direction power flow density inside the vacuum (denoted by P_V) is equal to the total normal direction transmitted power density (denoted by P_Σ). It is clear that P_Σ is the sum of P_α over all the transmitted *bulk* waves in solid 2, and we can write it using Eq.(1) as $P_\Sigma = \sum_\alpha |\bar{t}^{(1)}_{in\to V}\bar{t}^{(2)}_{V\to\alpha} f_m(d)|^2 P_{in}$, where α runs only over the bulk modes. The number of transmitted bulk modes can be from zero to three (in some cases four[24]), and if there is no bulk mode available, the power flow in both the vacuum and solid 2 are zero. On the other hand, the normal power flow inside the vacuum gap can be expressed using the Poynting's theorem under the quasistatic approximation as $P_V = 2|\bar{t}^{(1)}_{in\to V} f_m(d)|^2 \mathrm{Re}[\bar{r}^{(2)}_V] P_{in}$ (see Section II in the Supplementary Material for the derivation). As a result, from $P_V = P_\Sigma$ we find a relation

$$2\mathrm{Re}\left[\bar{r}^{(2)}_V\right] = \sum_{\alpha=\mathrm{bulk}} |\bar{t}^{(2)}_{V\to\alpha}|^2 \ , \quad (2)$$

which allows us to calculate the total transmitted power by simply using the single surface reflection coefficient $\bar{r}^{(2)}_V$, without having to sum over the transmitted bulk modes.

Furthermore, if we assume that the two solids consist of the same material with identical crystal orientations, two additional relations that link the single surface coefficients of the two solids can be found by exploiting the completeness of the eigensolutions of the scattering problem (see Section III in the Supplementary Material for the derivations). The first one relates the reflection coefficients $\bar{r}^{(i)}_V$ of the two solids as

$$\bar{r}_V \equiv \bar{r}^{(2)}_V = -\bar{r}^{(1)}_V \ . \quad (3)$$

The second one states that if the transmitted bulk wave mode γ in the solid 2 is the same mode as the incident

wave in solid 1, there exists a relation

$$\bar{t}^{(1)}_{\gamma\to V} = \bar{t}^{(2)}_{V\to\gamma}. \tag{4}$$

In addition, by comparing the relation (4) with Eq. (2), we find the condition

$$2\mathrm{Re}(\bar{r}_V) \geq |\bar{t}^{(1)}_{in\to V}|^2 \ , \tag{5}$$

where the equality is satisfied when there exists only one transmitted bulk wave mode in solid 2 and the mode is the same as the incident wave in solid 1. By applying the relations (2) and (3), P_Σ can then be simplified to

$$\frac{P_\Sigma}{P_{in}} = \frac{2\mathrm{Re}(\bar{r}_V)|\bar{t}^{(1)}_{in\to V}|^2}{4\mathrm{Re}(\bar{r}_V)^2 + \left(e^{2k_x d} - |\bar{r}_V|^2\right)^2 e^{-2k_x d}} \ , \tag{6}$$

which explicitly depends only on two single surface coefficients: $\bar{t}^{(1)}_{in\to V}$ and $\bar{r}_V$.

Eq. (6) shows that the total transmitted power P_Σ is always less than the incident power P_{in} if more than one transmitted bulk wave modes exist, since in that case the inequality Eq.(5) takes the "greater-than" sign. This result has the important implication that complete tunneling, i.e. the full transmission of the incident power, can't be achieved if the transmitted wave consists of multiple partial bulk waves, in contradiction to Ref.[5].

In contrast, if there is only one transmitted homogeneous bulk mode and it is the same mode as the incident wave, then the "equal" sign of Eq.(5) is valid, and Eq.(6) simplifies to

$$\frac{P_\Sigma}{P_{in}} = \frac{4\mathrm{Re}(\bar{r}_V)^2}{4\mathrm{Re}(\bar{r}_V)^2 + \left(e^{2k_x d} - |\bar{r}_V|^2\right)^2 e^{-2k_x d}}. \tag{7}$$

From Eq. (7), it is clear that the maximum transmitted power is *exactly* equal to the incident power ($P_\Sigma = P_{in}$) when the resonance condition

$$|\bar{r}_V| = e^{k_x d} \ , \tag{8}$$

is satisfied. This proves that (i) unity transmission (complete tunneling) of an acoustic wave across a vacuum gap is possible, and (ii) the condition for it depends explicitly only on the single surface reflection coefficient $\bar{r}_V$, the wave vector component k_x and the gap width d.

In particular, with a given material and crystal orientation, $\bar{r}_V$ is only a function of the incident angle and is independent of the gap width or the existence of the adjacent solid. We propose that, as a material parameter, $\bar{r}_V$ could be determined experimentally by measuring the effective surface permittivity $\epsilon_{\mathrm{eff}}(v_x)$[23, 25, 26] or the TM-wave surface impedance $Z_p(\omega, v_x)$[27, 28] of the piezoelectric solid. They are found to be related by expressions (see Section IV in the Supplementary Material

$$\bar{r}_V = i\frac{\epsilon_{\mathrm{eff}} - \epsilon_0}{\epsilon_{\mathrm{eff}} + \epsilon_0}, \quad \bar{r}_V = i\frac{1 + iv_x\epsilon_0 Z_p}{1 - iv_x\epsilon_0 Z_p}, \tag{9}$$

where ϵ_0 is the vacuum permittivity. The effective surface permittivity concept is useful in the study of piezoelectric materials, for example for the generation and detection of acoustic waves by transducers [26] or for determining the gap wave modes between piezoelectric solids[23]. We find the symmetric and antisymmetric gap wave conditions can be simply expressed by $\bar{r}_V = \pm i\exp(k_x d)$ (Section IV, Supplemental Material).

Numerical examples and physical interpretation of complete tunneling between identical ZnO crystals. We now turn to demonstrate the complete tunneling effect with numerical examples for two identical ZnO crystals, using the formalism developed in Ref.[22]. The first example is shown in Figure 2, where the two crystals are separated with a scaled gap width of $kd = 0.01$, and are both rotated first with respect to the x-axis by $\vartheta = 46.89°$ and then to the z-axis by $\varphi = 88°$ (see Ref.[22] for details on the crystal rotation procedure). The mode of the incident wave in this example is chosen to be the slowest quasi-transversal wave (ST), so that there exists a critical incident angle beyond which only one bulk transmitted wave can be found, thus satisfying the general condition for complete tunneling.

In Fig.2(a), we plot the transmittance into each bulk mode P_α/P_{in} as a function of the incident angle θ, where α can be the quasi-longitudinal (L), the fast quasi-transversal (FT) or the slow quasi-transversal (ST) mode, categorized based on their phase velocities. We see that for most angles, transmittance is low, except for the two sharp transmission peaks for the ST mode giving exactly unity transmission at angles between 75° and 80°. Abrupt cut-offs are visible for the transmitted L and FT modes, corresponding to the critical incident angles $\theta_{L_c} \approx 28°$ and $\theta_{FT_c} \approx 63.5°$. Beyond these critical angles, the corresponding modes become evanescent, bound on the surface of the solid with no direct energy transmission into the bulk.

Figure 2(b) provides a zoomed view on the resonant transmission peaks, now with two different scaled gap values $kd = 1$ (blue solid line) and $kd = 0.01$ (orange solid line), with an overlay of the $|\bar{r}_V|$ curve (black dashed line), helping us also to understand the doublet structure. The additional two colored dashed lines represent two values of the resonance condition of Eq.(8). It is clear that the unity transmission occurs where the resonance condition is valid, proving consistency between the analytical theory and the numerical approach. In addition, we see that with the increase of the scaled gap width from 0.01 to 1, the separation of the peaks is reduced, and with a further increase the two solutions would merge into one at the maximum of $|\bar{r}_V|$. With this particular ZnO crystal orientation, this maximum is about 4 as shown in the plot, which leads to a maximum gap width of $kd \approx 1.4$ to observe complete tunneling (merged unity transmission peak). For ZnO (ST wave velocity $v = 2780$ m/s), and a 2 GHz frequency relevant for device applications, this corresponds to a quite a long physical distance of $d = 300$ nm with the parameters and the orientation used

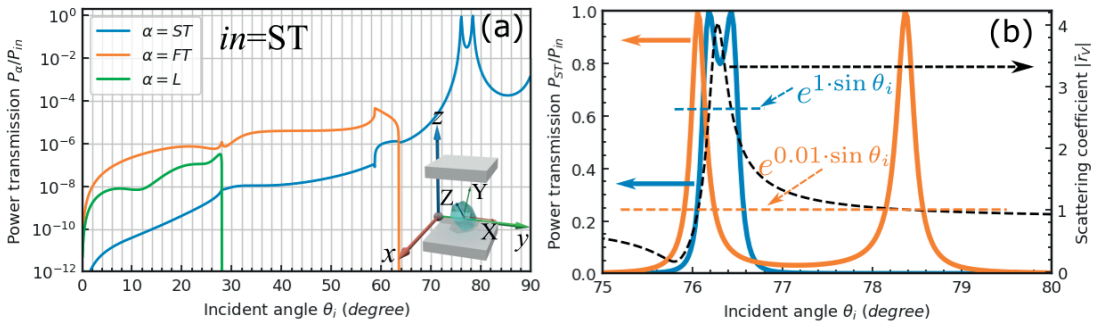

FIG. 2. **Angular dependence of the power transmittance of an incoming ST wave.** (a) Power transmittance P_α/P_{in} of the longitudinal $\alpha = L$ (green), the fast transverse $\alpha = FT$ (orange) and the slow transverse $\alpha = ST$ (blue) waves, for an incoming ST wave as function of the incident angle θ_i, for two identical ZnO crystals separated by a scaled gap $kd = 0.01$ and oriented with a zenith angle $\vartheta = 46.89°$ and an azimuth angle $\varphi = 88°$ (inset). We used the anisotropic crystal parameters $c_{11} = 20.97\times10^{10}$ N/m^2, $c_{33} = 21.09\times10^{10}$ N/m^2, $c_{44} = 4.247\times10^{10}$ N/m^2, $c_{12} = 12.11\times10^{10}$ N/m^2, $c_{13} = 10.51\times10^{10}$ N/m^2, $c_{66} = (c_{11} - c_{12})/2$, $\epsilon_{xx} = 8.55\epsilon_0$, $\epsilon_{zz} = 10.2\epsilon_0$, $e_{x5} = -0.48$ C/m^2, $e_{z1} = -0.573$ C/m^2, $e_{z3} = 1.32$ C/m^2, and the density $\rho = 5680$ kg/m^3, taken from Ref.[18]. (b) Zoomed view on the peaks of the transmittance (left axis) with two values $kd = 1$ (blue solid line) and $kd = 0.01$ (orange solid line). The single surface reflection coefficient $|\bar{r}_V|$ curve (black dashed line) is overlayed (right axis) together with $\exp(k_x d) = \exp(\sin\theta_i)$ (blue horizontal dashed line) and $\exp(k_x d) = \exp(0.01\sin\theta_i)$ (orange horizontal dashed line) to demonstrate the resonance condition, Eq.(8), for the two scaled gaps, respectively.

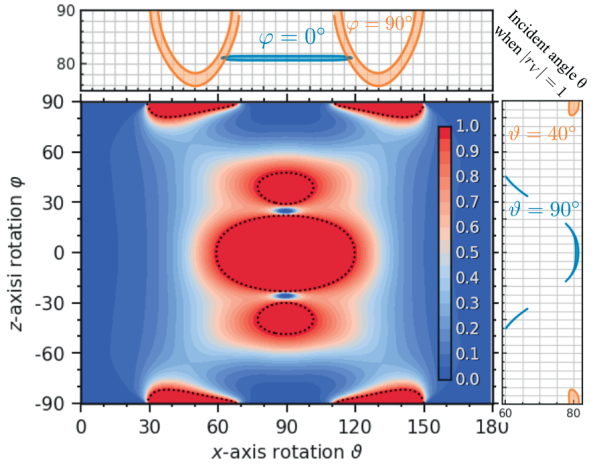

FIG. 3. **Crystal rotation map for complete tunneling between ZnO crystals.** Color scale of the ST-to-ST mode maximum power transmittance P_{ST}/P_{in} over all incident angles, plotted as function of crystal rotation angles ϑ and φ for anisotropic ZnO. The dotted lines encircle the regions where $|\bar{r}_V| > 1$. The panels on the top and on the right show the range of θ_i where $|\bar{r}_V| > 1$ for two fixed φ (top), or ϑ (right). Here, we fix $k_x d = kd\sin\theta_i$ instead of kd, as complete tunneling can be achieved by tuning k_x either by changing the incident angle θ_i or by the angular frequency ω.

in the example.

In general, the complete resonant tunneling can take place for a range of crystal orientations. In Fig. 3 we show the numerically calculated maximal power transmittance P_{ST}/P_{in} (over all θ_i) of an incident ST mode to a transmitted ST mode, as a function of all possible crystal rotations [29], using again parameters for anisotropic ZnO[18] and a fixed scaled gap $k_x d = 0.01$. We find a significant parameter space for orientations, with multiple separate regions, where complete tunneling is possible (dark red regions). To validate the consistency of the numerics with the analytical condition, Eq.(8), we also plot a set of dotted contour lines in Figure.3(a) to encircle the orientations satisfying $|\bar{r}_V| > 1$, where unity transmission is possible, finding excellent agreement. Another observation is that the incident angle θ_i satisfying complete tunneling varies for different crystal orientations, reaching as low values as 60° in some cases (right panel).

To understand the physics, we first consider the the three ellipsoidal unity transmission areas around $\vartheta = 90°$ [Figure 3(a)]. Inside these areas, the incident ST waves are not pure shear waves and therefore couple to the other partial waves (L, FT) at the surface. As a result, when the incoming ST wave has an incident angle beyond the critical angle of the FT mode, the reflected FT wave becomes evanescent, with its energy concentrated on the surface. For those orientations the FT-mode waves are predominately polarized in the direction of the c-axis, the direction of the piezoelectric dipole, creating a strong piezoelectric response. That excites large electric potential differences on the surface and hence gives rise to a strong electric coupling across the gap, which finally enables the resonant transmission. On the other hand, when the azimuth rotations approach $\varphi = \pm90°$ with $\vartheta = 90°$, the c-axis aligns with the x-axis and the ST mode becomes a pure shear mode, polarized perpendicular to the sagittal plane. Then the incident ST waves are very weakly piezoelectric, and also decouple from all other partial modes.

Other interesting features can also be observed in Figure 3. Nodes having low transmission at around $\varphi = \pm 25^\circ$ and $\vartheta = 90^\circ$ appear. This is because the electric potential excited by the reflected FT wave mode change polarity around these nodes, leading to minimized potential differences and weak coupling between the two surfaces. In addition, unity transmission is also observed in four small areas around $\varphi = \pm 90^\circ$, where the single surface reflection coefficient $\bar{r}^{(1)}_{ST\to FT}$ of the reflected FT partial waves increases significantly (not shown). This indicates an enhanced mode conversion between the ST and FT partial wave modes at these orientations, providing large electric potential differences on the solid-vacuum interface again via the evanescent FT wave, leading to strong tunneling signal. A more detailed discussion of the physical interpretation of the resonance can be found in Section V of the Supplemental Material.

Our numerical formalism can also be applied to the particular case studied with a simplified model in Ref.[5], the details of which can be found in Section VI of the Supplementary Material We do not find complete tunneling for the incoming modes and the crystal orientation in question, in contradiction to Ref.[5].

CONCLUSIONS

In conclusion, we have analytically and numerically proven it is possible for acoustic waves to completely tunnel across a vacuum gap between two piezoelectric solids, up to gap sizes of about a wavelength. We showed that such complete tunneling, with unity power transmittance, is possible only if one transmitted partial bulk mode is excited, it being the same mode as the incident wave. We derived a strikingly simple resonance tunneling condition for the complete tunneling effect, Eq.(8), and proved its validity and range of applicability with numerical examples for arbitrarily rotated ZnO crystals. As this is a strong and not a rare effect, it could have an impact in future acoustic wave devices, as well as in other application areas concerning phonons, such as controlling heat transport, optomechanics and quantum information science.

Data availability All relevant data are available from the authors upon request.

Code availability All relevant code for simulations are available from the authors upon request.

[1] K. Kim, B. Song, V. Fernández-Hurtado, W. Lee, W. Jeong, L. Cui, D. Thompson, J. Feist, M. T. Reid, F. J. García-Vidal, J. C. Cuevas, E. Meyhofer, and P. Reddy, Radiative heat transfer in the extreme near field, Nature **528**, 387 (2015).

[2] K. Kloppstech, N. Könne, S. A. Biehs, A. W. Rodriguez, L. Worbes, D. Hellmann, and A. Kittel, Giant heat transfer in the crossover regime between conduction and radiation, Nat. Commun. **8**, 14475 (2017).

[3] J. Cui, J. Zhang, T. Barayavuga, X. Wang, X. He, L. Yang, H. Xie, X. Mei, and W. Wang, Nanofabrication with the thermal AFM metallic tip irradiated by continuous laser, Integr. Ferroelectr. **179**, 140 (2017).

[4] A. Jarzembski, T. Tokunaga, J. Crossley, J. Yun, C. Shaskey, R. A. Murdick, I. Park, M. Francoeur, and K. Park, Role of acoustic phonon transport in near- to asperity-contact heat transfer, Phys. Rev. B **106**, 205418 (2022).

[5] M. Prunnila and J. Meltaus, Acoustic phonon tunneling and heat transport due to evanescent electric fields, Phys. Rev. Lett. **105**, 125501 (2010).

[6] D. P. Sellan, E. S. Landry, K. Sasihithlu, A. Narayanaswamy, A. J. McGaughey, and C. H. Amon, Phonon transport across a vacuum gap, Phys. Rev. B. **85**, 024118 (2012).

[7] B. N. Persson, A. I. Volokitin, and H. Ueba, Phononic heat transfer across an interface: Thermal boundary resistance, J. Phys.: Condens. Matter **23**, 045009 (2011).

[8] V. Chiloyan, J. Garg, K. Esfarjani, and G. Chen, Transition from near-field thermal radiation to phonon heat conduction at sub-nanometre gaps, Nat. Commun. **6**, 6755 (2015).

[9] B. V. Budaev and D. B. Bogy, On the role of acoustic waves (phonons) in equilibrium heat exchange across a vacuum gap, Appl. Phys. Lett. **99**, 053109 (2011).

[10] Y. Ezzahri and K. Joulain, Vacuum-induced phonon transfer between two solid dielectric materials: Illustrating the case of Casimir force coupling, Phys. Rev. B **90**, 115433 (2014).

[11] K. Sasihithlu, J. B. Pendry, and R. V. Craster, Van der Waals Force Assisted Heat Transfer, Z. Naturforsch. **72**, 181 (2017).

[12] J. B. Pendry, K. Sasihithlu, and R. V. Craster, Phonon-assisted heat transfer between vacuum-separated surfaces, Phys. Rev. B **94**, 075414 (2016).

[13] A. I. Volokitin, Effect of an Electric Field in the Heat Transfer between Metals in the Extreme Near Field, JETP Lett. **109**, 749 (2019).

[14] A. I. Volokitin, Contribution of the acoustic waves to near-field heat transfer, J. Phys.: Condens. Matter **32**, 215001 (2020).

[15] S. A. Biehs, A. Kittel, and P. Ben-Abdallah, Fundamental limitations of the mode temperature concept in strongly coupled systems, ZNA **75**, 803 (2020).

[16] A. Alkurdi, C. Adessi, F. Tabatabaei, S. Li, K. Termentzidis, and S. Merabia, Thermal transport across nanometre gaps: Phonon transmission vs. air conduction, International Journal of Heat and Mass Transfer **158**, 119963 (2020).

[17] T. Tokunaga, M. Arai, K. Kobayashi, W. Hayami, S. Suehara, T. Shiga, K. Park, and M. Francoeur, First-principles calculations of phonon transport across a vacuum gap, Phys. Rev. B **105**, 045410 (2022).

[18] B. Auld, *Acoustic fields and waves in solids*, 2nd ed. (Krieger, Malabar, Florida, 1990).

[19] S. Kaliski, The passage of an ultrasonic wave across a contactless junction between two piezoelectric bodies, Proc. Vibr. Probl. Warsaw **7**, 95 (1966).

[20] M. Balakirev and A. Gorchakov, Leakage of an elastic wave across a gap between piezoelectrics, Fiz. Tverd. Tela (Leningrad) **19**, 571 (1977), [Sov. Phys. Solid State **19**, 327 (1977)].
[21] M. Balakirev, S. Bogdanov, and A. Gorchakov, Tunneling of ultrasonic wave through a gap between lithium iodate crystals, Fiz. Tverd. Tela (Leningrad) **20**, 587 (1978), [Sov. Phys. Solid State, **20**, 338 (1978)].
[22] Z. Geng and I. J. Maasilta, Acoustic wave tunneling across vacuum gap between two piezoelectric crystals with arbitrary symmetry and orientation, Phys. Rev. Research **4**, 033073 (2022).
[23] A. N. Darinskii and M. Weihnacht, Gap Acousto-Electric Waves in Structures of Arbitrary Anisotropy, IEEE Trans. Ultrason. Ferroelectr. Freq. Control **53**, 412 (2006).
[24] A. G. Every and V. I. Neiman, Reflection of the electroacoustic waves in piezoelectric solids: Mode conversion into four bulk waves, J. Appl. Phys. **71**, 6018 (1992).
[25] G. Maugin, *Continuum mechanics of electromagnetic solids* (Elsevier, Amsterdam, the Netherlands, 1988).
[26] R. F. Milsom, N. H. Reilly, and M. Redwood, Analysis of Generation and Detection of Surface and Bulk Acoustic Waves by Interdigital Transducers, IEEE Trans. Sonics Ultrason. **SU-24**, 147 (1977).
[27] K. A. Ingebrigtsen, Surface waves in piezoelectrics, J. Appl. Phys. **40**, 2681 (1969).
[28] Y. Zhang, J. Desbois, and L. Boyer, New method to characterize the surface-generated bulk acoustic waves in piezoelectric substrates, J. Acoust. Soc. Am. **92**, 2499 (1992).
[29] ZnO has a crystallographic $6mm$ system with uniaxial symmetry[18], hence all the unique orientations of the crystal can be represented by the direction of the crystal c-axis (Z-axis) using a zenith angle $\vartheta \in (0^\circ, 180^\circ)$ and an azimuth angle $\varphi \in (-90^\circ, 90^\circ)$.

Acknowledgements
This study was supported by the Academy of Finland project number 341823.

Author contributions
Z. G. and I. M. conceived the idea, carried out the analytical derivations and wrote the manuscript. Z.G. carried out all the numerical calculations.

Competing interests
The authors declare no competing interests.

Supplemental Material: Complete tunneling of acoustic waves between piezoelectric crystals

Zhuoran Geng* and Ilari J. Maasilta†
Nanoscience Center, Department of Physics, University of Jyväskylä, P. O. Box 35, FIN-40014 Jyväskylä, Finland

I. DERIVATION OF TRANSMISSION COEFFICIENT USING EXTENDED STROH FORMALISM AND MULTIPLE REFLECTION APPROACH

Here, we revisit the derivations presented in Ref. [1] for the acoustic phonon tunneling transmission coefficient and power flow density in the piezoelectric solids.

In piezoelectric solids, the dynamics of a propagating plane (bulk) wave $\sim \exp(-i\boldsymbol{k}\cdot\boldsymbol{r}+i\omega t)$ are governed by the elastic equation of motion $\nabla\cdot\boldsymbol{\sigma}=\rho\partial^2\boldsymbol{u}/\partial t^2$, Gauss's law $\nabla\cdot\boldsymbol{D}=0$, together with the piezoelectric constitutive relations [2]:

$$\begin{aligned}\boldsymbol{\sigma}&=\boldsymbol{c}^E:\boldsymbol{S}-\boldsymbol{e}\cdot\boldsymbol{E}\\ \boldsymbol{D}&=\boldsymbol{e}:\boldsymbol{S}+\boldsymbol{\epsilon}^S\cdot\boldsymbol{E}\end{aligned}\tag{1}$$

where $\boldsymbol{S}$, $\boldsymbol{\sigma}$, $\boldsymbol{u}$, $\boldsymbol{D}$ are the elastic strain, elastic stress, mechanical displacement and electric displacement fields, ρ, $\boldsymbol{c}^E$, $\boldsymbol{e}$, $\boldsymbol{\epsilon}^S$ are the mass density, elastic stiffness tensor at constant electric field, piezoelectric stress tensor and electric permittivity tensor at constant strain, respectively. The double dot product indicates summation over paired indices between second-rank and higher-rank tensors, and the strain-displacement relation reads as $S_{ij}=(\partial u_i/\partial r_j+\partial u_j/\partial r_i)/2$.

An incident plane wave is scattered into a linear combination of partial waves at an interface, which are either reflected or transmitted. The general solutions of such partial waves that satisfy the governing equations take the expressions [3–5]:

$$\begin{aligned}\boldsymbol{u}&=\sum_\alpha b_\alpha\boldsymbol{A}_\alpha e^{-i(k_xx+k_yy+p_\alpha k_xz-\omega t)}\\ \Phi&=\sum_\alpha b_\alpha\phi_\alpha e^{-i(k_xx+k_yy+p_\alpha k_xz-\omega t)}\\ \boldsymbol{n}\cdot\boldsymbol{\sigma}&=ik_x\sum_\alpha b_\alpha\boldsymbol{L}_\alpha e^{-i(k_xx+k_yy+p_\alpha k_xz-\omega t)}\\ \boldsymbol{n}\cdot\boldsymbol{D}&=ik_x\sum_\alpha b_\alpha D_\alpha e^{-i(k_xx+k_yy+p_\alpha k_xz-\omega t)}\ ,\end{aligned}\tag{2}$$

in which $\boldsymbol{n}$ is the unit vector of the z-axis. $\boldsymbol{A}_\alpha,\phi_\alpha,\boldsymbol{L}_\alpha,D_\alpha$ are the normalized constants describing the polarization vector, the electric potential, the normal projection of the traction force and the normal projection of the electric displacement of a partial wave mode α, respectively. b_α are dimensionless amplitudes of the partial waves, and $p\equiv k_z/k_x$. To avoid redundant writing in the following expressions, we omit the common phase factor $\exp(-ik_xx-ik_yy+i\omega t)$ shared by all solutions.

In this study, we solved these governing equations under the framework of extended Stroh formalism, as described in Ref.[1], in which Eq.(1) is combined and rearranged into an eight-dimensional eigenvalue problem [6, 7] in the form of:

$$\boldsymbol{N}(v_x)\boldsymbol{\xi}_\alpha=p_\alpha\boldsymbol{\xi}_\alpha\ ,\tag{3}$$

where $\boldsymbol{N}$ is 8×8 real matrix and $v_x\equiv\omega/k_x$ is the x-component of the phase velocity. Generally, eight linearly independent eigenvectors $\boldsymbol{\xi}_\alpha=[\boldsymbol{A}_\alpha,\phi_\alpha,\boldsymbol{L}^n_\alpha,D^n_\alpha]^T$ and corresponding eigenvalues p_α can be obtained for partial wave modes $\alpha=1,...,8$. These eigenvectors follow the orthonormalization and completeness conditions

$$\boldsymbol{\xi}^T_\alpha\hat{\boldsymbol{T}}\boldsymbol{\xi}_\beta=\delta_{\alpha\beta}\tag{4}$$

$$\sum\boldsymbol{\xi}_\alpha\otimes\hat{\boldsymbol{T}}\boldsymbol{\xi}_\alpha=\hat{\boldsymbol{I}}_{8\times8}\ ,\tag{5}$$

where the operator $\otimes$ denotes the outer product of two matrices, $\delta_{\alpha\beta}$ is the Kronecker delta, $\hat{\boldsymbol{I}}_{8\times8}$ is 8×8 unit matrix, and $\hat{\boldsymbol{T}}$ takes the form:

$$\hat{\boldsymbol{T}}=\begin{bmatrix}\boldsymbol{O}_{4\times4}&\hat{\boldsymbol{I}}_{4\times4}\\ \hat{\boldsymbol{I}}_{4\times4}&\boldsymbol{O}_{4\times4}\end{bmatrix}\tag{6}$$

where $\boldsymbol{O}_{4\times4}$ and $\hat{\boldsymbol{I}}_{4\times4}$ are 4×4 zero and unity matrices.

The continuity of the electric potential ($\Phi^{(i)}=\Phi_V$, where the subscript $i=1,2$ indicates the medium index and the subscript V indicates the vacuum) and the normal component of electric displacement ($\boldsymbol{n}\cdot\boldsymbol{D}^{(i)}=\boldsymbol{n}\cdot\boldsymbol{D}_V$), as well as the condition of a mechanically free surface ($\boldsymbol{n}\cdot\boldsymbol{\sigma}^{(i)}=\boldsymbol{0}$) enforce the boundary conditions of the two solid-vacuum interfaces:

$$\begin{aligned}b^{(1)}_{in}\boldsymbol{U}^{(1)}_{in}+\sum_{\alpha=1}^4 b^{(1)}_\alpha\boldsymbol{U}^{(1)}_\alpha&=b_{V_+}\boldsymbol{U}_{V_+}+b_{V_-}\boldsymbol{U}_{V_-}\ ,\\ \sum_{\alpha=1}^4\tilde{b}^{(2)}_\alpha\boldsymbol{U}^{(2)}_\alpha&=b_{V_+}\boldsymbol{U}_{V_+}e^{-k_xd}+b_{V_-}\boldsymbol{U}_{V_-}e^{k_xd}\ ,\end{aligned}\tag{7}$$

in which we introduce 5×1 column vectors $\boldsymbol{U}^{(i)}_\gamma=[\phi^{(i)}_\gamma,D^{(i)}_\gamma,\boldsymbol{L}^{(i)}_\gamma]^T$ for wave modes $\gamma=in,\alpha$, where the subscript in indicates the incident wave mode, $\alpha=1,...,4$ corresponds to four physically allowed wave modes in their corresponding medium $i=1,2$, $\boldsymbol{U}_{V_\pm}=$

* zhgeng@jyu.fi
† maasilta@jyu.fi

$[\phi_{V_\pm}, D_{V_\pm}, 0, 0, 0]^T$, and $\tilde{b}_\alpha^{(2)} \equiv b_\alpha^{(2)} \exp(ip_\alpha^{(2)} k_x d)$ for simplicity. In the vacuum region, the electric potential and displacement fields take the form

$$\begin{aligned} \Phi_V(z) &= b_{V_+}\phi_{V_+} e^{k_x z} + b_{V_-}\phi_{V_-} e^{-k_x z} \\ \boldsymbol{n}\cdot\boldsymbol{D}_V(z) &= -\epsilon_0 k_x b_{V_+}\phi_{V_+} e^{k_x z} + \epsilon_0 k_x b_{V_-}\phi_{V_-} e^{-k_x z} \ , \end{aligned} \tag{8}$$

where $\phi_{V_\pm} = 1/\sqrt{\pm 2i\epsilon_0}$, noting the normalization condition for the vacuum mode $2\phi_{V_\pm} D_{V_\pm} = 1$.

The amplitude factors $b_\alpha^{(i)}$ can be solved from the boundary conditions of Eqs.(7), following the multiple reflection method introduced in Ref.[1]: The single surface reflection ($\bar{r}_{in\to\alpha}^{(i)}$, $\bar{r}_V^{(i)}$) and transmission ($\bar{t}_{V\to\alpha}^{(i)}$, $\bar{t}_{in\to V}^{(i)}$) coefficients are calculated first via scattering matrices $\mathbb{S}^{(i)}$ for solid $i = 1, 2$, and the total transmission coefficient t_α for a partial mode α is then obtained by coupling the single surface coefficients with a multiple reflection factor $f_m(d)$, which explicitly depends on the gap distance d. We note here that the overlined single surface coefficients describe the scattering of the electroacoustic wave as if there is no second adjacent solid.

The 5×2 scattering matrices $\mathbb{S}^{(1)}$ and $\mathbb{S}^{(2)}$ take the following form:

$$\begin{aligned} \mathbb{S}^{(1)} &= \begin{bmatrix} \bar{\boldsymbol{r}}^{(1)} & \bar{\boldsymbol{t}}^{(1)} \\ \bar{t}_{in\to V}^{(1)} & \bar{r}_V^{(1)} \end{bmatrix} \\ &= \big[\boldsymbol{U}_1^{(1)}, ..., \boldsymbol{U}_4^{(1)}, -\boldsymbol{U}_{V_+}\big]^{-1}\big[-\boldsymbol{U}_{in}^{(1)}, \boldsymbol{U}_{V_-}\big], \\ \mathbb{S}^{(2)} &= \begin{bmatrix} \bar{\boldsymbol{r}}^{(2)} & \bar{\boldsymbol{t}}^{(2)} \\ \bar{t}_{in\to V}^{(2)} & \bar{r}_V^{(2)} \end{bmatrix} \\ &= \big[\boldsymbol{U}_1^{(2)}, ..., \boldsymbol{U}_4^{(2)}, -\boldsymbol{U}_{V_-}\big]^{-1}\big[\boldsymbol{U}_{in}^{(2)}, \boldsymbol{U}_{V_+}\big] \end{aligned} \tag{9}$$

where the expression $\bar{\boldsymbol{r}}^{(i)} = [\bar{r}_{in\to 1}^{(i)}, ..., \bar{r}_{in\to 4}^{(i)}]^T$ and $\bar{\boldsymbol{t}}^{(i)} = [\bar{t}_{V\to 1}^{(i)}, ..., \bar{t}_{V\to 4}^{(i)}]^T$ are the single surface reflection and transmission coefficients of modes $\alpha = 1, ..., 4$.

The total transmission coefficient t_α from an incoming bulk wave in solid 1 into a partial wave of mode α in solid 2 can be obtained as

$$t_\alpha \equiv \frac{\tilde{b}_\alpha^{(2)}}{b_{in}^{(1)}} = \bar{t}_{in\to V}^{(1)} \bar{t}_{V\to\alpha}^{(2)} f_m(d) \tag{10}$$

where the multiple reflection factor is $f_m(d) = [\exp(k_x d) - \bar{r}_V^{(1)} \bar{r}_V^{(2)} \exp(-k_x d))]^{-1}$. Equation (10) is identical to Eq.(1) in the main text.

The time-averaged transmitted power flow density in the direction normal to the surfaces from solid 1 to 2 can be expressed by the real part of the piezoelectric Poynting vector in the normal direction[3]

$$P_\alpha = -\frac{\omega k_x}{4} |b_\alpha|^2 \boldsymbol{\xi}_\alpha^T \hat{\boldsymbol{T}} \boldsymbol{\xi}_\alpha^* \ . \tag{11}$$

For transmitted homogeneous (bulk) waves, $\boldsymbol{\xi}_\alpha^T \hat{\boldsymbol{T}} \boldsymbol{\xi}_\alpha^* = \pm \boldsymbol{\xi}_\alpha^T \hat{\boldsymbol{T}} \boldsymbol{\xi}_\alpha = \pm 1$, due to the Stroh-normalization condition, (Eq.(4)). Therefore $|t_\alpha|^2$ can be interpreted as the power flow ratio (the transmittance) of the transmitted bulk partial wave over the incident wave in the normal direction:

$$P_\alpha = |t_\alpha|^2 P_{in} \ . \tag{12}$$

II. POWER FLOW INSIDE VACUUM GAP

For a piezoelectric solid, an incoming acoustic wave can excite an electric potential inside the vacuum in the vicinity of its surface, and hence transmit power across the vacuum to an adjacent solid via means of an quasi-electrostatic field[1]. The time-averaged power flow $\boldsymbol{P}$ inside the vacuum gap can be expressed by the real part the complex Poynting vector of electromagnetism, $\boldsymbol{P} = \mathrm{Re}(\boldsymbol{E} \times \boldsymbol{H}^*)/2$, where $\boldsymbol{E}$ and $\boldsymbol{H}$ are the electric and magnetic fields, respectively.

Taking the divergence of the cross product of the fields and applying the cross product rule, we can obtain the equation

$$\nabla \cdot (\boldsymbol{E} \times \boldsymbol{H}^*) = (\nabla \times \boldsymbol{E}) \cdot \boldsymbol{H}^* - \boldsymbol{E} \cdot (\nabla \times \boldsymbol{H}^*) \ . \tag{13}$$

Under the quasistatic approximation, the rotational electric field component is set to zero, which corresponds to $\nabla \times \boldsymbol{E} = 0$ and $\boldsymbol{E} = -\nabla \Phi_V$, where Φ_V is the electrostatic potential inside the vacuum. In addition, for an electrically free surface with no net charge density or current, Gauss's law leads to $\nabla \cdot \boldsymbol{D} = 0$, and Ampere's circuital law relates the magnetic field to the electric displacement as $\nabla \times \boldsymbol{H} = \partial \boldsymbol{D}/\partial t$. By applying the dot product rule for this quasistatic case, Eq.(13) becomes

$$\begin{aligned} \nabla \cdot (\boldsymbol{E} \times \boldsymbol{H}^*) &= \nabla \cdot \left(\Phi_V \frac{\partial \boldsymbol{D}^*}{\partial t} \right) - \Phi_V \nabla \cdot \frac{\partial \boldsymbol{D}^*}{\partial t} \\ &= \nabla \cdot \left(\Phi_V \frac{\partial \boldsymbol{D}^*}{\partial t} \right) \ . \end{aligned} \tag{14}$$

As a result, the time-averaged power flow inside the vacuum in the direction normal to the interface can be expressed as

$$P_V \equiv \boldsymbol{n} \cdot \boldsymbol{P} = -\frac{1}{2} \mathrm{Re}\big[i\omega \Phi_V (D_V^n)^* \big] \ , \tag{15}$$

where $D_V^n \equiv \boldsymbol{n} \cdot \boldsymbol{D}_V$ is the normal component of the electric displacement in vacuum.

The expressions of Φ_V and D_V^n, derived in Ref.[1], are given as (by omitting the common phase factor $\exp(-ik_x x + i\omega t)$)

$$\begin{aligned} \Phi_V(z) &= b_{V_+}\phi_{V_+} e^{k_x z} + b_{V_-}\phi_{V_-} e^{-k_x z} \\ D_V^n(z) &= -\epsilon_0 k_x b_{V_+}\phi_{V_+} e^{k_x z} + \epsilon_0 k_x b_{V_-}\phi_{V_-} e^{-k_x z} \ , \end{aligned} \tag{16}$$

where ϵ_0 is the vacuum permittivity and $\phi_{V_\pm} = 1/\sqrt{\pm 2i\epsilon_0}$. The dimensionless amplitudes $b_{V_\pm}$ of the decaying and increasing partial waves in vacuum can be

expressed in terms of the single surface coefficients as

$$\begin{aligned} b_{V_+} &= \bar{t}^{(1)}_{in\to V} b^{(1)}_{in} + \bar{r}^{(1)}_{V} b_{V_-} \\ b_{V_-} &= \bar{r}^{(2)}_{V} b_{V_+} e^{-2k_x d} \ , \end{aligned} \tag{17}$$

where $b^{(1)}_{in}$ is the amplitude of the incident wave in solid 1.

Inserting Eqs.(16) and (17) into the expression of the vacuum power flow, Eq.(15), we obtain

$$\begin{aligned} P_V =& -\frac{\omega k_x}{4} 2\mathrm{Re}(b_{V_+} b^*_{V_-}) \\ =& -\frac{\omega k_x}{4} |b_{V_+}|^2 e^{-2k_x d} \mathrm{Re}\Big[2\mathrm{Re}(\bar{r}^{(2)}_V) \\ & + i(|\bar{r}^{(2)}_V|^2 e^{-2k_x(z+d)} - e^{2k_x(z+d)}) \Big] \\ =& -\frac{\omega k_x}{2} |b_{in} \bar{t}^{(1)}_{in\to V} f_m(d)|^2 \mathrm{Re}(\bar{r}^{(2)}_V) \ , \end{aligned} \tag{18}$$

where the first line shows the analogy with quantum mechanical tunneling. The above expression also shows that the power flow is constant inside the vacuum gap, independent of z. This makes sense since there is no input or output for the energy flux inside the vacuum gap. We also note that the incident power flow is $P_{in} = -\omega k_x |b_{in}|^2/4$ so that Eq.(18) reduced to

$$P_V = 2|\bar{t}^{(1)}_{in\to V} f_m(d)|^2 \mathrm{Re}(\bar{r}^{(2)}_V) P_{in} \ . \tag{19}$$

III. RELATIONS OF SINGLE SURFACE TRANSMISSION AND REFLECTION COEFFICIENTS

By explicitly writing the completeness of the Stroh eigenvectors, Eq.(5), one finds $\sum_\alpha \phi_\alpha D_\alpha = 1$, and that $\sum_\alpha \phi_\alpha \phi_\alpha$, $\sum_\alpha D_\alpha D_\alpha$, $\sum_\alpha \boldsymbol{L}^T_\alpha \boldsymbol{L}_\alpha$, $\sum_\alpha \phi_\alpha \boldsymbol{L}_\alpha$, $\sum_\alpha D_\alpha \boldsymbol{L}_\alpha$ are all zero or zero matrices. Here $\alpha = 1, ..., 8$ correspond to the eight solutions obtained from the eigenvalue problem of Eq.(3). For waves in the vacuum, we have $\phi_{V_+} D_{V_+} + \phi_{V_-} D_{V_-} = 1$ as a manifestation of the Stroh-normalization, and $\phi_{V_+}\phi_{V_+} + \phi_{V_-}\phi_{V_-} = D_{V_+} D_{V_+} + D_{V_-} D_{V_-} = 0$, which are computed using $\phi_{V_\pm} = 1/\sqrt{\pm 2i\epsilon_0}$ and $D_{V_\pm} = \pm i\epsilon_0 \phi_{V_\pm}$[1], and $\boldsymbol{L}_{V_\pm} = \boldsymbol{0}$ because the traction force is zero in vacuum.

In the case of tunneling between two identical solids, four of the solutions are the reflected wave modes in solid 1, *e.g.* the solutions $\alpha = 1, ..., 4$ are the reflected waves designated with indices $i = 1, ..., 4$ in solid 1, and the remaining four solutions are the transmitted wave modes in solid 2, *e.g.* the solutions $\alpha = 5, ..., 8$ are the transmitted waves designated with indices $i = 1, ..., 4$ in solid 2. As result, the relations we obtained from the completeness condition lead to an equation that reads as (similar to Eq.(11) in Ref.[8])

$$\sum_i^4 \boldsymbol{U}^{(1)}_i \otimes \boldsymbol{U}^{(1)}_i + \sum_i^4 \boldsymbol{U}^{(2)}_i \otimes \boldsymbol{U}^{(2)}_i = \boldsymbol{U}_{V_+} \otimes \boldsymbol{U}_{V_+} + \boldsymbol{U}_{V_-} \otimes \boldsymbol{U}_{V_-} \ . \tag{20}$$

Here we want to convert the outer products of the above equation into products of determinants of 5×5 matrices constructed from horizontally stacked column vectors of $\boldsymbol{U}$. We use the Laplace expansion of the determinant

$$||\boldsymbol{A}|| = \sum_{i=1}^{n} (-1)^{i+j} a_{ij} M_{ij}, \tag{21}$$

where the operator $||...||$ denotes the determinant of matrix $\boldsymbol{A}$, a_{ij} is the element of a $n \times n$ matrix $\boldsymbol{A}$, and M_{ij} is defined to be the determinant of a $(n-1) \times (n-1)$ matrix that results from $\boldsymbol{A}$ by removing the i-th row and the j-th column. One sees that the determinant can be calculated from one of the columns of the matrix $\boldsymbol{A}$, *e.g.* for $j = 5$, the corresponding cofactor is $C = (-1)^{i+5} M_{i5}$, which is independent of that column (a_{i5}). As result, if we introduce a 5×5 matrix $\boldsymbol{A} = [\boldsymbol{U}^{(1)}_1 \boldsymbol{U}^{(1)}_2 \boldsymbol{U}^{(1)}_3 \boldsymbol{U}^{(1)}_4 \boldsymbol{U}_\alpha]$ in which $\boldsymbol{U}_\alpha$ can be any of the following solutions $\boldsymbol{U}^{(1)}_i, \boldsymbol{U}^{(2)}_i$ or $\boldsymbol{U}_{V_\pm}$, one has $||\boldsymbol{A}|| = \sum (-1)^{i+5} a_{i5} M_{i5} = \boldsymbol{C}\boldsymbol{U}_\alpha$, where a_{i5} is the element of column vector $\boldsymbol{U}_\alpha$. The cofactors can be combined into a row vector $\boldsymbol{C}$ which is independent of $\boldsymbol{U}_\alpha$ and can be calculated from the remaining columns of $\boldsymbol{A}$ excluding $\boldsymbol{U}_\alpha$.

Let us assume a transmitted wave solution $\boldsymbol{U}^{(2)}_1$ which is both the incoming and the transmitted wave mode, and construct two row cofactor vectors $\boldsymbol{C}^L$ and $\boldsymbol{C}^R$ from two matrices $\boldsymbol{A}^L = [\boldsymbol{U}^{(1)}_1 \boldsymbol{U}^{(1)}_2 \boldsymbol{U}^{(1)}_3 \boldsymbol{U}^{(1)}_4 \boldsymbol{U}_\alpha]$ and $\boldsymbol{A}^R = [\boldsymbol{U}^{(2)}_2 \boldsymbol{U}^{(2)}_3 \boldsymbol{U}^{(2)}_4 \boldsymbol{U}_{V_-} \boldsymbol{U}_\alpha]$, respectively. Then we left multiply by $\boldsymbol{C}^L$ and right multiply by $\boldsymbol{C}^R$ Eq.(20), and, by eliminating the linearly dependent terms whose determinants equal zero, we obtain the relation

$$\frac{||\boldsymbol{U}^{(1)}_1 \boldsymbol{U}^{(1)}_2 \boldsymbol{U}^{(1)}_3 \boldsymbol{U}^{(1)}_4 \boldsymbol{U}^{(2)}_1||}{||\boldsymbol{U}^{(1)}_1 \boldsymbol{U}^{(1)}_2 \boldsymbol{U}^{(1)}_3 \boldsymbol{U}^{(1)}_4 \boldsymbol{U}_{V_+}||} = \frac{||\boldsymbol{U}^{(2)}_2 \boldsymbol{U}^{(2)}_3 \boldsymbol{U}^{(2)}_4 \boldsymbol{U}_{V_-} \boldsymbol{U}_{V_+}||}{||\boldsymbol{U}^{(2)}_2 \boldsymbol{U}^{(2)}_3 \boldsymbol{U}^{(2)}_4 \boldsymbol{U}_{V_-} \boldsymbol{U}^{(2)}_1||} \ . \tag{22}$$

Considering the boundary condition of a scattering problem of a single semi-infinite half space

$$b_\gamma \boldsymbol{U}^{(2)}_\gamma + \sum_{i=1}^{4} b_i \boldsymbol{U}^{(1)}_i = b_{V_+} \boldsymbol{U}_{V_+} \ , \tag{23}$$

where $\gamma = 1$ is the incident wave mode, it can be shown that the the LHS of Eq.(22) is the single surface transmission coefficient $\bar{t}^{(1)}_{\gamma\to V}$ of an incoming wave ($\boldsymbol{U}^{(2)}_{\gamma=1}$) into vacuum mode ($\boldsymbol{U}_{V_+}$), using Cramer's rule. Similarly, with the boundary condition

$$\sum_{i=1}^{4} b_i \boldsymbol{U}^{(2)}_i = b_{V_+} \boldsymbol{U}_{V_+} + b_{V_-} \boldsymbol{U}_{V_-} \ , \tag{24}$$

the RHS of Eq.(22) is the single surface transmitted coefficient $\bar{t}^{(2)}_{V\to\gamma}$ of an incoming vacuum wave ($\boldsymbol{U}_{V_+}$) to the same wave mode as the incident wave ($\boldsymbol{U}^{(2)}_{\gamma=1}$). Thereby, we arrive at a simple relation $\bar{t}^{(1)}_{\gamma\to V} = \bar{t}^{(2)}_{V\to\gamma}$, if the mode

solution of the transmitted wave in solid 2 is the same as the incident wave, *e.g.* $\boldsymbol{U}^{(2)}_{\gamma=1}$ as the solution for both waves in the above example.

We can also construct the cofactors $\boldsymbol{C}^L$ and $\boldsymbol{C}^R$ from the matrices $\boldsymbol{A}^L = [\boldsymbol{U}^{(1)}_1\boldsymbol{U}^{(1)}_2\boldsymbol{U}^{(1)}_3\boldsymbol{U}^{(1)}_4\boldsymbol{U}_\alpha]$ and $\boldsymbol{A}^R = [\boldsymbol{U}^{(2)}_1\boldsymbol{U}^{(2)}_2\boldsymbol{U}^{(2)}_3\boldsymbol{U}^{(2)}_4\boldsymbol{U}_\alpha]$, respectively, and obtain

$$\frac{||\boldsymbol{U}^{(1)}_1\boldsymbol{U}^{(1)}_2\boldsymbol{U}^{(1)}_3\boldsymbol{U}^{(1)}_4\boldsymbol{U}_{V_-}||}{||\boldsymbol{U}^{(1)}_1\boldsymbol{U}^{(1)}_2\boldsymbol{U}^{(1)}_3\boldsymbol{U}^{(1)}_4\boldsymbol{U}_{V_+}||} = -\frac{||\boldsymbol{U}^{(2)}_1\boldsymbol{U}^{(2)}_2\boldsymbol{U}^{(2)}_3\boldsymbol{U}^{(2)}_4\boldsymbol{U}_{V_+}||}{||\boldsymbol{U}^{(2)}_1\boldsymbol{U}^{(2)}_2\boldsymbol{U}^{(2)}_3\boldsymbol{U}^{(2)}_4\boldsymbol{U}_{V_-}||} \ . \tag{25}$$

We can also consider the boundary condition

$$\sum_{i=1}^{4} b_i\boldsymbol{U}^{(1)}_i = b_{V_+}\boldsymbol{U}_{V_+} + b_{V_-}\boldsymbol{U}_{V_-}\,, \tag{26}$$

which describes an evanescent wave in vacuum with an amplitude b_{V_-} scattering on the surface of the solid 1. The resulting reflection coefficient $\bar{r}^{(1)}_V \equiv b_{V_+}/b_{V_-}$ can then be expressed using the LHS of Eq.(25) using the Cramer's rule. Similarly, by considering a reciprocal boundary condition on the surface of solid 2

$$\sum_{i=1}^{4} b_i\boldsymbol{U}^{(2)}_i = b_{V_+}\boldsymbol{U}_{V_+} + b_{V_-}\boldsymbol{U}_{V_-}\,, \tag{27}$$

where the incident amplitude is set to be b_{V_+}, one finds that the reflection coefficient $\bar{r}^{(2)}_V$ is the RHS of Eq.(25). As a result, another important relation $\bar{r}^{(1)}_V = -\bar{r}^{(2)}_V$ is obtained.

IV. SURFACE IMPEDANCE AND EFFECTIVE PERMITTIVITY

At a surface, the electrical potential Φ and the electrical displacement $D^n = \boldsymbol{n}\cdot\boldsymbol{D}$ that is normal to the surface are dependent. For a wave propagating inside the xz-plane (as in the main text), the ratio of Φ and D^n is [9]:

$$\frac{\Phi}{D^n} = \frac{iv_x^2}{\omega}Z_p, \tag{28}$$

where Z_p is the TM-wave impedance defined by $Z_p = E_x/H_y$, the ratio of the transverse electric and magnetic fields.

By inserting the expressions of the electric displacement $D^n_V(z)$ and potential $\Phi_V(z)$ in vacuum at $z=-d$ from Eqs.(16), we obtain

$$Z(\omega, v_x) = \frac{i}{v_x\epsilon_0}\frac{b_{V_+}\phi_{V_+}e^{-k_xd} + b_{V_-}\phi_{V_-}e^{k_xd}}{b_{V_+}\phi_{V_+}e^{-k_xd} - b_{V_-}\phi_{V_-}e^{k_xd}} \ . \tag{29}$$

With the relations $b_{V_-} = \bar{r}_V b_{V_+}\exp(-2k_xd)$ and $\phi_{V_-} = i\phi_{V_+}$ that were obtained in Section II, and with $k_x = \omega/v_x$, the expression of the impedance is further simplified to:

$$\bar{r}_V = i\frac{1+iv_x\epsilon_0Z_p}{1-iv_x\epsilon_0Z_p}. \tag{30}$$

The effective surface permittivity can be obtained from the impedance[9, 10] as $\epsilon_{\text{eff}} = i/[v_xZ_p(\omega, v_x)]$, hence we can relate it with $\bar{r}_V$ with the expression

$$\bar{r}_V = i\frac{\epsilon_{\text{eff}}-\epsilon_0}{\epsilon_{\text{eff}}+\epsilon_0} \ . \tag{31}$$

In addition, the symmetric and antisymmetric conditions of the subsonic gap waves were given by Eqs.(8) in Ref.[11] and read as

$$\begin{aligned} \epsilon_0\tanh\left(\frac{k_xd}{2}\right) + \epsilon_{\text{eff}} &= 0 \\ \epsilon_0\coth\left(\frac{k_xd}{2}\right) + \epsilon_{\text{eff}} &= 0 \ . \end{aligned} \tag{32}$$

By inserting Eq.(31) in the above conditions, they reduce to $\bar{r}_V = -i\exp(k_xd)$ and $\bar{r}_V = i\exp(k_xd)$, respectively.

V. PHYSICAL INTERPRETATION OF THE RESONANCE CONDITION: DISPLACEMENT FIELD, ELECTRIC POTENTIAL AND POYNTING VECTOR AT THE INTERFACE

As discussed in the main text, acoustic wave tunneling is enabled by evanescent modes that are localized at solid-vacuum interfaces. In particular, the complete tunneling phenomenon requires resonant effects that can concentrate the energy of the waves at the surface and therefore excite large electric potentials. Here, we provide plots to visually demonstrate such resonant phenomena, by plotting examples of the displacement $\boldsymbol{u}$, the electric potential Φ and the time-averaged electroacoustic Poynting vector $\boldsymbol{P}$ fields at the surface of the solids using the numerical example for ZnO crystals shown in Figure 2 of the main text (crystal rotation angles $\vartheta = 46.89°$ and $\varphi = 88°$, incoming ST wave), for which complete tunneling is possible.

When the resonant tunneling condition is satisfied, which means an incident angle $\theta = 76.06°$ or $\theta = 78.37°$ in the case we discuss here, the incoming bulk ST wave in solid 1 completely tunnels across the vacuum gap to the adjacent solid 2, and therefore no reflected bulk ST wave propagates into the depth of solid 1. However, such a reflected wave can still propagate along the surface of solid 1, having a decaying displacement amplitude in the direction normal to the surface, as demonstrated in Figure.1(a). In this solution, three partial modes, the longitudinal (L), the faster transversal (FT) and the electrical (E) are coupled and become a generalized Rayleigh wave solution [2], whereas the reflected bulk slow transversal (ST) wave has an exactly zero amplitude, and therefore

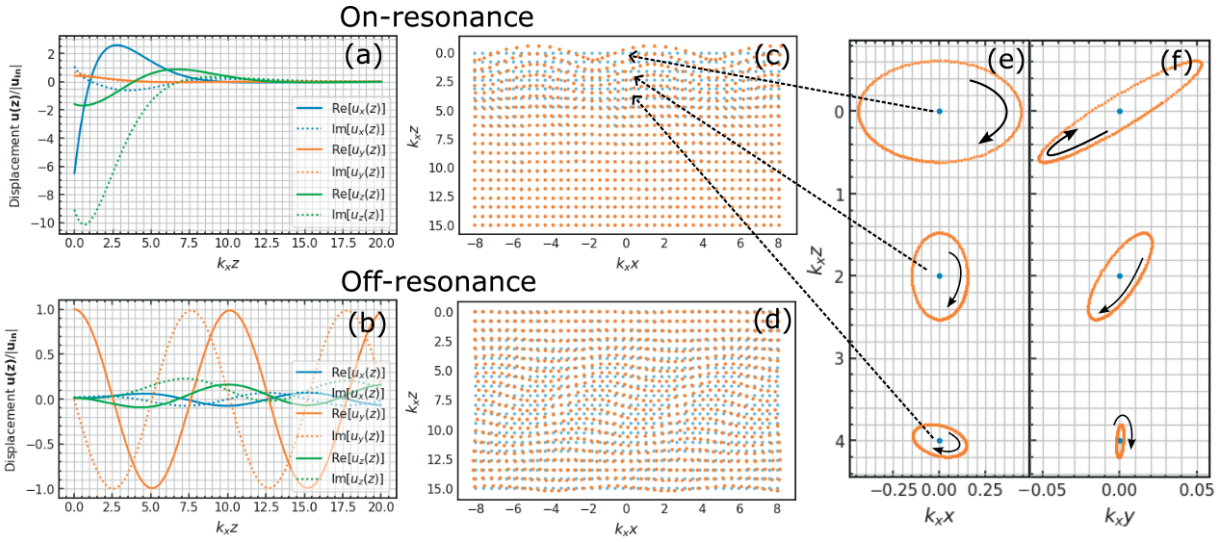

FIG. 1. The scattered particle displacement field $\boldsymbol{u}$ at the resonant incident angle $\theta = 76.06°$ [(a),(c),(e)] and at off-resonant angle $\theta = 60°$ [(b),(d)]. Panels (a) and (b) show the three components u_x (blue), u_y (orange) and u_z (green) of the complex displacement vector amplitude (solid = real part, dotted = imaginary part) as a function of the z-axis position inside solid 1. The values are normalized to the amplitude of the incident displacement vector $|\boldsymbol{u}_{in}|$. Panels (c) and (d) show schematically the displacement fields in the sagittal plane using a snapshot of the displacement of the positions of imaginary particles (orange dots) from their equilibrium positions (blue dots). Panels (e) (x-z plane projection) and (f) (y-z plane projection) show the time evolution of three such particles [equilibrium positions (x,y,z)=(0,0,0), (0,0,2) and (0,0,4)] for the resonant case (c), for one period of oscillation from $\omega t = 0$ to $\omega t = 2\pi$.

doesn't contribute to the coupled wave solution. This generalized Rayleigh wave is not a true pure surface eigenmode (which couldn't be excited by a incoming bulk mode), but is "leaky", as it couples to a scattered bulk mode in solid 2 through the tunneling phenomenon.

Figure 1(c) schematically shows what the reflected waveform looks like in the resonant tunneling case, by plotting pieces of the solid as particles (orange dots) displaced from their equilibrium positions (blue dots) in solid 1. A strong wave motion is present at the surface of the solid ($k_x z = 0$), but disappears into the depth of the solid. In addition, in Fig.1(e) and (f) the motions of three "particles" near the surface at equilibrium positions $(k_x x, k_x y, k_x z)$=(0,0,0), (0,0,2) and (0,0,4) are shown in $x-z$ and $x-y$ planes as a function of time from $\omega t = 0$ to $\omega t = 2\pi$, with the incident angle the same as in panels (a) and (c). The elliptical particle motions (the orange dots) resemble the classical Rayleigh-type surface wave motion, justifying the use of the term generalized Rayleigh wave.

In comparison, with an incident angle of $\theta = 60°$ corresponding to off-resonant conditions, the wave motion is strong in the bulk of the solid, and there is no surface mode or decay of the displacement vectors, as can be seen in Figs.1(b) and (d).

We should emphasize that the above surface wave solution does not exist on a single surface, but is a result of the resonant tunneling. Subsequently, it is very sensitive to the conditions, *e.g.* the incident angle, the gap distance, and the crystal orientations, and a small change in any of them will break the exact resonance and lead to a finite amplitude of the reflected bulk ST mode.

Figure 2 presents time snapshots of the normalized electric potentials Φ inside solid 1 for two different incident angles, $\theta = 76.06°$ [on resonance, panels (a)-(f)] and $\theta = 60°$ [off-resonance, panels (g)-(l)]. In the resonant case, the sum of the electric potentials Φ of all the reflected partial waves in solid 1 [Figure.2(b)] is localized near the surface ($k_x z = 0$) and decays to zero into the depth of the solid, as expected for a surface wave mode. Notably, the amplitude of the potential is also much higher than the incident bulk ST wave amplitude [Fig.2(a)], more than 17 orders of magnitude at the maximum. We also see that the partial modes of the reflected waves E [Fig.2 (c)], L [Fig.2 (d)] and FT [Fig.2 (e)] are all evanescent and have similarly high potentials, whereas the only reflected bulk ST mode has a practically zero amplitude ($\sim 10^{-12}$). We note that the small but finite amplitude of the reflected ST mode in this example is simply because of the numerical precision of the computation, and is exactly zero, as proven analytically in the main text.

As a comparison, the sum of the reflected waves in the off-resonant case, in Fig.2 (h) has a propagating component into the bulk, and its maximum potential at the surface ($\sim 10^{13}$) is about four orders of magnitude smaller

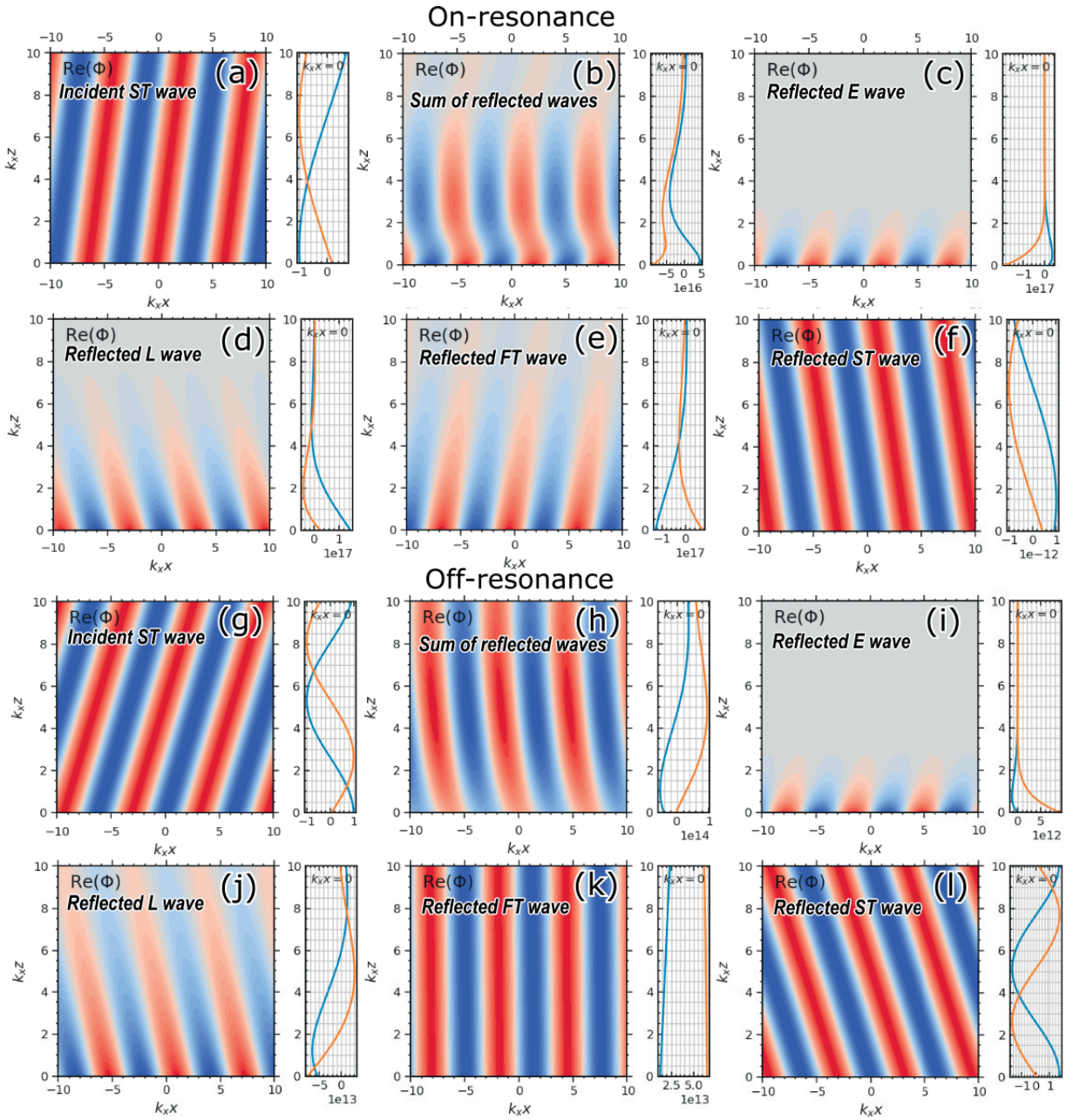

FIG. 2. Snapshot of the normalized electric potential Φ inside solid 1 on resonance (incident angle $\theta = 76.06^\circ$), panels (a)-(f), and off-resonance (incident angle $\theta = 60^\circ$), panels (g)-(l). All values are scaled to the amplitude of the incident Φ. Scaled axes $k_x x$ and $k_x z$ represent the spatial coordinates x and z. The solid-vacuum interface is at $k_x z = 0$. Panels (a) and (g) show the real part of Φ of an incident slow transverse (ST) wave, (b) and (h) the sum of of all reflected waves, (c) and (i) the reflected electrical (E), (d) and (j) the longitudinal (L), (e) and (k) the fast transversal (FT), and (f) and (l) the slow transverse (ST) partial modes. In each plot, the main panel shows the color scale of Re(Φ) inside the sagittal plane. The right panels show the real (blue) and imaginary (yellow) parts of Φ as function of the scaled coordinate $k_x z$ at $k_x x = 0$.

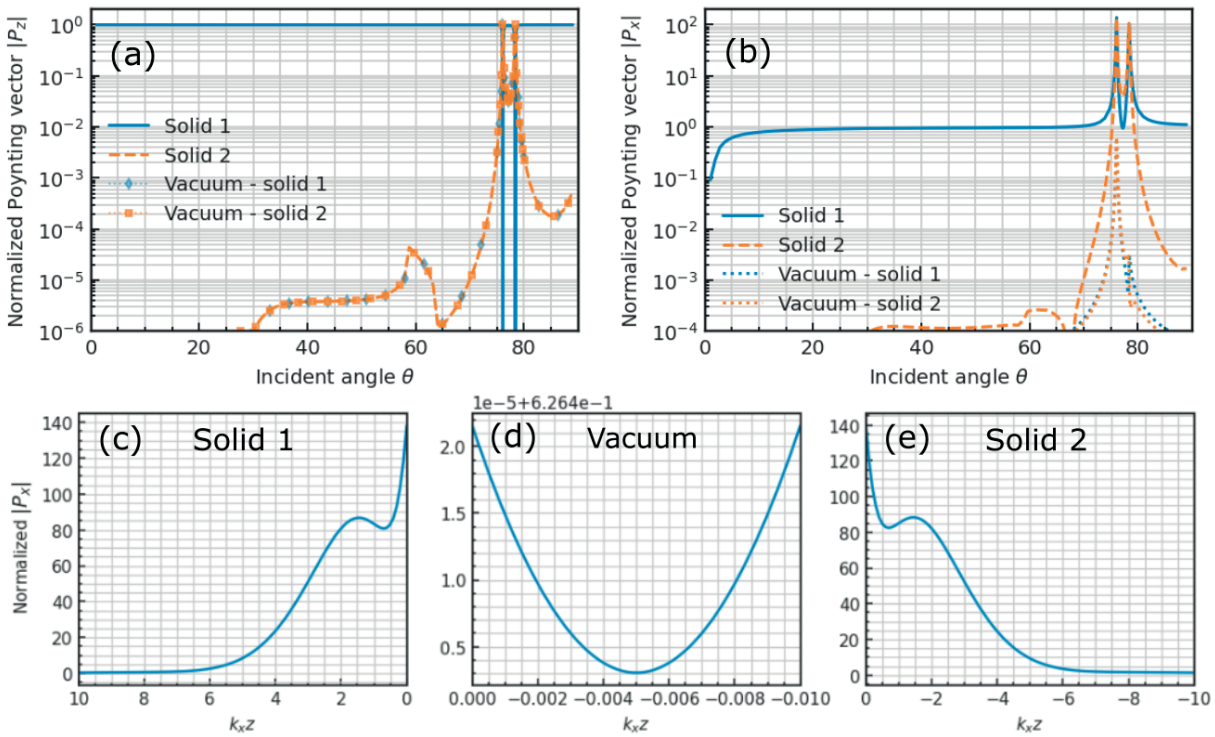

FIG. 3. The absolute values of the normal P_z (a) and parallel P_x (b) components of the time-averaged electroacoustic Poynting vector at various surfaces vs. incident angle θ. The blue solid line is the reflected wave at the solid 1 surface inside solid 1, the orange dashed line is the transmitted wave at the solid 2 surface inside solid 2, and the blue and orange dotted lines with symbols are the transmitted waves on the vacuum side of the surface of solid 1 and 2, respectively. In panels (c)-(e), the parallel component of the Poynting vector P_z is plotted at the resonant condition $\theta = 76.06$, as function of the z-axis position, in solid 1 (c), in the vacuum gap (d) and in solid 2 (e). All Poynting vectors are normalized to the incident Poynting vector of the same component.

than in the resonant case. The reflected partial modes L [Fig.2(j)] and FT [Fig.2(k)] dominate the electrical potentials, and, in particular, the FT wave is still a bulk mode (its critical angle is about 64°), giving rise to a significant bulk reflection. Moreover, the reflected ST wave also has an amplitude comparable to the incident wave, and is thereby also contributing to bulk reflection.

The normal ($\boldsymbol{P}_z$) and parallel ($\boldsymbol{P}_x$) components of the time-averaged Poynting vector at the surfaces of both solids both inside the solid and out on the vacuum side are plotted as a function of the incident angle in Figures 3(a) and (b), respectively. These power flows are normalized to the respective components of the incident Poynting vector, i.e. $|\boldsymbol{P}_{x,in}| = 1$ in (a) and $|\boldsymbol{P}_{z,in}| = 1$ in (b).

With most incident angles, the magnitude of the reflected power flow in the normal direction [3(a)] at the surface of solid 1 is close to unity (equal to the incident flow with an opposite sign). However, the reflected flow quickly drops to zero while the transmitted power rises to unity at the two resonant angles $\theta = 76.06$ and $\theta = 78.37°$, which is the key takeaway of the main text. We also see that the power flow in the normal direction in the vacuum equals to the transmitted power in solid 2, which has also been discussed in the main text.

It is even more interesting to look at the power flow component parallel to the surfaces, presented in Figure 3(b). We again find the two resonances, now exhibiting peaks at the surfaces of *both* solids, with a power flow density more than two orders of magnitude higher than that of the incoming wave. Such a high power flow density is the result of the excitation of the surface wave mode, as was discussed above, which concentrates and propagates the energy of the scattered wave along the surfaces. We should also note that the higher-than-incident power flow density does not break the energy conservation, because the energy density increases only at the vicinity of the surfaces and decays exponentially into the bulk, as demonstrated for the resonant condition $\theta = 76.06$ in Figures 3(c) and (e) for both solids. Figure 3(d) also shows the parallel power flow inside the vacuum gap for the same condition, being symmetric as function of the z-axis position, but having a magnitude orders of magnitude below the one on the side of the solids. These plots

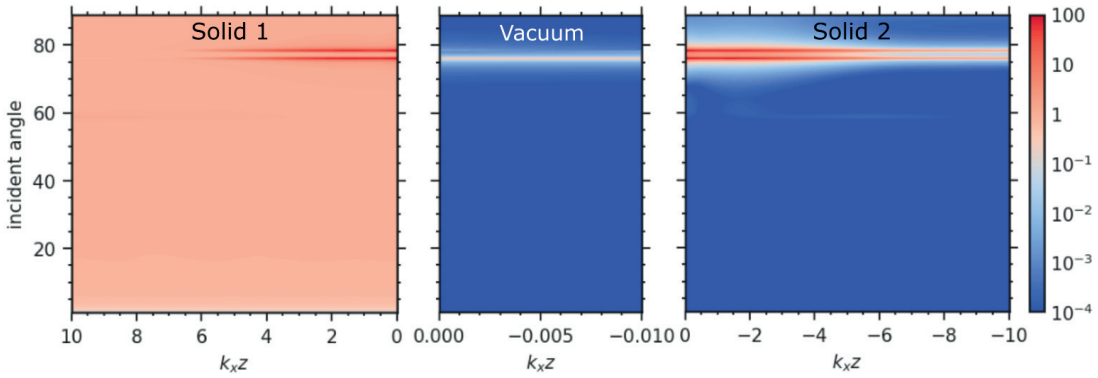

FIG. 4. The normalized, parallel component of the Poynting vector $|\boldsymbol{P}_x|$ as function of z-axis positions and incident angles inside the solid 1, 2 and the vacuum.

clearly demonstrate the coupled nature of this surface wave mode: both surfaces are involved in a symmetric way, coupled by the tunneling effect.

For completeness, we also plot the color-scaled parallel power flow density $|\boldsymbol{P}_x|$ as function of both z-axis position and the incident angle θ in Figure 4 for both solids and the vacuum gap. It can be seen that the flow in solid 1 generally equals the incident flow, except in the two narrow ranges around the resonance angles where it is two orders of magnitude higher. In addition, only these resonant tunneling conditions give rise to such large power flow inside the solid 2, and only the first resonance carries significant power inside the vacuum gap.

VI. NUMERICAL EXAMPLE COMPARING TO PREVIOUS LITERATURE

Here, we again consider two identical ZnO crystals. The material parameters and the orientations of the crystals are chosen to be exactly the same as those used in Ref.[12], in which the Z-axis of the crystal is aligned with the z-axis of the laboratory coordinates. In this case, piezoelectric response can only be excited by the polarizations inside the sagittal plane (xz-plane) from the longitudinal (L) and vertical shear (SV) partial wave modes. The horizontal shear (SH) wave mode, which polarizes perpendicular to the sagittal plane, stays purely mechanical and decouples from the other two partial modes as well as from the electrostatic field. Thus the contribution of the SH mode can be omitted, and the total transmitted power is the sum of the power of L and SV mode waves $P_\Sigma = P_L + P_{SV}$.

In Figure.5, we plot $P_\Sigma/P_{\rm in}$ for an incoming L wave [panel (a)] and for an incoming SV wave [panel (b)] as functions of both the incident angle θ_i and $kd = k_x d/\sin\theta_i$. Comparing these plots to Fig.(2) in Ref.[12], we observe a significantly lower transmittance, with a maximum of only 0.6%, far lower than the claimed unity transmittance in Ref.[12].

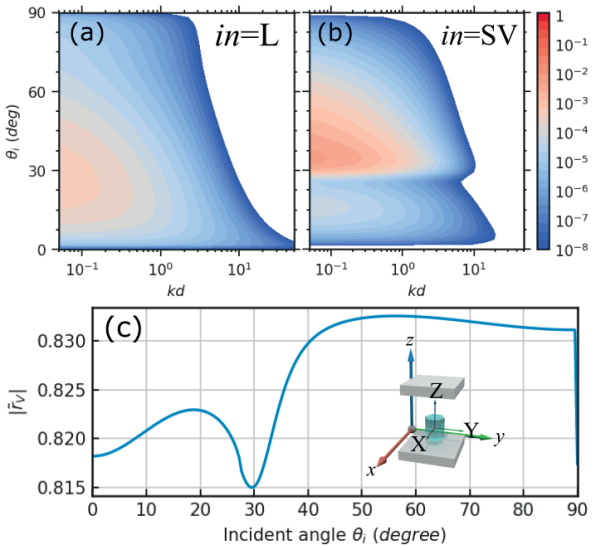

FIG. 5. The total transmitted power $(P_L + P_{SV})/P_{in}$ (color scale) of an incoming (a) longitudinal (L) and (b) vertically shear (SV) wave as function of scaled gap kd and incident angle θ_i. Two identical ZnO crystals are oriented such that the crystal XYZ coordinates coincide with the laboratory xyz coordinates [as illustrated in (c)]. The materials parameters used for isotropic ZnO were $c_{11} = c_{33} = 209.7 \times 10^9$ N/m^2, $c_{44} = c_{66} = 42 \times 10^9$ N/m^2, $c_{12} = c_{13} = c_{11} - 2c_{44}$, $\epsilon_{xx} = \epsilon_{zz} = 10\epsilon_0$, $e_{z3} = 1.3$ C/m^2, $e_{x5} = e_{z1} = 0$ C/m^2 and $\rho = 5600$ kg/m^3, which are the same as those used in Ref.[12]. (c) The single surface reflection coefficient $|\bar{r}_V|$ of incoming SV wave is plotted as a function of incident angle θ_i. Note that it stays below unity for all θ_i.

We argue that when the transmitted L and SV partial waves are both bulk modes, *e.g.* an incoming L wave with $\theta_i \in (0, 90°)$ or an incoming SV wave with $\theta_i < 31°$ which is the critical angle of the reflected L mode, Eqs. (2) and (5) of the main text require $2\mathrm{Re}(\bar{r}_V) = |\bar{t}^{(2)}_{V\to L}|^2 +$

$|\bar{t}^{(2)}_{V\to SV}|^2 > |\bar{t}^{(1)}_{in\to V}|^2$ where the subscript in is either L or SV, depending on the incident wave mode. Hence the total transmitted power P_Σ is always smaller than the incident power P_{in} based on Eq. (6) of the main text. On the other hand, for an incoming SV wave with incident angle $\theta_i > 31^\circ$ beyond the critical angle of the L mode, there is only one transmitted bulk wave (SV), but the resonant tunneling condition, Eq. (8) of the main text,is not satisfied. This is because $\exp(k_x d) > 1$ for a finite gap size, whereas the absolute value of single surface reflection coefficient $|\bar{r}_V| < 1$, as shown in panel (c) of Figure 5. As a result, unity transmission cannot be achieved with this configuration, in contradiction to the claim made in Ref.[12].

[1] Z. Geng and I. J. Maasilta, Acoustic wave tunneling across vacuum gap between two piezoelectric crystals with arbitrary symmetry and orientation, Phys. Rev. Research **4**, 033073 (2022).

[2] B. Auld, *Acoustic fields and waves in solids*, 2nd ed. (Krieger, Malabar, Florida, 1990).

[3] V. I. Al'shits, A. N. Darinskii, and A. L. Shuvalov, Theory of reflection of acoustoelectric waves in a semiinfinite piezoelectric medium. I. Metallized surface, Kristallografiya **34**, 1340 (1989), [Sov. Phys. Crystallogr. **34**, 808 (1989)].

[4] V. I. Al'shits, A. N. Darinskii, and A. L. Shuvalov, Theory of reflection of acoustoelectric waves in a semiinfinite piezoelectric medium. II. Nonmetallized surface, Kristallografiya **35**, 7 (1990), [Sov. Phys. Crystallogr. **35**, 1 (1990)].

[5] V. I. Al'shits, A. N. Darinskii, and A. L. Shuvalov, Theory of reflection of acoustoelectric waves in a semiinfinite piezoelectric medium. III. Resonance reflection in the neighborhood of a branch of outflowing waves, Kristallografiya **36**, 284 (1991), [Sov. Phys. Crystallogr. **36**, 145 (1991)].

[6] D. M. Barnett and J. Lothe, Dislocations and line charges in anisotropic piezoelectric insulators, Phys. Status Solidi B **67**, 105 (1975).

[7] J. Lothe and D. M. Barnett, Integral formalism for surface waves in piezoelectric crystals. Existence considerations, J. Appl. Phys. **47**, 1799 (1976).

[8] V. I. Al'shits, A. N. Darinskii, and A. Shuvalov, Acoustoelectric waves in bicrystal media in conditions of a rigid contact or a vacuum gap at an interface, Kristallografiya **38**, 22 (1993), [Crystallogr. Rep. **38**, 147 (1993)].

[9] K. A. Ingebrigtsen, Surface waves in piezoelectrics, J. Appl. Phys. **40**, 2681 (1969).

[10] Y. Zhang, J. Desbois, and L. Boyer, New method to characterize the surface-generated bulk acoustic waves in piezoelectric substrates, J. Acoust. Soc. Am. **92**, 2499 (1992).

[11] A. N. Darinskii and M. Weihnacht, Gap Acousto-Electric Waves in Structures of Arbitrary Anisotropy, IEEE Trans. Ultrason. Ferroelectr. Freq. Control **53**, 412 (2006).

[12] M. Prunnila and J. Meltaus, Acoustic phonon tunneling and heat transport due to evanescent electric fields, Phys. Rev. Lett. **105**, 125501 (2010).

PIII

HEAT TRANSFER ACROSS A VACUUM GAP INDUCED BY PIEZOELECTRICALLY MEDIATED ACOUSTIC PHONON TUNNELING

by

Z. Geng & I. J. Maasilta

arXiv:2303.05084

Manuscript

Heat transfer across a vacuum gap induced by piezoelectrically mediated acoustic phonon tunneling

Zhuoran Geng* and Ilari J. Maasilta†
Nanoscience Center, Department of Physics, University of Jyväskylä, FI-40014 Jyväskylä, Finland
(Dated: March 10, 2023)

In contradictin to the common concept that acoustic phonons can only travel inside a material medium, they can in fact "tunnel" across a vacuum gap with the help of piezoelectricity, transmitting a significantly stronger heat flux than that of blackbody radiation. Here, we present a theoretical formulation for the heat flux of such piezoelectrically mediated heat transfer, applicable to any anisotropic piezoelectric crystals with an arbitrary orientation. A few numerical results are demonstrated and compared to heat transfer driven by other close-range mechanisms, including near-field radiative heat transfer and other acoustic phonon tunneling mechanisms. We find that piezoelectrically mediated heat transfer has a significant effect when the vacuum gap size is smaller than the phonon characteristic thermal wavelength, and its heat flux can dominate heat transfer between piezoelectric solids over all other known heat transfer mechanisms at temperatures below 50 K.

It is known that heat can be transfered between macroscopic bodies via three different channels, namely, conduction, convection and radiation. Out of those, radiation is the only possible channel between two materials separated by a vacuum gap, and the corresponding heat flux is well understood based on Planck's law of radiation. However, when the separation between two material bodies decreases, heat flux exceeding that of Planck's law by several orders of magnitude has been observed in experiments[1–3]. Among the mechanisms that can lead to such super-Planckian radiation, near field radiative heat transfer (NFRHT) mediated by photon tunneling[4–7] is the most studied one. Analogous to quantum mechanical tunneling, this photon tunneling becomes relevant when the vacuum gap distance is below the photon thermal wavelength, which is about $\sim 10\,\mu$m at room temperature.

With advances in nanotechnology, vacuum gaps with sizes in the nanometer-to sub-nanometer range can be achieved in experiments[8–11]. This has stimulated active research in recent years also on the heat transfer driven by the tunneling of acoustic phonons[11–23] in addition to photons, as their thermal wavelengths are at that length scale. However, the concept of acoustic phonon tunneling is far from obvious, as a phonon, being a vibration of the atomic lattice, requires the presence of a medium to propagate. In the past decade, a few mechanisms that can mediate acoustic phonon tunneling have been suggested, the van der Waals force[16–19] the electrostatic force[19–21], or the non-local contribution of acoustic phonons to NFRHT in polar crystals [24]. Nevertheless, these studies show that the heat flux due to these mechanisms decay rapidly with the gap width (d^{-7} and d^{-9} for van der Waals and electrostatic mechanisms, respectively), and hence provide non-trivial contributions to the heat transfer only when a vacuum gap $d < 1$ nm at room temperature[19].

There exists yet another, much less studied acoustic phonon tunneling mechanism, which utilizes piezoelectricity. A thermally excited acoustic phonon impinging on a free surface of a piezoelectric solid can create a decaying, evanescent electric field leaking into the vacuum. Such field couples to the lattice deformations of a second piezoelectric solid placed within the phonon wavelength, leading to a transmission of heat across the vacuum. Such piezoelectrically mediated heat transfer (PEMHT) was previously suggested and studied in Ref. [12], however the theoretical estimation in that study was based on a highly simplified model, in which the isotropic material parameters were assumed and only two phonon modes were considered. Moreover, their results are not in agreement with those derived from the more general acoustic wave tunneling formalism for piezoelectric materials developed in Refs.[25, 26], and hence the PEMHT phenomenon needs to be re-examined.

In this work, we present a general formulation for the piezoelectrically mediated heat transfer via acoustic phonon tunneling, which can be applied to arbitrarily anisotropic and oriented piezoelectric crystals. Numerical examples are investigated and compared to other close-range heat transfer mechanisms, including non-piezoelectric tunneling of acoustic phonons and near-field radiative transfer (photon tunneling). We find that PEMHT can dominate heat transfer at temperatures below 50 K. At the end, numerical examples of PEMHT using different piezoelectric materials with varying crystal orientations are discussed.

We consider two piezoelectric, semi-infinite solids which are placed parallel to each other and separated by a vacuum gap of width d, as shown in Fig.1. Both solids can be rotated to arbitrary orientations described by a set of Euler angles denoting the relation between the intrinsic crystal coordinates and the laboratory coordinates xyz (see [27] for more details on crystal orientation). In our model, these solids are assumed to be

* zhgeng@jyu.fi
† maasilta@jyu.fi

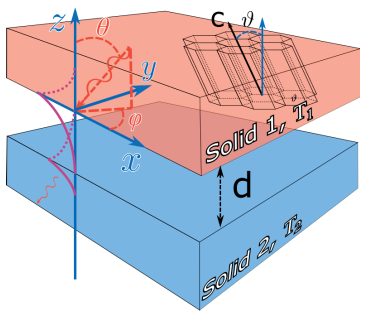

FIG. 1. Two piezoelectric solids 1, 2, at temperatures T_1 and T_2, are separated by a vacuum gap of width d. An incoming acoustic phonon (red) with an incident zenith angle θ and azimuth angle φ tunnels across the vacuum from solid 1 and transfers heat to the adjacent solid 2. In this study, we demonstrate results for hexagonal crystals, (ZnO,AlN), whose orientation can be described by a rotation angle ϑ between the crystal c-axis and the laboratory z-axis.

continuous and anisotropic, satisfying linear elastic constitutive equations[25, 28].

We assume that the thermal acoustic phonons in solid 1 impinging on the gap consist of three bulk acoustic wave modes $\alpha = 1, 2, 3$[25], where each wave mode can be described by a time-harmonic displacement field

$$\boldsymbol{u}_\alpha = b_\alpha \boldsymbol{A}_\alpha \exp(i\omega_\alpha t - i\boldsymbol{k}\cdot\boldsymbol{r}), \tag{1}$$

where $\boldsymbol{k}$ is the wave vector, $\boldsymbol{r} = (x, y, z)$ is the position vector in the laboratory coordinates, ω_α is the angular frequency of the phonon mode, $\boldsymbol{A}_\alpha$ is the Stroh-normalized[25] polarization vector and b_α is the dimensionless amplitude of the mode[25].

In PEMHT, the emitted heat flux J^{PE} from the solid $\gamma = 1, 2$ across the gap can then be expressed as

$$J_\gamma^{\mathrm{PE}}(T_\gamma, d) = \sum_\alpha \int \frac{\mathrm{d}^3k}{(2\pi)^3}\hbar\omega_\alpha(\boldsymbol{k})n(\omega_\alpha, T_\gamma) \times \left(\hat{\boldsymbol{n}}_\gamma \cdot \frac{\partial\omega_\alpha}{\partial\boldsymbol{k}}\right)\Theta\left(\hat{\boldsymbol{n}}_\gamma \cdot \frac{\partial\omega_\alpha}{\partial\boldsymbol{k}}\right)\mathcal{T}_\alpha(\theta, \varphi, k, d), \tag{2}$$

where $n(\omega_\alpha, T_\gamma) = [\exp(\hbar\omega_\alpha/k_B T_\gamma) - 1]^{-1}$ is the Bose-Einstein distribution describing the thermal occupation of the phonon mode of energy $\hbar\omega_\alpha(\boldsymbol{k})$, $\hat{\boldsymbol{n}}_\gamma$ is the *outward* unit normal of the vacuum-solid interface, and $\mathcal{T}_\alpha$ is the power transmittance of mode α [26].

The term $\hat{\boldsymbol{n}}_\gamma \cdot \partial\omega_\alpha/\partial\boldsymbol{k}$ in Eq.(2) describes the group velocity of the phonon wave mode α in the direction of the outward normal of the vacuum-interface, and can be expressed as[27]:

$$\hat{\boldsymbol{n}}_\gamma \cdot \frac{\partial\omega_\alpha}{\partial\boldsymbol{k}} = \frac{1}{2}\frac{\sin\theta}{\rho v_\alpha(\theta,\varphi)|\boldsymbol{A}_\alpha(\theta,\varphi)|^2}\hat{\xi}_\gamma(\theta,\varphi), \tag{3}$$

where ρ is the density of the solid. The phase velocity term $v_\alpha = \omega_a/k$ depends on the material, crystal orientation and incident angles (θ, φ), and can be solved from the piezoelectrically stiffened Christoffel equation [Eq.(8.147) in Ref.[28]]. Furthermore, the polarization vector $\boldsymbol{A}_\alpha$ is obtained from the normalized eigenvector of the extended Stroh matrix [Eq.(3) in Ref.[25]], whereas for the bulk waves, $\hat{\xi}_\gamma = \pm 1$ (J/m) is obtained from the Stroh-normalization[26], whose sign determines the energy flow direction of the phonon along the unit vector $\hat{\boldsymbol{n}}_\gamma$.

In addition, a Heaviside step function $\Theta(f)$, which equals to unity (zero) when $f > 0$ ($f < 0$), is used to correctly select the phonons whose group velocities point from the solid towards the vacuum. It is important to note that in anisotropic crystals, the direction of phonon propagation, signified by the direction of the group velocity $\partial\omega_\alpha/\partial\boldsymbol{k}$, is generally different from the wave front direction given by the wave vector $\boldsymbol{k}$. It is possible for a phonon that tunnels outward from solid 1 to 2 to have an inward wave vector in the normal direction, i.e. $(\hat{\boldsymbol{n}}_\gamma \cdot \partial\omega_\alpha/\partial\boldsymbol{k}) < 0$ but $(\hat{\boldsymbol{n}}_1 \cdot \boldsymbol{k}) > 0$. Therefore, to fully account for all the possible incident acoustic phonons impinging on the surface towards the vacuum, we have to integrate over the complete k-space in Eq.(2) including the inward half-hemisphere, but choosing the outward traveling phonons with the help of the Heaviside step function $\Theta[\hat{\boldsymbol{n}}_\gamma \cdot (\partial\omega_\alpha/\partial\boldsymbol{k})]$.

By following the methods presented in Ref.[25], the total tunneled power transmittance of an incoming wave mode α, coupling into all possible bulk modes in the second solid, takes the form[26]:

$$\mathcal{T}_\alpha(\theta, \varphi, k, d) = \frac{2\mathrm{Re}\left[r_V^{(2)}\right]\left|t_{\alpha\to V}^{(1)}\right|^2 e^{-2kd\sin\theta}}{\left|1 - r_V^{(1)} r_V^{(2)} e^{-2kd\sin\theta}\right|^2}, \tag{4}$$

where $t^{(i)}$ and $r^{(i)}$ are the single surface transmission and reflection coefficients, which describe the scattering of the acoustic wave at the surface of solid $i = 1, 2$ as if there is no adjacent second solid. To be more specific, we denote with $t_{\alpha\to V}^{(1)}$ the coefficient of an incoming α mode wave transmitted into an evanescent wave (electrical potential) in vacuum from solid 1, and with $r_V^{(i)}$ the coefficient of an evanescent wave coming from vacuum reflected on the surface of solid i. For given material parameters, crystal orientations and incident wave mode α, these coefficients are functions of the incident angles θ and φ, independent of k and d, and can be obtained numerically using the boundary conditions at the solid-vacuum interface, following the formalism presented in Ref.[25].

The net heat flux between solid 1 at temperature T_1 and solid 2 at temperature T_2 is the difference between their corresponding emitted heat fluxes, and reads as $\Delta J^{\mathrm{PE}} = J_1^{\mathrm{PE}}(T_1, d) - J_2^{\mathrm{PE}}(T_2, d)$. Furthermore, in the limit where the power transmittance [Eq.(4)] is set to unity and isotropy is assumed for the group velocity, given then by $(\hat{\boldsymbol{n}}_\gamma \cdot \partial\omega_\alpha/\partial\boldsymbol{k}) = v_\alpha\cos\theta$, the heat flux Eq.(2) simplifies to $J_\gamma = \sum_\alpha \pi^2 k_B^4 T_\gamma^4/120 v_\alpha^2\hbar^3$, recovering the expression for phonon blackbody radiation for isotropic matter[29].

To demonstrate PEMHT numerically, we consider the case of two ZnO crystals with a hexagonal 6mm symmetry, with their material constants taken from Ref.[28]. These solids are separated by a vacuum gap of width d, and are rotated identically such that their crystal c-axes are aligned with the laboratory y-axis (hence $\vartheta = \pi/2$, see Fig.1). In Fig.2 we plot the emitted heat flux $J^{\rm PE}(T,d)$ between the two solids as a function of the emitter temperature T and gap width d. By introducing the characteristic thermal wavelength λ_T [12, 19, 21], defined as $\lambda_T = 2\pi v_\alpha \hbar/k_B T$, we find that the plot can be divided into two regions roughly separated by the black dotted line signifying the condition $d = \lambda_T \approx (0.2\ \mu\text{m})/T$, where we used an average phonon phase velocity [$v = (\sum_\alpha v_\alpha)/3$] of 3900 m/s for ZnO.

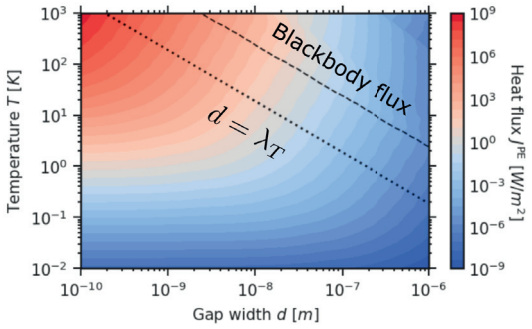

FIG. 2. Contour plot of the total emitted heat flux $J^{\rm PE}$ of all phonon wave modes for ZnO as function of temperature T and gap width d. The dotted line is $T = 2\pi\hbar v/k_B d$, denoting the condition $d = \lambda_T$ where $v = 3900$ m/s. The dashed line is $J^{\rm PE} = \pi^2 k_B^4 T^4/60c^2\hbar^3$, signifying the blackbody radiation limit.

Towards the lower-left region, the heat flux decreases strongly with decreasing temperature, but saturates with the gap width. This saturation comes about because only the power transmittance $\mathcal{T}_\alpha$ is a function of the gap width d in Eq.(2), and this dependency is only expressed via the exponential term $\sim \exp(-kd)$ in Eq.(4)[25]. As a result, for a gap width $d \ll \lambda_T \sim 1/k$, $\mathcal{T}$ becomes constant, and the heat flux $J^{\rm PE}$ is hence determined by the thermal distribution function $n(\omega, T)$, which is strongly modified by the temperature. In contrast, the exponential decay of $\mathcal{T}$ dominates the heat flux towards the upper-right section. In the large-gap limit ($d \gg \lambda_T$), the heat flux is practically "switched-off" and becomes insensitive to the change of temperature. In addition, a black dashed line marks where the heat flux from PEMHT equals to that of the blackbody radiation at the same temperature [$J^{\rm PE}(T,d) = \pi^2 k_B^4 T^4/60c^2\hbar^3$ where c the speed of light]. The comparison between the dashed and dotted lines shows that PEMHT, if "switched-on" ($d \le \lambda_T$), generally contributes at least three orders of magnitude stronger heat flux than blackbody radiation at a given temperature, making it a non-trivial source in the context of near-field heat transfer.

In addition, at room temperature, PEMHT is stronger than blackbody radiation even at a gap width close to 10 nm. This is very different to the other acoustic phonon tunneling mechanisms described in literature [14, 17, 19–21, 24], for which non-trivial heat flux occurs in the sub-nanometer length scale at room temperature. In Fig.3, the heat flux carried by various relevant close-range mechanisms are compared, including the near-field radiative heat transfer (NFRHT, [5, 7]) for ZnO [30, 31] and Au [32], phonon tunneling for Au mediated by van der Waals force [19] and electrostatic force (for 1 V bias across the vacuum) [20, 21], and the blackbody radiation (maximal far-field radiative heat transfer).

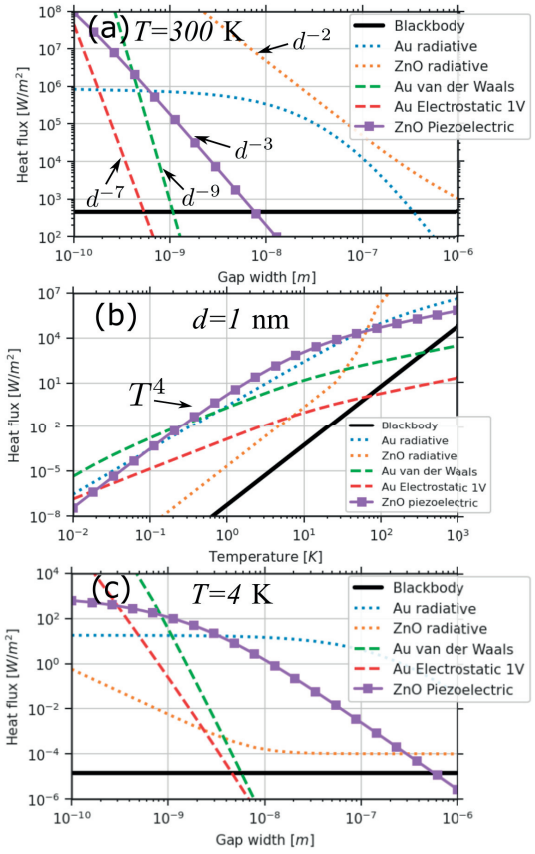

FIG. 3. Comparison of the emitted heat fluxes driven by different close-range mechanisms. (a) The heat fluxes as a function of the gap width at 300 K. Purple square marker is PEMHT of ZnO, the dotted lines are NFRHT for Au (blue) and ZnO (orange). The dashed lines are the acoustic phonon tunneling in Au mediated by van der Waals force (green) and 1 V electrostatic potential difference (red). (b) The heat fluxes as function of temperature with a fix gap width of 1 nm. (c) The heat fluxes as a function of gap width at 4 K.

In panel (a) of Fig.3, the heat fluxes of all the above mentioned mechanisms at 300 K are plotted as a function of the gap width d. It is clear that at room temperature,

NFRHT for Au and ZnO, denoted by the blue and orange dotted lines, respectively, is significantly stronger than the heat transfer mediated by the acoustic phonon mechanisms. Moreover, the heat fluxes driven by the van der Waals force and the electrostatic force scale as d^{-9} and d^{-7}, respectively [21], hence they only have non-trivial contributions below $d < 1$ nm at room temperature, and will fall off rapidly with the increase of the gap width. In contrast, PEMHT (square symbols) scales as d^{-3}, similar to that for NFRHT (photon tunneling). Consequently, PEMHT quickly dominates the other phonon tunneling mechanisms at larger-than-nanometer scales, being a relatively "long-range" phenomenon.

One interesting observation in Fig.3 (a) is that the NFRHT of ZnO is particularly strong. This happens[7] because the surface-phonon polaritons of ZnO can be excited at infrared frequencies [30, 31], matching the spectrum of the room temperature thermal photons, and hence enhancing the heat flux. But this also infers that one should expect a strong attenuation of the NFRHT once the excitations are stopped, *i.e.* when the temperature is lowered. This is confirmed in Fig.3(b), in which the heat fluxes are plotted as a function of the temperature for a fixed gap width of 1 nm. There is a clear cut-off of the NFRHT flux at about 100 K for ZnO.

More interestingly, PEMHT becomes stronger than the fluxes from all other mechanisms, including NFRHTs, between 0.1 K to 50 K. At this temperature range, the power transmittance of the PEMHT increases exponentially as the thermal wavelengths of the acoustic phonons increase, eventually saturating at sub-Kelvin range (see Fig.2). With the temperature lowered even further, the PEMHT flux is determined by the phonon state energy term (phonon thermal spectrum), and therefore has a T^4 dependence on the temperature, similar to the NFRHT of ZnO in the low temperature limit. Meanwhile, the other acoustic phonon tunneling mechanisms, scaling more slowly than the PEMHT, begin to dominate the heat transfer at the temperatures below 0.1 K.

From the above numerical analyses, we believe that PEMHT can be experimentally observed using modern nanofabrication techniques at cryogenic temperatures. As an example,in Fig.3 (c) we demonstrate the heat fluxes from all the above mentioned mechanisms, as a function of the gap width at 4 K. One finds that the PEMHT of ZnO (purple squares) dominates the heat flux up to a gap width as high as $d \sim 300$ nm, compared to the NFRHT of ZnO (orange dotted line) and blackbody radiation (black line). With further lowering of the temperature or reduction of the gap width, PEMHT will become more prominent and easier to observe.

Next, we plot in Fig.4 the emitted PEMHT for two different piezoelectric materials, ZnO and AlN[33], as a function of the orientation angle ϑ, with a fixed gap width of 1 nm and a temperature of 0.1 K, to illustrate the influence of the material choice and orientations.

Obvious similarities are shared by the heat fluxes of ZnO (solid line) and AlN (dotted line). For example,

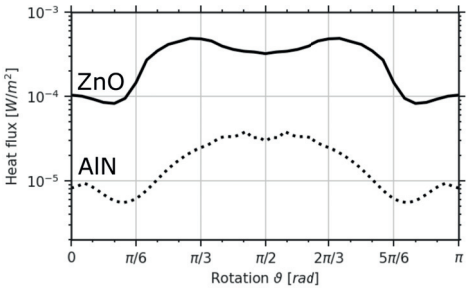

FIG. 4. Comparison of emitted PEMHT as a function of the crystal rotation angle ϑ for ZnO (solid line) and AlN (dotted line). The heat fluxes are calculated for a gap width of 1 nm at a temperature of 0.1 K.

for both materials the flux is generally stronger around the orientation $\vartheta = \pi/2$, contrasting to those around 0 and π, and sharp slopes appear around 20° and 40° leading to more than five-fold, step-like variations of the heat flux. These similarities come about because both materials have the $6mm$-wurtzite crystal symmetry. The underlying physics of these features is that as ϑ is the angle between the normal of the solid-vacuum interface and the crystal's piezoelectric axis (the c-axis), and when ϑ is close to 90°, the c-axis is more aligned with the surface. As a result, the reflected evanescent modes, which propagate only on the surface, can excite a stronger piezoelectric response, leading to an enhanced electrostatic coupling across the vacuum. It has been shown that even complete tunneling of certain acoustic modes can be achieved for ZnO, when ϑ is between 60° and 120°[26].

In addition, PEMHT for ZnO is about one order of magnitude stronger than that of AlN. This is mostly due to the differences in their phase velocities. When the characteristic wavelength λ_T is much larger than the gap width, the heat flux scales roughly with v_α^{-3}. As a result, a ten-fold difference in the heat flux is expected since AlN has an average phase velocity $v \approx 7500$ m/s, whereas it is about $v \approx 3900$ m/s for ZnO.

To summarize, we presented a general formulation for piezoelectrically mediated heat transfer (PEMHT) via acoustic phonon tunneling. Such a formulation can be used to compute the heat flux across a vacuum gap, between arbitrarily anisotropic and oriented piezoelectric crystals. Our analytical and numerical studies reveal that PEMHT provides a significant heat flux, generally more than three orders of magnitude stronger than that from the blackbody radiation when the gap width d is smaller than the phonon characteristic thermal wavelength λ_T. By comparing to other near-field mechanisms, our study shows that PEMHT can dominate the heat flux at temperatures below 50 K.

Finally we remark that with the currently available nano-fabrication and cryogenic measurement techniques, PEMHT could possibly be investigated experimentally. We believe that further understanding and engineering

of acoustic phonon tunneling can be crucial for many application areas such as nano-electronics, low temperature detectors, quantum information devices and others, for which increasing demand for heat manipulation and management exists.

This study was supported by the Academy of Finland project number 341823.

[1] G. Domoto, R. Boehm, and C. Tien, Experimental investigation of radiative transfer between metallic surfaces at cryogenic temperatures, J. Heat Transfer **92**, 412 (1970).

[2] B. Song, A. Fiorino, E. Meyhofer, and P. Reddy, Near-field radiative thermal transport: From theory to experiment, AIP Adv. **5**, 053503 (2015).

[3] C. Lucchesi, R. Vaillon, and P. O. Chapuis, Radiative heat transfer at the nanoscale: Experimental trends and challenges, Nanoscale Horiz. **6**, 201 (2021).

[4] D. Polder and M. Van Hove, Theory of Radiative Heat Transfer between Closely Spaced Bodies, Phys. Rev. B **4**, 3303 (1971).

[5] J. B. Pendry, Radiative exchange of heat between nanostructures, J. Phys.: Condens. Matter **11**, 6621 (1999).

[6] A. I. Volokitin and B. N. Persson, Radiative heat transfer between nanostructures, Phys. Rev. B **63**, 205404 (2001).

[7] K. Joulain, J.-P. Mulet, F. Marquier, R. Carminati, and J.-J. Greffet, Surface electromagnetic waves thermally excited: Radiative heat transfer, coherence properties and Casimir forces revisited in the near field, Surf. Sci. Rep. **57**, 59 (2005).

[8] K. Kim, B. Song, V. Fernández-Hurtado, W. Lee, W. Jeong, L. Cui, D. Thompson, J. Feist, M. T. Reid, F. J. García-Vidal, J. C. Cuevas, E. Meyhofer, and P. Reddy, Radiative heat transfer in the extreme near field, Nature **528**, 387 (2015).

[9] K. Kloppstech, N. Könne, S. A. Biehs, A. W. Rodriguez, L. Worbes, D. Hellmann, and A. Kittel, Giant heat transfer in the crossover regime between conduction and radiation, Nat. Commun. **8**, 14475 (2017).

[10] J. Cui, J. Zhang, T. Barayavuga, X. Wang, X. He, L. Yang, H. Xie, X. Mei, and W. Wang, Nanofabrication with the thermal AFM metallic tip irradiated by continuous laser, Integr. Ferroelectr. **179**, 140 (2017).

[11] A. Jarzembski, T. Tokunaga, J. Crossley, J. Yun, C. Shaskey, R. A. Murdick, I. Park, M. Francoeur, and K. Park, Role of Acoustic Phonon Transport in Near-to Asperity-Contact Heat Transfer, Phys. Rev. B **106**, 205418 (2022).

[12] M. Prunnila and J. Meltaus, Acoustic phonon tunneling and heat transport due to evanescent electric fields, Phys. Rev. Lett. **105**, 125501 (2010).

[13] D. P. Sellan, E. S. Landry, K. Sasihithlu, A. Narayanaswamy, A. J. McGaughey, and C. H. Amon, Phonon transport across a vacuum gap, Phys. Rev. B. **85**, 024118 (2012).

[14] B. N. Persson, A. I. Volokitin, and H. Ueba, Phononic heat transfer across an interface: Thermal boundary resistance, J. Phys.: Condens. Matter **23**, 045009 (2011).

[15] V. Chiloyan, J. Garg, K. Esfarjani, and G. Chen, Transition from near-field thermal radiation to phonon heat conduction at sub-nanometre gaps, Nat. Commun. **6**, 6755 (2015).

[16] B. V. Budaev and D. B. Bogy, On the role of acoustic waves (phonons) in equilibrium heat exchange across a vacuum gap, Appl. Phys. Lett. **99**, 053109 (2011).

[17] Y. Ezzahri and K. Joulain, Vacuum-induced phonon transfer between two solid dielectric materials: Illustrating the case of Casimir force coupling, Phys. Rev. B **90**, 115433 (2014).

[18] K. Sasihithlu, J. B. Pendry, and R. V. Craster, Van der Waals Force Assisted Heat Transfer, Z. Naturforsch. **72**, 181 (2017).

[19] J. B. Pendry, K. Sasihithlu, and R. V. Craster, Phonon-assisted heat transfer between vacuum-separated surfaces, Phys. Rev. B **94**, 075414 (2016).

[20] A. I. Volokitin, Effect of an Electric Field in the Heat Transfer between Metals in the Extreme Near Field, JETP Lett. **109**, 749 (2019).

[21] A. I. Volokitin, Contribution of the acoustic waves to near-field heat transfer, J. Phys.: Condens. Matter **32**, 215001 (2020).

[22] K. Y. Fong, H. K. Li, R. Zhao, S. Yang, Y. Wang, and X. Zhang, Phonon heat transfer across a vacuum through quantum fluctuations, Nature **576**, 243 (2019).

[23] S. A. Biehs, A. Kittel, and P. Ben-Abdallah, Fundamental limitations of the mode temperature concept in strongly coupled systems, ZNA **75**, 803 (2020).

[24] M. G. Viloria, Y. Guo, S. Merabia, R. Messina, and P. Ben-Abdallah, Radiative heat exchange driven by the acoustic vibration modes between two solids at the atomic scale (2023), arXiv:2302.00520.

[25] Z. Geng and I. J. Maasilta, Acoustic wave tunneling across a vacuum gap between two piezoelectric crystals with arbitrary symmetry and orientation, Phys. Rev. Res. **4**, 033073 (2022).

[26] Z. Geng and I. J. Maasilta, Complete tunneling of acoustic waves between closely spaced piezoelectric crystals, arXiv:2209.08287 (2023).

[27] See Supplemental Material at [URL will be inserted by publisher].

[28] B. Auld, *Acoustic fields and waves in solids*, 2nd ed. (Krieger, Malabar, Florida, 1990).

[29] E. T. Swartz and R. O. Pohl, Thermal boundary resistance, Rev. Mod. Phys. **61**, 605 (1989).

[30] N. Ashkenov, B. N. Mbenkum, C. Bundesmann, V. Riede, M. Lorenz, D. Spemann, E. M. Kaidashev, A. Kasic, M. Schubert, M. Grundmann, G. Wagner, H. Neumann, V. Darakchieva, H. Arwin, and B. Monemar, Infrared dielectric functions and phonon modes of high-quality ZnO films, J. Appl. Phys. **93**, 126 (2003).

[31] P. Ooi, S. Lee, S. Ng, Z. Hassan, and H. A. Hassan, Far Infrared Optical Properties of Bulk Wurtzite Zinc Oxide Semiconductor, J. Mater. Sci. Technol. **27**, 465 (2011).

[32] P.-O. Chapuis, S. Volz, C. Henkel, K. Joulain, and J.-J. Greffet, Effects of spatial dispersion in near-field radiative heat transfer between two parallel metallic surfaces, Phys. Rev. B **77**, 035431 (2008), arXiv:0802.1899v1.

[33] K. Tsubouch and N. Mikoshiba, Zero-Temperature-Coefficient SAW Devices on AlN Epitaxial Films, IEEE

Trans. Sonics Ultrason. **32**, 634 (1985).
[34] V. Laude, A. Reinhardt, and A. Khelif, Equality of the energy and group velocities of bulk acoustic waves in piezoelectric media, IEEE Trans. Ultrason. Ferroelectr. Freq. Control **52**, 1869 (2005).
[35] A. G. Every and V. I. Neiman, Reflection of electroacoustic waves in piezoelectric solids: Mode conversion into four bulk waves, J. Appl. Phys. **71**, 6018 (1992).

Supplementary material: Heat transfer across a vacuum gap induced by piezoelectrically mediated acoustic phonon tunneling

Zhuoran Geng, Ilari J. Maasilta

April 3, 2023

1 Crystal orientation

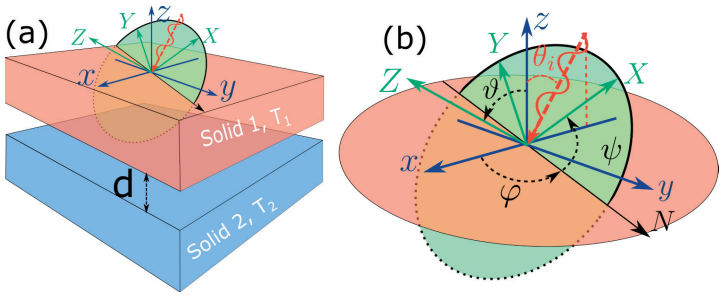

Figure 1: A schematic of the laboratory coordinates xyz and the orientation of the crystal intrinsic coordinates XYZ. (a) shows the general layout of the vacuum separated piezoelectric solids 1 and 2, with the two coordinate frames illustrated for solid 1. (b) shows the details of the rotation angles for the crystals and the incident angle of the phonon (red). The orientation of the crystals is signified by a set of Euler angles $(\vartheta, \varphi, \psi)$. An incoming acoustic phonon (red) has a zenith angle θ and an azimuth angle φ.

In this work, crystal orientation is described using the Euler angle system with respect to a fixed laboratory coordinate system, the same as in Ref.[1]. In this system, as illustrated in Fig.1, a set of Cartesian laboratory coordinates xyz (blue axes) is chosen to describe the spatial position, whereas a set of orthogonal XYZ coordinates (green axes) is chosen to describe the intrinsic crystal coordinates. The relation between these two frames can be fully expressed by three angles: ϑ, φ, and ψ as illustrated in panel (b) of Fig.1.

It is particularly important to note here that for the case of a semi-infinite half-space solid, the rotation of the azimuth angle φ of the crystal is in fact equivalent to a rotation of the phonon incident azimuth angle, both signifying

the same rotational degree of freedom. Therefore, the rotation of φ should only be taken into account once in the mathematical formulation to avoid duplication. For example, we can describe the crystal orientation using only the angles ϑ and ψ, and use θ and φ to describe the incident angle of the phonon.

The formulation presented in the main text takes the material tensors, such as the elastic stiffness tensor $\boldsymbol{c}^E$, the piezoelectric strain tensor $\boldsymbol{e}$, and the electric permittivity tensor $\boldsymbol{\epsilon}^S$, after the rotation transformation by three angles (ϑ, ψ and φ). The details of the crystal rotation procedures and the transformation of the material tensors have been introduced and explained in Ref.[1].

It is also worth to note that the material tensors will not change with the rotation ψ about the crystal Z-axis for a crystal with uniaxial symmetry, which is the case for ZnO and AlN used as example materials in the main article. As a result, the crystal orientation can be simplified further to only a single rotation angle ϑ.

2 Group velocity in Stroh-formalism

In piezoelectric solids, the direction of the phonon group velocity doesn't align with that of the phase velocity in general. For a non-dissipative medium, phonon group velocity is identical to the energy flow velocity, and thereby can be obtained from the ratio of the time-averaged acoustic Poynting vector $\boldsymbol{S}$ and the average stored mechanical energy density $(u_K+u_S)/2$, where u_K the peak stored kinetic energy and u_S the peak stored elastic energy [2, 3].

The normal component of the Poynting vector takes the form[1]

$$\hat{\boldsymbol{n}}_\gamma \cdot \boldsymbol{S}_\alpha = \frac{1}{4}\omega_\alpha k \sin\theta |b_\alpha|^2 \hat{\xi}, \tag{1}$$

where for the bulk waves, $\hat{\xi} = \pm 1$ (J/m) is obtained from the Stroh-normalization[4], where the sign determines the direction of the Poynting vector. For bulk waves in an elastic medium, the peak elastic and kinetic stored energies are equal[2] and hence read as

$$(u_S)_\alpha = (u_K)_\alpha = \frac{1}{2}\rho \left| \frac{d\boldsymbol{u}_\alpha}{dt} \right|^2 = \frac{1}{2}\rho\omega_\alpha^2 |b_\alpha|^2 |\boldsymbol{A}_\alpha|^2, \tag{2}$$

where ρ is the density of the solid. As a result, the normal component of the group velocity can be expressed as:

$$\hat{\boldsymbol{n}}_\gamma \cdot \frac{\partial \omega_\alpha}{\partial \boldsymbol{k}} = \frac{\hat{\boldsymbol{n}}_\gamma \cdot \boldsymbol{S}_\alpha}{\frac{1}{2}(u_K + u_S)} = \frac{1}{2}\frac{\sin\theta}{\rho v_\alpha |\boldsymbol{A}_\alpha|^2}\hat{\xi}, \tag{3}$$

It is worth to mention here that, for an outward normal vector $\hat{\boldsymbol{n}}_\gamma$, a positive value of Eq.(3) indicates that the phonon travels in the direction from the solid towards the vacuum.

3 Near field radiative heat transfer

The near field radiative heat transfer (NFRHT) of two closely spaced parallel surfaces separated by a vacuum gap of width d has been very well studied. The associated heat flux between surface 1 with temperature T_1 and surface 2 with temperature T_2 can be obtained from $J_{1\to2}^{\mathrm{rad}} = J_1^{\mathrm{rad}} - J_2^{\mathrm{rad}}$ in which J_i^{rad} reads as[5, 6]

$$J_i^{\mathrm{rad}} = \frac{1}{\pi^2}\sum_{\sigma=p,s}\int_0^\infty\int_0^\infty \mathrm{d}\omega k_\parallel \mathrm{d}k_\parallel \frac{\hbar\omega}{e^{\hbar\omega/k_BT_i}-1}\frac{\mathrm{Im}(R_{\sigma1})\mathrm{Im}(R_{\sigma2})e^{-2k_\parallel d}}{|1-R_{\sigma1}R_{\sigma2}e^{-2k_\parallel d}|^2}, \quad (4)$$

where ω is the angular frequency, $k_\parallel$ is the component of $\boldsymbol{k}$-vector parallel to the surface, T_i is the temperature of surface $i = 1, 2$, and $R_{\sigma1}$ and $R_{\sigma2}$ are the reflection coefficients of surfaces 1 and 2 for wave mode $\sigma = p, s$. These coefficients are given by

$$R_p = \frac{\epsilon k_\perp - k'_\perp}{\epsilon k_\perp + k'_\perp}, \quad R_s = \frac{k_\perp - k'_\perp}{k_\perp + k'_\perp}, \quad (5)$$

where $\epsilon \equiv \epsilon(\omega)$ is the relative dielectric function of the metal, and $k_\perp$ and $k'_\perp$ are the components of $\boldsymbol{k}$-vectors perpendicular to the surface on the vacuum and material sides, respectively,

$$k_\perp = i\sqrt{k_\parallel^2 - \omega/v_c^2}, \quad k'_\perp = i\sqrt{k_\parallel^2 - \epsilon\omega/v_c^2}, \quad (6)$$

where v_c is the speed of light.

The Drude-model dielectric function of Au takes form[7]

$$\epsilon(\omega) = \epsilon_b - \frac{\omega_p^2}{\omega^2 + i\omega\nu}, \quad (7)$$

where we have used $\epsilon_b = 1$, $\omega_p = 1.71 \times 10^{16}\,\mathrm{s}^{-1}$, $\nu = 4.05 \times 10^{13}\,\mathrm{s}^{-1}$.

For the dielectric function of ZnO[8, 9], the vertical and parallel vibrational modes have different transverse-optical (TO) and longitudinal-optical (LO) frequencies. Thereby we have used ϵ_i for different polarizations to substitute ϵ in Eqs.(4),(5),(6), which reads as

$$\epsilon_i(\omega) = \epsilon_{\infty,i}\frac{\omega_{\mathrm{LO},i}^2 - \omega^2 - i\omega\gamma_i}{\omega_{\mathrm{TO},i}^2 - \omega^2 - i\omega\gamma_i}, \quad (8)$$

where $i = p, s$ describe the electric field polarization parallel or perpendicular to the crystal Z-axis, $\gamma_p = \gamma_s = 13\,\mathrm{cm}^{-1}$ is the damping parameter, and the rest of the parameters are given in Table 1:

4 Heat transfer mediated by other phonon tunneling mechanisms

Two other phonon tunneling mechanisms are discussed in the main text: coupling mediated by the van der Waals force and the electrostatic force. The heat

	$i=p$	$i=s$
$\epsilon_{\infty,i}$	3.78	3.7
$\omega_{\mathrm{LO},i}$ [cm^{-1}]	574	589
$\omega_{\mathrm{TO},i}$ [cm^{-1}]	384	411

Table 1: Parameters for the dielectric function of ZnO.

flux mediated by these mechanisms can be expressed in a general form developed by Volokitin[10] and given by

$$\begin{aligned} J_i^{\mathrm{Ph}} = \frac{1}{\pi^2}\int_0^\infty \mathrm{d}\omega \frac{\hbar\omega}{\exp(\hbar\omega/k_B T_i)-1} \\ \times \int_0^\infty \mathrm{d}k_\parallel\, k_\parallel \frac{b^2 \mathrm{Im}M_1 \mathrm{Im}M_2}{|(1-aM_1)(1-aM_2)-b^2M_1M_2|^2}, \end{aligned} \tag{9}$$

in which a and b parametrize the coupling mechanism and are defined as

$$\sigma_1 = au_1 - bu_2, \quad \sigma_2 = au_2 - bu_1, \tag{10}$$

where σ_i and u_i are the stress and displacement on surface $i = 1, 2$; M is the susceptibility of the material, $u = M\sigma$, and can be obtained as

$$M = \frac{i}{\rho c_t^2}\left(\frac{\omega}{c_t}\right)^2 \frac{p_l}{S}, \tag{11}$$

where

$$\begin{aligned} S = \left[\left(\frac{\omega}{c_t}\right)^2 - 2k_\parallel^2\right]^2 + 4k_\parallel^2 p_t p_l \\ p_t = \sqrt{\left(\frac{\omega}{c_t}\right)^2 - k_\parallel^2}, \quad p_l = \sqrt{\left(\frac{\omega}{c_l}\right)^2 - k_\parallel^2}, \end{aligned} \tag{12}$$

in which ρ, c_t, and c_l are the material density, the transverse phase velocity, and the longitudinal phase velocity, respectively.

For the van der Waals interaction, a and b read as

$$a = \frac{H}{2\pi d^4}, \quad b = \frac{H k_\parallel^2 K_2(k_\parallel d)}{4\pi d^2}, \tag{13}$$

where H is the Hamaker constant and $K_2(x)$ is the modified Bessel function of the second kind and second order. We note that by inserting Eqs.(13) into Eq.(9), we confirm that it becomes identical with Eq.(41) in Ref.[6].

With an electrostatic potential difference V between the surfaces, a and b take the form [10]

$$a = \frac{\epsilon_0 V^2 k_\parallel}{d^2}\frac{e^{k_\parallel d}+e^{-k_\parallel d}}{e^{k_\parallel d}-e^{-k_\parallel d}}, \quad b = \frac{\epsilon_0 V^2}{d^2}\frac{2k_\parallel}{e^{k_\parallel d}-e^{-k_\parallel d}}, \tag{14}$$

where we give the equations in SI units, unlike in the original work [10, 11] which uses CGS units.

For acoustic phonon tunneling between two Au surfaces, we use the following parameter values: $\rho = 1.92 \times 10^4\,\mathrm{kgm}^{-3}$, $c_t = 1200\,\mathrm{ms}^{-1}$, $c_l = 3240\,\mathrm{ms}^{-1}$, and $H = 34.7 \times 10^{-20}\,\mathrm{J}$[10].

5 Comparing ZnO and AlN with $LiNbO_3$

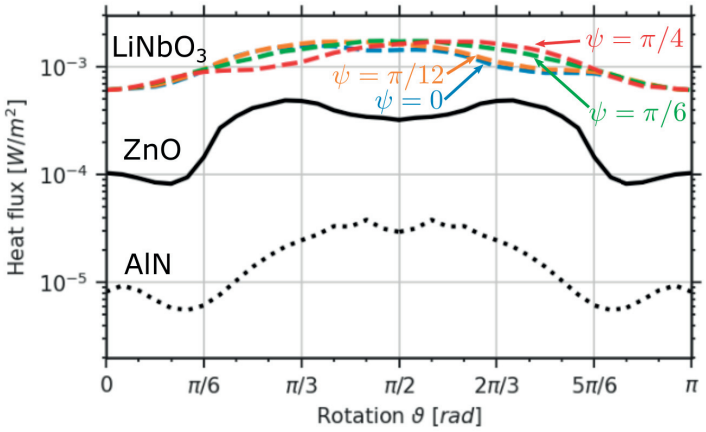

Figure 2: Comparison of emitted PEMHT as a function of the crystal rotation angle ϑ for ZnO (solid line), AlN (dotted line) and $LiNbO_3$ (colored dashed lines). Four different ψ rotations 0 (blue), $\pi/12$ (orange), $\pi/6$ (green), and $\pi/4$ (red) are plotted for $LiNbO_3$ as its has no uniaxial crystal symmetry. All heat fluxes are calculated for a gap width of 1 nm at a temperature of 0.1 K.

To add to Fig.4 of the main article, we compare the PEMHT of another piezoelectric material, $LiNbO_3$, with ZnO and AlN as a function of crystal rotation. The piezoelectric material constants adopted in the calculations are

$LiNbO_3$ has a trigonal crystal system without the uniaxial symmetry. Consequently, its PEMHT is expected to change with ψ rotations. We demonstrate the PEMHT of $LiNbO_3$ with four different ψ rotations, $0, \pi/12, \pi/6$, and $/\pi/4$ in Fig.2 as a function of ϑ rotation. By comparing to the results for ZnO, we find that PEMHT is even stronger for $LiNbO_3$, despite the fact that the phase velocities of these two materials are close. This is explained by $LiNbO_3$ having much larger piezoelectric stress constants e, as listed in Table.2, leading to an enhanced piezoelectric response on the solid-vacuum interface.

	ZnO[2]	AlN[12]	$LiNbO_3$[2]
c^E $(10^{10}Nm^{-2})$			
c_{11}	20.97	34.5	20.3
c_{33}	21.09	39.5	24.5
c_{44}	4.247	11.8	6
c_{66}	4.43	11	7.5
c_{12}	12.11	12.5	5.3
c_{13}	10.51	12	7.5
c_{14}			0.9
e (Cm^{-2})			
e_{15}	-0.48	-0.48	3.7
e_{22}			2.5
e_{31}	-0.573	-0.58	0.2
e_{33}	1.32	1.55	1.3
ϵ^S (ϵ_0)			
ϵ_{xx}	8.55	9.04	44
ϵ_{zz}	10.2	10.7	29
Density ρ (kgm^{-3})	5680	3260	4700
Crystal class	$6mm$	$6mm$	$3m$

Table 2: Anisotropic piezoelectric material constants used in the numerical calculations.

References

[1] Z. Geng and I. J. Maasilta, "Acoustic wave tunneling across a vacuum gap between two piezoelectric crystals with arbitrary symmetry and orientation," *Phys. Rev. Research*, vol. 4, no. 3, p. 033073, 2022.

[2] B. Auld, *Acoustic fields and waves in solids*. Malabar, Florida: Krieger, second ed., 1990.

[3] V. Laude, A. Reinhardt, and A. Khelif, "Equality of the energy and group velocities of bulk acoustic waves in piezoelectric media," *IEEE Trans. Ultrason. Ferroelectr. Freq. Control*, vol. 52, no. 10, pp. 1869–1871, 2005.

[4] Z. Geng and I. J. Maasilta, "Complete tunneling of acoustic waves between piezoelectric crystals." arXiv:2209.08287, 2022.

[5] K. Joulain, J.-P. Mulet, F. Marquier, R. Carminati, and J.-J. Greffet, "Surface electromagnetic waves thermally excited: Radiative heat transfer, coherence properties and Casimir forces revisited in the near field," *Surf. Sci. Rep.*, vol. 57, pp. 59–112, may 2005.

[6] J. B. Pendry, K. Sasihithlu, and R. V. Craster, "Phonon-assisted heat transfer between vacuum-separated surfaces," *Phys. Rev. B*, vol. 94, no. 7, p. 075414, 2016.

[7] P.-O. Chapuis, S. Volz, C. Henkel, K. Joulain, and J.-J. Greffet, "Effects of spatial dispersion in near-field radiative heat transfer between two parallel metallic surfaces," *Phys. Rev. B*, vol. 77, p. 035431, jan 2008.

[8] N. Ashkenov, B. N. Mbenkum, C. Bundesmann, V. Riede, M. Lorenz, D. Spemann, E. M. Kaidashev, A. Kasic, M. Schubert, M. Grundmann, G. Wagner, H. Neumann, V. Darakchieva, H. Arwin, and B. Monemar, "Infrared dielectric functions and phonon modes of high-quality ZnO films," *J. Appl. Phys.*, vol. 93, no. 1, pp. 126–133, 2003.

[9] P. Ooi, S. Lee, S. Ng, Z. Hassan, and H. A. Hassan, "Far Infrared Optical Properties of Bulk Wurtzite Zinc Oxide Semiconductor," *J. Mater. Sci. Technol.*, vol. 27, no. 5, pp. 465–470, 2011.

[10] A. I. Volokitin, "Contribution of the acoustic waves to near-field heat transfer," *J. Phys.: Condens. Matter*, vol. 32, no. 21, p. 215001, 2020.

[11] A. I. Volokitin, "Effect of an Electric Field in the Heat Transfer between Metals in the Extreme Near Field," *JETP Lett.*, vol. 109, no. 11, pp. 749–754, 2019.

[12] K. Tsubouch and N. Mikoshiba, "Zero-Temperature-Coefficient SAW Devices on AlN Epitaxial Films," *IEEE Trans. Sonics Ultrason.*, vol. 32, no. 5, pp. 634–644, 1985.

PIV

EXPERIMENTAL DEMONSTRATION OF HEAT TRANSFER MEDIATED BY ACOUSTIC PHONON TUNNELING BETWEEN VACUUM SEPARATED PIEZOELECTRIC SOLIDS

by

Z. Geng & I. J. Maasilta

Manuscript

Request a copy from the author.